Terms and Conditions of Use of Digitised Theses from Trinity College Library Dublin

Copyright statement

All material supplied by Trinity College Library is protected by copyright (under the Copyright and Related Rights Act, 2000 as amended) and other relevant Intellectual Property Rights. By accessing and using a Digitised Thesis from Trinity College Library you acknowledge that all Intellectual Property Rights in any Works supplied are the sole and exclusive property of the copyright and/or other IPR holder. Specific copyright holders may not be explicitly identified. Use of materials from other sources within a thesis should not be construed as a claim over them.

A non-exclusive, non-transferable licence is hereby granted to those using or reproducing, in whole or in part, the material for valid purposes, providing the copyright owners are acknowledged using the normal conventions. Where specific permission to use material is required, this is identified and such permission must be sought from the copyright holder or agency cited.

Liability statement

By using a Digitised Thesis, I accept that Trinity College Dublin bears no legal responsibility for the accuracy, legality or comprehensiveness of materials contained within the thesis, and that Trinity College Dublin accepts no liability for indirect, consequential, or incidental, damages or losses arising from use of the thesis for whatever reason. Information located in a thesis may be subject to specific use constraints, details of which may not be explicitly described. It is the responsibility of potential and actual users to be aware of such constraints and to abide by them. By making use of material from a digitised thesis, you accept these copyright and disclaimer provisions. Where it is brought to the attention of Trinity College Library that there may be a breach of copyright or other restraint, it is the policy to withdraw or take down access to a thesis while the issue is being resolved.

Access Agreement

By using a Digitised Thesis from Trinity College Library you are bound by the following Terms & Conditions. Please read them carefully.

I have read and I understand the following statement: All material supplied via a Digitised Thesis from Trinity College Library is protected by copyright and other intellectual property rights, and duplication or sale of all or part of any of a thesis is not permitted, except that material may be duplicated by you for your research use or for educational purposes in electronic or print form providing the copyright owners are acknowledged using the normal conventions. You must obtain permission for any other use. Electronic or print copies may not be offered, whether for sale or otherwise to anyone. This copy has been supplied on the understanding that it is copyright material and that no quotation from the thesis may be published without proper acknowledgement.
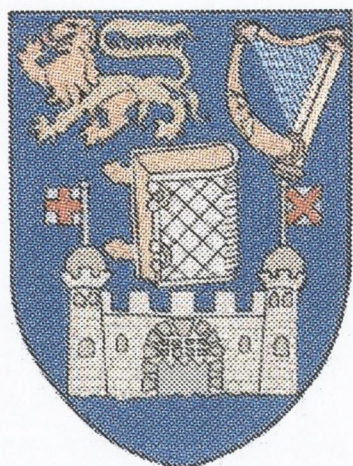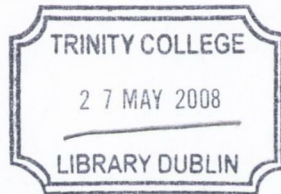
Electron Transport in Molecular Devices

By

Cormac Toher

A thesis submitted for the degree of
Doctor of Philosophy
School of Physics
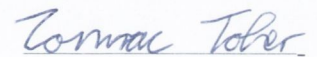Trinity College Dublin

2008

Declaration

I, Cormac Toher, hereby declare that this dissertation has not been submitted as an exercise for a degree at this or any other University.

It comprises work performed entirely by myself during the course of my Ph.D. studies at Trinity College Dublin. I was involved in a number of collaborations, and where it is appropriate my collaborators are acknowledged for their contributions.

A copy of this thesis may be lended or copied by the Trinity College Library upon request by a third party provided it spans single copies made for study purposes only, subject to normal conditions of acknowledgement.

Cormac Toher

Cormac Toher

Abstract

The study of electronic transport in molecular devices is one of much research interest, with potential applications in a range of different fields. These devices have been experimentally constructed using many different techniques, and also modelled using several computational methods. The method most commonly used to perform such calculations is the non-equilibrium Green's function formalism combined with density functional theory (DFT). However, DFT calculations based on local exchange and correlation functionals contain self-interaction errors. The primary purpose of this work is to investigate the effects of these errors on electronic transport calculations. We describe the origin of the self-interaction error in DFT, as well as its consequences including the absence of the derivative discontinuity in approximate local exchange-correlation potentials. Exact and approximate self-interaction corrections to remove these errors are also described.

Transport calculations were performed using the non-equilibrium Green's function code SMEAGOL for a variety of metal-molecule junctions. We use a tight-binding Hamiltonian to show that the derivative discontinuity can open conductance gaps in the I-V curves. An atomic self-interaction correction (ASIC) to DFT is used to investigate the effect of correcting the alignment between the energy levels in the molecule and the Fermi level in the metal. Both of these methods improve the agreement between theory and experiment.

Finally, the use of SMEAGOL to simulate STM tunnelling current measurements for alkanethiol molecules is investigated. We show how the difference in the strength of the interaction between the molecule and the tip compared to the substrate can lead to strong asymmetry in the I-V curves.

i

Acknowledgements

Over the last four years, I received a lot of help and support from a large number of people, without whom none of this research would have been possible.

First of all, I would like to thank my supervisor Prof. Stefano Sanvito. When I joined his group four years ago, he had one other student and one postdoc based in the arches underneath the railway. Now, his group is one of the largest in the School of Physics, and he has established himself as one of the leaders in the field of computational materials science and molecular electronics. I have benefitted greatly from his advice and teaching during my time in his research group.

Secondly, I need to thank our external collaborators Prof. Kieron Burke, formerly of Rutgers in New Jersey and now based in University of California, Irvine, and Prof. Alessio Filippetti from the University of Cagliari, Italy. Without the assistance of both of these researchers the work described in this thesis could not have been performed. It was our discussions with Kieron during a visit he made to our group over three years ago that led to us investigating the effect of the derivative discontinuity in electronic transport. Alessio developed the pseudo-SIC approximation on which ASIC, used in calculations in this thesis, is based. He also calculated the discontinuous self-consistent potentials which we used in conjunction with the tight-binding Hamiltonian.

As I mentioned above, Stefano's group has grown large, with a current total of ten postgraduate students and two postdocs, as well as two former poststudents and two former postdocs. However, there are a few former and current group members whose assistance was vital to the work performed in this thesis. Alex Rocha was Stefano's very first student, and he did the bulk of the work of developing SMEAGOL, in collaboration with groups in Lancaster, England and Oviedo, Spain. He has since graduated and is now a postdoctoral researcher in his native Brazil. He provided a lot of assistance during the three and a half years in which we were both in Stefano's group, and also during his return visit while I was writing this thesis. Chaitanya Das Pemmaraju was responsible for implementing ASIC in SIESTA, and teaching me the rules of cricket, and is also currently in the process of finishing his PhD. Miguel

Contents

List of Figures

List of Tables

Chapter 1

Introduction

The field of molecular electronics began with the suggestion of Aviram and Ratner that an organic molecule could be used as a logic gate [1]. In recent years, several examples of molecular devices in the form of metal-molecule-metal junctions have been constructed using a variety of methods such as mechanical break junctions and scanning tunnelling microscopes (STM). The study of the electronic transport properties of such devices is currently becoming one of much research interest.

Possible applications of such devices range from novel computer architectures [2, 3, 4, 5], which will be smaller, faster, cheaper to manufacture and consume less power; to highly sensitive chemical sensors [6, 7, 8]; to diagnostic medical tools which can identify individual viruses or proteins [9]. Another interesting application which has been suggested recently is to use molecular electronics to sequence strands of DNA, where individual base-pairs are distinguished by their transverse conductivity [10, 11].

One major advantage of molecular electronics over traditional semiconductor electronics is that circuits can be manufactured via self-assembly. Lithographic fabrication is becoming increasingly expensive as microchip components continue to shrink, and self-assembly, whereby molecules are deposited on the surface, would allow circuits with component sizes an order of magnitude smaller than those in current commercial computer processors to be manufactured at much lower cost. It is also possible that molecules could be selected to give very low "off" currents, thus reducing power usage and cooling requirements. Another possible application for molecular electronics is in the manufacture of cheap, fast, high-density, non-volatile memory, similar to the concepts proposed for magnetic random access memory (MRAM)[12].

However, the applications related to computing are only a small section of the possibilities offered by molecular electronic devices. There have been several proposals for chemical and biological sensors, in which molecules, viruses, antibodies,

1

proteins, etc. are detected by their effects on the electronic properties of nanotubes [6, 7] or nanowires [8]. There is also a lot of research currently being done on the electronic transport properties of DNA, from sequencing strands of DNA by measuring the conductivity of individual base pairs[10, 11], to understanding how DNA molecules can transport charge along their length [13, 14, 15]. Research is also being performed on using strands of DNA as a template to position molecular devices in electronic circuits [16, 17]. Because of the base-pairing mechanism in DNA, where each type of base will only bond to one other base, it is possible to set up lock and key type mechanisms, so that a molecular device with a short strand of DNA attached will attach to a specific point on a DNA wire. Also, metal atoms, such as silver or gold, can then be deposited on the exposed parts of the DNA strands after the molecular devices have been positioned in order to form a conducting circuit.

A typical molecular device consists of a thiolated organic molecule sandwiched between two metallic electrodes. The sulfur atoms in the thiol groups anchor the molecules to the metal surfaces. The metal normally used for such experiments is gold, due to its high conductivity and resistance to corrosion. Nickel electrodes are also used in spintronic experiments, where spin polarised currents are measured [18]. However, nickel has the disadvantage of oxidising relatively rapidly (compared to gold or silver), with nickel oxide forming on the surface and making repeated measurements difficult. The organic molecules used fall into two main groups: conjugated molecules such as benzenedithiol (BDT), biphenyldithiol (BPD) and triphenyldithiol (tricene) which have delocalised carbon π bonds across the molecule and thus relatively high conductivities; and non-conjugated molecules such as alkanethiols, or benzenedimethanethiol (BDMT) in which the π conjugation is broken by the methyl groups.
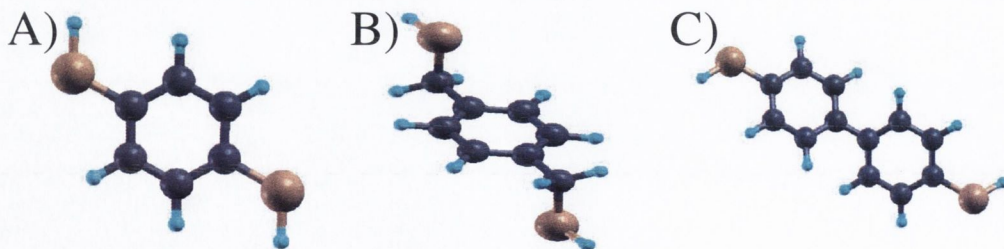
Figure 1.1: Simple organic molecules used in molecular electronics experiments: (A) Benzenedithiol (BDT), (B) benzenedimethanethiol (BDMT),(C) biphenyldithiol (BPD). Colour code: C=black, S=brown, H=blue.

Several different methods have been used to construct such devices, such as

mechanically controllable break junctions [19, 20, 21, 22, 23, 24, 25], STM tips [25, 26, 27, 28], lithographically fabricated nanoelectrodes [29], and colloid solutions [30]. Break junction molecular devices are created by attaching a thin metal wire to a flexible substrate, where the wire is surrounded by a solution containing the molecule. The molecules form a self-assembled monolayer (SAM) over the surface of the metal. The wire is then stretched by bending the flexible substrate. When the wire breaks, one of the molecules on the metal surface may bridge the gap formed. The bending is usually controlled by the elongation of a piezoelectric element placed underneath the substrate as shown in figure 1.2(a), so that the width of the gap in the wire can be controlled with extreme precision. In a typical experiment, the gap is closed and reformed multiple times, so that several devices are formed and statistical measurements can be taken.
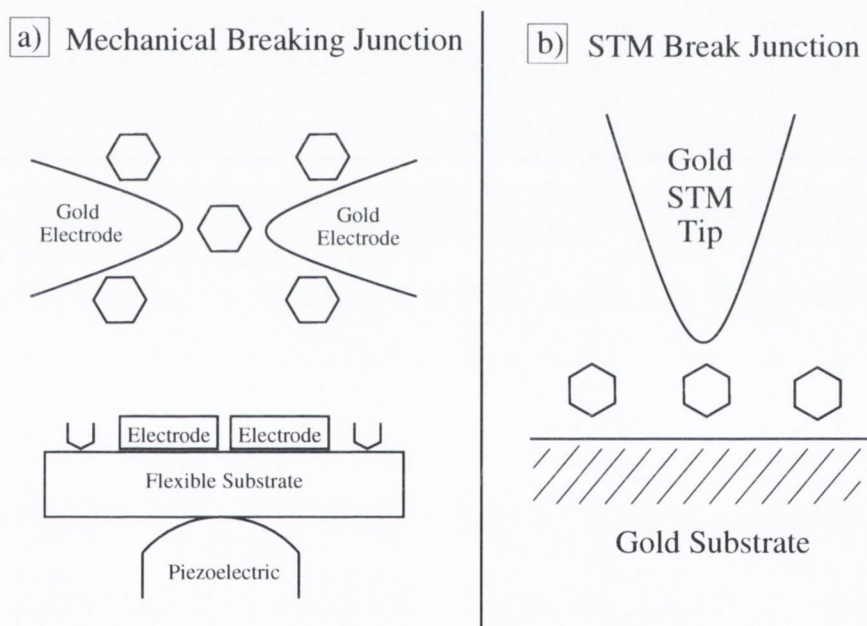
Figure 1.2: Schematic of experimental set up for (a) mechanical breaking junction and (b) STM breaking junction. In a mechanical breaking junction, a metallic nanowire is coated with a layer of molecules and then stretched to breaking point. A single molecule is thus trapped in the gap formed. In the STM breaking junction, a metallic substrate is coated with sparse layer of molecules. One of the molecules is then located and contacted to the tip, which is then pulled upwards to form the device.

The devices can also be constructed using an STM breaking junction [26, 27, 28], as shown in figure 1.2. A sparse monolayer of molecules can be deposited on a surface of the metal, which forms one electrode. Then, the STM tip, which is formed

from the same metal as the surface, can be used to contact the top of one of the molecules. This forms a circuit, allowing the *I-V* characteristics of the molecule to be investigated. The tip can then be pulled upwards to stretch the contact until it breaks. Once again, this procedure can be repeated multiple times to obtain statistical measurements. Alternatively, metal nanoparticles can be attached to the top of the molecules which are attached to a substrate. The nanoparticles are then contacted by the tip of an STM [31, 32] or an atomic force microscope (AFM) [33], completing the circuit and allowing transport measurements to be made.

The electrodes can also be fabricated using lithographic techniques, with the size of the gap between the electrodes being manufactured to be equal to the length of the molecule in question. The molecules can then be deposited in the gap [29]. Their presence is usually monitored and confirmed by a scanning electron microscope (SEM). Finally, instead of directly depositing the molecules in the gap, the molecules can be combined with a solution of colloid nanoparticles of the metal, so that a metal particle attaches to each end of the molecule. These structures are then deposited between the lithographically fabricated nanoelectrodes, with their presence in the gap being confirmed using a tunnelling electron microscope (TEM) [30].

Unfortunately, there is much disagreement between the experimental results obtained using these different methods for these and other molecules. For example, for BDT contacted to gold the values of the zero-bias conductance vary from $10^{-5}G_0$ [19] observed with a mechanical break junction, to $0.011G_0$ [26] measured by an STM. In order to explain these differences, researchers have turned to theoretical models. Different computational methods used to investigate such systems range from the non-equilibrium Green's function formalism (NEGF) [34, 35, 36] combined with electronic structure methods [37, 38, 39, 40, 41, 42] such as density functional theory (DFT)[43, 44, 45]; to empirical tight-binding methods [46, 47, 48, 49], many-body methods [50, 51, 52, 53, 54, 55, 56] and time-dependent density functional theory (TDDFT) [57, 58]. However, these methods also disagree on the results, and they show that the electronic transport properties of a metal-molecule junction can be highly sensitive to how the molecule attaches to the metal surface.

The NEGF formalism combined with DFT [37, 38, 39, 40, 41, 42], using a local exchange correlation functional such as the local density approximation (LDA) [44] or the generalised gradient approximation (GGA)[59, 60, 61], is the most commonly used *ab initio* method for electronic transport calculations. It has the advantage of combining accurate results with good scaling - there are methods which are currently under development which scale linearly with the number of atoms [62]. Un-

fortunately, often the results obtained with NEGF-DFT do not match those of the experiments, giving zero-bias conductances for a variety of metal-molecule anchoring geometries higher than those measured experimentally [63, 64, 65, 66, 67, 68, 69, 70]. Some of these problems may be due to the fact that the true metal-molecule contact geometry is unknown. Another possibility is that the problem lies in the approximations made to the electronic structure methods used. DFT is only valid for the ground state of a system, and so, strictly speaking, it is not correct to use it when a finite potential bias is applied. TDDFT [57] has been formulated to deal with this problem, as well as to calculate excited states. However, TDDFT is computationally quite heavy, and to date has mainly been applied to single atoms and simplified models. Finally, the local exchange correlation functionals usually used with DFT contain self-interaction errors [71], which can result in the energy levels of the molecule being in the wrong place. This error can also result in the suppression of the derivative discontinuity [72, 73], which would affect how the molecular orbitals respond to changes in their occupation. It is the effects of these self-interaction errors on electronic transport calculations [74], as well as possible solutions to the problem [75, 76], that are the main focus of the research presented in this thesis.
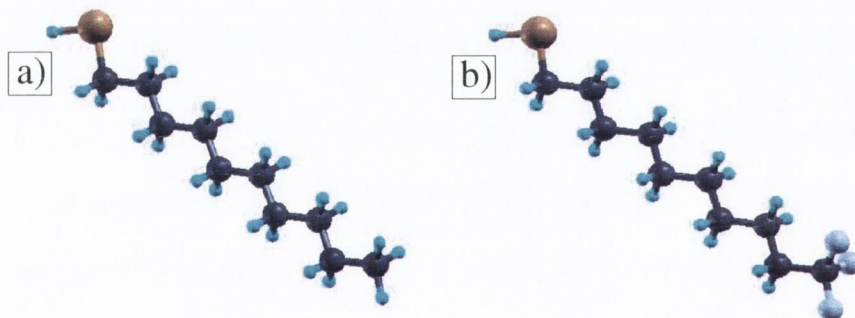
Figure 1.3: Decanethiol molecule (a) with CH_3-endgroup and (b) with CF_3-endgroup. Colour code: C=black, S=brown, H=blue, F=purple.

The electron transport properties of organic molecules can also be studied without actually forming two contacts, by using a scanning tunnelling microscope [77, 78]. If the molecules are attached to a metallic surface, the STM probe tip can be placed in the vicinity of the molecule end group, and the tunnelling current through the molecule can be measured. Normally, calculations for such systems are performed using the Tersoff-Hamann method [79, 80], in which the tip is assumed to be sufficiently far from the molecule that it does not affect its electronic structure. However, if the STM tip is close to the molecule, then the interaction between the tip and the

molecule will become important, and a method such as NEGF combined with DFT will need to be used. One such set of measurements is that performed by Pflaum et. al. [81] on CH_3- and CF_3-terminated decanethiol, as shown in figure 1.3. In this set of experiments, a much stronger asymmetry was observed in the I-V curves for the CF_3-endgroup than for the CH_3-endgroup. It was suggested that this difference was due to the interaction between the molecule endgroup and the STM tip with an applied bias. This type of effect cannot be investigated using the Tersoff-Hamann model, instead requiring a method such as NEGF.

1.1   Dissertation Layout

In this thesis, I will describe the methods used to perform electronic structure and transport calculations for molecular devices. I will present the results of such calculations for a variety of different metal-molecule junctions. In particular, I will investigate how errors in the approximations made in electronic structure theory affect the results of electron transport calculations.

In chapter two, I will give a brief introduction to density functional theory (DFT) [43], including the Kohn-Sham formalism [44] and the SIESTA [82, 83, 84] implementation. The self-interaction problem [71] and its consequences will be described, including the absence of the derivative discontinuity in approximate local exchange-correlation potentials [72, 73]. Both exact and approximate self-interaction corrections (SIC) [71, 75] to remove these errors will then be described.

In chapter three, I will describe a simple model for electron transport in molecules [85]. Using this model, I will demonstrate how certain features of the electronic structure of metal-molecule junctions, such as the level alignment, the strength of the interaction between the leads and the molecule, and the response of the level to changes in its occupation, affect the conductance.

In chapter four, the non-equilibrium Green's function formalism (NEGF) [34, 35, 36] will be described. It will be shown how this method has been combined with DFT to form the SMEAGOL program [37, 38, 39], and then used to calculate the electronic structure of infinite, non-periodic systems which have an external potential bias applied. I will also show how to use this method to calculate transmission probabilities and I-V curves for such systems.

In chapter five, I will present the results of electron transport calculations for the BDT molecule attached to gold electrodes [74]. These calculations were performed using a self-consistent tight-binding Hamiltonian, which incorporated discontinuities

into the dependence of the molecular orbitals on their occupation. This system will be used to study the effect of the derivative discontinuity on electron transport in molecular devices under a variety of different conditions.

In chapter six, the results of electron transport calculations for a variety of molecular devices performed using self-interaction corrected DFT are presented. An approximate SIC, the atomic self-interaction correction (ASIC) [75], has been incorporated in to SIESTA, which forms the basis for the non-equilibrium transport code SMEAGOL. This method was used to perform calculations for molecular devices formed from BDT, BPD and BDMT sandwiched between gold electrodes, and the results are discussed.

In chapter seven, we move away from the self-interaction problem, and instead look at simulating STM electron transport measurements using SMEAGOL. In particular, the results of some ongoing calculations for alkanethiols on a gold surface will be presented. A comparison to some experimental measurements performed on a similar system [81] will be made, and future directions for these calculations will be suggested.

Finally, the conclusions which can be drawn from this work will be discussed. Some suggestions for solving some of the remaining problems highlighted by the work in this thesis will also be discussed.

Chapter 2

Density Functional Theory and Self-Interaction Errors

The molecular devices described in this thesis contain of the order of one hundred atoms, while the valence orbitals which need to be described may number in the thousands. Describing such devices accurately using computational techniques which will produce results within a reasonable time frame is a major electronic structure problem. Many-body problems with large numbers of particles do not have analytical solutions, and the exact numerical methods are infeasible as they do not scale well with increasing system size. Therefore, any electronic structure method used to calculate the properties of such devices will have to contain approximations. These include empirical methods such as the tight-binding method, and ab initio methods such as Hartree-Fock theory and density functional theory (DFT) [45, 86].

DFT is one of the most popular ab initio methods, particularly for large systems and electronic transport calculations, due to its blend of accuracy and computational efficiency. The main approximation in this method is in using local exchange-correlation functionals, which may contain self-interaction errors - the interaction of an electron with its own potential. Corrections to remove this self-interaction error will be described in this chapter, and the effects of these corrections on electronic transport calculations for metal-molecule junctions will be explored in later chapters.

The basic problem to be solved for any many-particle system in quantum mechanics is the many-body Schrödinger equation, which takes the form of an eigenvalue problem for a Hamiltonian operator $\hat{H}$ acting on a many-body wave function ψ, giving an energy E

$$\hat{H}\psi = E\psi \,. \tag{2.1}$$

The full quantum mechanical Hamiltonian operator $\hat{H}$ for the many-body system

has the form

$$\hat{H} = \sum_i^{N_e} -\frac{\hbar^2}{2m_e}\nabla^2_{\mathbf{r}_i} + \sum_I^{N_N} -\frac{\hbar^2}{2M_I}\nabla^2_{\mathbf{R}_I} + \frac{1}{2}\sum_{I \neq J}^{N_N} \frac{e^2 Z_I Z_J}{|\mathbf{R}_I - \mathbf{R}_J|} \tag{2.2}$$

$$-\sum_{i,I}^{N_e,N_N} \frac{e^2 Z_I}{|\mathbf{r}_i - \mathbf{R}_I|} + \frac{1}{2}\sum_{i \neq j}^{N_e} \frac{e^2}{|\mathbf{r}_i - \mathbf{r}_j|}, \tag{2.3}$$

where $\mathbf{r}_i$ is the position operator for the i-th electron and $\mathbf{R}_I$ is the position operator for the I-th nucleus. The first and second terms represent the kinetic energy for the the electrons with mass m_e and the nuclei with mass M_I. The third term represents the Coulomb interaction between the nuclei, the fourth term represents the Coulomb interaction between the nuclei and the electrons, and the fifth term represents the electron-electron interaction.

The first approximation which can be made to help simplify this problem is the Born-Oppenheimer approximation, in which the nuclear motion and the electronic parts of the wave function are separated. The masses of the nuclei are much larger than those of the electrons, so that in classical terms they move at a far lower speed than the electrons. Hence the electronic wave function can be separated from that of the nuclei as follows

$$\psi = \psi(\mathbf{r}_1, \mathbf{r}_2, \ldots, \mathbf{r}_i, \ldots, \mathbf{r}_{N_e}; \mathbf{R}_1, \mathbf{R}_2, \ldots, \mathbf{R}_I, \ldots, \mathbf{R}_{N_N}) \tag{2.4}$$

$$= \psi_e(\mathbf{r}_1, \mathbf{r}_2, \ldots, \mathbf{r}_i, \ldots, \mathbf{r}_{N_e})\psi_N(\mathbf{R}_1, \mathbf{R}_2, \ldots, \mathbf{R}_I, \ldots, \mathbf{R}_{N_N}). \tag{2.5}$$

Hence, an electronic structure theory can treat the positions of the nuclei as being fixed, and just solve for the many-body electron wave function.

Once the Born-Oppenheimer approximation has been made, and the nuclear part of the Hamiltonian separated out, the Hamiltonian $\hat{H}$ for a system of interacting electrons can be written in the form

$$\hat{H} = \hat{T} + \hat{V}_{ee} + \sum_i v(\mathbf{r}_i), \tag{2.6}$$

where $\hat{T}$ is the kinetic energy, $\hat{V}_{ee}$ is the energy due to the electron-electron interaction, and $\sum_i v(\mathbf{r}_i)$ is the external potential, which includes contributions due the interaction of the electrons with the nuclei, as well as with applied electric fields.

2.1   Hartree-Fock Theory

One of the most popular methods for solving the electronic Schrödinger equation for many-particle systems is that of Hartree-Fock [45, 86]. It involves solving self-consistently for the many-body electron wave function.

Since electrons are fermions, the total electronic wave function must be antisymmetric. This condition is trivially satisfied for a Slater determinant of single-particle wave functions $\phi_i(\mathbf{r_j})$, and so this makes a good initial approximation for the many-body electronic wave function.

$$\Psi^e_{HF} = \frac{1}{\sqrt{N!}}\det\left[\phi_i(\mathbf{r_j})\right]. \tag{2.7}$$

The single-particle wave functions $\phi_i(\mathbf{r_j})$ are usually modelled as localised orbitals, such as linear combinations of Gaussian-type orbitals. These orbitals are then used in a self-consistent calculation to minimise the total energy, which corresponds to the ground state of the system.

$$E^{\mathrm{GS}}_{\mathrm{HF}} = \sum_{\min\Psi^e_{HF}} \frac{\langle\Psi^e_{HF}|\hat{H}|\Psi^e_{HF}\rangle}{\langle\Psi^e_{HF}|\Psi^e_{HF}\rangle}. \tag{2.8}$$

Hartree-Fock theory can be extended by using linear combinations of Slater determinants to approximate the many-body electronic wave function. These additional determinants describe different configurations of the electrons in the molecule, i.e. they describe excited states of the system. This approach is known as configuration interaction [45, 86], and can be used to describe excitations and calculate electron correlation.

Unfortunately, Hartree-Fock calculations do not scale well with system size. The size of the calculation increases as N^5, where N is the number of basis functions. Therefore, while it is useful for small molecules and systems with periodic boundary conditions with small unit cells, it is not practical for calculating the large, extended molecule type devices with hundreds of atoms which are described in this thesis.

2.2   Density Functional Theory

Density functional theory (DFT) [45, 86] was originally proposed by Hohenberg and Kohn [43]. They demonstrated that finding the ground-state many-body wave function is equivalent to obtaining the ground-state charge density. They also showed that the ground state charge density for a given potential is unique. Kohn and Sham

[44] then used this to formulate a method where a system of non-interacting single particle equations were solved instead to obtain the ground-state charge density of the real system.

2.2.1 Hohenberg-Kohn Theorem

Hohenberg and Kohn [43] showed that the potential of a system of electrons is uniquely specified by the ground-state charge density for that system. This can be proved by *reductio ad absurdum* by showing that there being two different potentials which give the same ground state charge density $\rho(\mathbf{r})$ will result in a contradiction.

The fact that the charge density for a specific system is unique allows it to be used as the relevant variable instead of the many-body wave function. This is hugely beneficial in terms of making large electronic structure problems tractable, as while the wave function has to be calculated for each particle, the charge density is given by a single value at each point in space. Thus, the $3N!$ variables required to specify the wave function at a point in space are reduced to the 3 variables required to describe the charge density.

Note that, strictly speaking, this theorem is only valid for ground states. For example, unoccupied states have zero charge density, and thus are meaningless in standard DFT. Therefore, DFT should not be used for applications which involve empty states such as calculating band gaps in semiconductors. One solution to this problem is to used time-dependent DFT (TDDFT) [57], in which electrons are temporarily excited into higher states, allowing them to be calculated.

2.2.2 Kohn-Sham Equations

The Hohenberg-Kohn theorem shows that finding the ground state of the system is equivalent to finding the ground state charge density. Kohn and Sham [44] were able to map the problem of finding the ground state charge density onto that of solving a system of non-interacting single-particle Schrödinger equations. This offers a practical method of solving DFT problems, which in principle can include any many-body ground state electronic structure problem.

In order to derive these equations, we start by defining the universal functional F of the charge density $\rho(\mathbf{r})$ to be the minimum expectation value of sum of the kinetic energy operator $\hat{T}$ and electron-electron interaction potential $\hat{V}_{ee}$.

$$F[\rho_{\uparrow}, \rho_{\downarrow}] = \min\langle \hat{T} + \hat{V}_{ee} \rangle, \tag{2.9}$$

where $\rho_\uparrow$ and $\rho_\downarrow$ are the spin-up and spin-down charge densities. This universal functional F can be broken into three parts

$$F[\rho_\uparrow, \rho_\downarrow] = T[\rho_\uparrow, \rho_\downarrow] + U[\rho] + E_{\mathrm{XC}}[\rho_\uparrow, \rho_\downarrow] \,. \tag{2.10}$$

where $T[\rho_\uparrow, \rho_\downarrow]$ is the "non-interacting" kinetic energy, $U[\rho]$ is the "Hartree" energy (i.e. the classical Coulomb energy), and $E_{\mathrm{XC}}[\rho_\uparrow, \rho_\downarrow]$ is the "exchange-correlation" energy. The spin charge densities, ρ_σ, can then be written as a sum over a set of orthonormal orbitals $\psi_{\alpha\sigma}(\mathbf{r})$, which are weighted by Fermi functions $0 \leq f_{\alpha\sigma} \leq 1$

$$\rho_\sigma = \sum_\alpha f_{\alpha\sigma} |\psi_{\alpha\sigma}(\mathbf{r})|^2 \,; \rho = \rho_\uparrow + \rho_\downarrow \,. \tag{2.11}$$

The "non-interacting" kinetic energy, $T[\rho_\uparrow, \rho_\downarrow]$ can be defined in terms of these orthonormal orbitals as shown in equation (2.12), where the minimum is taken over the all possible values of $f_{\alpha\sigma}$ and $\psi_{\alpha\sigma}$ which produce the given spin charge densities.

$$T[\rho_\uparrow, \rho_\downarrow] = \min \left[\sum_\alpha f_{\alpha\sigma} \langle \psi_{\alpha\sigma}(\mathbf{r}) | \left(-\frac{1}{2} \nabla^2 \right) | \psi_{\alpha\sigma}(\mathbf{r}) \rangle \right] \,. \tag{2.12}$$

The Hartree energy, $U[\rho]$, is the energy due to the classical Coulomb electron-electron interaction, and so has the form

$$U[\rho] = \frac{1}{2} \int d^3r \int d^3r' \frac{\rho(\mathbf{r})\rho(\mathbf{r}')}{|\mathbf{r} - \mathbf{r}'|} \,. \tag{2.13}$$

The exchange-correlation energy, E_{XC}, contains the remaining part electron-electron interaction energy. The exact form of this energy is as yet unknown, and must be approximated. Various approximations to this energy which are currently in use are described in section 2.2.4.

The variational principle gives that $\langle \hat{H} \rangle \geq E^{\mathrm{GS}}$, where E^{GS} is the ground state energy, so that

$$F[\rho_\uparrow, \rho_\downarrow] + \sum_i v(\mathbf{r}_i)\rho(\mathbf{r}) \geq E^{\mathrm{GS}} \,, \tag{2.14}$$

where $v(\mathbf{r}_i)$ is the part of the potential which is not due to electron-electron interactions, and includes the potential of the atomic nuclei as well as any external applied electric fields. Next we can introduce $\tilde{E}$, which is the expectation value of the many-body electron Hamiltonian, with respect to the orthonormal orbitals $\psi_{\alpha\sigma}(\mathbf{r})$

$$\tilde{E} = F[\rho_\uparrow, \rho_\downarrow] + \int d^3 r v(\mathbf{r})\rho(\mathbf{r})$$

$$= \sum_\alpha f_{\alpha\sigma} \langle \psi_{\alpha\sigma}(\mathbf{r})| \left(-\frac{1}{2}\nabla^2\right) |\psi_{\alpha\sigma}(\mathbf{r})\rangle + U[\rho]$$

$$+ E_{XC}[\rho_\uparrow, \rho_\downarrow] + \int d^3 r v(\mathbf{r})\rho(\mathbf{r}) .$$

To find the ground state of the system, this has to be minimised with respect to the orthonormal orbitals $\psi_{\alpha\sigma}(\mathbf{r})$, subject to the constraint that the orbitals are normalised. To handle this constraint, introduce the Lagrangian multipliers $\epsilon_{\alpha\sigma} f_{\alpha\sigma}$ to get the Euler equation

$$\frac{\delta}{\delta\psi_{\alpha\sigma}(\mathbf{r})} \left[\tilde{E} - \sum_{\alpha'\sigma'} \epsilon_{\alpha'\sigma'} f_{\alpha'\sigma'} \int d^3 r' |\psi_{\alpha\sigma}(\mathbf{r})|^2 \right] = 0 . \tag{2.15}$$

Differentiating $\tilde{E}$ with respect to the wave function $\psi_{\alpha\sigma}(\mathbf{r})$, using the relationship between the wave function and the charge density given in equation (2.11), gives the following result

$$\frac{\delta}{\delta\psi_{\alpha\sigma}(\mathbf{r})}\tilde{E} = \sum_{\alpha\sigma} \left[-\frac{1}{2}\nabla^2 + v^\sigma_{EFF}\right] f_{\alpha\sigma}\psi_{\alpha\sigma}(\mathbf{r}) , \tag{2.16}$$

Inserting the result from equation (2.16) into equation (2.15), an equation for $\epsilon_{\alpha\sigma}$ and $\psi_{\alpha\sigma}$ can be obtained

$$\sum_{\alpha\sigma} f_{\alpha\sigma} \left[-\frac{1}{2}\nabla^2 + V^\sigma_{EFF}\right] \psi_{\alpha\sigma}(\mathbf{r}) - \sum_{\alpha\sigma} f_{\alpha\sigma}\epsilon_{\alpha\sigma}\psi_{\alpha\sigma}(\mathbf{r}) = 0 . \tag{2.17}$$

This can be separated into a set of Schrödinger-like equations for the effective potential v^σ_{EFF}, with eigenvalues $\epsilon_{\alpha\sigma}$. These are the Kohn-Sham equations, and can be written as follows

$$\left[-\frac{1}{2}\nabla^2 + V^\sigma_{EFF}\right] \psi_{\alpha\sigma}(\mathbf{r}) = \epsilon_{\alpha\sigma}\psi_{\alpha\sigma}(\mathbf{r}) . \tag{2.18}$$

The effective potential, V^σ_{EFF}, in the Kohn-Sham equations is defined as

$$V^\sigma_{EFF} = v(\mathbf{r}) + V_H(\rho) + V^\sigma_{XC}(\rho, \mathbf{r}) . \tag{2.19}$$

The Coulomb or Hartree potential, $V_H(\rho(\mathbf{r}))$, is given by the derivative of the Coulomb energy $U[\rho]$ with respect to the charge density $\rho(\mathbf{r})$

$$V_H(\rho(\mathbf{r})) = \frac{\delta}{\delta\rho(\mathbf{r})}U[\rho] = \int d^3 r' \frac{\rho(\mathbf{r}')}{|\mathbf{r} - \mathbf{r}'|} . \tag{2.20}$$

The Hartree potential for a given charge density $\rho(\mathbf{r})$ can be obtained by solving the Poisson equation for that charge density

$$-\nabla^2 V_\mathrm{H}(\mathbf{r}) = \rho(\mathbf{r}) \, . \tag{2.21}$$

Similarly, the exchange-correlation potential, V_XC^σ, is given by the derivative of the exchange-correlation energy E_XC with respect to the charge density $\rho(\mathbf{r})$

$$V_\mathrm{XC}^\sigma = \frac{\delta}{\delta\rho(\mathbf{r})} E_\mathrm{XC}[\rho_\uparrow, \rho_\downarrow] \, . \tag{2.22}$$

The Kohn-Sham set of equations (2.18) can then be solved to obtain the Kohn-Sham eigenvalues $\epsilon_{\alpha\sigma}$ and the Kohn-Sham eigenvectors $\psi_{\alpha\sigma}$, and these are then used to construct a new charge density $\rho(\mathbf{r})$. The new potential (which is a functional of the charge density) is then calculated, and the procedure is repeated self-consistently until the charge density converges. Since the Hohenberg-Kohn theorem shows that the ground-state charge density is unique, this will be the charge density of the actual system.

The Kohn-Sham eigenvalues are the eigenvalues of the fictitious, non-interacting Kohn-Sham orbitals, and as such do not necessarily correspond to physical observables. The actual observables obtained from DFT are additive properties such as the total energy or the charge density. For example, the total electronic energy of a system is equal to the sum over the eigenvalues ϵ_i of the occupied Kohn-Sham states, along with terms to correct the electron-electron interaction [45],

$$E_\mathrm{TOT} = \sum_i f(\epsilon_i - E_\mathrm{F})\epsilon_i - \frac{1}{2}\int \frac{\rho(\mathbf{r})\rho(\mathbf{r}')}{|\mathbf{r} - \mathbf{r}'|} d\mathbf{r} d\mathbf{r}' + E_{XC}[\rho] - \int v_{XC}(\mathbf{r})\rho(\mathbf{r}) d\mathbf{r} \, , \tag{2.23}$$

where f is the Fermi distribution and E_F is the Fermi energy. To get the total energy of the system, the energy due to the interactions between the nuclei would also have to be included. The expression for the charge density is the sum over the Kohn-Sham orbitals, weighted by a set of Fermi functions as shown in equation (2.11).

2.2.3   Kohn-Sham eigenvalues

The Kohn-Sham eigenvalues, $\epsilon_{\alpha\sigma}$, are the eigenvalues of the single-particle Kohn-Sham equations. They are the eigenvalues corresponding to the Kohn-Sham orbitals, which are a set of fictitious, non-interacting orbitals. As such, they do not necessarily correspond to the single-particle energy levels of the real system. However, in practice

Kohn-Sham eigenvalues are often used to calculate band structures for materials, i.e. they are interpreted as single-particle energies. Additionally, in electronic transport calculations, the resonances in the transmission coefficients correspond to the position of these eigenvalues. Hence, it is important to understand what these eigenvalues do physically correspond to. Janak [87] showed that the Kohn-Sham eigenvalue is the derivative of the total energy with respect to its occupation, and hence that the highest occupied Kohn-Sham eigenvalue (the Kohn-Sham HOMO) is equal to the negative of the ionisation energy of the system.

In order to prove this theorem, the function $\tilde{E}$ is first rewritten so that the dependence on the orbital occupation, $f_{\alpha\sigma}$, is explicit

$$\tilde{E} = \sum_{\alpha\sigma} f_{\alpha\sigma} \langle \psi_{\alpha\sigma} | -\frac{1}{2}\nabla^2 | \psi_{\alpha\sigma} \rangle + \sum_{\alpha\sigma} f_{\alpha\sigma} \langle \psi_{\alpha\sigma} | V_{\text{EFF}}^\sigma | \psi_{\alpha\sigma} \rangle . \quad (2.24)$$

Differentiating $\tilde{E}$ with respect to the orbital occupation $f_{\alpha\sigma}$ gives

$$\frac{\delta}{\delta f_{\alpha\sigma}} \tilde{E} = \int d^3r \psi_{\alpha\sigma}^*(\mathbf{r})[-\frac{1}{2}\nabla^2 + V_{\text{EFF}}^\sigma]\psi_{\alpha\sigma}(\mathbf{r}) . \quad (2.25)$$

But, using the Kohn-Sham equation (2.18) and assuming the wave functions are normalised gives

$$\int d^3r \psi_{\alpha\sigma}^*(\mathbf{r})[-\frac{1}{2}\nabla^2 + V_{\text{EFF}}^\sigma]\psi_{\alpha\sigma}(\mathbf{r}) = \int d^3r \psi_{\alpha\sigma}^*(\mathbf{r})\epsilon_{\alpha\sigma}\psi_{\alpha\sigma}(\mathbf{r})$$
$$= \epsilon_{\alpha\sigma} \int d^3r \psi_{\alpha\sigma}^*(\mathbf{r})\psi_{\alpha\sigma}(\mathbf{r}) = \epsilon_{\alpha\sigma} .$$

Hence, the derivative of the energy with respect to the occupation of a state is equal to the Kohn-Sham eigenvalue of that state

$$\frac{\delta}{\delta f_{\alpha\sigma}} \tilde{E} = \epsilon_{\alpha\sigma} . \quad (2.26)$$

This allows the eigenvalue of highest occupied Kohn-Sham orbital, $\epsilon_{\text{HOMO}}^{\text{KS}}$ to be interpreted as the ionisation potential of the system, as removing one electron from this level changes the total energy of the system by an amount $\epsilon_{\text{HOMO}}^{\text{KS}}$. Therefore, in principle, this eigenvalue should correspond to the highest occupied orbital of the real system. This is the only energy level among all of the Kohn-Sham states which is directly interpretable in terms of a single-particle energy.

2.2.4 Exchange-Correlation Energy

The exchange-correlation (XC) energy, E_{XC}, includes all of the contributions to the energy coming from non-classical electron-electron interactions, including the fact that the "real" many-body wave function may not be a simple Slater determinant. Unfortunately, there is no analytic or numerical expression for the exact form of E_{XC}. The exact form of the exchange energy, E_{EXX}, which is used in Hartree-Fock theory, is given by

$$E_{EXX} = \frac{1}{2} \sum_{\sigma} \sum_{\alpha,\alpha'} f_{\alpha\sigma} f_{\alpha'\sigma} \int d^3r \int d^3r' \frac{\psi_{\alpha\sigma}^*(\mathbf{r})\psi_{\alpha'\sigma}^*(\mathbf{r}')\psi_{\alpha'\sigma}(\mathbf{r})\psi_{\alpha\sigma}(\mathbf{r}')}{|\mathbf{r} - \mathbf{r}'|} . \tag{2.27}$$

However, this expression is non-local and involves calculating complicated integrals. Also, it does not include electron correlation effects, and so is not the full XC energy.

Generally, in DFT calculations, approximated local exchange-correlation potentials are used. The two approximations which are used most often are the Local Density Approximation (LDA) [44] and the Generalised Gradient Approximation (GGA) [59, 60, 61]. Both of these are local approximations in that the potential at a particular point only depends on the charge density and/or its derivatives at that point. More sophisticated approximations include "exact exchange" formulations, which use the full, exact form for the exchange energy [88] with local correlation. However, these methods are more demanding computationally, and have not yet been implemented for finite bias calculations.

The simplest approximation for E_{XC} is LDA, and its spin-polarised version, the Local Spin Density Approximation (LSDA) [44]. In this, the exchange-correlation energy at a point is taken to be equal to that of a uniform electron gas of that density at that point

$$E_{XC}^{LSDA} = \int d^3r \rho(\mathbf{r})\epsilon_{XC}(\rho^\uparrow, \rho^\downarrow) . \tag{2.28}$$

where ϵ_{XC} is the exchange-correlation energy density for the uniform electron gas.

This approximation can be extended to produce GGA [59, 60, 61] by including terms depending on the gradient of the charge density. One formulation of GGA is the Perdew-Burke-Enzerhof (PBE) [61] form

$$E_{XC}^{GGA} = \int d^3r F(\rho^\uparrow, \rho^\downarrow, \nabla\rho^\uparrow, \nabla\rho^\downarrow) . \tag{2.29}$$

GGA should describe systems in which the charge density fluctuates rapidly better than LDA does. GGA is popular in the chemistry community where it is used to calculate bond lengths in molecules, which are corrected somewhat compared to LDA. However, for bulk materials such as metals in which the charge density does not vary rapidly, LDA may give results which compare better to experiments.

Unfortunately, there are problems with both GGA and LDA functionals, particularly when describing strongly correlated systems where the charge density varies rapidly or is extremely localised, i.e. for systems which are very different from a homogenous electron gas. One of the most significant of these is the self-interaction error described in section 2.6, where an electron interacts with the exchange-correlation potential generated by itself. This in turn can have the effect of obscuring the derivative discontinuity described in section 2.6.1. Also, ionisation potentials in molecules and the position of the valence band in semiconductors are frequently calculated incorrectly using these potentials. Local potentials such as LDA and GGA also fail to describe non-local effects, such as Van der Waal's forces.

Another failure of local XC functionals is their response to an external applied electric field. The part of the field originating from the XC potential induced in response to the applied field should be such as to counteract the external field. This is the case with exact XC potentials. However, for LDA or GGA, the induced field is in the same direction as the external field. This results in the polarisability of molecules being overestimated, particularly conjugated polymers. This may have important implications for electronic transport calculations, where an electric field is applied to a molecular junction. Such a failure can be corrected using exact exchange based functionals, or by using self-interaction corrected functionals [89, 90]

One method of correcting for the effects of strong localisation is the LDA+U scheme [91], in which the exchange-correlation energies of highly localised orbitals is replaced by the Hubbard U energy [92]. This method involves two parameters, U and J, which need to be fitted for each orbital of each species for which they are used, so that the calculations are no longer strictly *ab initio*. The self-interaction error can also be removed directly, as described in section 2.6.

Other formulations for the exchange-correlation potential include hybrid functionals such as B3LYP [93, 94], which involves combining LDA, GGA and Hartree-Fock exchange and is mainly used in chemistry. There are also "meta-GGAs" [95] which incorporate higher order derivatives of the charge density.

2.3   Pseudopotentials

Most of the chemical, electronic and structural properties of materials are determined by interactions between the outermost or "valence" electrons. The energy of the inner or "core" electrons is usually much lower, and so they are unlikely to be available for bond formation or electrical conduction. Therefore, it is often not necessary to explicitly include these core orbitals in the self-consistent calculation.

The pseudopotential approximation involves removing the core electrons and the nuclear potential and replacing them by a weaker effective potential called a "pseudopotential" [86, 96]. This has the advantage of reducing the total number of particles in the calculation, which in turn can significantly improve computational efficiency. For example, a set of valence orbitals consisting of just the $5d$, $6s$, and $6p$ orbitals tends to describe gold very well, with all of the lower energy electrons, in the $1s$, $2s$, $2p$, $3s$, $3p$, $3d$, $4s$, $4p$, $4d$, $4f$, $5s$, and $5p$ orbitals included in the pseudopotential. In this way, a gold atom can be described by just 11 electrons, and not by 79. Which orbitals are required to be included in the self-consistent calculation will vary from species to species, and will also depend on which properties need to be described accurately.

This pseudopotential acts on a set of pseudo wave functions rather than on the true valence wave functions. The true wave functions may oscillate wildly near the core in order to be orthogonal to the core states. However, the pseudo-wave functions can be constructed so that they behave smoothly in the core. This in turn will improve computational efficiency and stability, removing singularities which may cause problems. The pseudo-wave function is constructed so as to match the true wave function outside of a certain cut-off radius r_c, as shown in figure 2.1.

The pseudopotential wave functions are constructed such that the scattering properties of the atomic orbitals are preserved. As these are, in general, different for each angular momentum channel, the pseudopotential is angular momentum dependent. Hence, a pseudopotential must be constructed for each angular momentum channel used in the calculation [86, 96].

There are several different methods which can be used to generate pseudopotentials. The method generally used in calculations presented in this work is the Troullier-Martins parameterisation [96].

To calculate the pseudopotential for an angular momentum channel l, the radial Kohn-Sham equation is solved self-consistently to obtain the all-electron atomic wave function for angular momentum channel l, ψ_l^{AE}, and its eigenvalues ϵ_l
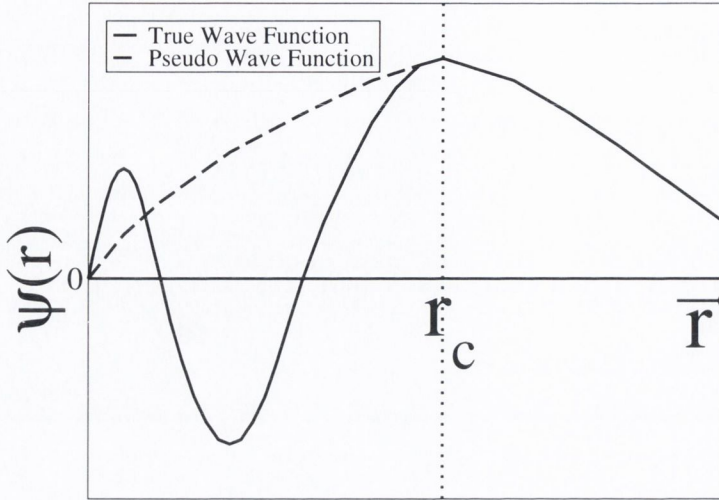
Figure 2.1: True (all-electron) and pseudo wave functions as a function of atomic radius r. Inside the cut-off radius r_c, the true wave functions oscillate rapidly whereas the pseudo wave functions do not. The two wave functions match outside the radius r_c.

$$\left[-\frac{1}{2}\frac{d^2}{dr^2} + \frac{l(l+1)}{2r^2} + V(\rho, r) \right] r\psi_{nl}^{\mathrm{AE}} = \epsilon_{nl} r\psi_{nl}^{\mathrm{AE}}. \tag{2.30}$$

where $V(\rho, r)$ is the total DFT potential for the atom given by

$$V(\rho, r) = \frac{-Z}{r} + V_{\mathrm{H}}(\rho, r) + V_{\mathrm{XC}}(\rho(\mathbf{r})). \tag{2.31}$$

The charge density for the atom, $\rho(\mathbf{r})$, is the sum over the atomic wave functions $\sum_{n,l}\psi_{nl}^{\mathrm{AE}}$. The pseudo-wave-functions, ψ_{nl}^{PS}, are then constructed such that they have no nodes, that they match the true atomic wave functions outside some cut-off radius r_c as shown in figure 2.1, that charge is conserved, and so that they give the same eigenvalues ϵ_{nl} as the true wave functions

$$\psi_{nl}^{\mathrm{PS}}(r) = \psi_{nl}^{\mathrm{AE}}(r), r > r_c; \int_0^{r_{c_l}} |\psi_{nl}^{\mathrm{PS}}(r)|^2 r^2 dr = \int_0^{r_{c_l}} |\psi_{nl}^{\mathrm{AE}}(r)|^2 r^2 dr. \tag{2.32}$$

Once these pseudo-wave-functions have been constructed, the corresponding pseudopotential can be obtained by inverting the radial Schrödinger equation

$$V^{\mathrm{PS}}(\rho, r) = \epsilon_{nl} - \frac{l(l+1)}{2r^2} + \frac{1}{2r\psi_{nl}^{\mathrm{PS}}(r)}\frac{d^2}{dr^2} r\psi_{nl}^{\mathrm{PS}}(r). \tag{2.33}$$

However, this is the screened pseudopotential, i.e. the potential screened by the valence electrons. The screening by the valence electrons depends on the environment in which they are placed, so this pseudopotential cannot be used for bulk

calculations. Instead, the ionic pseudopotential, $V_{\mathrm{ION}}^{\mathrm{PS}}(r)$, is calculated by subtracting off the Hartree and exchange-correlation potentials due to the valence pseudo-wave-functions, $V_{\mathrm{H}}^{\mathrm{VA}}(r)$ and $V_{\mathrm{XC}}^{\mathrm{VA}}(r)$

$$V_{\mathrm{ION}}^{\mathrm{PS}}(r) = V^{\mathrm{PS}}(r) - V_{\mathrm{H}}^{\mathrm{VA}}(r) - V_{\mathrm{XC}}^{\mathrm{VA}}(r) . \tag{2.34}$$

Note that each angular momentum component l sees a different potential. Thus, the ionic pseudopotential operator can be split up into a local part, and a non-local part which is angular momentum dependent

$$\hat{V}_{\mathrm{ION}}^{\mathrm{PS}}(r) = \hat{V}_{\mathrm{ION,Local}}^{\mathrm{PS}}(r) + \sum_l V_{\mathrm{ION,Nonlocal}_l}^{\mathrm{PS}}(r)\hat{P}_l . \tag{2.35}$$

where $\hat{P}_l$ is an operator which projects out the lth angular momentum component of the wave function. Thus, the non-local part of the pseudopotential for angular momentum channel l is

$$V_{\mathrm{ION,Nonlocal}_l}^{\mathrm{PS}}(r) = V_{\mathrm{ION}_l}^{\mathrm{PS}}(r) - V_{\mathrm{ION,Local}}^{\mathrm{PS}}(r) . \tag{2.36}$$

The non-local part of the pseudopotential, $V_{\mathrm{ION,Nonlocal}_l}^{\mathrm{PS}}(r)$, is actually semi-local in that it has a radial dependence which is local and an angular momentum dependence which is non-local. This introduces long range interactions into the Hamiltonian, thus increasing the number of matrix elements of the Hamiltonian which have to be calculated. Hence, it is transformed to a fully non-local form using Kleinman-Bylander projectors [97]

$$V_{\mathrm{ION,Nonlocal}_l}^{\mathrm{KB}}(r) = \frac{|V_{\mathrm{ION,Nonlocal}_l}^{\mathrm{PS}}(r)\phi_{0_l}^{\mathrm{PS}}(r)\rangle\langle\phi_{0_l}^{\mathrm{PS}}(r)V_{\mathrm{ION,Nonlocal}_l}^{\mathrm{PS}}(r)|}{\langle\phi_{0_l}^{\mathrm{PS}}(r)|V_{\mathrm{ION,Nonlocal}_l}^{\mathrm{PS}}(r)|\phi_{0_l}^{\mathrm{PS}}(r)\rangle} . \tag{2.37}$$

where $\phi_{0_l}^{\mathrm{PS}}(r)$ is the atomic pseudo-wave-function for angular momentum channel l.

Thus, a pseudopotential for each atomic species in the calculation can be constructed in advance. A pseudopotential must be constructed for each angular momentum channel present in the calculation. Care must be taken to use the same exchange-correlation functional to generate the pseudopotential as is used in the self-consistent calculation for the valence electrons. Pseudopotentials should be tested before use to check that they produce the same energy levels as an all-electron calculation for a variety of electron configurations. This ensures transferability, allowing the pseudopotentials to be used for systems where there is charge transfer between atoms.

2.4   The Basis Set

In order to solve the Kohn-Sham equations, either equations must be solved directly in real space by writing the wave functions and the charge density over a numerical grid (which can be computationally expensive), or the Kohn-Sham orbitals must be written over a basis set. One, relatively conceptually simple basis set is constructed from a linear combination of plane waves

$$\psi_i(\mathbf{r}) = \sum_k A_i(\mathbf{k}) \exp(i\mathbf{k} \cdot \mathbf{r}) . \qquad (2.38)$$

Plane wave basis sets have the advantage of being easy to improve systematically by increasing the number of plane waves. Operators and the charge density are also easy to calculate with this type of basis set, due to the efficiency of the Fast Fourier Transform algorithm. However, they have the disadvantage of needing a large number of functions to describe localised orbitals, and also of using many basis functions to describe vacuum regions where there is little charge density. Hence, they tend to be more useful for describing bulk systems, particularly metals, but rather inefficient when it comes to describing isolated molecules.

Another type of basis set which can be used is a localised basis set, where Kohn-Sham wave functions are approximated by a linear combination of atomic orbitals

$$\psi_i(\mathbf{r}) = \sum_l C_l^i \phi_l(\mathbf{r}) . \qquad (2.39)$$

Here, $\phi_l(\mathbf{r})$ are atomic-like orbitals. These can be Gaussian, Slater or numerical orbitals. The advantage of such a basis set is that it describes localised orbitals well, and does not waste a large number of basis functions describing vacuum. However, they are more difficult to improve systematically than plane wave basis sets.

2.5   The SIESTA Implementation of DFT

There are several different numerical implementations of density functional theory available. They mostly differ in the form of the basis set used to represent the Kohn-Sham orbitals. The implementation used to perform the calculations described in this thesis is that contained in the "Spanish Initiative for the Estimation of Systems with Thousands of Atoms" or "SIESTA" [82, 83, 84]. SIESTA uses a localised basis set consisting of numerical atomic orbitals which are the product of a numerical radial

function and a real spherical harmonic. The atomic wave function for an orbital n on an atom I located at position $\mathbf{R}_I$ is given by

$$\phi_{Ilmn} = \phi_{Iln}(r_I)Y_{lm}(\hat{\mathbf{r}}_I) . \tag{2.40}$$

The angular momentum numbers are l and m, and $\mathbf{r}_I = \mathbf{r} - \mathbf{R}_I$. The radial functions ϕ_{Iln} are defined numerically using a cubic spline interpolation on a fine mesh.

To calculate a minimal basis set (known as a single-ζ basis set), the method of Sankey and Niklewski [98] is used, where the basis orbitals are the eigenfunctions of the pseudoatom. The radial function ϕ_l for angular momentum channel l is the eigenfunction of the pseudopotential for that angular momentum, V_l^{PS}, for an energy $\epsilon_l + \delta\epsilon_l$, where $\delta\epsilon_l$ is chosen so that the first node of the eigenfunction occurs at the cut-off radius r_l^c

$$\left[-\frac{1}{2r}\frac{d^2}{dr^2}r + \frac{l(l+1)}{2r^2} + V_l^{\mathrm{PS}}(r) \right] \phi_l(r) = [\epsilon_l + \delta\epsilon_l]\phi_l(r) . \tag{2.41}$$

where $\phi_l(r_l^c) = 0$. Alternatively, $\delta\epsilon_l$ can be fixed instead, and then r_l^c for that orbital will be the position of the first node in the wave function. This radial cut-off of the basis functions reduces the number of overlap integrals, increasing the sparsity of the Hamiltonian and thus improving computational efficiency.

To allow more variational freedom in the calculation, a "multiple-ζ" basis set can be used, where there is more than one basis function per atomic orbital. The spherical harmonics remain the same, but new "higher-ζ" radial functions are constructed. To generate such a basis in SIESTA, the "split-valence" method is adapted to numerical atomic orbitals [82, 83]. The "higher-ζ" functions have the same tail as the first ζ (original) function beyond a split radius r_l^s, but change to a polynomial behaviour inside this radius. Hence, the second ζ orbital is of the form

$$\phi_l^{2\zeta}(r) = \begin{cases} r^l(a_l - b_l r^2) & \text{if } r < r_l^s; \\ \phi_l^{1\zeta}(r) & \text{if } r \geq r_l^s. \end{cases} \tag{2.42}$$

The constants a_l and b_l are determined by condition that both the wave function and its first derivative must be continuous at $r = r_l^s$.

Polarised orbitals can also be constructed to account for the deformation induced by bond formation. These are basis orbitals in which the spherical harmonics with higher orbital momentum are included while the radial functions remain unchanged

$$\phi_{l',n,m} = \phi_{l,n}Y_{l+1,m} . \tag{2.43}$$

Once the basis orbitals have been constructed, the Kohn-Sham Hamiltonian matrix elements can be obtained from integrals of the form

$$H_{i,j} = -\frac{\hbar^2}{2m} \int \phi_i(\mathbf{r}-\mathbf{R_I})\nabla^2\phi_j(\mathbf{r}-\mathbf{R_J})d\mathbf{r} + \int \phi_i(\mathbf{r}-\mathbf{R_I})V_{\mathrm{EFF}}(\mathbf{r})\phi_j(\mathbf{r}-\mathbf{R_J})d\mathbf{r}. \quad (2.44)$$

where $\mathbf{R_I}$ is the position of the Ith atom.

$V_{\mathrm{EFF}}(\mathbf{r})$ is the effective Kohn-Sham potential described in equation (2.19), which is a functional of the charge density. First, an initial charge density, ρ_0, is constructed from the atomic charge densities. The exchange-correlation potential part of $V_{\mathrm{EFF}}(\mathbf{r})$ can be calculated as described in section (2.2.4). The Hartree potential, V_{H}, can be calculated by solving the Poisson equation (2.21) in reciprocal space using a Fast Fourier Transform (FFT) algorithm. Therefore, this part of SIESTA method requires the system to have periodic boundary conditions.

This Hamiltonian matrix can then be diagonalised to obtain the eigenvalues, ϵ_i, and eigenvectors, $\psi_i(\mathbf{r})$, of the Kohn-Sham equations. The Kohn-Sham eigenvectors are linear combinations of the SIESTA basis functions

$$\psi_i = \sum_j c_i^j \phi_j. \quad (2.45)$$

These can then be used to calculate the new density matrix, which in turn can be used to calculate a new effective potential. This procedure is repeated until the density matrix converges.

This localised basis set allows SIESTA to accurately describe systems with thousands of orbitals without using an unreasonable amount of computing resources. In fact, there is a method under development which would allow SIESTA to scale linearly with system size - the so-called order-N method [62]. Also, the tight-binding like Hamiltonian which the localised basis set produces is easily incorporated into the non-equilibrium Green's function method, which is the formalism which is used to calculate the electron transport.

2.6   The Self-Interaction Error

In the local and semi-local exchange-correlation potentials used in DFT calculations such LDA and GGA described above, there is a problem in that the interaction of an electron with itself is non-zero. This must be corrected for in order to accurately describe highly localised systems in particular [71]. These self-interaction errors are responsible for local functionals producing incorrect ionisation potentials for

molecules due to the extra electron-electron interaction energy. They also contribute to incorrect positions being calculated for the valence bands for semiconductors and to the absence of a derivative discontinuity in the energy at integer occupation.

For $\alpha = \alpha'$, i.e. the interaction of an electron with itself, the exact exchange energy given in equation (2.27) becomes

$$
E_{\text{EXX}}[\rho_{\alpha\sigma}, 0] = \frac{1}{2} \sum_{\sigma} \sum_{\alpha} f_{\alpha\sigma}^2 \int d^3r \int d^3r' \frac{|\psi_{\alpha\sigma}(\mathbf{r})|^2 |\psi_{\alpha\sigma}(\mathbf{r}')|^2}{|\mathbf{r} - \mathbf{r}'|} \tag{2.46}
$$

$$
= \frac{1}{2} \int d^3r \int d^3r' \frac{\rho_{\alpha\sigma}(\mathbf{r})\rho_{\alpha\sigma}(\mathbf{r}')}{|\mathbf{r} - \mathbf{r}'|} = \sum_{\alpha\sigma} U[\rho_{\alpha\sigma}] . \tag{2.47}
$$

Therefore, for exact exchange, the self-interaction errors in the Coulomb and exchange energies cancel each other out

$$
U[\rho_{\alpha\sigma}] + E_{\text{EXX}}[\rho_{\alpha\sigma}, 0] = 0 . \tag{2.48}
$$

However, for an approximate local exchange-correlation energy $E_{\text{XC}}^{\text{Approx}}$, such as LDA or GGA, the self-interaction energy can be non-zero.

$$
U[\rho_{\alpha\sigma}] + E_{\text{XC}}^{\text{Approx}}[\rho_{\alpha\sigma}, 0] \neq 0 . \tag{2.49}
$$

This is the self-interaction error. The self-interaction corrected exchange correlation energy, $E_{\text{XC}}^{\text{SIC}}$, can then be defined as [71]

$$
E_{\text{XC}}^{\text{SIC}} = E_{\text{XC}}^{\text{Approx}}[\rho_{\uparrow}, \rho_{\downarrow}] - \sum_{\alpha\sigma} \delta_{\alpha\sigma} . \tag{2.50}
$$

where $\delta_{\alpha\sigma}$ is the self-interaction correction for the Kohn-Sham orbital $\psi_{\alpha\sigma}$, and is equal to the sum of the Coulomb and exchange-correlation self-interaction energies

$$
\delta_{\alpha\sigma} = U[\rho_{\alpha\sigma}] + E_{\text{XC}}^{\text{Approx}}[\rho_{\alpha\sigma}, 0] , \tag{2.51}
$$

where $\rho_{\alpha\sigma} = |\psi_{\alpha\sigma}|^2$ is the charge density associated with the Kohn-Sham orbital $\psi_{\alpha\sigma}$. There is now a new system of single-particle Schrödinger equations from which one can calculate a new set of orbitals $\overline{\psi}_{\alpha\sigma}$ and occupations $\overline{f}_{\alpha\sigma}$

$$
[-\frac{1}{2}\nabla^2 + \overline{V}_{\text{EFF}}^{\alpha\sigma}]\overline{\psi}_{\alpha\sigma}(\mathbf{r}) = \epsilon_{\alpha\sigma}^{\text{SIC}}\overline{\psi}_{\alpha\sigma}(\mathbf{r}) . \tag{2.52}
$$

The new effective potential $\overline{V}_{\text{EFF}}^{\alpha\sigma}$ is orbital dependent and is given by

$$
\overline{V}_{\text{EFF}}^{\alpha\sigma} = [v(\mathbf{r}) + V_H(\rho) + V_{\text{XC}}^{\sigma,\text{Approx}}(\rho, \mathbf{r})] - [V_H(\rho_{\alpha\sigma}; \mathbf{r}) + V_{\text{XC}}^{\sigma,\text{Approx}}([\rho_{\alpha\sigma}, 0]; \mathbf{r})] . \tag{2.53}
$$

The term which has been subtracted off in equation (2.53) is the SIC potential for orbital $\psi_{\alpha\sigma}$, $V_{\alpha\sigma}^{\text{SIC}}$

$$V_{\alpha\sigma}^{\text{SIC}} = V_H(\rho_{\alpha\sigma};\mathbf{r}) + V_{\text{XC}}^{\sigma,\text{Approx}}([\rho_{\alpha\sigma},0];\mathbf{r}) . \tag{2.54}$$

Thus the SIC affects the eigenvalues of the system in two ways: directly via the correction to the potential and indirectly via the changes to the orbitals in going from $\psi_{\alpha\sigma}$ to $\overline{\psi}_{\alpha\sigma}$.

The problem of finding the energy minimum is complicated by the fact that the potential is orbital dependent and $E_{\text{XC}}^{\text{SIC}}$ is not invariant under unitary rotations of the occupied KS orbitals, which instead leave ρ invariant. This can be avoided by introducing a second set of orbitals $\phi^{\alpha\sigma}$ related to the canonical KS orbitals $\psi^{\alpha\sigma}$ by a unitary transformation M

$$\psi_{\alpha\sigma} = \sum_m M_{\alpha\sigma m}\phi_{\alpha\sigma} . \tag{2.55}$$

The energy functional can then be minimised by varying both the KS orbitals and the unitary transformation M, leading to the system of KS-like equations

$$H_n^\sigma \psi_\sigma = [H_0^\sigma + \Delta V_{\alpha\sigma}^{\text{SIC}}]\psi_{\alpha\sigma}(\mathbf{r}) = \epsilon_{\alpha\sigma}^{\text{SIC}}\psi_{\alpha\sigma}(\mathbf{r}) , \tag{2.56}$$

where H_0^σ is the Hamiltonian for the approximate uncorrected exchange-correlation functional, The new SIC potential, $\Delta V_{\alpha\sigma}^{\text{SIC}}$, can then be written as

$$\Delta V_{\alpha\sigma}^{\text{SIC}} = \sum_m M_{\alpha\sigma m} V_{\alpha\sigma}^{\text{SIC}}\frac{\phi_{\alpha\sigma}}{\psi_{\alpha\sigma}} = \sum_m V_{\alpha\sigma}^{\text{SIC}} \hat{P}_m^\phi , \tag{2.57}$$

where $\hat{P}_m^\phi$ is the projector $|\phi_{\alpha\sigma}\rangle\langle\phi_{\alpha\sigma}|$.

2.6.1 Derivative Discontinuity

In the electronic transport calculations using the NEGF formalism described in this work, the total number of particles on the molecule is not necessarily conserved. Therefore, it is possible for there to be a non-integer number of electrons on the molecule. Hence it is important that the formulation of DFT used for transport calculations gives accurate results for fractional occupation.

Perdew et. el. [72, 73] extended DFT to work for non-integer occupation. In doing so, they showed that the exact exchange-correlation functional (which is unknown) must have a "derivative discontinuity" in the energy at integer occupations, otherwise molecules would dissociate with non-integer particle number at large separation. This

"derivative discontinuity" refers to a discontinuity in the derivative of the energy with respect to occupation.

To extend DFT to describe charge densities for a non-integer number of electrons, let $N = M + \omega$, where M is a non-negative integer and $0 \leq \omega \leq 1$. The wave function will then be a statistical mixture of ψ_M (the wave function of the M electron state giving a density ρ_M) and ψ_{M+1} (the wave function of the $M + 1$ electron state giving a density ρ_{M+1}). The respective probabilities of each state are $1 - \omega$ and ω, since $(1 - \omega)M + \omega(M + 1) = M + \omega$. Hence the final charge density is given by

$$\rho(\mathbf{r}) = (1 - \omega)\rho_M(\mathbf{r}) + \omega\rho_{M+1}(\mathbf{r}) \,. \tag{2.58}$$

Minimising the total energy with respect to number conserving variations of the charge density $\rho(\mathbf{r})$ yields the lowest average energy that can be achieved by $M + \omega$ electrons

$$E = (1 - \omega)E_M + \omega E_{M+1} \,. \tag{2.59}$$

This is true for all ensembles giving density $\rho(\mathbf{r})$ with $M + \omega$ electrons provided E_M vs. M is concave upward (which it usually is for electrons [71]). A plot of this energy E versus particle number N is shown by the solid line in figure (2.2). The energy changes linearly between integer occupations. There is a kink at integer occupation which is the derivative discontinuity.

Given that the chemical potential is $\mu = \frac{\partial E}{\partial N}$ and $N = M + \omega$, where M is a fixed integer, we find that $\frac{\partial E}{\partial \omega} = \mu$.

If Z is the nuclear charge, and hence the number of electrons on the neutral atom, then for $Z - 1 < N < Z$, $M = Z - 1$, μ is given by

$$E = (1 - \omega)E_{Z-1} + \omega E_Z \Rightarrow \mu = \frac{\partial E}{\partial \omega} = E_Z - E_{Z-1} \,. \tag{2.60}$$

Similarly, for $Z < N < Z + 1$, $M = Z$, μ is given by

$$E = (1 - \omega)E_Z + \omega E_{Z+1} \Rightarrow \mu = \frac{\partial E}{\partial \omega} = E_{Z+1} - E_Z \,. \tag{2.61}$$

Now, the ionisation potential I is $E_{Z-1} - E_Z$ and electron affinity A is $E_Z - E_{Z+1}$. Therefore

$$\mu = \begin{cases} -I = E_Z - E_{Z-1} & \text{if } Z - 1 < N < Z; \\ -A = E_{Z+1} - E_Z & \text{if } Z < N < Z + 1. \end{cases} \tag{2.62}$$

Therefore, for N tending to Z from below; i.e. $N \to Z$, $N < Z$; then $\frac{\partial E}{\partial N} = -I$. However, for N tending to Z from above; i.e. $N \to Z$, $N > Z$; then $\frac{\partial E}{\partial N} = -A$.
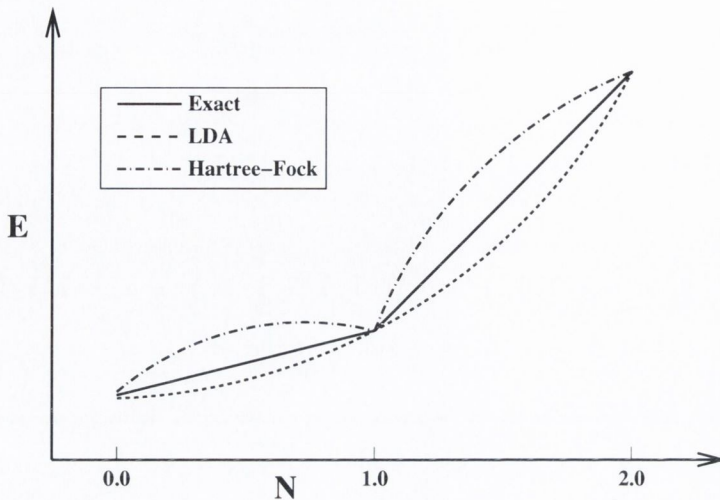
Figure 2.2: A schematic illustration of the energy as a function of occupation. The "exact" energy is that given by the extension introduced by Perdew et. al. described here. The energy given by LDA does not have a derivative discontinuity at integer occupation. Hartree-Fock does have a derivative discontinuity, but the total energy is usually higher than it should be.

Hence, there is a discontinuity in $\frac{\partial E}{\partial N}$ of size $I - A$ at integer occupations. This is the derivative discontinuity.

From equation (2.26), we have that the derivative of the energy with respect to the occupation of highest occupied Kohn-Sham orbital (the HOMO orbital) is equal to the Kohn-Sham eigenvalue associated with that orbital. Hence, a discontinuity in the derivative of the energy would correspond to a discontinuity in the KS eigenvalue, as shown in figure 2.3.

Note also that the chemical potential, μ, of the system has already been shown to be equal to $\mu = \frac{\partial E}{\partial \omega}$, where ω is the occupation of the final orbital. Therefore, the chemical potential is the same as the eigenvalue of the highest occupied Kohn-Sham orbital. Thus, the discontinuity in the KS HOMO is the same as the discontinuity in the chemical potential.

This derivative discontinuity explains the dissociation of atoms at large separation. Consider two well-separated atoms $\mathbf{X}$ and $\mathbf{Y}$ in an otherwise empty universe. The two atoms have different chemical potentials μ_X and μ_Y, with $\mu_Y < \mu_X$, as shown in the diagram in figure 2.4.

Then shifting $\delta N_Y > 0$ electrons from $\mathbf{X}$ to $\mathbf{Y}$ will reduce the energy by a factor

$$\delta E_{XY} = (\mu_Y - \mu_X)\delta N_Y < 0. \tag{2.63}$$
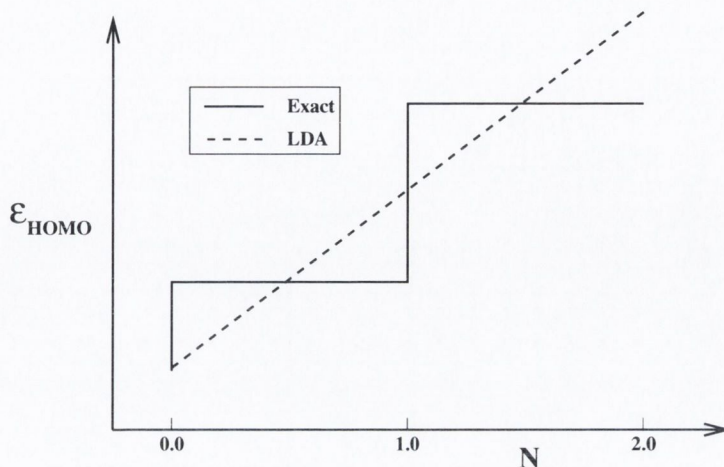
Figure 2.3: A schematic illustration of the derivative of the energy as a function of oc-
cupation. The "exact" energy is that given by the extension introduced by
Perdew et. al. [72, 73] described here. The energy given by LDA does not
have a derivative discontinuity at integer occupation. Hartree-Fock does have
a derivative discontinuity, but the total energy is usually higher than it should
be.

Therefore the total energy E_{XY} would be minimised by having a net positive
charge on **X** and a net negative charge on **Y**. This would be true for any separation,
but is not true in reality.

The existence of the derivative discontinuity of size $I - A$ at integer occupation
as described above solves this problem. Adding an infinitesimal charge δ to a previ-
ously unoccupied orbital would cause it to jump discontinuously. Hence, the lowest
unoccupied molecular orbital (LUMO) of the N electron system would not be the
same as the highest occupied molecular orbital of the $N + \delta$ electron system; i.e.
$\epsilon_{LUMO}^{KS}(N) \neq \epsilon_{HOMO}^{KS}(N + \delta)$. Instead of the energy of a KS eigenstate increasing lin-
early as charge is added, it should shift in a stepwise fashion as shown in figure 2.3,
so that adding a fraction of an electron would cause the level to move up to the same
point as adding a full electron. The chemical potential and ϵ_{HOMO}^{KS} coincide, so μ also
jumps discontinuously by $I - A$ when a fractional charge is added. Hence, transfer-
ring a fraction of an electron from atom **X** to atom **Y** would cause μ_Y to change by
$I - A$, while μ_Y remained the same. Since $I - A > 0$ for all atoms, this would not
be energetically favourable, and hence fractional charges are not exchanged between
atoms at large separation.

The exchange-correlation potential, v_{XC}, is given by the derivative of the exchange-
correlation energy E_{XC} with respect to the charge density. Hence, the derivative
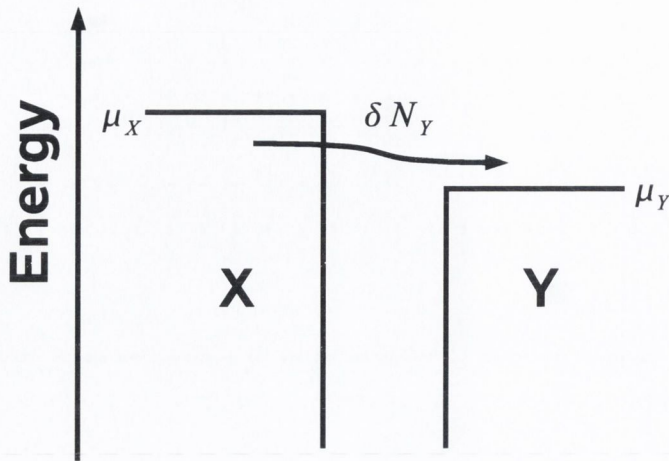
Figure 2.4: Two well-separated atoms **X** and **Y**, with $\mu_Y < \mu_X$. Does a transfer of charge δN_Y result in a lowering of the total energy of the system?

discontinuity in the energy implies that there is also a discontinuity present in the potential.

Part of the reason for the absence of the derivative discontinuity in approximate local functionals such as LDA and GGA is due to the self-interaction error. The interaction energy between two electric charges is proportional to the product of these charges. Hence, if the charge density on a specific orbital is $\rho_{\alpha\sigma}$, then the self-interaction energy due to that orbital will be proportional to $\rho_{\alpha\sigma}^2$. Therefore, a total energy calculated using a Hamiltonian which contains self-interaction errors will contain a term which is quadratic in the occupation of a specific orbital $\psi_{\alpha\sigma}$. Hence, the derivative of the energy with respect to $\rho_{\alpha\sigma}$ (which, from Janak's theorem is the Kohn-Sham eigenvalue of that state, $\epsilon_{\alpha\sigma}$) will have a term which is linear in $\rho_{\alpha\sigma}$

$$\epsilon_{\alpha\sigma} = \frac{\partial E}{\partial \rho_{\alpha\sigma}} \sim \rho_{\alpha\sigma} + \ldots . \tag{2.64}$$

Therefore, the self-interaction error causes the derivative of the energy with respect to the occupation to be linear rather than discontinuous. A full self-interaction correction should remove this linear term, and at least partially restore the discontinuity.

Without Derivative Discontinuity

With Derivative Discontinuity
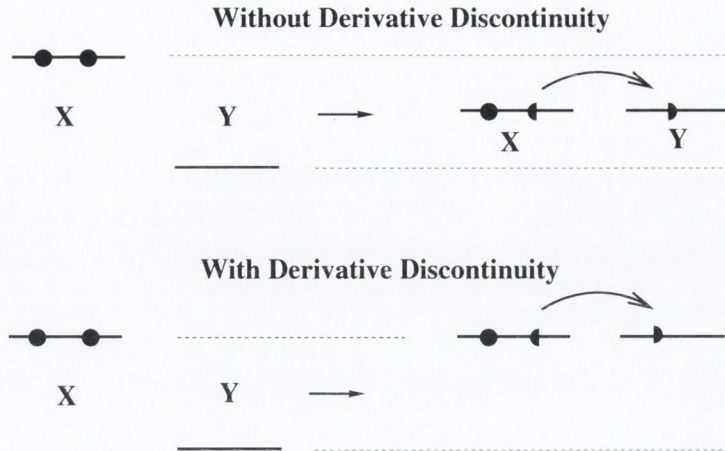
Figure 2.5: Two well-separated atoms **X** and **Y**, where the LUMO of **Y** is below the HOMO of **X**. If no derivative discontinuity is present, a fractional charge can be transferred between the atoms, and the levels will move in proportion to the amount of charge exchanged as shown. However, if the derivative discontinuity is present, transferring a fraction of an electron onto the LUMO of **Y** will cause it to shift upwards as if an integer electron was transferred, while the HOMO of **X** will not shift downwards until an entire electron is transferred out.

2.6.2   Atomic-SIC

The full self-interaction correction described above is orbital dependent and computationally very costly. It is difficult to implement for extended systems and periodic boundary conditions, which are required by the SIESTA implementation. These problems can be solved by using an atomic approximation to the full self-interaction correction known as ASIC [75]. This approximation is based on pseudo-SIC method in which the self-interaction corrections are included in the pseudopotential, as suggested by Vogel et. al [99] and extended by Filipetti et. al [100].

First, the orbitals ϕ_α introduced in equation (2.55) which minimise the SIC functional are assumed to be atomic-like orbitals Φ_α , so that the SIC potential becomes

$$\sum_m V_m^{\text{SIC}} \hat{P}_m^\phi \rightarrow \sum_m \tilde{V}_m^{\text{SIC}} \hat{P}_m^\Phi , \tag{2.65}$$

where $\tilde{v}_m^{\text{SIC}}$ and $\hat{P}_m^\Phi$ are the potential and projector associated with the atomic orbitals Φ_m.

The potential for each atomic orbital Φ_α is already calculated at the pseudopotential generation stage. Therefore, the self-interaction correction to the potential can be calculated for each atomic orbital, and then added on to the pseudopotential for that orbital. The Kohn-Sham single particle all-electron equation for an orbital

α in an atom using a self-interaction corrected LDA exchange-correlation potential
is

$$[-\nabla^2 - \frac{2Z}{r} + V_{\mathrm{H}}(\rho) + V_{\mathrm{XC}}^{\mathrm{LDA}}(\rho) - V_{\mathrm{H}}(\rho_\alpha) - V_{\mathrm{XC}}^{\mathrm{LDA}}(\rho_{\alpha,\uparrow}, 0)]\psi_\alpha = \epsilon_\alpha^{\mathrm{SIC}}\psi_\alpha . \quad (2.66)$$

Replacing the potential term $-\frac{2Z}{r}$ by a pseudopotential $V_{\mathrm{PS},\alpha}$ gives the equation
for the pseudoatom

$$[-\nabla^2 + V_{\mathrm{PS},\alpha} + V_{\mathrm{H}}(\rho') + V_{\mathrm{XC}}^{\mathrm{LDA}}(\rho') - V_{\mathrm{H}}(\rho_\alpha) - V_{\mathrm{XC}}^{\mathrm{LDA}}(\rho_{\alpha,\uparrow}, 0)]\psi_{\mathrm{PS},\alpha} = \epsilon_\alpha^{\mathrm{SIC}}\psi_{\mathrm{PS},\alpha}, \quad (2.67)$$

where ρ' is the total charge density of the valence pseudo-wave-functions. Thus,
a self-interaction corrected pseudopotential for orbital α, $V_{\mathrm{PS},\alpha}^{\mathrm{SIC}}$, can be defined as

$$V_{\mathrm{PS},\alpha}^{\mathrm{SIC}} = V_{\mathrm{PS},\alpha} - V_{\mathrm{H}}(\rho_\alpha) - V_{\mathrm{XC}}^{\mathrm{LDA}}(\rho_{\alpha,\uparrow}, 0) = V_{\mathrm{PS},\alpha} + \delta V_\alpha^{\mathrm{SIC}} . \quad (2.68)$$

However, $V_{\mathrm{PS},\alpha}^{\mathrm{SIC}}$ has a long range tail and so needs to be adjusted to perform bulk
calculations. Fortunately, atomic charge densities are localised so long range tails
have only a small effect on the energy eigenvalues. The important term is that of
the SIC Coulomb potential acting on the wave function, i.e. $V_{\mathrm{H}}(\rho_\alpha)\psi_{\mathrm{PS},\alpha}$. To remove
the problem, a cut-off radius r_{loc} is defined beyond which the difference made to the
eigenvalues by SIC is insignificant. Then, by adding a term $\frac{2}{r_{loc}}$ to both sides, the
potentials will go to zero at r_{loc} and can be cut off at this point. This only has the
effect of redefining the zero of the energy scale. The Kohn-Sham equation becomes

$$[-\nabla^2 + V_{\mathrm{PS},\alpha} + \delta V_\alpha^{\mathrm{SIC}} + \frac{2}{r_{loc}} + V_{\mathrm{H}}(\rho') + V_{\mathrm{XC}}^{\mathrm{LDA}}(\rho')]\psi_{\mathrm{PS},\alpha} = \left(\epsilon_\alpha^{\mathrm{SIC}} + \frac{2}{r_{loc}}\right)\psi_{\mathrm{PS},\alpha}. \quad (2.69)$$

Hence the final SIC pseudopotential is now given by

$$V_{\mathrm{PS},\alpha}^{\mathrm{SIC}} = \begin{cases} V_{\mathrm{PS},\alpha} + \delta V_\alpha^{\mathrm{SIC}} + \frac{2}{r_{loc}} & \text{if } r \leq r_{loc}; \\ 0 & \text{if } r > r_{loc}. \end{cases} \quad (2.70)$$

The total atomic SIC potential can be cast as in terms of nonlocal projectors,
similar to the Kleinman-Bylander projectors for the nonlocal part of the pseudopotential

$$\hat{V}_{\mathrm{SIC}} = \sum_\alpha \frac{|[V_{\mathrm{H}}(\rho_\alpha) + V_{\mathrm{XC}}^{\mathrm{LDA}}(\rho_\alpha, 0)]\phi_\alpha(\mathbf{r})\rangle\langle\phi_\alpha(\mathbf{r})[V_{\mathrm{H}}(\rho_\alpha) + V_{\mathrm{XC}}^{\mathrm{LDA}}(\rho_\alpha, 0)]|}{\langle\phi_\alpha(\mathbf{r})|[V_{H}(\rho_\alpha) + V_{\mathrm{XC}}^{\mathrm{LDA}}(\rho_\alpha, 0)]|\phi_\alpha(\mathbf{r})\rangle} . \quad (2.71)$$

ϕ_α are the pseudo-atomic orbitals. The pseudo-SIC Kohn-Sham equations now become

$$[-\nabla^2 + \hat{V}_{\mathrm{PS}} + \hat{V}_{\mathrm{H}} + \hat{V}_{\mathrm{XC}}^{\mathrm{LDA}} - \hat{V}_{\mathrm{SIC}}]\psi_n = \epsilon_n \psi_n . \tag{2.72}$$

The above corrections are calculated for an orbital with occupation ρ_α, the occupation of that orbital in the neutral atom. However, if the orbital is in a bulk material, the occupation of that orbital may change as it hybridises with the orbitals on other atoms. The orbital may be fractionally occupied, in which case applying the pseudo-SIC potential as if the orbital was fully occupied would result in an overcorrection.

One option would be to solve these equations fully self-consistently, with the SIC potential being recalculated for each value of ρ_α at each iteration. This would increase the computational cost of the correction. To avoid this, a linear scaling can be imposed. The occupation of an atomic orbital, ρ_α, is given by

$$\rho_\alpha = p_\alpha |\phi_\alpha|^2 . \tag{2.73}$$

In the bulk system, the occupation number p_α can be calculated by projecting the atomic orbital onto the Kohn-Sham states

$$p_\alpha = \sum_n f_n \langle \psi_n | \phi_\alpha \rangle \langle \phi_\alpha | \psi_n \rangle . \tag{2.74}$$

The total SIC correction can then be calculated initially for $p_\alpha = 1$, i.e. for the atomic orbital fully occupied, and then rescaled by the actual value of p_α

$$V_\alpha^{\mathrm{SIC}}(\rho_\alpha) = V_{\mathrm{H}}(\rho_\alpha) + V_{\mathrm{XC}}(\rho_\alpha, 0) = p_\alpha [V_{\mathrm{H}}(\rho_\alpha(p_\alpha = 1)) + V_{\mathrm{XC}}(\rho_\alpha(p_\alpha = 1), 0)] . \tag{2.75}$$

The drawback of this linear approximation is that interesting effects, such as discontinuities in the potential like the derivative discontinuity described above, may be lost.

This approximation for the self-interaction correction has been implemented in SIESTA and tested for a variety of different systems including molecules, metals and semiconductors. In particular, the agreement between experimental ionisation potentials for organic molecules and those calculated with DFT is dramatically improved using the atomic-SIC correction [75].

2.7   Conclusion

Density functional theory is a reliable and efficient electronic structure theory for a variety of different many-electron systems. In principle the theory itself is exact for ground state systems, although strictly speaking it is not valid for excited states. However, the exact form of the exchange-correlation potential is unknown, and has to be approximated. Commonly used approximations include LDA and GGA. Unfortunately, these approximate local potentials may contain self-interaction errors, which may cause the highest occupied molecular orbital to be in the wrong place, or cause the suppression of the derivative discontinuity.

These errors can be removed by the self-interaction corrections described in this chapter. The atomic self-interaction correction (ASIC) which has been implemented in SIESTA produces ionisation potentials which agree remarkably well with experimental values. However, the atomic and linear scaling approximations used in this method remove the derivative discontinuity. To at least partially obtain the derivative discontinuity, either the full-SIC or an exact-exchange based functional would need to be used. Unfortunately, both of these methods are orbital dependent and have not as yet been extended to finite bias. In the following chapters, the effects of these errors on calculations of the electronic transport properties of a variety of metal-molecule junctions will be explored in detail.

Chapter 3

Simple Model for Electron Transport

Using density functional theory [43, 44], as described in chapter 2, the calculation of the electronic structure of molecular devices containing hundreds of atoms becomes possible. DFT can then be combined with the non-equilibrium Green's function formalism [34, 35, 36] described in chapter 4 to calculate the electronic transport properties of such devices [37, 38, 39, 40, 41, 42]. However, while being able to perform *ab initio* calculations for large systems is very useful, the complexity of such methods, as well as the sheer number of variables involved, can make them difficult to understand intuitively. Therefore, simple models along the lines of that described by Datta et. el. [85], which capture some of the key aspects of electronic transport in these devices can be valuable in illustrating the role played in quantum transport by the different features of the electronic structure.

The molecular electronic devices currently under investigation typically consist of a molecule sandwiched between two metallic electrodes or "leads", as shown in figure 3.1. The leads could be surfaces or nanowires, while the molecule could be a point contact, a single organic molecule, or in general something which generates a scattering potential.
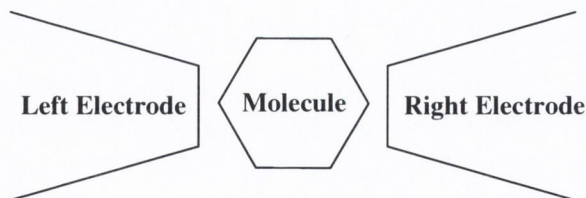
Figure 3.1: Diagram of the typical set-up for molecular electronics experiments. A single molecule is sandwiched between two metallic electrodes or "leads".

Electron transport at low bias through molecular junctions usually involves only

a small number of the orbitals on the molecule. This allows us to construct a simple model in which the electronic structure of the molecule is represented by a single energy level. Such a model already incorporates many of the physical properties which are important for transport. In this chapter, we will use this approach to illustrate some of the basic features of electron transport in molecular junctions. In particular, it will be shown how the conductance of the device depends on the strength of the coupling between the level and the electrodes, on the alignment between the molecular level and the states in the electrodes, and on the response of the level to changes in its occupation [74].

3.1   The Simple Model
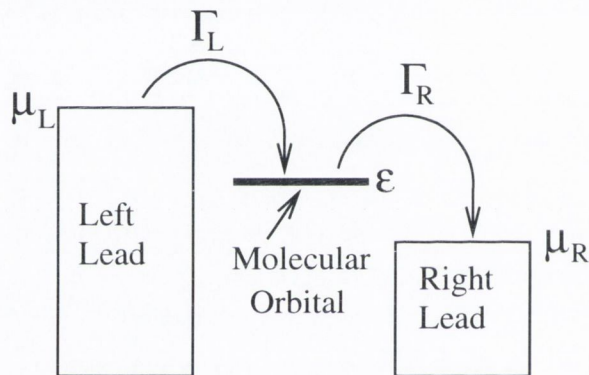
Figure 3.2: Energy level diagram for simple model. The molecule is represented by a single energy level ϵ, coupled to two metallic leads. When a potential bias is applied, the two leads will have different chemical potentials, μ_L and μ_R. The strength of the interaction or "coupling" between the leads and the molecule is described by parameters Γ_L and Γ_R, which control the rate at which electrons can enter or leave the molecular level.

A molecule can be modelled by a single orbital of energy ϵ, which is connected to two leads, as shown in figure 3.2. The leads are modelled as electron reservoirs which are kept at two different chemical potentials μ_L and μ_R. The charge in the system then redistributes. The left lead will try to impose an occupation N_L on the molecular orbital (i.e. it will try to establish an equilibrium situation), and the right lead will try to impose a charge N_R,

$$N_{L/R} = 2f(\epsilon, \mu_{L/R}),\tag{3.1}$$

where $f(\epsilon, \mu_{L/R})$ are the Fermi functions of the left and right leads respectively

$$f(\epsilon, \mu) = \frac{1}{1 + \exp\left(\frac{\epsilon - \mu}{k_B T}\right)} \ . \tag{3.2}$$

The level is assumed to be spin degenerate so that it can hold up to two electrons. This is accounted for by the factor of 2 in the expression for the occupation.

Thus the "average" charge N on the molecule can be calculated by using a simple balance between the electron flow from the left lead into the level and the electron flow out into the right lead. The current from the left lead into the orbital, I_L, is proportional to the difference between the actual occupation of the orbital, N, and the "equilibrium" occupation the lead is trying to impose, N_L

$$I_L = \frac{e\Gamma_L}{\hbar} (N_L - N) \ . \tag{3.3}$$

Similarly, the current from the right lead into the molecular orbital, I_R, is given by

$$I_R = \frac{e\Gamma_R}{\hbar} (N - N_R) \ , \tag{3.4}$$

where $\Gamma_i/\hbar$ is the transmission rate between the ith contact and the molecule. Γ depends on the strength of the interaction or "coupling" between the molecular level and the lead.

In a steady state situation where the charge on the molecular level is constant, the rate at which electrons enter the level will be the same as the rate at which they leave, and so the two currents described above should be equal, i.e., $I_L = I_R$. This can be used to obtain an equation for the average charge on the level, N

$$N = 2 \left(\frac{\Gamma_L f(\epsilon, \mu_L) + \Gamma_R f(\epsilon, \mu_R)}{\Gamma_L + \Gamma_R} \right) \ . \tag{3.5}$$

Note that if the transmission rates between the molecule and the two different contacts, Γ_L and Γ_R, are equal, then the equation for the occupation becomes

$$N = f(\epsilon, \mu_L) + f(\epsilon, \mu_R) \ , \tag{3.6}$$

i.e. the level occupation is now independent from the transmission rates Γ_L and Γ_R.

If the level is below the chemical potential of both of the leads, then it will be full, i.e. it will contain two electrons, and if it is above the chemical potential of both of the leads, it will contain zero electrons. However, if the leads have different chemical potentials and the level is in between them, then it will have an occupation

between zero and two. In the case where the coupling to both leads is the same, the level will contain one electron when it is positioned between the chemical potentials of the two leads. In the same framework the steady state current can be calculated from the condition $I_L = -I_R$ to be

$$I = \frac{2e}{\hbar} \frac{\Gamma_L \Gamma_R}{\Gamma_L + \Gamma_R} \left(f(\epsilon, \mu_L) - f(\epsilon, \mu_R) \right) . \tag{3.7}$$

Self-consistency can be added to the problem by assuming that the energy of the molecular orbital, ϵ, is dependent on its occupation, N

$$\epsilon = \epsilon_0 + U_{SCF}(N) \tag{3.8}$$

where U_{SCF} is a self-consistent or "charging" potential. The actual form of U_{SCF} will be discussed later, and it will be demonstrated that it can have a significant effect on the electron transmission.

The interaction of the molecule with the infinite leads has the effect of broadening the orbitals. To account for this, discrete level can be replaced by a Lorentzian density of states (DOS)

$$D(E) = \frac{1}{2\pi} \frac{\Gamma}{(E - \epsilon)^2 + \left(\frac{\Gamma}{2}\right)^2} , \tag{3.9}$$

with $\Gamma = \Gamma_L + \Gamma_R$. This Lorentzian is centred at $E = \epsilon$ and its width is determined by Γ. The stronger the coupling of the orbital to the leads, the broader the density of states for that orbital will be. The occupation is then given by an integral over energy of the density of states multiplied by the probability of a state being occupied

$$N = 2 \int_{-\infty}^{\infty} dE D(E) \frac{\Gamma_L f(E, \mu_L) + \Gamma_R f(E, \mu_R)}{\Gamma_L + \Gamma_R} , \tag{3.10}$$

The occupation and position of the energy level can then be calculated self-consistently as shown the flowchart in figure 3.3. First, an initial value is taken for the level occupation N and position ϵ, and this is then used to calculate the density of states $D(E)$. Then the integral in equation (3.10) is solved to obtain the new value of N, the occupation of the level. The new position of the level is then calculated and the procedure is repeated until the difference between the values of N for two separate iterations is less than a certain tolerance. This is analogous to the self-consistent procedure used to obtain the charge density in more complex methods such as DFT as described in chapter 2, where single level occupation N replaces the charge density ρ and the single level energy ϵ replaces the Hamiltonian H.

```
┌─────────────────────────────────────┐
│ Level (Simple Model): ε(N)          │        ┌──────────────────────────┐
│ Hamiltonian (large system): H(ρ)    │───────▶│ Density of States D(E)   │
└─────────────────────────────────────┘        └──────────────────────────┘
                ▲                                            │
                │                                            ▼
┌──────────────────────────┐        ┌──────────────────────────────────────────────┐
│ Check for Convergence:   │        │ Level Occupation (Simple Model): N            │
│ Finish if converged;     │◀───────│                                              │
│ Repeat loop if not.      │        │ Charge Density matrix (large system): ρ      │
└──────────────────────────┘        └──────────────────────────────────────────────┘
```
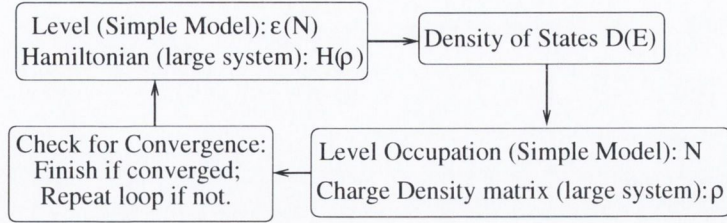
Figure 3.3: Self-consistent loop for the calculation of the level occupation. An initial approximation is taken for the level occupation N and position ϵ, and this is then used to calculate the density of states $D(E)$. $D(E)$ is then integrated as shown in equation (3.10) to get a new value for the occupation, and the procedure is repeated until the level occupation converges. This method is analogous to that for calculating the charge density and Hamiltonian for a more complex system using DFT as described in chapter 2.

Finally, when the level occupation has converged the current can be obtained from the following energy integral

$$I = \frac{2e}{\hbar} \int_{-\infty}^{\infty} dE D(E) \frac{\Gamma_L \Gamma_R}{\Gamma_L + \Gamma_R} \left(f(E, \mu_L) - f(E, \mu_R) \right) . \tag{3.11}$$

The integrand is only non-zero in the region in which $f(E, \mu_L) - f(E, \mu_R) \neq 0$. Therefore, this integral only needs to be performed over an energy window around the chemical potentials μ_L and μ_R known as the "bias window", as $f(E, \mu_L) - f(E, \mu_R)$ approaches zero rapidly outside such a window. Thus the I-V curve will depend on the density of states of the molecule in this bias window, and on the strength of the coupling between the level and the leads, Γ_L and Γ_R.

3.1.1 Effect of Level Position

The I-V curve will depend on the position of the level, ϵ, as the density of states, $D(E)$, is centred around this energy. The closer the level is to the chemical potential of the leads, the smaller the conductance gap of the molecule. This can be seen in the I-V curves shown in figure 3.4.

Here the chemical potential of both electrodes is -5.0eV at zero bias, and no charging effects have been included (i.e. the position of the level does not change with its occupation). When the energy level is aligned with the Fermi level of the leads, it starts to conduct as soon as a voltage is applied. However, when the level is further away from the Fermi level, it will not start to conduct until it is between the chemical potentials of the two leads - i.e. until it is within the bias window. Thus, the resonances in the transmission probability correspond to energy levels in
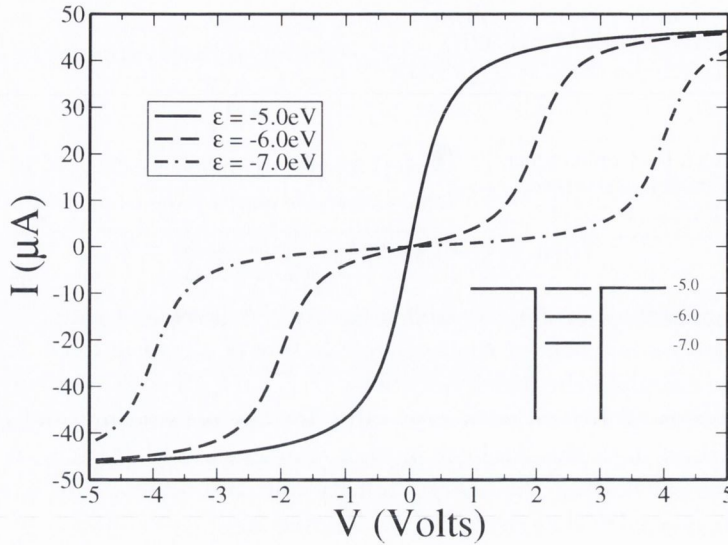
Figure 3.4: *I-V* curves for different positions of the energy level ϵ. The Fermi energy of the leads is located at -5.0eV. The coupling to each lead is symmetric and equal to 0.2eV. As can be seen, moving the level further from the chemical potential of the leads opens up the conductance gap.

the molecule, as shown in figure 3.5. The total size of the conductance gap (the gap between the positive and negative bias points where the system starts to conduct) is given by $4|\epsilon - \mu_0|$, where μ_0 is the chemical potential of both of the leads at zero bias.

3.1.2   Effect of Coupling Strength

The *I-V* curve also depends on the strength of the coupling between the level and the left and right leads, Γ_L and Γ_R. Obviously, the stronger the coupling, the larger the total current I would be expected to be. This can be seen in the *I-V* curves shown in figure 3.6. However, stronger coupling also means that the density of states of the level, $D(E)$, will be broader. Therefore, the shape of the *I-V* curve also changes. The stronger the coupling, the broader the level and thus the smoother the *I-V* curve will be.

3.2   Charging Effects

The effect of the charging of the level on the electronic transport depends on the form of the charging potential U_{SCF}, and on the strength of the interactions Γ_L and Γ_R between the level the leads. The simplest dependence of the energy of the level
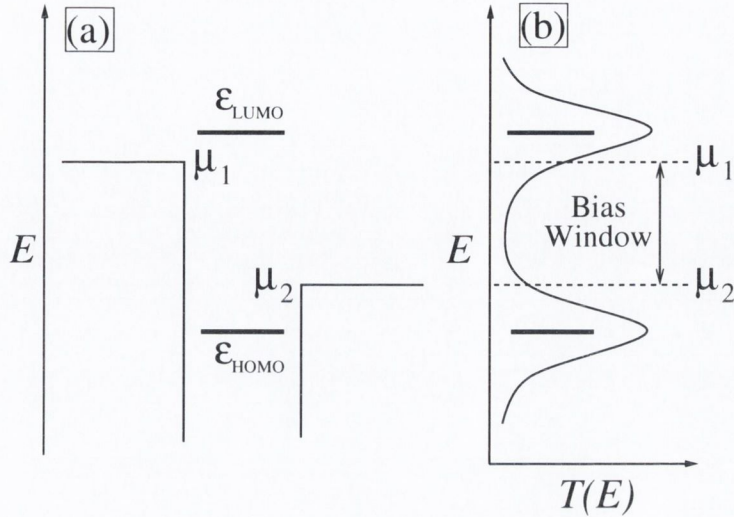
Figure 3.5: Diagram showing (a) energy levels of two molecular orbitals and (b) transmission coefficients. The resonances in the transmission probability, $T(E)$, correspond to energy levels in the molecule. The current is the integral over the transmission coefficients within the bias window.

on its occupation would be a linear one

$$\epsilon = \epsilon_0 + U(N - N_0),\qquad(3.12)$$

where U is a constant and N_0 is the occupation of the level when it is at energy ϵ_0. This is what would be expected from the molecule if it was acting as a simple capacitor.

For $U = 0.0\text{eV}$, i.e. where the energy of the level is independent of its occupation, the current will reach its maximum quickly (for small biases V), as shown in figure 3.7. In this case, the size of the conductance gap will be $4|\epsilon_0 - \mu_0|$, as before. However, if U is non-zero, the level will shift as it charges, so that it remains partially outside the bias window. The conductance gap will remain $4|\epsilon_0 - \mu_0|$, but the maximum in the current will not be reached until the bias reaches $2|\epsilon_0 - \mu_0| + 2U$, as shown in figure 3.7.

A second effect due to charging is the introduction of asymmetries into the I-V curves if Γ_L and Γ_R are not equal. As can be seen from equation (3.11), and as can be seen from figure 3.9, if $U = 0.0\text{eV}$ (i.e. if the energy of the level is independent of its occupation), then the I-V curve will be symmetric even if the coupling to the leads is asymmetric (i.e. if $\Gamma_L \neq \Gamma_R$). However, with asymmetric coupling, the electrons can enter and leave from one lead more easily that the other. Hence, if the direction of the bias is such that the lead with the stronger coupling to the level is
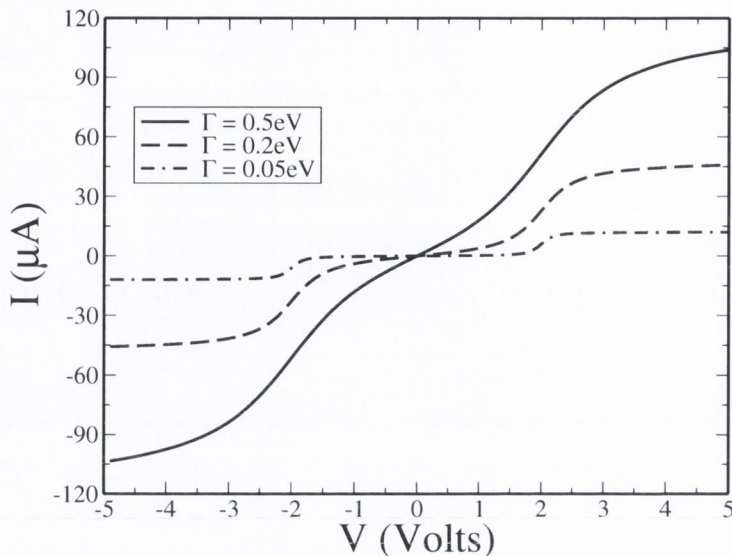
Figure 3.6: *I-V* curves for strength of coupling leads-molecule coupling Γ. The Fermi energy of the leads is located at -5.0eV. The coupling to each lead is symmetric, and the level is at -6.0eV. As can be seen, increasing the strength of the coupling increases the size of the current, and also changes the shape of the *I-V* curve.

at the higher chemical potential, then the steady-state occupation of the level in the bias window will be greater than one electron, as shown in figure 3.8a. Similarly if it has the lower chemical potential, then the steady-state occupation of the level will be less than one electron.

Therefore, if $|U| > 0.0\text{eV}$ so that the energy of the level depends on its occupation, then its position will be altered depending on the bias direction, as shown in figure 3.8b. In the case where $\Gamma_L > \Gamma_R$ and $U = 1.0\text{eV}$, the level tracks μ_L for positive bias as the level charges due to the strong coupling with the left lead, but remains in approximately the same position for negative bias. Since the level remains outside the bias window for longer at positive bias, the *I-V* curve will be asymmetric, as shown in figure 3.9.

3.2.1   Effect of Discontinuity in Charging Potential

The linear dependence of the energy of the molecular orbitals on their occupations is a good approximation to the most commonly used exchange-correlation potentials in DFT such as LDA [44] and GGA [59, 60, 61]. However, as explained in chapter 2, both of these have problems - they lack the presence of the derivative discontinuity [72, 73]. To demonstrate the effect of a derivative discontinuity on electronic
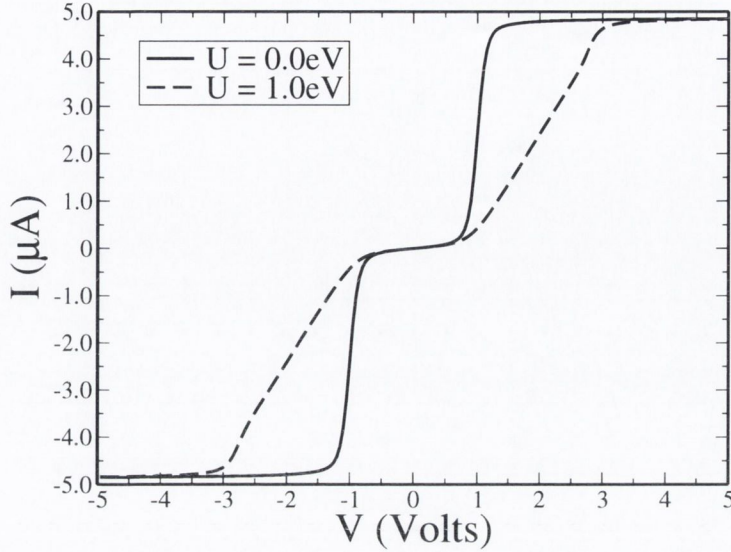
Figure 3.7: *I-V* curves for simple model for different values of U. For $U = 0\text{eV}$, the energy
level does not shift as its occupation changes, and so it reaches its maximum
current straight away. However, for $U = 1\text{eV}$, the level starts to shift upwards
as it is filled, and so is not completely inside the bias window until the bias
reaches $3V$. The coupling between the level and the contacts is symmetric with
both Γ_L and Γ_R equal to 0.02eV; ϵ_0 is -4.5eV and μ_0 is -5.0eV.

transport, we will now introduce a discontinuous charging potential for this simple
model. The energy of the level as a function of its occupation is described as follows

$$U_{\text{SCF}} = \frac{U_b}{1 + \exp\left(\frac{C_b - N}{W}\right)} + \frac{U_t}{1 + \exp\left(\frac{C_t - N}{W}\right)} , \tag{3.13}$$

where N is the occupation of the level, C_b and C_t are parameters which control the
positions of the discontinuities, U_b and U_t are parameters which control the height of
the two steps, and W is a parameter which controls the width of the discontinuities.
The values chosen for these parameters are 0.05 for C_b, 1.05 for C_t, $\frac{1}{3}$ for U_b, $\frac{2}{3}$ for
U_t, and 0.01 for W. These values give a function of the form shown in figure 3.10.

The discontinuous potential rises sharply from zero occupation, then levels off,
and then rises sharply again at an occupation of one electron. This approximates
the derivative discontinuity in the energy which has been shown to be present in the
true DFT potential at integer occupation. Note that the energy increase required
to populate the orbital with two electrons is much larger than needed to populate
with just one electron. The linear potential is then constructed so as to match the
discontinuous potential at occupations of 0.0, 0.5, and 1.5 electrons [101]. Note that
our linear potential flattens out at an occupation of ~ 1.6 electrons, when it goes
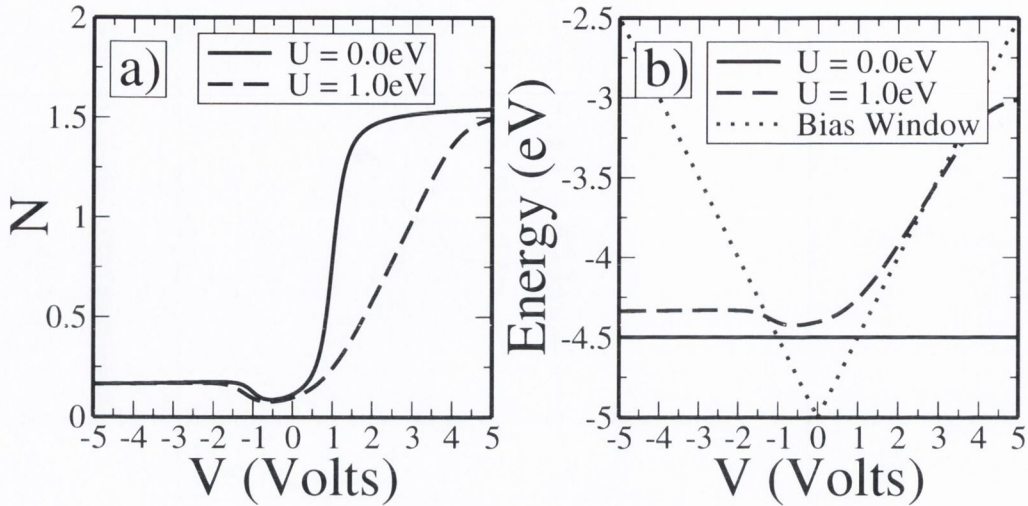
Figure 3.8: Plot of (a) level occupation and (b) level position as a function of bias for simple model for asymmetric coupling for different values of U. For both values of U, the level charges asymmetrically, having higher occupation at positive bias where $\mu_L > 0$. For $U = 0eV$ where there are no charging effects the level remains at the same energy. However, for $U = 1eV$, the different occupation of the level depending on the bias direction does affect its position. It moves up with the chemical potential of the left (strongly coupled) lead at positive bias, and remains in the same position for negative bias. The coupling between the level and the contacts is asymmetric with $\Gamma_L = 0.2eV$ and $\Gamma_R = 0.02eV$; ϵ_0 is -4.5eV and μ_0 is -5.0eV.

above 0.0eV. This is an actual problem with approximate XC potentials such as LDA where certain negative ions are calculated to be unbound, but which are stable in reality.

The discontinuous potential can have the effect of preventing the level from charging or discharging, which in turn should affect the transport characteristics of the system. The size and nature of this effect will depend on the strength of the coupling between the leads and the molecular orbital, and on the alignment of the level with the chemical potentials of the leads.

Figure 3.11 shows the I-V curve and plots of the level occupation and position as a function of applied bias when the coupling between the leads and the molecule is weak. Γ_L and Γ_R are both set equal to $0.02eV$, and the Fermi level of the leads is set to -5.0eV. As shown in panel (a), with the discontinuous potential the level cannot start to fill until a bias of $\sim 2.0V$ is applied, whereas it can start to charge at 0.0V with the linear potential. This is because the discontinuous potential causes the level to rise rapidly as soon as any charge is added. Therefore, as shown in panel
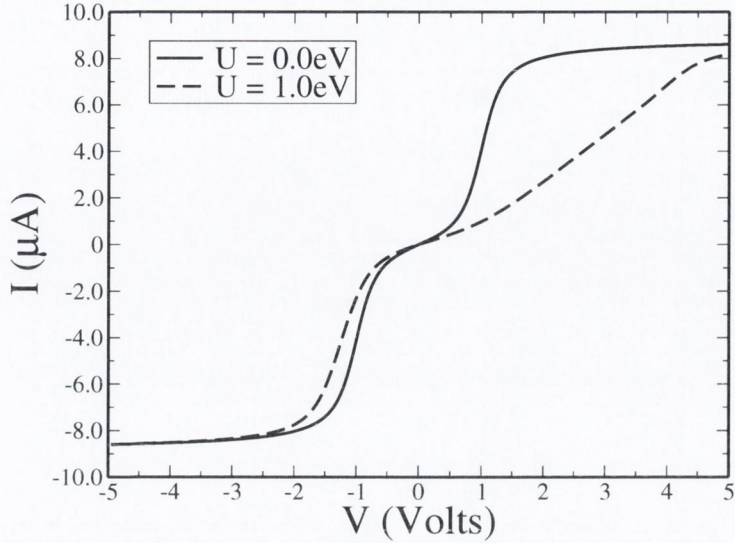
Figure 3.9: *I-V* curves for simple model for asymmetric coupling for different values of *U*.
For *U* = 0.0eV where there are no charging effects, the *I-V* curve is symmetric
despite the coupling to the leads being asymmetric. However, for *U* = 1.0eV,
the different occupation of the level depending on the bias direction affects its
position, and hence the *I-V* curve is asymmetric with respect to bias. The
coupling between the level and the contacts is asymmetric with $\Gamma_L = 0.2$eV
and $\Gamma_R = 0.02$eV; ϵ_0 is -4.5eV and μ_0 is -5.0eV.

(b), the level will remain pinned just above the higher of the two chemical potentials
until the plateau in the charging potential at ~ -3.8eV is reached. This occurs at a
bias of $\sim 2.0V$. At this point the level can fill rapidly without moving. This has a
major effect on the *I-V* characteristics of the system. If the level is pinned outside
the bias window and cannot charge, then it will not conduct. Therefore, as shown in
panel (c) of figure 3.11, the discontinuous charging potential has the effect of opening
up a gap in the *I-V* curve compared to the linear potential. This conductance gap
is from -2.0V to 2.0V, which corresponds to the applied bias required to bring the
level to the top of the discontinuity.

For the linear potential, on the other hand, the level can start to charge as soon
as it is in the bias window. As shown in panel (b), the level is pinned right at
the chemical potential, rather than just above it as in the case of the discontinuous
potential. Therefore, the level can start to conduct as soon as a bias is applied, and
there is no conductance gap.

When the coupling between the level and the leads is strong however, the discon-
tinuous charging potential has much less of an effect on the *I-V* curve. Figure 3.12
shows plots of the occupation and position of the level and the *I-V* curve with both
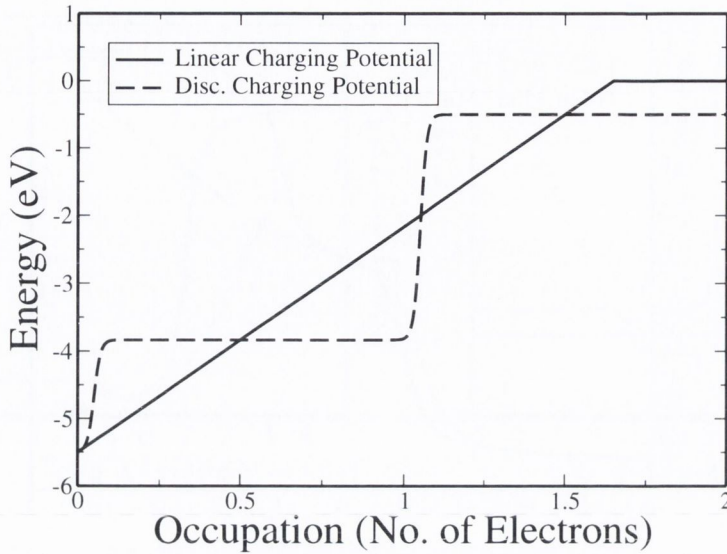
Figure 3.10: Self-consistent potentials for simple transport model. One potential shows
discontinuities at integer occupation, while the other is linear and is fitted so
that it matches the discontinuous potential at occupations of 0.0, 0.5, and 1.5
electrons.

Γ_L and Γ_R equal to 1.2eV.

Strong coupling between the leads and the molecular level causes its the density
of states to be broadened to a much greater extent. Therefore, even if the centre of
the DOS is pinned above the bias window, some of its tail will be within the bias
window, allowing conduction. The DOS at zero bias for both potentials for strong
coupling are shown in figure 3.13. Part of the Lorentzian will be below the Fermi level
at zero bias and so the level fills and rises until the centre reaches the first plateau in
the charging potential. Thus as the bias window is opened, the level can now charge
or discharge without changing energy, instead remaining fixed in position, as shown
in figure 3.12(b).

This may actually be physically realistic since stronger coupling between the level
and the contacts would allow electrons to delocalise, allowing fractional charging and
hence a more linear increase in the energy (as predicted by LDA for the homogeneous
electron gas).

The behaviour is somewhat different when the chemical potential of the leads at
zero bias is at or just above that required for there to be integer (i.e. one or two
electrons) occupation of the molecular level, as is shown in figure 3.14. For example,
if the chemical potential of the leads is in such a position so that the conducting
level is fully occupied by two electrons at zero bias (i.e. if conduction is through
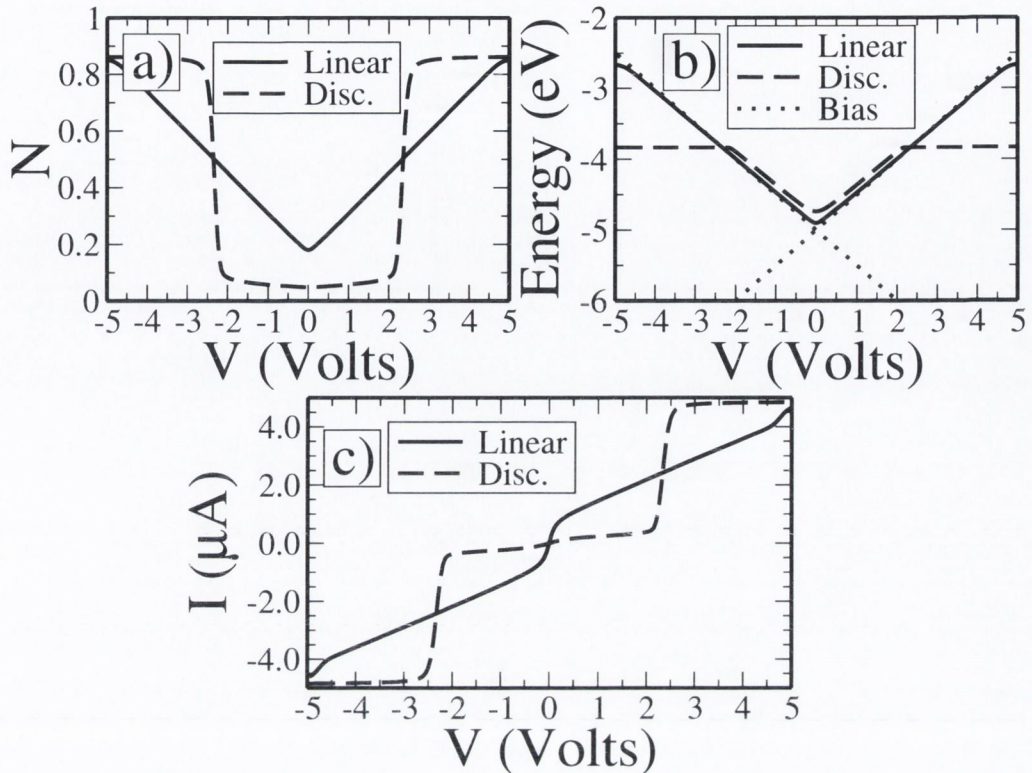
Figure 3.11: Occupation (a) and position (b) of molecular energy level, and *I-V* curves (c) for weak symmetric coupling between the leads and the orbital. Γ_L and Γ_R are both equal to $0.02eV$, and μ_0 (the Fermi level of the leads) is set to -5.0eV. For the discontinuous charging potential, the level remains outside the bias window and does not charge until a certain voltage is reached, as shown in panels (a) and (b). This in turn opens up a conductance gap in the *I-V* curve, as shown in panel (c).

the HOMO), then it will lose almost an entire electron without moving as soon as it enters the bias window, as shown in figure 3.14. Thus, the level in a discontinuous potential may have a higher conductance under these circumstances than in a linear potential.

3.3 Conclusion

Our simple model illustrates some of the key concepts underpinning the theory of electron transport through molecules. Electron transport through a molecule attached between two electrodes with different chemical potentials will occur through a particular orbital if that molecular orbital is coupled to the electrodes and lies between their chemical potentials. The occupation of the molecular level will be
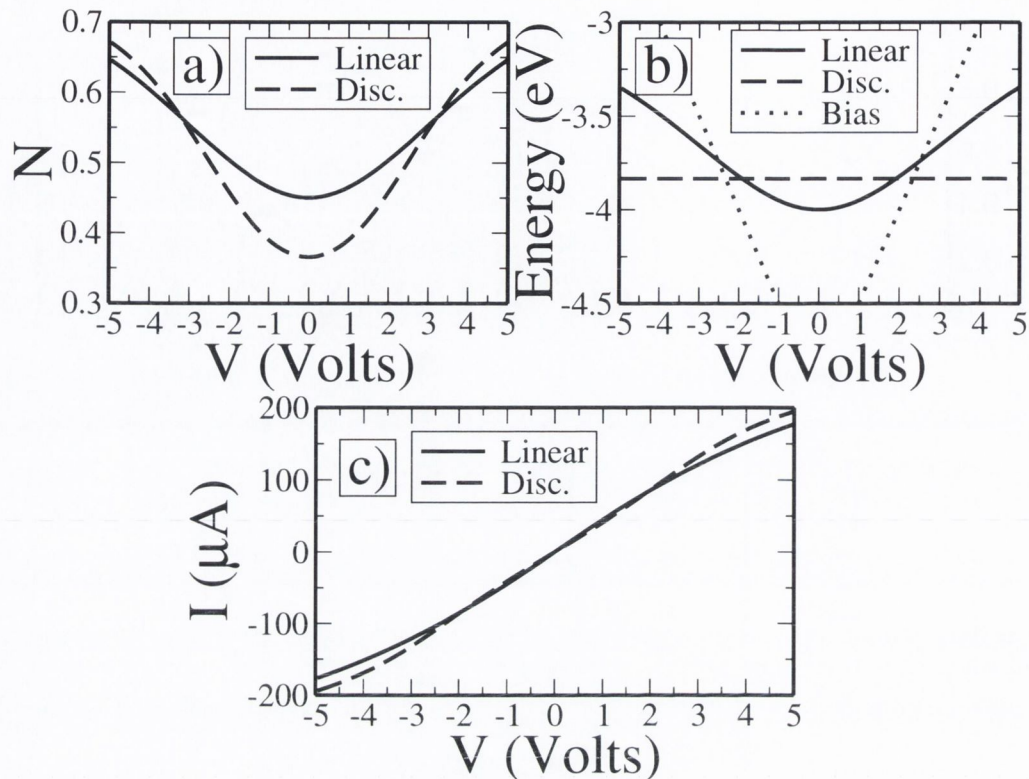
Figure 3.12: Occupation (a) and position (b) of molecular energy level, and *I-V* curves (c) for strong symmetric coupling between the leads and the orbital. Γ_L and Γ_R are both equal to 1.2eV, and μ_0 (the Fermi level of the leads) is set to -5.0eV. For the both the linear and discontinuous charging potentials, the levels are broad and increasing the bias does not alter the occupation of the level very much, as shown in panel (a). The energy of the level does not change much, and the nature of the charging potential has only a small effect on the *I-V* curve.

determined by its position relative to the chemical potentials of the electrodes, and the symmetry of the coupling between the level and the electrodes. If the energy of the level itself is dependent on its occupation, this, combined with asymmetric coupling to the electrodes, can lead to asymmetry in the *I-V* curves for the device.

The nature of the dependence of level on its occupation can strongly affect the transport properties of the system. A discontinuous charging potential can open up conductance gaps in the *I-V* curve, depending on the relative positions of the molecular orbitals and the chemical potential of the leads. This effect is particularly significant for weak coupling between the molecule and the leads, and tends to disappear for stronger coupling.

In the following chapters, this method for calculating electronic transport will
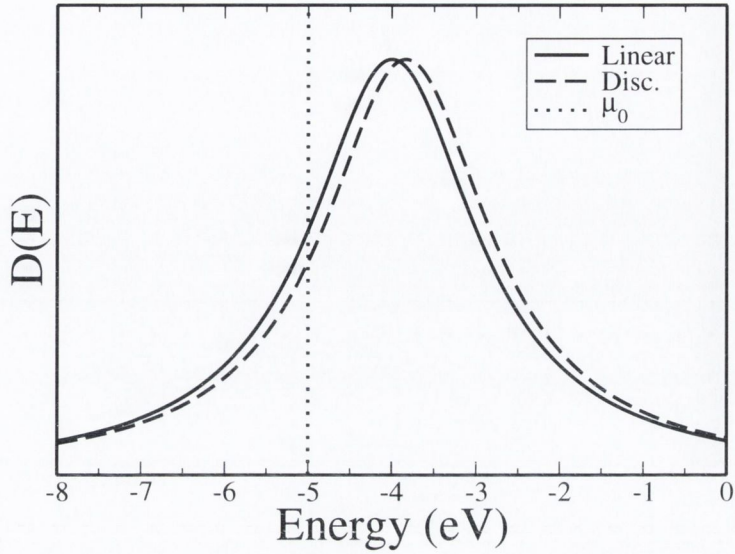
Figure 3.13: DOS of level at zero bias for strong coupling. Γ_L and Γ_R are both equal to
1.2eV, and μ_0 (the Fermi level of the leads) is set to -5.0eV. Note how part of
the tail of the DOS lies below the chemical potential of the leads for both types
of charging potential. Therefore, for the discontinuous charging potential, the
level will contain enough charge to move up to the flat part of the potential
where it will conduct.

be generalised and extended to more realistic systems. The effects of level position,
coupling strength and asymmetry, and the nature of the response of the level to
changes in occupation will all be studied in detail for a variety of metal-molecule
junctions.
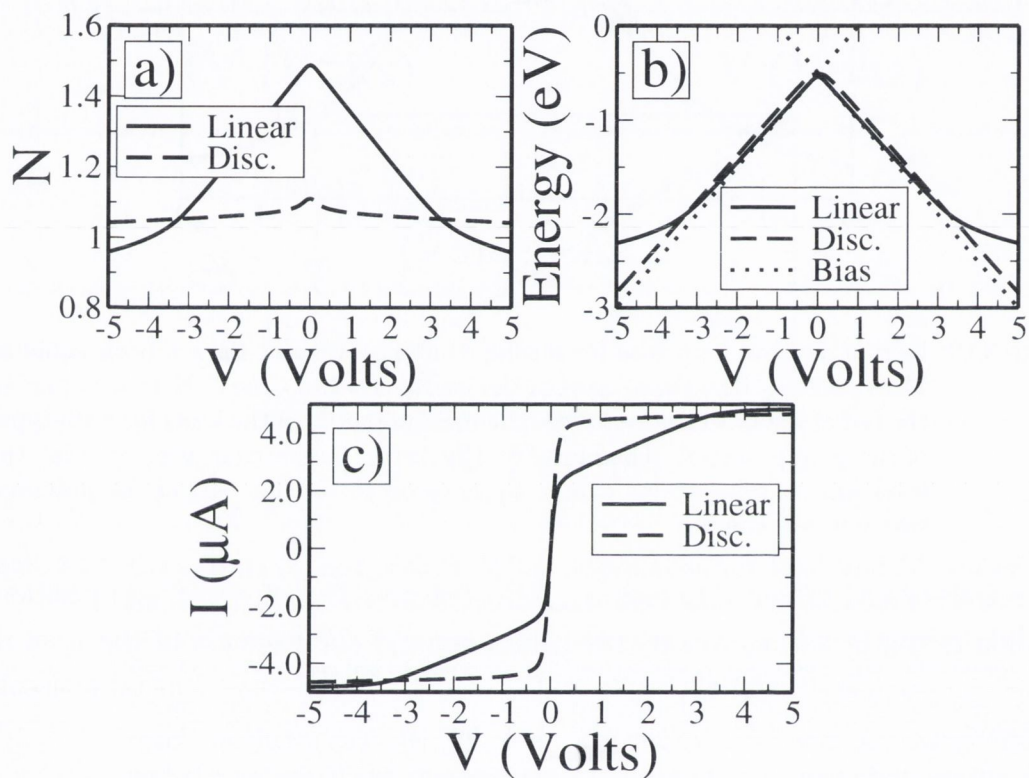
Figure 3.14: Occupation (a) and position (b) of molecular energy level, and *I-V* curves
(c) for weak symmetric coupling between the leads and the orbital. Γ_L and
Γ_R are both equal to 0.02eV, and μ_0 (the Fermi level of the leads) is set to
-0.5eV. The linear and discontinuous charging potentials are still the same as
for the previous calculations. The occupation and position of the levels drop
with bias, remaining within the bias window so that there is no conductance
gap.

Chapter 4

Non-Equilibrium Green's Function Formalism

Modern electronic devices have been now been reduced to a size where it is necessary to use a full quantum mechanical description to model their behaviour. The electronic transport properties of molecular devices need to be calculated using quantum mechanical scattering theory to determine the transmission probabilities. There are several methods for doing this. Among them, the most popular is the non-equilibrium Green's function formalism (NEGF) [34, 35, 36, 38, 102] combined with an electronic structure method such as density functional theory (DFT) [43, 44, 45, 86]. Other schemes include time-dependent DFT [57, 58] or many-body methods [50, 51, 52, 53, 54, 55, 56]. The calculations described in this thesis are performed using the NEGF combined with a tight-binding Hamiltonian; and with the SMEAGOL program [37, 38, 39], in which NEGF is combined with the DFT program SIESTA [82, 83, 84]. There are also several other numerical implementations of NEGF with DFT [40, 41, 42].

The typical system modelled using these methods is shown in figure 4.1. In the calculations described in this thesis, the device typically consists of an organic molecule sandwiched between two metallic electrodes. However, the method described here can also be applied to other types of devices, such as constrictions in metal or semiconductor nanowires, or to solid state devices consisting of multiple thin layers of different materials.

The electrodes, usually referred to as "leads", are typically treated as being periodic in the direction of the electronic transport and their Hamiltonian is usually written in terms of "principal layers". The entire system is unbounded, so that the Hamiltonian of the full system would be infinite in size, but it is not periodic due to the translational symmetry being broken by the presence of the scattering region. For the problem to be solved computationally, this infinite system has to be

51

mapped onto a finite one. This can be done by writing the problem in terms of the retarded Green's function for the entire system, as described in section 4.2. A few of the principal layers of the leads are usually included with the molecule to form a "scattering region". The Hamiltonian for the scattering region is finite and can be calculated using an electronic structure method such as DFT. However, this finite Hamiltonian is non-Hermitian, which corresponds to the total number of particles in the scattering region not necessarily being conserved.
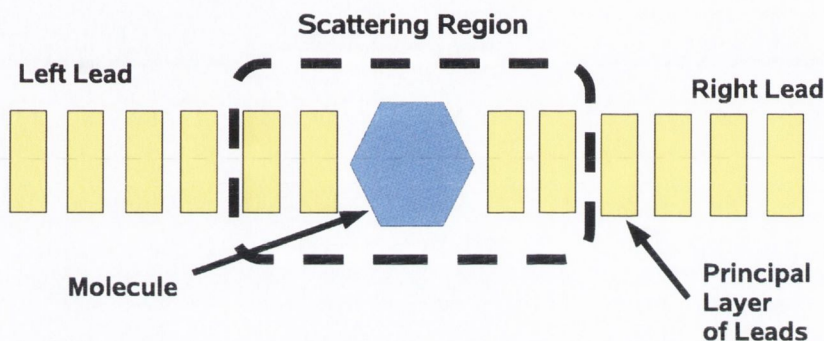
Figure 4.1: The typical system investigated in transport calculations is broken into three parts: a left and right "lead" and a "scattering region"

The Hamiltonian of the scattering region combined with the self-energies of the leads produce a finite effective Hamiltonian for the entire system. This can then be used to calculate the transport properties of the molecule, such as the transmission coefficients and the I-V curves.

4.1   Green Functions for Simple Model

In chapter 3, a simple model for electron transport through a single molecular level was introduced. This model can be reformulated in terms of Green's functions [85, 103]. This formulation of the simple model will serve as an introduction to Green's functions, and their use in calculating electron transport.

The Green's function for an operator $\hat{O}$ is defined to be the function which, when operated on by $\hat{O}$, gives the delta-function

$$\hat{O}G(\mathbf{r}, \mathbf{r}') = \delta(\mathbf{r} - \mathbf{r}').\tag{4.1}$$

By converting to matrix notation, i.e. by expanding G over a finite basis set, the δ-function is replaced by the identity matrix I to get

$$\hat{O}G = I .\tag{4.2}$$

If the function $\psi(\mathbf{r})$ is an eigenvector of the operator $\hat{O}$, then the eigenvalue equation can be written in the form

$$\hat{O}\psi(\mathbf{r}) = E\psi(\mathbf{r}) .\tag{4.3}$$

where E is the eigenvalue. By writing this equation in matrix format we get

$$(ES - \hat{O})\psi = 0 .\tag{4.4}$$

where S is the overlap matrix and ψ is a column vector. In the case of an orthogonal basis set, the overlap matrix will simply be equal to the identity matrix. The Green's function, $G(E)$ for the operator $(\hat{O} - ES)$ is then given by

$$(ES - \hat{O})G(E) = I .\tag{4.5}$$

For transport calculations, the relevant operator is the Hamiltonian of the scattering region. For the simple model, the Hamiltonian describes only the position of the level ϵ, with a broadening due to the coupling to the leads, Γ_L and Γ_R. Thus, the Green's function for the simple model is given by

$$G(E) = \left(E - \epsilon + i\frac{\Gamma_{\mathrm{L}} + \Gamma_{\mathrm{R}}}{2} \right)^{-1} ,\tag{4.6}$$

where E is the energy. The density of states for the system is then given by the imaginary part of the Green's function

$$D(E) = -\frac{1}{\pi}\mathrm{Im}(G(E)) .\tag{4.7}$$

The number of electrons on the level is once again an integral over the occupied states

$$N = \frac{1}{\pi} \int_{-\infty}^{\infty} dE \left(|G(E)|^2 \Gamma_{\mathrm{L}} f(E, \mu_{\mathrm{L}}) + |G(E)|^2 \Gamma_{\mathrm{R}} f(E, \mu_{\mathrm{R}}) \right) .\tag{4.8}$$

Finally, the current is given by an energy integral of the form

$$I = \frac{2e}{h} \int_{-\infty}^{\infty} dE \Gamma_{\mathrm{L}} \Gamma_{\mathrm{R}} |G(E)|^2 \left(f(E, \mu_{\mathrm{L}}) - f(E, \mu_{\mathrm{R}}) \right) .\tag{4.9}$$

In the next section, this formulation will be generalised to more realistic systems, using more complex Hamiltonians and considering leads with realistic band structures.

4.2   Green Functions for Open System

The typical system calculated using the NEGF formalism is shown in figure 4.2. It is assumed to be described by a Hamiltonian written over some finite basis set formed by atomic orbital like functions. A scatterer such as an organic molecule is sandwiched between two conducting electrodes or "leads". These leads are periodic in the transport direction and are ideally broken into sections called principal layers. Each layer is described by a matrix Hamiltonian H_0. The interaction between two neighbouring principal layers are described by a Hamiltonian H_1 in one direction, and H_{-1} in the opposite direction. For systems which preserve time-reversal symmetry, $H_{-1} = H_1^\dagger$.

The scattering region is described by a finite Hamiltonian H_M, and the interaction with the left and right leads are described by matrices H_{LM} and H_{RM} respectively. Typically, a sufficiently large number of principal layers of the leads are included in the scattering region to allow the charge density to converge to its bulk value, thus screening the potential of the molecule. This allows the leads to be calculated independently of the scattering region, i.e. it is assumed that the presence of the molecule does not alter the electronic structure of the leads beyond a certain distance. The full Hamiltonian, H, of this infinite system is given by

$$
H = \begin{pmatrix}
. & . & . & . & . & . & . & . & . & . & . \\
. & 0 & H_{-1} & H_0 & H_1 & 0 & . & . & . & . & . \\
. & . & 0 & H_{-1} & H_0 & H_{LM} & 0 & . & . & . & . \\
. & . & . & 0 & H_{ML} & H_M & H_{MR} & 0 & . & . & . \\
. & . & . & . & 0 & H_{RM} & H_0 & H_1 & 0 & . & . \\
. & . & . & . & . & 0 & H_{-1} & H_0 & H_1 & 0 & . \\
. & . & . & . & . & . & . & . & . & . & .
\end{pmatrix} \tag{4.10}
$$

The Schrödinger equation associated with this Hamiltonian is

$$
H\psi = ES\psi\,, \tag{4.11}
$$

where S is the overlap matrix (the identity matrix in the case of an orthogonal basis set), ψ is the wave function (the eigenvectors of this Hamiltonian) and E is the energy. Broadening δ is added to the energy, and the Green's function equation for the entire system becomes

$$
(\lim_{\delta \to 0}(E + i\delta)S - H)G(E) = I\,, \tag{4.12}
$$

where $\delta > 0$ gives G^R, the retarded Green's function, and $\delta < 0$ gives G^A, the advanced Green's function. We will use the retarded Green's function G^R here, in which δ tends to zero from above.
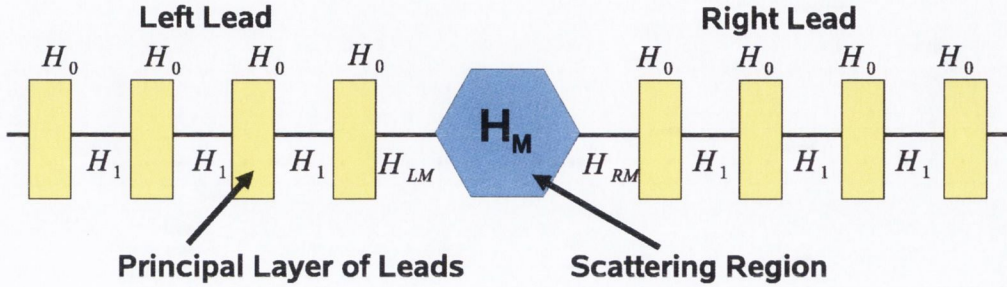
Figure 4.2: Diagram of the system investigated in electron transport calculations, showing the left and right leads and a scattering region in the middle

The matrices in equation (4.12) are infinite, so it is useful to break the Hamiltonian into three parts: the scattering region in the middle, (H_M), the left and right leads, (H_L and H_R respectively), as shown in figure 4.2. The full Hamiltonian H of the infinite system can be written in block matrix form

$$H = \begin{pmatrix} H_L & H_{LM} & 0 \\ H_{ML} & H_M & H_{MR} \\ 0 & H_{RM} & H_R \end{pmatrix}. \tag{4.13}$$

The interaction between the scattering region and the leads is described by the semi-infinite submatrices H_{LM}, H_{ML}, H_{RM}, and H_{MR}, as shown. The matrices which describe the leads, H_L and H_R, are infinite. Since principal layers are included between the scattering region on each side, the non-zero part of these submatrices effectively consists of the Hamiltonians describing interaction between two principal layers in the leads, H_1 and H_{-1}.

The overlap matrix S can be broken up into sections in a fashion similar to that of the Hamiltonian, where a similar notation to that in equation (4.13) applies

$$S = \begin{pmatrix} S_L & S_{LM} & 0 \\ S_{ML} & S_M & S_{MR} \\ 0 & S_{RM} & S_R \end{pmatrix}. \tag{4.14}$$

If the Green's function G and the identity matrix I are also broken up in a similar manner, then equation (4.12) for the Green's function can also be written in block matrix form

$$\begin{pmatrix} \epsilon S_L - H_L & \epsilon S_{LM} - H_{LM} & 0 \\ \epsilon S_{ML} - H_{ML} & \epsilon S_M - H_M & \epsilon S_{MR} - H_{MR} \\ 0 & \epsilon S_{RM} - H_{RM} & \epsilon S_R - H_R \end{pmatrix} \begin{pmatrix} G_L & G_{LM} & G_{LR} \\ G_{ML} & G_M & G_{MR} \\ G_{RL} & G_{RM} & G_R \end{pmatrix}$$
$$= \begin{pmatrix} I & 0 & 0 \\ 0 & I_M & 0 \\ 0 & 0 & I \end{pmatrix} , \quad (4.15)$$

where I_M is the $N \times N$ identity matrix, with N being the number of basis orbitals in the scattering region. For convenience, we have defined $\epsilon = (\lim_{\delta \to 0}(E + i\delta))$.

When the two matrices in equation (4.15) are formally multiplied, the central row of $(\epsilon S - H)$ multiplied by the central column of $G(E)$ gives the following equation

$$(\epsilon S_{ML} - H_{ML})G_{LM} + (\epsilon S_M - H_M)G_M + (\epsilon S_{MR} - H_{MR})G_{RM} = I_M . \quad (4.16)$$

Similarly, expressions for G_{LM} and G_{RM} can be obtained by multiplying the first and third block rows of $(\epsilon S - H)$ by the central column of $G(E)$ and then rearranging

$$G_{LM} = -(\epsilon S_L - H_L)^{-1}(\epsilon S_{LM} - H_{LM})G_M . \quad (4.17)$$

$$G_{RM} = -(\epsilon S_R - H_R)^{-1}(\epsilon S_{RM} - H_{RM})G_M . \quad (4.18)$$

The Hamiltonians describing the isolated leads (i.e. the semi-infinite leads where no scattering region is present) are H_L and H_R. Hence the retarded Green's functions of the isolated leads, G_L^{0R} and G_R^{0R}, which are the retarded Green's functions calculated at the last principal layer of the isolated leads, are

$$(\epsilon S_L - H_L)G_L^{0R} = I \Rightarrow G_L^{0R} = (\epsilon S_L - H_L)^{-1} , \quad (4.19)$$

$$(\epsilon S_R - H_R)G_R^{0R} = I \Rightarrow G_R^{0R} = (\epsilon S_R - H_R)^{-1} . \quad (4.20)$$

By substituting the expressions for G_{LM} and G_{RM} from equations (4.17) and (4.18) back into equation (4.16), we obtain an expression for the Green's function of the scattering region, G_M

$$-(\epsilon S_{ML} - H_{ML})G_L^{0R}(\epsilon S_{LM} - H_{LM})G_M + (\epsilon S_M - H_M)G_M$$
$$-(\epsilon S_{MR} - H_{MR})G_R^{0R}(\epsilon S_{RM} - H_{RM})G_M = I_M . \quad (4.21)$$

We now introduce the self-energies, Σ_L and Σ_R, of the left and right leads, which have the form

$$\Sigma_{\mathrm{L}} = (\epsilon S_{\mathrm{ML}} - H_{\mathrm{ML}})G_{\mathrm{L}}^{0\mathrm{R}}(\epsilon S_{\mathrm{LM}} - H_{\mathrm{LM}}), \tag{4.22}$$

$$\Sigma_{\mathrm{R}} = (\epsilon S_{\mathrm{MR}} - H_{\mathrm{MR}})G_{\mathrm{R}}^{0\mathrm{R}}(\epsilon S_{\mathrm{RM}} - H_{\mathrm{RM}}). \tag{4.23}$$

These self-energies contain all of the information about how the leads affect the scattering region. Hence we obtain an expression for the Green's function of the scattering region, G_M, in terms of the H_M and the self-energies of the leads

$$(\lim_{\delta \to 0}(E + i\delta)S - H_{\mathrm{M}} - \Sigma_{\mathrm{L}} - \Sigma_{\mathrm{R}})G_{\mathrm{M}} = I_{\mathrm{M}}. \tag{4.24}$$

Therefore, the Green's function of the scattering region, G_M, can be obtained by inverting equation (4.24)

$$G_M = (\lim_{\delta \to 0}(E + i\delta)S - H_{\mathrm{M}} - \Sigma_{\mathrm{L}} - \Sigma_{\mathrm{R}})^{-1}. \tag{4.25}$$

From this, we can define the effective Hamiltonian, H_{EFF}, for the scattering region in the presence of the leads as the sum of the Hamiltonian of the scattering region H_{M} and the leads self energies Σ_{L} and Σ_{R}

$$H_{\mathrm{EFF}} = H_{\mathrm{M}} + \Sigma_{\mathrm{L}} + \Sigma_{\mathrm{R}}. \tag{4.26}$$

Note that this Hamiltonian is non-Hermitian. This is because it is the Hamiltonian of an open system; charge can enter and leave the scattering region from the leads so that the total number of particles is not necessarily conserved.

The non-Hermitian part of H_{EFF} is due to the self-energies Σ_{L} and Σ_{R}. The anti-Hermitian part of these self-energies controls the rate, Γ, at which electrons can enter and leave the scattering region

$$\Gamma_{\mathrm{L/R}} = i[\Sigma_{\mathrm{L/R}} - \Sigma_{\mathrm{L/R}}^{\dagger}]. \tag{4.27}$$

Analogous to the coupling terms in chapter 3, Γ_{L} and Γ_{R} are matrices which describe the rate at which electrons are transferred between the scattering region and the left and right leads, respectively.

For convenience, we can combine the left and right self-energies into one

$$\Sigma_{\mathrm{L}} + \Sigma_{\mathrm{R}} = \Sigma. \tag{4.28}$$

Hence, in general, the retarded and advanced Green's functions for the the scattering region, G^{R} and G^{A}, can be written as

$$G^{\mathrm{R}} = (\lim_{\delta \to 0^{+}}(E + i\delta)S - H_{\mathrm{M}} - \Sigma^{\mathrm{R}})^{-1}, \tag{4.29}$$
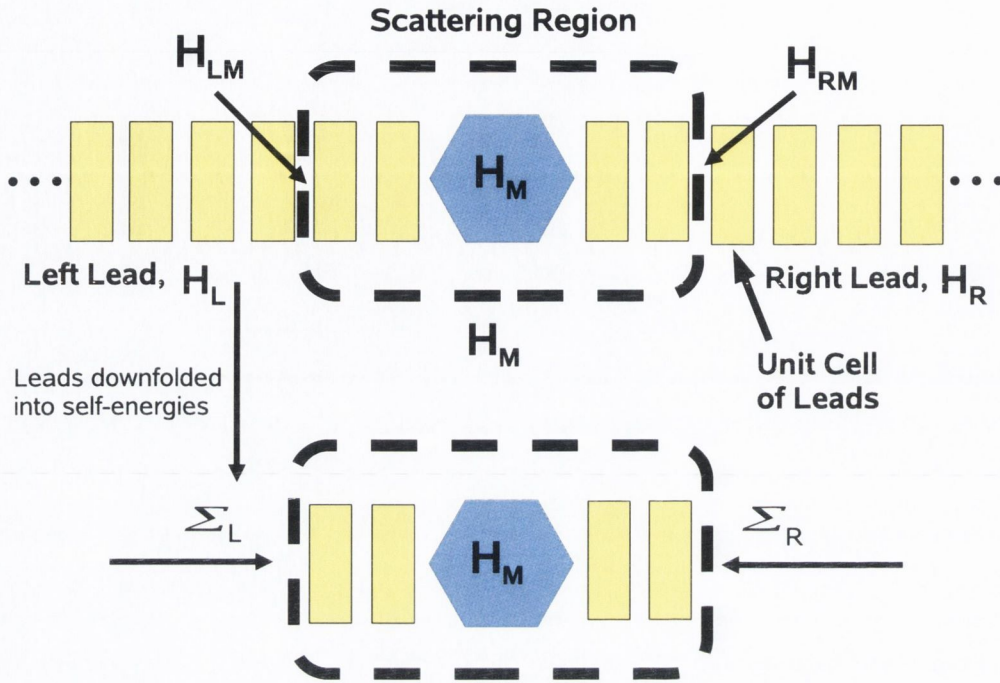
Figure 4.3: Diagram of system showing how the left and right leads can be downfolded into self-energies.

$$G^{A} = \left(\lim_{\delta \to 0^{-}} (E + i\delta)S - H_{M} - \Sigma^{A} \right)^{-1} . \tag{4.30}$$

where Σ^{R} and Σ^{A} are the retarded and advanced self-energies, calculated using the retarded and advanced Green's functions for the leads as shown in equations (4.22) and (4.23). Similarly, the overall net rate at which electrons are transferred between the leads and the scattering region, is given by $\Gamma = \Gamma_{L} + \Gamma_{R} = \Sigma^{R} - \Sigma^{A}$.

4.3   Calculating the charge density with NEGF

In the case of a mean field theory such as density functional theory (DFT), the Hamiltonian of the scattering region, H_{M}, is a functional of the charge density ρ

$$H_{M} = H_{M}[\rho] . \tag{4.31}$$

In order to calculate the charge density ρ of the scattering region connected to the leads, we need to use the non-equilibrium Green's function formalism [34, 35, 36, 38, 102] to find the relationship between ρ and the retarded Green's function

for the scattering region, G^R. We start by introducing the lesser Green's function, $G^<(\mathbf{k}, \mathbf{k}'; t, t')$, which is effectively a generalisation of the distribution function $f(\mathbf{k}; t)$. This is also proportional to the correlation between wave functions, so that $G^< \sim \psi(\mathbf{r})\psi^*(\mathbf{r}')$. The density matrix, is given by $G^<$ calculated at $t = t'$

$$\rho(\mathbf{k}, \mathbf{k}'; t) = -i\left[G^<(\mathbf{k}, \mathbf{k}'; t, t')\right]_{t=t'}. \tag{4.32}$$

Using a Fourier Transform to go from the time representation to the energy representation, the density matrix for the scattering region can be written as an integral over energy of the lesser Green's function

$$\rho = \frac{1}{2\pi i} \int G^<(E)dE. \tag{4.33}$$

Let us consider the equilibrium case first, where the charge distribution is given by the product of the density of states and the Fermi function of the leads. The spectral function, $A(E) = i[G^R(E) - G^A(E)]$, is a generalised density of states, whose trace in fact corresponds to the density of states, $D(E) = \frac{1}{2\pi}Tr[A(E)]$. Hence, the lesser Green's function, which is the charge density as a function of energy, is given at equilibrium (zero bias) by $G^<(E) = -if_0(E)A(E)$, where $f_0(E)$ is the Fermi function of the leads assumed at equilibrium. Since $G^A(E) = G^{R\dagger}(E)$, the spectral function is given by $A(E) = 2\text{Im}[G^R(E)]$, and so the equation for the lesser Green's function at equilibrium becomes

$$G^< = 2i\text{Im}[G^R(E)]f(E - \mu), \tag{4.34}$$

where μ is the chemical potential of the system. This allows the density matrix of the scattering region to be calculated in terms of the retarded Green's function.

However, this expression is only true at equilibrium. When the system is out of equilibrium, e.g. when a finite bias is applied, the different contacts are at different chemical potentials. Therefore the charge distribution in the scattering region is no longer described by a single Fermi function, and equation (4.34) can no longer be used. Instead, an expression must be derived for $G^<$ in terms of G^R and the chemical potentials of each lead.

In order to describe the more general non-equilibrium situation, we first need to introduce the "in-scattering" and "out-scattering" functions Σ^{IN} and Σ^{OUT}, which describe the rate at which electrons can enter and leave the scattering region. It can be shown [34] that $G^<$ is related to G_{M}^{R} and Σ^{IN} by the expression in equation (4.35)

$$G^< = -iG^R \Sigma^{IN} G^{R\dagger} = -iG^R \Sigma^{IN} G^A \,. \tag{4.35}$$

Hence, we now have an expression for the lesser Green's function (and hence the charge density ρ) in terms of the Green's functions of the scattering region and the in-scattering function. Now, Γ describes the net rate at which electrons enter and leave the scattering region, so $\Gamma = \Sigma^{IN} + \Sigma^{OUT}$. Γ can also be expressed in terms of the difference of inverse of the retarded and advanced Green's functions given in equations (4.29) and (4.30)

$$(G^R)^{-1} - (G^A)^{-1} = \Sigma^A - \Sigma^R = i\Gamma \,. \tag{4.36}$$

Therefore, by multiplying equation (4.36) on the left by G^R and on the right by G^A we obtain expression for the spectral function $A(E)$

$$G^R[(G^R)^{-1} - (G^A)^{-1}]G^A = iG^R \Gamma G^A \,. \tag{4.37}$$

$$\Rightarrow A(E) = -i[G^A - G^R] = G^R \Gamma G^A \,. \tag{4.38}$$

From the discussion for the equilibrium case above, the lesser Green's function was related to the spectral function by $G^<(E) = -if_0(E)A(E)$, where f_0 is the equilibrium Fermi distribution. This can be used to combine equation (4.35) with equation (4.38) to obtain an expression for Σ^{IN} in terms of Γ

$$G^< = -iG^R \Sigma^{IN} G^A = -if_0(E)A(E) = -if_0(E)G^R \Gamma G^A \,. \tag{4.39}$$

Hence, at equilibrium, the in-scattering and out-scattering functions Σ^{IN} and Σ^{OUT} are simply given by

$$\Sigma^{IN} = f_0(E)\Gamma; \quad \Sigma^{OUT} = \Gamma - \Sigma^{IN} = [1 - f_0(E)]\Gamma \,. \tag{4.40}$$

For the non-equilibrium case with multiple leads, assume that each lead p is in equilibrium with a Fermi distribution $f_p(E)$. Then the in-scattering function for each lead p will be given by

$$\Sigma_p^{IN} = f_p(E)\Gamma_p \,, \tag{4.41}$$

and the total in-scattering function Σ^{IN} is given by a sum over all of the leads p. In the case of two leads, left (L) and right (R), we have

$$\Sigma^{IN} = f_L(E)\Gamma_L + f_R(E)\Gamma_R \,. \tag{4.42}$$

Hence, in the non-equilibrium case, for two leads with chemical potentials μ_L and μ_R which are coupled to the scattering region by Γ_L and Γ_R respectively, the lesser Green's function is given by

$$G^< = iG_M^R[f(E - \mu_L)\Gamma_L + f(E - \mu_R)\Gamma_R]G_M^{R\dagger} . \tag{4.43}$$

Therefore, the density matrix ρ can be evaluated for the scattering region in the presence of a potential bias by integrating this expression for $G^<$ over the energy E

$$\rho = \frac{1}{2\pi} \int [G_M^R\Gamma_L G_M^{R\dagger}f(E - \mu_L) + G_M^R\Gamma_R G_M^{R\dagger}f(E - \mu_R)]dE . \tag{4.44}$$

This is the central result of the non-equilibrium Green's function formalism [34, 35, 36, 38, 102], linking the charge density ρ of the scattering region to the retarded Green's function G^R. It allows the electronic structure of a scattering region connected to two semi-infinite leads to be calculated self-consistently at a finite applied bias.

However, this integral is hard to perfrom numerically since it is unbound and the Green's function has poles on the real axis. To solve these problems, the integrands are split into an equilibrium part which is calculated in the complex plane using a contour integral, and an out of equilibrium part, which is non-zero over a finite energy window.

The lesser Green's function, $G_M^<$, can, in fact, be written as

$$G_M^< = iG_M^R\Gamma_L G_M^{R\dagger}f(E - \mu_L) + iG_M^R\Gamma_R G_M^{R\dagger}f(E - \mu_R) . \tag{4.45}$$

By adding and subtracting the term $iG_M^R\Gamma_R G_M^{R\dagger}f(E - \mu_L)$, we obtain

$$\begin{aligned}
G_M^< &= i[G_M^R\Gamma_L G_M^{R\dagger}f(E - \mu_L) + G_M^R\Gamma_R G_M^{R\dagger}f(E - \mu_L)] \\
&\quad + i[G_M^R\Gamma_R G_M^{R\dagger}f(E - \mu_R) - G_M^R\Gamma_R G_M^{R\dagger}f(E - \mu_L)] \\
&= iG_M^R[\Gamma_L + \Gamma_R]G_M^{R\dagger}f(E - \mu_L) \\
&\quad + iG_M^R\Gamma_R G_M^{R\dagger}[f(E - \mu_R) - f(E - \mu_L)] .
\end{aligned} \tag{4.46}$$

If we now substitute the result $\Gamma = i[(G_M^{R\dagger})^{-1} - (G_M^R)^{-1}]$ from equation (4.36) into the equation for $G_M^<$, we obtain

$$
\begin{aligned}
G_{\mathrm{M}}^{<} &= i^2 G_{\mathrm{M}}^{\mathrm{R}}[(G_{\mathrm{M}}^{\mathrm{R\dagger}})^{-1} - (G_{\mathrm{M}}^{\mathrm{R}})^{-1}]G_{\mathrm{M}}^{\mathrm{R\dagger}} f(E - \mu_{\mathrm{L}}) \\
&\quad + i G_{\mathrm{M}}^{\mathrm{R}}\Gamma_{\mathrm{R}}G_{\mathrm{M}}^{\mathrm{R\dagger}}[f(E - \mu_{\mathrm{R}}) - f(E - \mu_{\mathrm{L}})] \\
&= -[G_{\mathrm{M}}^{\mathrm{R}} - G_{\mathrm{M}}^{\mathrm{R\dagger}}]f(E - \mu_{\mathrm{L}}) + i G_{\mathrm{M}}^{\mathrm{R}}\Gamma_{\mathrm{R}}G_{\mathrm{M}}^{\mathrm{R\dagger}}[f(E - \mu_{\mathrm{R}}) - f(E - \mu_{\mathrm{L}})] \\
&= -2i Im[G_{\mathrm{M}}^{\mathrm{R}}]f(E - \mu_{\mathrm{L}}) + i G_{\mathrm{M}}^{\mathrm{R}}\Gamma_{\mathrm{R}}G_{\mathrm{M}}^{\mathrm{R\dagger}}[f(E - \mu_{\mathrm{R}}) - f(E - \mu_{\mathrm{L}})] . \quad (4.47)
\end{aligned}
$$

The first part is the same as the expression for $G_{\mathrm{M}}^{<}$ at equilibrium, so the equilibrium part of density matrix, ρ_{EQ}, is given by

$$
\rho_{\mathrm{EQ}} = -\frac{1}{\pi} \int dE \; Im[G_{\mathrm{M}}^{\mathrm{R}}]f(E - \mu_{\mathrm{L}}) . \quad (4.48)
$$

Note that this integral is the same as that which would be obtained by using the expression for the lesser Green's function at equilibrium. This integral runs from $-\infty$ to $+\infty$, and the Green's function has poles along the real axis. Hence, this integral is calculated using the contour integral shown in figure 4.4. This contour runs along the line segment L and the circle segment C, and then along the real axis from $E_{\mathrm{B}} + i\delta$ to $\infty + i\delta$, where E_{B} is a point on the real energy axis below the bottom of the valence band (i.e. below the lowest energy state being treated in the calculation).
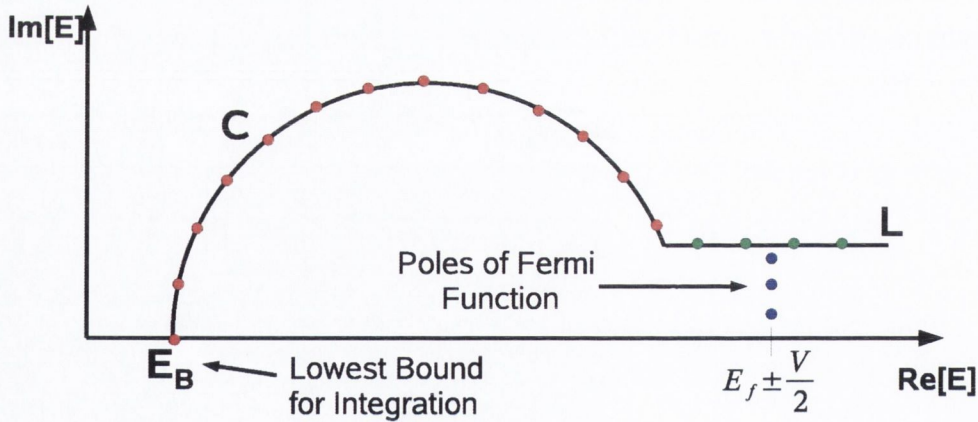
Figure 4.4: Contour used to integrate equilibrium part of density matrix.

The residue theorem states that the integral around a contour is equal to $2\pi i$ times the sum over the residues, which leads us to the result

$$
\oint dz G_{\mathrm{M}}^{\mathrm{R}}(z) f_{\mathrm{L}}(z) = 2\pi i \sum Res[G_{\mathrm{M}}^{\mathrm{R}}(z) f_{\mathrm{L}}(z)] . \quad (4.49)
$$

The only poles enclosed by the contour are the poles of the Fermi function which occur at $z_n = (2n + 1)i\pi k_B T$, and the residues of the Fermi function are $-k_B T$. Therefore the contour integral becomes

$$\oint dz G_{\mathrm{M}}^{\mathrm{R}}(z) f_{\mathrm{L}}(z) = -2\pi i k_B T \sum [G_{\mathrm{M}}^{\mathrm{R}}(z_n)] . \tag{4.50}$$

The integral along the contour can be broken into three parts, the first along the real axis, the second along the circle segment C, and the third along the line segment L

$$\oint dz G_{\mathrm{M}}^{\mathrm{R}}(z) f_{\mathrm{L}}(z) = \int_{E_{\mathrm{B}}}^{\infty} dz G_{\mathrm{M}}^{\mathrm{R}}(z) f_{\mathrm{L}}(z) + \int_{C} dz G_{\mathrm{M}}^{\mathrm{R}}(z) f_{\mathrm{L}}(z) + \int_{L} dz G_{\mathrm{M}}^{\mathrm{R}}(z) f_{\mathrm{L}}(z) . \tag{4.51}$$

The integral we are actually interested in calculating is that along the real axis from E_{B} to ∞. Using the expression for the integral around the full contour in equation (4.49), this can be written in terms of the integral over the segments C and L and the sum over the residues

$$\int_{E_{\mathrm{B}}}^{\infty} dE G_{\mathrm{M}}^{\mathrm{R}}(E) f_{\mathrm{L}}(E - \mu) = -\int_{C} dz G_{\mathrm{M}}^{\mathrm{R}}(z) f_{\mathrm{L}}(z)$$
$$- \int_{L} dz G_{\mathrm{M}}^{\mathrm{R}}(z) f_{\mathrm{L}}(z) - 2\pi i k_B T \sum [G_{\mathrm{M}}^{\mathrm{R}}(z_n)] . \tag{4.52}$$

A Gaussian quadrature [104] can be used to calculate the integral along C and L, as the Green's function is well-behaved away from the real axis.

The remainder of the density matrix, ρ_{NEQ}, is given by

$$\rho_{\mathrm{NEQ}} = \frac{1}{2\pi} \int G_{\mathrm{M}}^{\mathrm{R}} \Gamma_{\mathrm{R}} G_{\mathrm{M}}^{\mathrm{R}\dagger} [f(E - \mu_{\mathrm{R}}) - f(E - \mu_{\mathrm{L}})] . \tag{4.53}$$

This is only non-zero in the region where $f(E - \mu_{\mathrm{R}})$ and $f(E - \mu_{\mathrm{L}})$ are not equal, which corresponds approximately to the bias window with some broadening due to temperature. Therefore, this integral can be calculated with reasonable accuracy by taking a finite energy window and using a technique such as Simpson's Rule, as shown in figure 4.5.

We can now finally describe a self-consistent procedure to calculate the density matrix of the scattering region. First, a trial charge density, typically starting either from a previously converged ground state electronic structure calculation (which in turn would typically use the atomic charge densities as the starting configuration) is used to compute the Hamiltonian of the scattering region, H_{M}
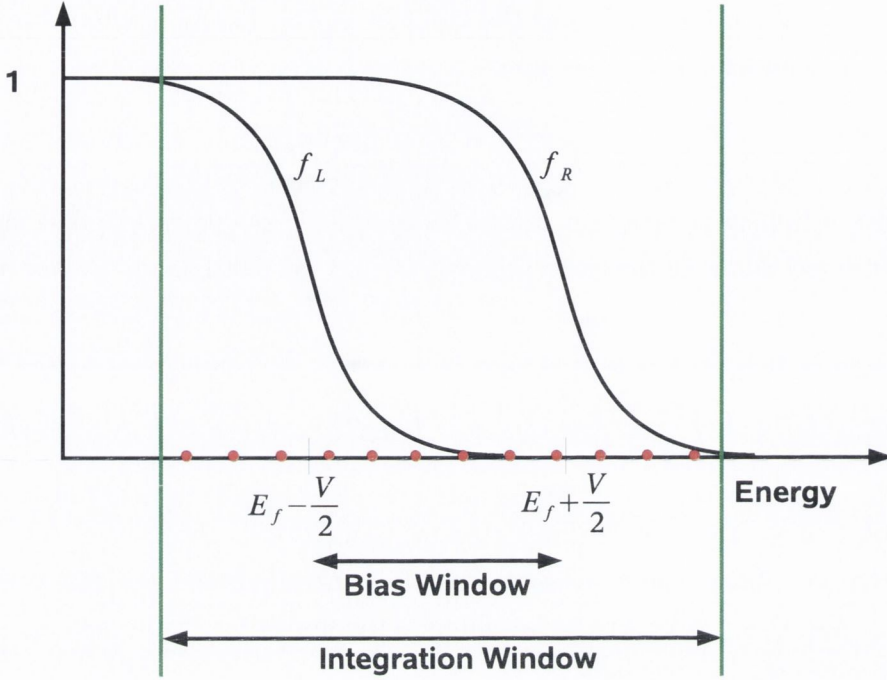
Figure 4.5: Energy window for integration of non-equilibrium part of density matrix.

$$H_{\mathrm{M}} = H_{\mathrm{M}}[\rho^0(\mathbf{r})]; \quad \rho^0(\mathbf{r}) = \langle \mathbf{r}|\rho_{\mathrm{M}}^0|\mathbf{r}\rangle . \tag{4.54}$$

This can then be used to calculate the Green's function, which in turn can be used to construct a new charge density as described above. This new charge density is then used to calculate an updated Hamiltonian, and so on until the convergence criterion is met

$$\mathrm{Max}\|\rho_{\mathrm{M}}^j - \rho_{\mathrm{M}}^{j+1}\| < \delta . \tag{4.55}$$

This means that the density matrix is converged when the difference between each matrix element at the jth iteration and the corresponding matrix element at the $j+1^{\mathrm{th}}$ iteration is less than some tolerance parameter δ.

This density matrix can then be used to calculate other properties of the open system such as the density of states or transmission probabilities.

4.4   Calculating the Current with NEGF

Once the charge density and effective Hamiltonian of the scattering region have been
calculated, the next step is to calculate the conductance and *I-V* characteristics of
the device.

Using the Landauer-Büttiker formalism [105], the conductance of a device can
be associated with the transmission probability of an electron wave function to cross
a scattering potential. Consider the simple scattering potential shown in figure 4.6.
An incoming wave function e^{ikx} in general has a component re^{-ikx} which is reflected
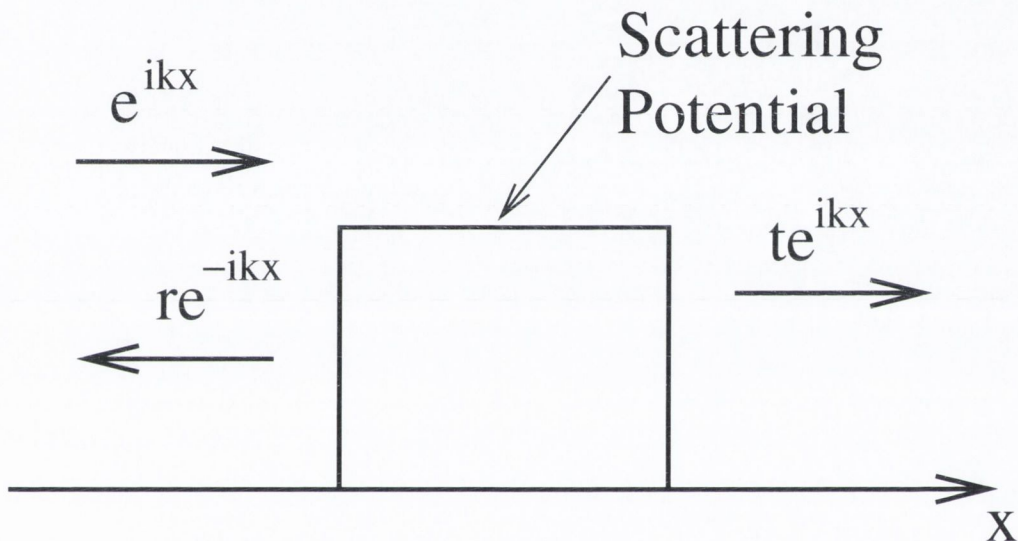
Figure 4.6: One-dimensional scattering potential with incoming wave function e^{ikx}, which
has transmitted and reflected components, te^{ikx} and re^{-ikx}

by the potential, and a component te^{ikx} which is transmitted through the potential.
The total flux is conserved, i.e. $|r|^2+|t|^2 = 1$. In a periodic system with no scattering
potential, each electron wave function contributes $\frac{e^2}{h}$ to the current per spin. If the
system is spin degenerate, then each conduction channel can carry two electrons,
and so each will contribute one quantum of conductance, $G_0 = 2\frac{e^2}{h}$. For multi-
dimensional systems, there can be multiple scattering states with the same energy.
The transmission and reflection coefficients, t and r, will then be matrices, where,
for example, element t_{ij} is the coefficient for a wave function being transmitted from
the ith scattering state or channel on the left of the scattering potential into the jth
channel on the right.

The total Landauer-Büttiker conductance, Γ, at a given energy E, can then be
defined as being the trace of the product of the transmission matrix with its adjoint

[106]

$$\Gamma = G_0 Tr[tt^\dagger] \, . \tag{4.56}$$

The total current, I, in the linear response limit is then given by

$$I = G_0(\mu_L - \mu_R)Tr[tt^\dagger] \, , \tag{4.57}$$

where μ_L and μ_R are the chemical potentials of the left and right lead, and t is calculated at the Fermi level of the leads.

Alternatively, the current can be expressed in terms of the Green's function for the scattering region G_M^R [34, 107] by using expressions for the probability current density $\mathbf{J}(\mathbf{r})$ and the Hamiltonian of the scattering region H_M. This can be extended to finite bias, yielding

$$I = \frac{e}{h} \int dE \ Tr[\Gamma_L G_M^{R\dagger} \Gamma_R G_M^R](f(E - \mu_L) - f(E - \mu_R)) \, . \tag{4.58}$$

From the expression for the Landauer-Büttiker current, the transmission coefficients can be identified with the term $Tr[\Gamma_L G_M^{R\dagger} \Gamma_R G_M^R]$

$$T(E, V) = Tr[\Gamma_L G_M^{R\dagger} \Gamma_R G_M^R] \, . \tag{4.59}$$

Thus, the current I is essentially the integral over energy of the transmission coefficients $T(E, V)$ in the region in which the Fermi functions of the leads are not equal to each other (i.e. the bias window). The transmission coefficients $T(E, V)$ correspond to the probability of an electron being transmitted from one side of the scattering region to the other at an energy E. They are generally dependent on the potential bias V applied to the system. The position and width of the peaks in transmission coefficients are determined by the positions of the molecular orbitals and the strength of the coupling between those orbitals and the leads.

The full self-consistent procedure for calculating the charge density, the transmission and the current using the non-equilibrium Green's function formalism is shown in figure 4.7.

4.5   NEGF for Periodic Boundary Conditions

The NEGF method as described up to this point applies to one-dimensional or quasi-one dimensional systems. However, the devices investigated in the experiments modelled in this thesis typically involve the molecules being attached to relatively large

Lead's Self-energy

$$\Sigma_{L,R} = \tau \, g_{L,R}(E)\tau^*$$

$$\Gamma_{L,R} = i(\Sigma_{L,R} - \Sigma_{L,R}^\dagger)$$

Scatterer's Green function

$$G(E) = [E - H_s(n) - \Sigma_L - \Sigma_R]^{-1}$$

Density Matrix

$$n = \frac{1}{2\pi}\int_{-\infty}^{\infty}[f(E,\mu_L)G\Gamma_L G^\dagger + f(E,\mu_R)G\Gamma_R G^\dagger]dE$$

Current

$$I = \frac{2e}{\hbar}\int_{-\infty}^{\infty}[Tr(\Gamma_L G\Gamma_R G^\dagger)\,(f(E,\mu_L) - f(E,\mu_R))]dE$$
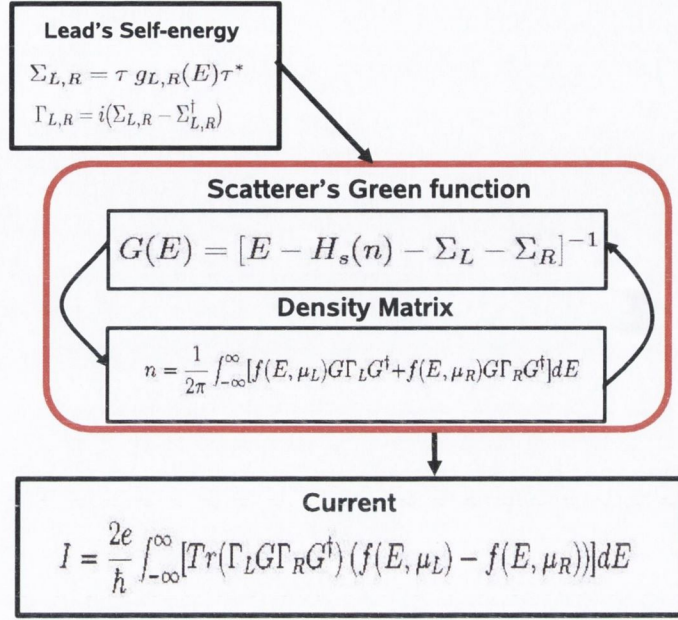
Figure 4.7: Flowchart showing the self-consistent procedure used to calculate the density matrix and the current using the non-equilibrium Green's function formalism

metallic electrodes, the cross-sections of which have far more atoms than it is feasible to perform calculations for. Unfortunately, modelling the contacts as nanowires with perhaps as few as nine atoms in the cross-section can introduce artificial gaps into the band structure due to quantum confinement. This causes serious problems with electronic transport calculations, creating artificial gaps in the transmission coefficients. Hence, if possible, it is preferable to introduce periodic boundary conditions in the directions perpendicular to that of the transport.

From Bloch's theorem, the Hamiltonian of a 3D system can be written in the form

$$H_{\mathbf{k}} = \sum_{j=0}^{N} H_j e^{i\mathbf{k}\cdot\mathbf{r}_j} \,. \tag{4.60}$$

where H_j is the Hamiltonian coupling the 0th unit cell to the jth unit cell, $\mathbf{r}_j$ is position of the jth unit cell relative to the 0th one, and $\mathbf{k}$ is the reciprocal lattice vector. The Schrödinger equation associated with this Hamiltonian is

$$\sum_{j=0}^{N} H_j e^{i\mathbf{k}\cdot\mathbf{r}_j} u_k - E \sum_{j=0}^{N} S_j e^{i\mathbf{k}\cdot\mathbf{r}_j} u_k = 0 \,, \tag{4.61}$$

where u_k is a function with the same periodicity as the lattice. Note that these equations are separable, so that the problem can be solved by diagonalising $H_{\mathbf{k}}$ for each value of $\mathbf{k}$. The integral of the resulting eigenvectors, $\psi_i^{\mathbf{k}}$, with respect to $\mathbf{k}$ gives the density matrix of the system.

Similarly, the retarded Green's function for the scattering region, G^{R}, as given in equation (4.29), can be adapted to the case of periodic boundary conditions

$$G_{\mathrm{M}}^{\mathrm{R}}(E,\mathbf{k}) = (\lim_{\delta \to 0}(E+i\delta)S(E,\mathbf{k})) - H_{\mathrm{M}}(E,\mathbf{k}) - \Sigma^{\mathrm{R}}(E,\mathbf{k}))^{-1}. \qquad (4.62)$$

This Green's function can be calculated separately for each value of $\mathbf{k}$. The density matrix is then obtained by integrating the $\mathbf{k}$-dependent density matrix over all the values of $\mathbf{k}$ in the Brillouin zone

$$\rho = \frac{1}{2\pi} \int d\mathbf{k} \int [G_{\mathrm{M}}^{\mathrm{R}} \Gamma_{\mathrm{L}} G_{\mathrm{M}}^{\mathrm{R\dagger}} f(E-\mu_{\mathrm{L}}) + G_{\mathrm{M}}^{\mathrm{R}} \Gamma_{\mathrm{R}} G_{\mathrm{M}}^{\mathrm{R\dagger}} f(E-\mu_{\mathrm{R}})]dE. \qquad (4.63)$$

This integral can be performed by splitting it into equilibrium and non-equilibrium parts, as shown in equations (4.48) and (4.53).

For the *ab initio* transport calculations described in this thesis, two k-points were sampled in each of the directions perpendicular to the transport. For the calculations of electronic structure of the unit cell of the leads, 100 k-points were sampled.

4.6   Calculating Self-Energies and Green's Functions for the Leads

From equations (4.22) and (4.23), we have that the self-energies for the left and right leads, Σ_{L} and Σ_{R}, are given by

$$\Sigma_{\mathrm{L}} = (\epsilon S_{\mathrm{ML}} - H_{\mathrm{ML}})G_{\mathrm{L}}^{0\mathrm{R}}(\epsilon S_{\mathrm{LM}} - H_{\mathrm{LM}}), \qquad (4.64)$$

$$\Sigma_{\mathrm{R}} = (\epsilon S_{\mathrm{MR}} - H_{\mathrm{MR}})G_{\mathrm{R}}^{0\mathrm{R}}(\epsilon S_{\mathrm{RM}} - H_{\mathrm{RM}}). \qquad (4.65)$$

$G_{\mathrm{L}}^{0\mathrm{R}}$ and $G_{\mathrm{R}}^{0\mathrm{R}}$ are the retarded Green's functions of the isolated leads. Due to the inclusion of principal layers in the scattering region on both sides, H_{ML} and H_{MR} usually consist of the Hamiltonians describing the interactions between principal layers in the leads, H_1 and H_{-1}. Therefore, constructing the self-energies reduces to calculating the retarded Green's functions of the leads. In SMEAGOL, these are calculated semi-analytically using the scheme introduced by Sanvito et. al. [108].

There are also recursive algorithms available to calculate these functions, although they have not been implemented in SMEAGOL.

As explained previously, the leads are assumed to be periodic in the direction of the transport, with H_0 being the Hamiltonian describing each principal layer, and H_1 describing the coupling between principal layers. Since each layer only interacts with its neighbouring layer, the Hamiltonian of the leads is in block tridiagonal form

$$
H = \begin{pmatrix}
\cdot & \cdot & \cdot & & \cdot & & \cdot & & \cdot & & \cdot & \cdot \\
\cdot & 0 & H_{-1} & H_0 & H_1 & 0 & & \cdot & & \cdot & \cdot \\
\cdot & \cdot & 0 & H_{-1} & H_0 & H_1 & 0 & & \cdot & \cdot \\
\cdot & \cdot & & 0 & H_{-1} & H_0 & H_1 & 0 & & \cdot \\
\cdot & \cdot & \cdot & & \cdot & & \cdot & & \cdot & \cdot & \cdot
\end{pmatrix} \tag{4.66}
$$

The Schrödinger equation for this system is of the form

$$
H_0 \psi_z + H_1 \psi_{z+1} + H_{-1} \psi_{z-1} = ES\psi_z . \tag{4.67}
$$

where $H_{-1} = H_1^\dagger$ in the case of time reversal symmetry. For an infinite, quasi-one-dimensional system such as this, the wave function takes the form of Bloch states

$$
\psi_z = \sqrt{n_k} e^{ikz} \phi_k . \tag{4.68}
$$

where k is the reciprocal lattice vector and $\sqrt{n_k}$ is a normalisation factor. Substituting this into equation (4.67) gives

$$
[(H_0 - ES_0) + (H_1 - ES_1)e^{ik} + (H_{-1} - ES_{-1})e^{-ik}]\phi_k = 0 . \tag{4.69}
$$

Solving this equation for e^{ikz} allows the value of k to be determined for a given value of E. This is done be rewriting the above equation in matrix form so that

$$
\begin{pmatrix} -(H_1 - ES_1)^{-1}(H_0 - ES_0) & (H_1 - ES_1)^{-1}(H_{-1} - ES_{-1}) \\ I & 0 \end{pmatrix} \begin{pmatrix} \phi_k \\ e^{-ik}\phi_k \end{pmatrix}
$$
$$
= \begin{pmatrix} e^{ik}\phi_k \\ \phi_k \end{pmatrix} = e^{ik} \begin{pmatrix} \phi_k \\ e^{-ik}\phi_k \end{pmatrix} \tag{4.70}
$$

The eigenvalues and eigenvectors of this matrix are e^{ik} and ϕ_k respectively. Therefore, k as a function of E can be obtained by diagonalising this matrix. Problems with this method may occur when $(H_1 - ES_1)$ is singular and so cannot be inverted.

For an orthogonal basis set the retarded Green's function of the doubly infinite system can be calculated from ϕ_k and k. This retarded Green's function, $G_{zz'}$, has

the form of a wave function except at the source point, $z = z'$, and so we use the following ansatz [108]

$$G_{zz'} = \begin{cases} \sum_{l=1}^{N} \phi_{k_l} e^{ik_l(z-z')} w_{k_l}^{\dagger} & z \geq z'; \\ \sum_{l=1}^{N} \phi_{\bar{k}_l} e^{i\bar{k}_l(z-z')} w_{\bar{k}_l}^{\dagger} & z \leq z' \end{cases} \tag{4.71}$$

where $k = -\bar{k}$, with k representing the right and left moving plane waves, and $w_{k_l}^{\dagger}$ and $w_{\bar{k}_l}^{\dagger}$ are vectors whose form is to be determined. The summation runs over all possible scattering channels.

$G_{zz'}$ is a Green's function, and thus must satisfy the equation

$$(ES - H)G_{zz'} = \delta_{zz'} \tag{4.72}$$

where H is the Green's function of a doubly infinite lead. $G_{zz'}$ must also be continuous at $z = z'$, i.e. the values given by the expressions for $z \geq z'$ and $z \leq z'$ should be the same at this point. These conditions can be used to show that the Green's function for the doubly infinite lead is of the form

$$G_{zz'} = \begin{cases} \sum_{l=1}^{N} \phi_{k_l} e^{ik_l(z-z')} \tilde{\phi}_{k_l}^{\dagger} V^{-1} & z \geq z'; \\ \sum_{l=1}^{N} \phi_{\bar{k}_l} e^{i\bar{k}_l(z-z')} \tilde{\phi}_{\bar{k}_l}^{\dagger} V^{-1} & z \leq z' \end{cases} \tag{4.73}$$

where V is given by

$$V = \sum_{l=1}^{N} (H_{-1} - ES_{-1}) [\phi_{k_l} e^{-ik_l} \tilde{\phi}_{k_h}^{\dagger} - \phi_{\bar{k}_l} e^{-i\bar{k}_l} \tilde{\phi}_{\bar{k}_h}^{\dagger}] . \tag{4.74}$$

This is the Green's function for a quasi-one dimensional system (i.e. one which is periodic in the transport direction), and which extends to infinity in both directions. The leads for the system we wish to study only extend to infinity in one direction, as they end at the interface with the scattering region. Consider the left lead which runs from $z = -\infty$ to $z = z_0 - 1$ (the scattering region starts at $z = z_0$). Then the boundary condition is that the Green's function must vanish at $z = z_0$. This condition can be obtained by subtracting from $G_{zz'}$ a wave function of the form

$$\Delta_z(z', z_0) = \sum_{l,h}^{N} \phi_{\bar{k}_h} e^{i\bar{k}_h z} \Delta_{hl}(z, z_0) . \tag{4.75}$$

The surface Green's function, $\tilde{G}_{z_0 z'}(z_0)$ is then given by

$$\tilde{G}_{z_0 z'}(z_0) = G_{z_0 z'} - \Delta_z(z', z_0) . \tag{4.76}$$

If we take $\Delta_z(z', z_0)$ to be of the form

$$\Delta_z(z', z_0) = \sum_{l,h}^{N} \phi_{\overline{k}_h} e^{i\overline{k}_h(z-z_0)} \tilde{\phi}_{\overline{k}_h}^{\dagger} \phi_{k_l} e^{ik_l(z_0-z')} \tilde{\phi}_{k_l}^{\dagger} V^{-1} . \tag{4.77}$$

Then for $z = z_0$, so that z' is in the lead and $z \geq z'$

$$\tilde{G}_{z_0 z'}(z_0) = \sum_{l=1}^{N} \phi_{k_l} e^{ik_l(z_0-z')} \tilde{\phi}_{k_l}^{\dagger} V^{-1}$$

$$- \sum_{l,h}^{N} \phi_{\overline{k}_h} e^{i\overline{k}_h(z_0-z_0)} \tilde{\phi}_{\overline{k}_h}^{\dagger} \phi_{k_l} e^{ik_l(z_0-z')} \tilde{\phi}_{k_l}^{\dagger} V^{-1} = 0 . \tag{4.78}$$

Similarly, for $z' = z_0$, so that z is in the lead and $z \leq z'$, $\tilde{G}_{z_0 z'}(z_0) = 0$.

The surface Green's function is the Green's function for the last slice of the leads, which for the left lead will be at $z_0 - 1$. At this point $z = z' = z_0 - 1$, so that $e^{ik_l(z-z')} = 1$. Hence, the surface Green's function, $G_L = \tilde{G}_{z_0-1,z_0-1}(z_0)$, is given by

$$G_L = \tilde{G}_{z_0-1,z_0-1}(z_0) = \sum_{l=1}^{N} \phi_{k_l} \tilde{\phi}_{k_l}^{\dagger} V^{-1} - \sum_{l,h}^{N} \phi_{\overline{k}_h} e^{-i\overline{k}_h} \tilde{\phi}_{\overline{k}_h}^{\dagger} \phi_{k_l} e^{ik_l} \tilde{\phi}_{k_l}^{\dagger} V^{-1} . \tag{4.79}$$

$$\Rightarrow G_L = [I - \sum_{l,h}^{N} \phi_{\overline{k}_h} e^{-i\overline{k}_h} \tilde{\phi}_{\overline{k}_h}^{\dagger} \phi_{k_l} e^{ik_l} \tilde{\phi}_{k_l}^{\dagger}] V^{-1} . \tag{4.80}$$

Similarly, for the right lead, the first slice is taken to be at $z_0 + 1$, and the lead runs to $+\infty$. Hence the corresponding surface Green's function, G_R, is given by

$$G_R = \tilde{G}_{z_0+1,z_0+1}(z_0) = [I - \sum_{l,h}^{N} \phi_{k_l} e^{ik_l} \tilde{\phi}_{k_l}^{\dagger} \phi_{\overline{k}_h} e^{-i\overline{k}_h} \tilde{\phi}_{\overline{k}_h}^{\dagger}] V^{-1} . \tag{4.81}$$

The main weakness of using this method for calculating the Green's functions of the leads is that it requires the inversion of the matrix $(H_1 - ES_1)$. For certain systems, particularly when the orbitals of the atoms in the leads are strongly localised, this matrix can be singular.

This can also occur if the unit cell of the leads is not chosen carefully, for example if it is unnecessarily long. For example, consider the linear atomic chain shown in figure 4.8.

Each atom is coupled only to its nearest neighbour with hopping parameter γ. In the first case, each unit cell only contains one atom, and so H_1 is just equal to γ, and so is invertible. However, in the second case, we consider two atoms in each
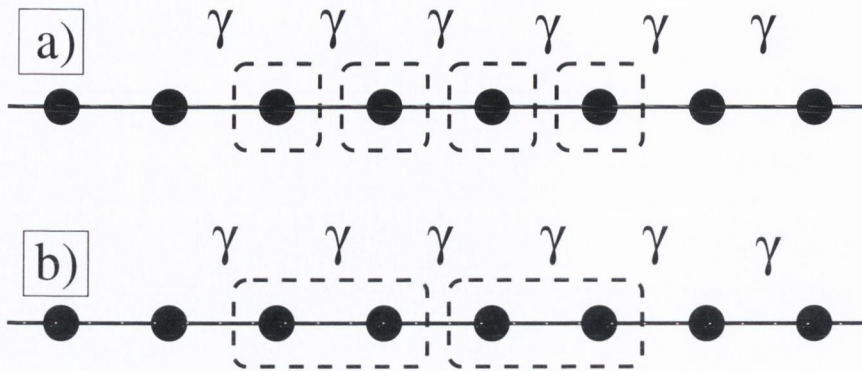
Figure 4.8: Linear atomic chains of atoms with (a) one and (b) two atoms in the unit cell. If the atoms are only coupled with their nearest neighbours, then in chain (b), the matrix H_1 describing the coupling between neighbouring cells will be singular.

principal layer, and the left atom in one principal layer will not interact with the left atom in the next principal layer. Hence, H_1 for this particular system has the form

$$H_1 = \begin{pmatrix} 0 & 0 \\ \gamma & 0 \end{pmatrix} \tag{4.82}$$

This matrix is obviously not invertible. In this case, the problem can be solved easily by choosing a different unit cell for the leads. However, for more realistic systems with multiple orbitals this is not always possible. Transition metals can be particularly troublesome due to the highly localised nature of the "d" orbitals.

This problem can be solved by performing a generalised singular value decomposition [109], combined with a decimation procedure to remove the degrees of freedom which do not couple to the other principal layers [38].

4.7   Conclusion

The non-equilibrium Green's function formalism described here can be used to perform calculations for open systems which are not at equilibrium, such as nanoscale devices with have an applied bias. As such, it can be used to calculate electron transport processes in a variety of systems, from metal-molecule junctions, to nanowires and multilayer devices. It allows the effects of finite bias to be modelled self-consistently, and can be used to plot the transmission coefficients and I-V curves of such systems. It can be used with different electronic structure methods such as tight-binding or density functional theory. This method has been combined with the density functional theory code SIESTA [82, 83, 84] described previously to form the SMEAGOL

[37, 38, 39] program.

Chapter 5

Molecular Electronics and the Derivative Discontinuity

Nanoelectronics has now advanced to the point where devices are being constructed from single molecules. Such molecular devices have the potential to revolutionise multiple diverse fields, from computer architecture [2, 3, 4, 5, 12] to chemical sensors [6, 7, 8] and medical diagnostics [9, 10, 11].

One of the first molecular devices was manufactured by Reed et. al. [19] in 1997. It consisted of a benzenedithiol (BDT) molecule connected between two gold point contacts, constructed by using a mechanically controlled breaking junction (MCBJ) as described in the introductory chapter of this thesis. Electronic transport measurements performed on this device found very low conductivity, with a conductance gap between -1V and 1V, and a current of the order of $0.3\mu A$ at 5V. To put this current in perspective, the quantum of conductance, G_0, is equal to $77\mu S$, so that the current through a single open conductance channel would be $77\mu A$ at 1V and $385\mu A$ at 5V, assuming a linear I-V curve. The zero-bias conductance was very low, of the order of $10^{-5}G_0$. However in more recent experiments, such as that of Xiao et. al. [26], a zero-bias conductance of $0.011G_0$ was obtained for the same molecule using an STM breaking junction. This is three orders of magnitude higher than that observed by Reed et. al. No significant conductance gap was observed, and a current of the order of $1\mu A$ was measured at 0.7V. In the same work, transport measurements were also performed on benzenedimethanethiol (BDMT) using the same method. For this molecule, a conductance of $6 \times 10^{-4}G_0$ was observed, with a current of the order of 50nA being measured at a bias of 0.6V. It should be noted that in the work of Xiao et. al., several hundred measurements were made for each molecule, with a new molecular junction being constructed for each measurement. This allows statistical histograms of the conductance to be plotted for each molecule, increasing the reliability of the results.

Another MCBJ experiment has been performed since for BDT attached to gold electrodes by Tsutsui et. al. [24]. They found two sets of zero bias conductances: one set of "low-conductance states" where they observe conductance values of $0.004G_0$, $0.005G_0$ and $0.011G_0$, which are values similar to those observed by Xiao et. al. [26]; but also a set of "high-conductance" peaks, with values of $0.09G_0$, $0.14G_0$ and $0.23G_0$. Both the MCBJ and STM breaking junction methods were used by Ulrich et. al. [25], with the STM measurements being performed at room temperature (293K) and the MCBJ experiments being performed at low temperature (30K). For the room temperature measurements for BDT, clear peaks could not be observed in the conductance histograms, but in the case of the low temperature mechanical break junction measurements, a peak was discernible at $0.011G_0$, the same value as that observed by Xiao et. al. For the configuration giving this conductance value, a current of the order of $3\mu A$ was measured at 1V, with no conductance gap observed. The transport properties of BDMT were also investigated in this work, with the observed conductance values being between $0.0002G_0$ and $0.004G_0$.

Ghosh et. al. [29] used a combination of electron-beam lithography and electromigration to fabricate gold electrodes, and then deposited BDT and BDMT molecules in the gap between them. They observed high conductances for BDT, of the order of $0.1G_0$ (similar to the high conductance regime observed by Tsutsui et. al.). A current of the order of $30\mu A$ was observed at 2V, with no conductance gap in the I-V curve. For BDMT, a conductance of $5 \times 10^{-4}G_0$ was observed, similar to that measured by Xiao et. al., with a current of order the order of 200nA at 2V. Dadosh et. al. [30] investigated the transport properties of BDMT and biphenyldithiol (BPD) by mixing a solution of the molecules with a gold colloid, so that the molecules would attach to the gold nanoparticles, tethering two of them together. The resulting dimer was then trapped between two electrodes and the transport properties measured. In this work, very low conductances were observed, with BPD giving a conductance of the order of $10^{-5}G_0$, while BDMT gave a conductance of the order of $10^{-7}G_0$.

Thus, there are large variations in the experimentally measured results for the transport properties of these molecular junctions, even when very similar methods are used to perform the measurements. The usual explanation given for this large spread in the data is that of variation in the contact geometry between the molecule and the metal surface. Other possibilities include there being different numbers of molecules present in the junction, or the molecule not being chemically bonded to one or both of the electrodes.

Unfortunately, to date *ab initio* quantum transport calculations have not been of

much assistance in solving this problem. Calculations using NEGF and DFT with
local exchange-correlation (XC) functionals give results for the conductance which
are even higher than those obtained by any of the experiments [63, 64, 65, 66, 67, 68,
69, 70]. One of the earliest calculations performed for the BDT molecular junction
was that by DiVentra et. al. [63]. Their results showed a conductance gap in the I-V
curve between -1V and 1V similar to that observed in Reed et. al.'s experiments, but
obtained a current of 150μA at 5V. For a different configuration, with the molecule
attached to a single gold adatom on each surface, the current dropped to 6μA at 5V.
However, these calculations were performed using a jellium model for the electronic
structure of the electrodes.

Calculations in which the leads are treated more realistically include those of
Xue et. al. [64, 65], which were performed using the BPW91 GGA XC functional to
calculate the electronic structure of the extended molecule with a modified version
of GAUSSIAN98. For BDT, they find a zero bias conductance of the order of $0.1G_0$,
with a current of the order of 50μA at 4V. For BPD, the zero bias conductance of the
order of $0.02G_0$, with a current of the order of 40μA at 4V. However, the extended
molecule which they use for their calculations only includes six atoms from each lead,
and the leads themselves are described semi-empirically.

Stokbro et. al. [68] used the TranSIESTA method to investigate BDT attached
to gold using both LDA and GGA XC functionals. They obtained similar results
for both LDA and GGA, with conductances in the range of $0.36G_0$ to $0.44G_0$, which
are higher than that observed in any of the experiments, and a current of the order
of 100μA at 5V. Basch et. al. [66] also used the TranSIESTA method with an
LDA XC functional to calculate the transport properties for both BDT and BDMT
attached to gold leads. The set up in both of these calculations and those of Stokbro
et. al. are very similar to our own as described in Chapter 6. Their results show
zero bias conductances in the range of $0.2G_0$ to $0.8G_0$ depending on the anchoring
geometry, with a current of the order of 25μA at 0.6V. For BDMT attached to gold
electrodes, they obtained zero bias conductance in the range of $0.006G_0$ to $0.05G_0$,
with a current of the order of 300nA to 500nA at 0.6V.

Many body methods have also been used to investigate electronic transport in
BDT attached to gold leads. Delaney et. al. [51] used a method based on the
configuration interaction formalism. They obtained an I-V with a conductance gap
between -2V and 2V, with a current of the order of 3μA at 5V. The zero-bias conduc-
tance observed was of the order of $10^{-3}G_0$. However, this method uses distribution
functions to describe the effect of the semi-infinite leads, instead of self-energies as

in the non-equilibrium Green's function formalism. This in turn may lead to the broadening of the molecular orbitals being incorrectly described, which may explain the large conductance gap.

Several of these *ab initio* calculations also demonstrate that altering the contact geometry to reduce the strength of the interaction between the molecule and the metal results in the HOMO of the molecule being pinned to the Fermi level of the metal, so that a high zero-bias conductance is still observed [64, 65, 66, 67]. This is discussed at length in chapter 6, where DFT calculations are performed for multiple anchoring configurations of the BDT molecule on the gold surface.

One explanation as to why the calculations fail to describe any of the experiments is that the local exchange-correlation (XC) functionals used in the calculations contain self-interaction errors, as described in chapter 2. One effect of the self-interaction error is to suppress the derivative discontinuity, which should be present in the true XC functional. In chapter 3, the effect on the electronic transport of a non-linear dependence of the energy of the level on its occupation was demonstrated using a simple model. Here, a similar concept is applied to the system of BDT sandwiched between gold electrodes, to investigate the effects of a discontinuous potential on the conductance of this junction [74]. However, in order to recover the derivative discontinuity in DFT, the full self-interaction correction would have to be applied self-consistently [71]. This is difficult to implement for extended systems and is also computationally very costly. Therefore, we instead modelled the system using a self-consistent tight-binding Hamiltonian, in which the dependence of the energy of the energy level of the valence orbitals for each atom on the occupation was calculated using self-interaction corrected DFT [101].

5.1   Self-Consistent Tight-Binding Hamiltonian

The non-equilibrium Green's function formalism (NEGF) [34, 35, 36, 38] works with a number of different Hamiltonians, such as the DFT Hamiltonian described previously. In order to examine the effect of a derivative discontinuity on the electronic transport properties of a metal-molecule junction, we used the NEGF method with a self-consistent tight-binding Hamiltonian [110, 111]. This is a relatively simple Hamiltonian, which helps to prevent the calculations from becoming too computationally expensive. This is important, since the discontinuous charging potentials being investigated here can cause some convergence problems. Also, since it is not an *ab initio* Hamiltonian, the various parameters used can be varied independently

in order to study their effect on the system.

To introduce the tight-binding method, first consider an infinite linear chain of identical atoms, as shown in figure 5.1. Allow one state, $|j\rangle$, per atom. The wave
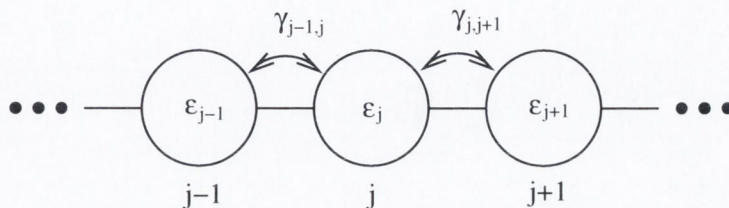

Figure 5.1: Infinite linear chain of atoms, labelled by index j. In the tight-binding approximation, each atomic orbital is characterised by an "on-site energy" ϵ_j, and the nearest neighbour hopping parameters $\gamma_{j,j+1}$.

function of the entire chain, $|\psi\rangle$, will be a linear combination of atomic orbitals.

$$\psi = \sum_{j=1}^{N} \psi_j |j\rangle , \tag{5.1}$$

where $|j\rangle$ are the atomic orbitals. These are assumed to be orthonormal, so that $\langle i|j\rangle = \delta_{ij}$. The Schrödinger equation for this system is $H|\psi\rangle = E|\psi\rangle$, where H is the Hamiltonian and E are the eigenvalues. By expanding the wave function $|\psi\rangle$ over the basis $|j\rangle$ and projecting over the state $|i\rangle$ gives

$$\sum_{j=1}^{N} \psi_j \langle i|H|j\rangle = E \sum_{j=1}^{N} \psi_j \langle i|j\rangle . \tag{5.2}$$

If we assume that the atomic orbitals are tightly bound to the nucleus (the "tight-binding" approximation), so that only the matrix elements between nearest neighbour orbitals do not vanish, we obtain

$$\langle i|H|j\rangle = \begin{cases} \epsilon_j & \text{if } i = j; \\ \gamma_{ij} & \text{if } i = j \pm 1; \\ 0 & \text{Otherwise.} \end{cases} \tag{5.3}$$

Here, ϵ_j is the "on-site energy" of atom j, which is energy of the atomic state if the atom is disconnected from the rest of the chain, modified to take into account the effect of the crystal field. The "hopping parameter", γ_{ij}, describes the hopping between orbitals situated on neighbouring atoms. The rate at which electrons can move between two orbitals is given by $\frac{\gamma_{ij}}{\hbar}$. For a chain of identical atoms, where $\epsilon_j = \epsilon$ and $\gamma_{j-1,j} = \gamma_{j,j+1} = \gamma$ for all j, the Schrödinger equation associated with atom j becomes

$$\gamma\psi_{j-1} + \epsilon\psi_j + \gamma\psi_{j+1} = E\psi_j \,. \tag{5.4}$$

Take $\psi_j = e^{ikj}$ as a trial solution for equation (5.4). For atom j, this gives

$$\gamma e^{ik(j-1)} + \epsilon e^{ikj} + \gamma e^{ik(j+1)} = E e^{ikj} \,, \tag{5.5}$$

$$\Rightarrow (\epsilon - E) + \gamma(e^{-ik} + e^{ik}) = 0 \,. \tag{5.6}$$

Since $e^{-ik} + e^{ik} = 2\cos(k)$, we get a dispersion relation for the energy E in terms of k

$$E = \epsilon + 2\gamma\cos(k) = 0 \,. \tag{5.7}$$

From this, it can be seen that the tight-binding Hamiltonian has two main parameters: the on-site energy ϵ and the "hopping" parameter γ. The on-site energy represents the potential energy. It determines the energy of the orbital in an atom, or the position of the centre of the band in a solid. In our Hamiltonian, the on-site energy of a particular orbital is a function of the electronic occupation of that orbital. The form of this function will be discussed later. The hopping parameter, or coupling, represents the kinetic part of the Hamiltonian. It corresponds to the probability of an electron "hopping" between atoms. From equation (5.7), it can be seen that it is the parameter which determines the width of a band.
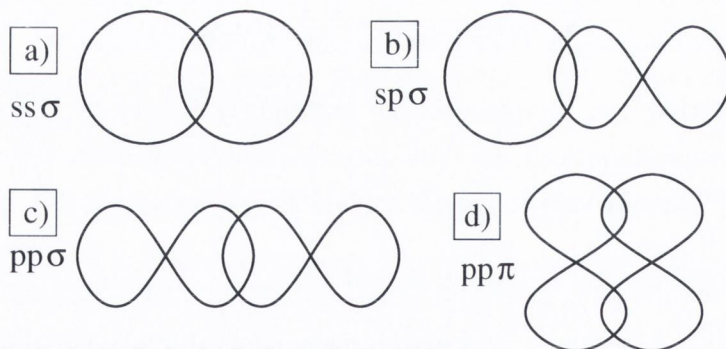

Figure 5.2: Different types of hoppings for s and p orbitals: (a) $ss\sigma$ hopping, between two s orbitals; (b) $sp\sigma$ hopping, between an s and p orbital; (c) $pp\sigma$ hopping, between two p orbitals oriented along the same axis; (d) $pp\pi$ hopping, between two p orbitals oriented along parallel axes

The tight-binding method can be extended to three-dimensional systems by considering the interactions between the nearest neighbour atoms in every direction.

As shown in equation (5.8), the value of γ depends on both the type and relative orientation of the orbitals, and the distance d between the atoms [111].

$$\gamma_{ll'm} = \frac{\hbar^2}{m_e} \frac{\eta_{ll'm}}{d^2} . \tag{5.8}$$

The parameter $\eta_{ll'm}$ depends on the type of hopping in question, $(ss\sigma, sp\sigma, pp\pi,$ etc), i.e. on the geometry of the orbitals relative to each other, as shown in figure 5.2. The distance between the atoms is d, $\hbar$ is Planck's constant and m_e is the electron mass.

These parameters can be determined by fitting experimental band structures and orbital spectra, or they can be calculated using ab initio methods such as DFT [112]. The values for $\eta_{ll'm}$ for s and p orbitals are given in table 5.1, and are taken from Harrison [111].

Coupling Type	Relative Strength
$\eta_{ss\sigma}$	-1.40
$\eta_{sp\sigma}$	1.84
$\eta_{pp\sigma}$	3.24
$\eta_{pp\pi}$	-0.81

Table 5.1: Table showing relative coupling strengths of different bond types between s and p orbitals [111].

In the case where the orbitals are at an angle θ with respect to each other as shown in figure 5.3, the p orbital should be broken into components parallel and perpendicular to the axis joining the two atoms.
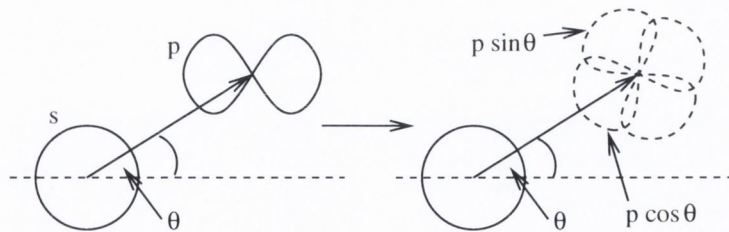

Figure 5.3: Interaction between s and p orbitals at an angle θ to each other. The p-orbital is split into components parallel and perpendicular to the bond axis. The perpendicular component does not interact with the s-orbital due to symmetry, so the bond is $\gamma_{sp\sigma} \cos \theta$.

The component of the p-orbital which is perpendicular to the direction of the axis joining the two atoms does not interact with the p-orbital due to symmetry.

The interaction is therefore between the s-orbital and the component of the p-orbital along the axis joining the two molecules, and is equal to $\gamma_{sp\sigma} \cos \theta$. In the case of an interaction between two p-orbitals at an angle to each other, the orbitals should both be split into parallel and perpendicular components to give a sum over $pp\sigma$ and $pp\pi$ interactions.

5.2   Self-Consistent Potential

As described above, the on-site energy is a function of the occupation of the orbital it is associated with. As for the simple model described in chapter 3, this can be written as

$$\epsilon = \epsilon_0 + U_{\text{SCF}}(\rho) . \tag{5.9}$$

where ϵ_0 refers to the neutral atom, and $U_{\text{SCF}}(\rho)$ is a self-consistent potential. As in the simple model, two different potentials are considered; one which is obtained from a self-interaction corrected (SIC) DFT calculation for the free atom, and the other calculated in the same way for the LDA potential. In particular, the SIC-type potentials for sulphur (S) and carbon (C) atoms were calculated using a self-interaction corrected plane-wave DFT code [101]. They are the energy eigenvalue of the relevant orbital as a function of its occupation. As for the simple model, the LDA
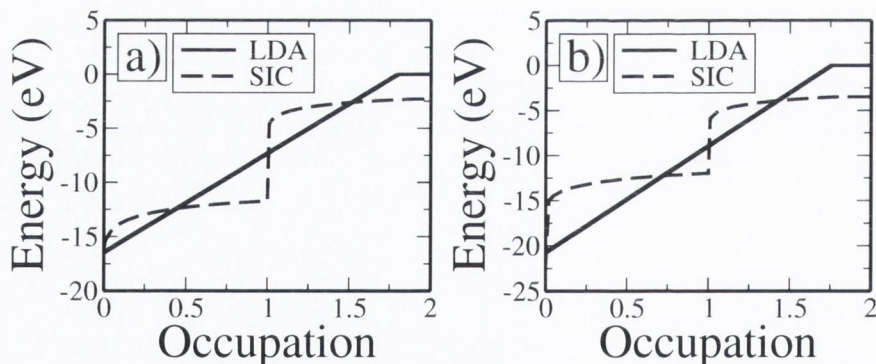

Figure 5.4: Self consistent potentials for (a) carbon and (b) sulphur. The SIC-type potentials are calculated using self-interaction corrected DFT for the free atom [101]. The energy of the atomic eigenvalue is calculated as a function of its occupation. The LDA-type potential was then fitted to match the SIC-type potential at occupations of 0.0, 0.5, and 1.5 electrons. Note the discontinuities in the SIC-type potential at integer occupation.

and SIC-type potentials should match at occupations of 0.0, 0.5, and 1.5 electrons [101]. Hence, the LDA-type potential was fitted to the SIC-type potential so that the

sum of the square of the distance between the two potentials at these occupations was minimised. The LDA and SIC-type potentials for C and S are shown in figure 5.4.

The SIC-type potential is only applied to the orbitals used to represent the molecule, i.e. the C and S π orbitals. The gold leads are assumed to be metallic with highly delocalised electrons, allowing local fractional charging. Therefore, for the gold atoms U_{SCF} is assumed to be directly proportional to the charge, i.e. $U_{\mathrm{SCF}} = N - N_0$, where N_0 is the occupation of the local orbital at neutrality.

These self-consistent potentials are for the position of the atomic orbitals as a function of occupation. These atomic orbitals form the basis set for the calculation. To calculate the occupation of the atoms at a given potential bias, the density of states and the corresponding density matrix are calculated using the NEGF method described in chapter 4. This gives the occupation of the molecular orbitals, which are linear combinations of atomic orbitals. The charge density can then be projected over the atomic orbital basis set, and the self-consistent potential is then calculated for each atomic orbital as a function of its occupation. This determines the new on-site energy for each orbital, which is then used to to construct the new Hamiltonian. The procedure is then repeated iteratively until convergence.

Note that this means that the self-consistent potentials, and hence the positions of the discontinuities, are calculated based on the occupation of the atomic orbitals rather then the molecular orbitals. This may cause problems in that the discontinuities may occur at the wrong place if, for example, the molecular orbitals have integer occupation but the the atomic orbitals do not due to electrons being delocalised across several atoms. The result of this is that there are fewer, larger steps in the level energy as a function of occupation.

5.3   Calculation Details

The system we wish to study here is a benzenedithiol (BDT) molecule attached to fcc (100) Au leads, as is shown in figure 5.5. The yellow atoms are gold, the brown are sulphur, the black are carbon, and the blue are hydrogen.

In order to simplify the calculations, only one orbital per atom is used. For the gold atoms just the $6s$ orbitals are used, as the Fermi level lies in the s band, with the d orbitals more localised and about 2eV below the Fermi level. They are thus less likely to contribute to the current at low bias. The density of states (DOS) obtained from a DFT-LDA calculation which shows the positions of all of the valence orbitals
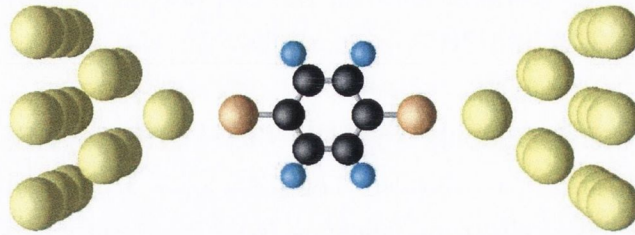
Figure 5.5: BDT attached to fcc (100) gold leads. Colour code: Au=yellow, C=black, S=brown, H=blue.
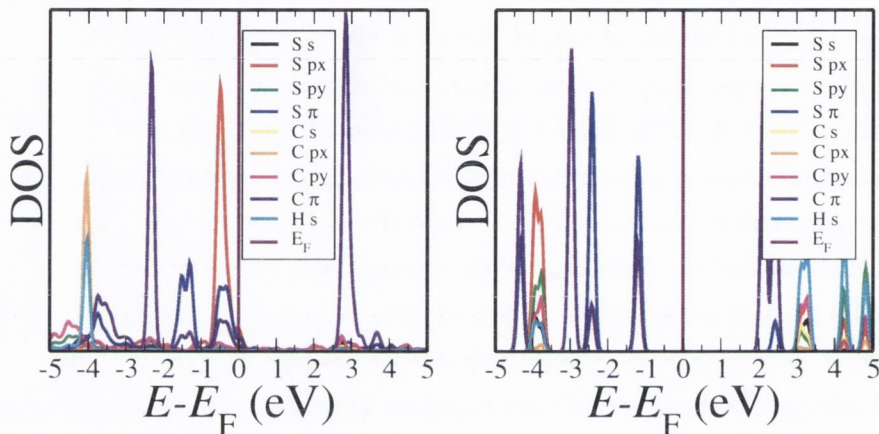

Figure 5.6: Density of States (from DFT with LDA) for the molecular orbitals for (a) BDT on Gold and (b) isolated BDT Molecule.

of the molecule is shown in figure 5.6. From this DOS, it can be seen that the only molecular orbitals which are close to the Fermi level are the S and C π orbitals, which are the p orbitals lying perpendicular to the plane of the benzene ring. They are coupled to each other via a $pp\pi$ bond (see figure 5.2), and are delocalised across the entire molecule, so they will conduct electrons. None of the other carbon orbitals lie near the Fermi level. The only other state which is near the Fermi level is the S "p_x" state just below E_F. However, this state is perpendicular to the C π orbitals, and so will not interact with them. Therefore, the state is not delocalised across the molecule and will not conduct. For this reason, the sulphur and carbon atoms can be described just using the the p orbitals which lie perpendicular to the plane of the benzene ring. The hydrogen atoms not considered since the molecular orbitals to which they contribute are far from the Fermi level.

In the calculations described in this chapter, the BDT molecule is attached to a
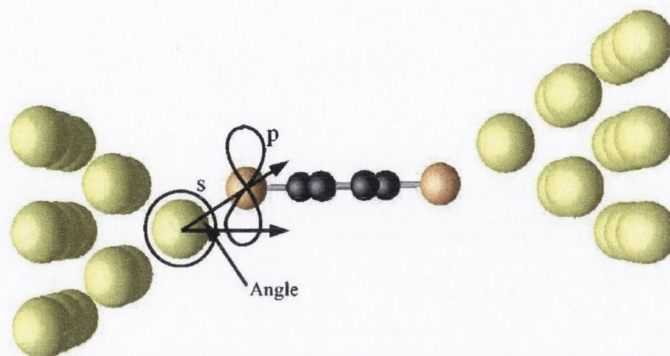
Figure 5.7: BDT attached to fcc (100) gold leads. The angle between the end gold atom
and the sulphur atom can be adjusted to control the strength of the interac-
tion between the molecule and the leads. Colour code: Au=yellow, C=black,
S=brown, H=blue.

gold fcc (100) nanowire. The nanowire ends in a tip, going from a 3x3 cross-section,
to 2x2, to a single atom. The S atoms of the BDT molecule are attached to these
last gold atoms. However, because of symmetry, the s orbital of the gold will not
couple to the π orbital of the sulphur when the molecule is in line with the gold
atoms at the tip, and so no current will flow at all. To overcome this problem, the
angle between the gold and the sulphur is varied from 5° to 30° as shown in figure
5.7 to allow the s and p orbitals to interact. By changing this angle, the strength of
the coupling between the molecule and the leads can be controlled and so the effect
of this on the I-V curve can be investigated.

The band alignment between the gold and the molecule was chosen so as to give
results for the I-V curve which, with an LDA-style potential matched those which
had been calculated using SMEAGOL for the same geometry [113]. Thus, for the
calculations in which the effect of coupling strength on the transport properties is
investigated, the Fermi level is set to -7.1eV. However, the effect of changing the
band alignment and the Fermi level is also investigated.

5.4 Effect of derivative discontinuity for different coupling strengths.

The effect of derivative discontinuity on the conductance of the Au-BDT molecular
junction was investigated for a variety of different coupling strengths. The strength of
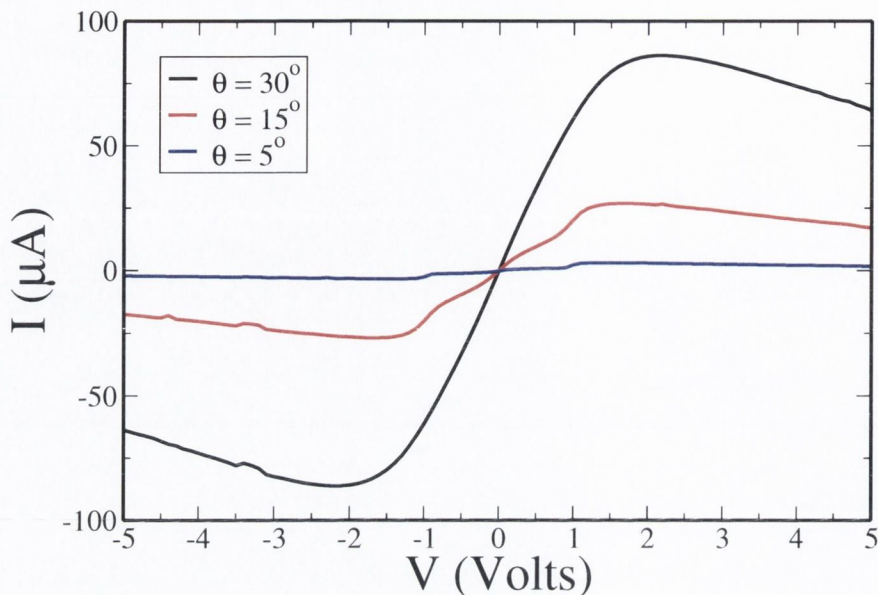the metal-molecule coupling is extremely sensitive to the Au-S angle shown in figure

Figure 5.8: *I-V* Curves for BDT on Au fcc (100) for different coupling strengths between the molecule and the metal. This coupling strength is adjusted by changing the gold-sulphur angle shown in figure 5.7. Increasing this angle from 5° to 30° can cause the size of the current to increase by up to two orders of magnitude.

5.7, and so this parameter can be used to control the size of the interaction between the molecule and the leads. As the size of the angle is increased, the interaction between the *s* and *p* orbitals increases and so the coupling strength increases. This in turn has a major effect on the magnitude of the current, as shown in figure 5.8. Changing this one angle from 5° to 30° can cause the size of the current to increase by up to two orders of magnitude. Thus the *I-V* characteristics of this system are highly dependent on the exact geometric configuration of the contact between the metal and the molecule. Similar results to this have been reported elsewhere [47].

To investigate the effect of the derivative discontinuity in the limit of weak coupling between the leads and the molecule, the sulphur-gold angle was set to 5°. The density of states for this system is shown in figure 5.9 for both types of potentials. These have been calculated using the NEGF method, and so include the effect of the infinite leads. The sulphur and carbon π states are relatively narrow due to the weak metal-molecule coupling. For both types of potentials, the two molecular states on either side of the gold Fermi level mainly consist of hybridised C and S π and π^* states, with E_F pinned just below the π^* level. For convenience, these particular states will be referred to as the π and π^* states, and in this case they form the HOMO and the LUMO of the molecular junction.
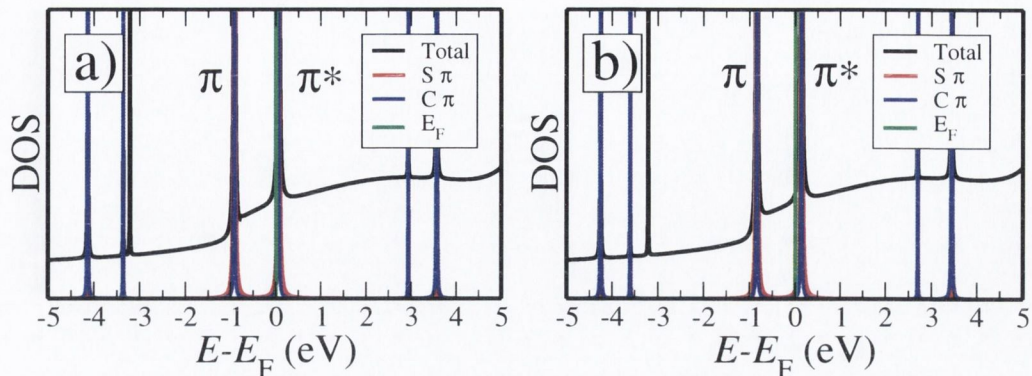
Figure 5.9: Density of states for tight-binding (a) LDA and (b) SIC for BDT on Gold for
the weak coupling limit in which the gold-sulphur angle is set to 5°. Note how
the two states on either side of the gold E_F are mostly due to the sulphur π
and π^* states. The gold E_F is pinned just below the π^* state for both types of
charging potentials. The molecular levels are narrow due to the weak coupling
to the leads.

The occupation and position of the HOMO and the LUMO (the π and π^* states),
and the I-V curves for this configuration are shown in figure 5.10, while the transmis-
sion coefficients are shown in figures 5.11 and 5.12. To understand the relationship
between the level occupations and their position relative to the bias window, first
recall the discussion of the simple model in chapter 3. If the molecule is coupled
symmetrically to the leads, then if the level is below the chemical potential of both
leads, it will be fully occupied (i.e. it will contain two electrons, assuming it is spin
degenerate). If it is above both chemical potentials, it will be empty, and if it is be-
tween the two potentials (i.e. if it is inside the bias window), it will be half-occupied
(i.e. it will contain one electron).

With this in mind, the results in figures 5.10, 5.11 and 5.12 can be understood.
For the LDA-type potential, the Fermi level of the metal is at the centre of the π^*
state. As such, it is partially occupied, as shown in figure 5.10(a). It charges slightly
as the voltage is increased, and the level position tracks the position of the higher
chemical potential as shown in figure 5.10(b), so that part of the level is within
the bias window. From figures 5.11 and 5.12, the resonance in the transmission
coefficients which corresponds to this level is also partially within the bias window.
Hence, as shown in panels (c) and (d) of figure 5.10, there is no conductance gap
in the I-V curve, and the current increases rapidly at low bias. Up to 1V, the
conduction will be through the π^* state only. Above 1V, the bias window becomes
large enough to also include the π state, and conduction can now take place through
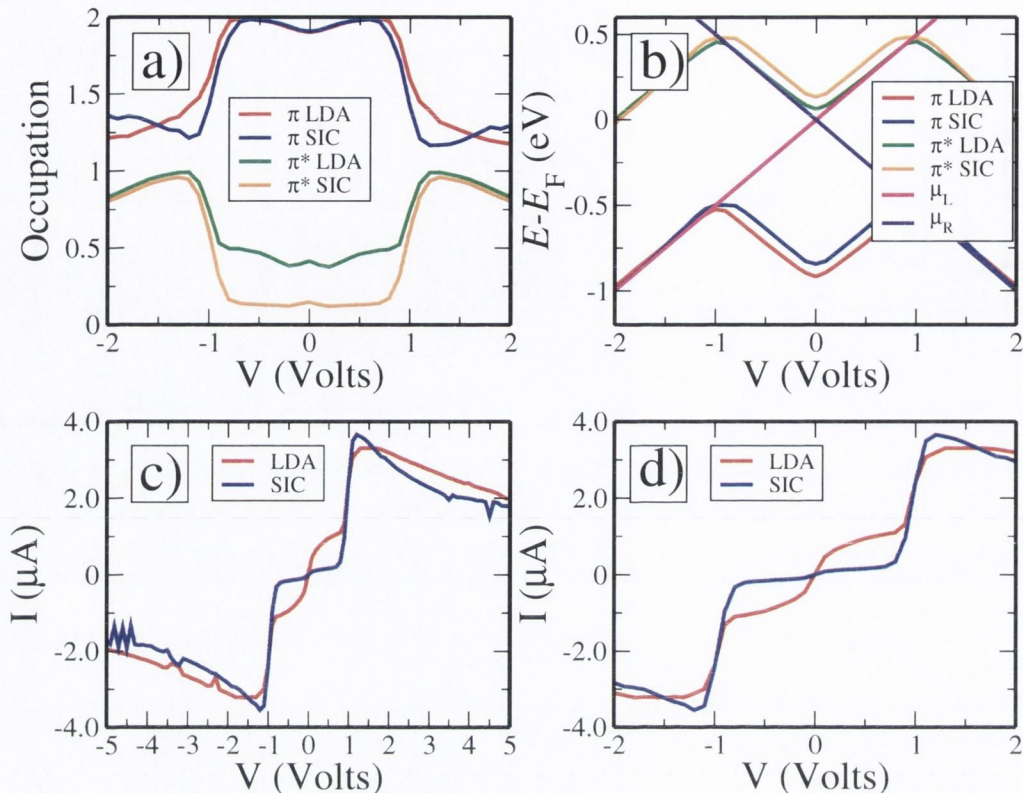
Figure 5.10: The (a) occupation and (b) position of the π and π^* states for both the LDA-type and SIC-type charging potentials for BDT on Gold. *I-V* curves for (c) bias range from -5V to +5V, and (d)from -2V to +2V. Note conductance gap from -1V to +1V with the SIC-type potential. This is the weak coupling limit, where the Au-S angle is set to 5°.

this state also.

For the SIC-type potential, as for the discontinuous potential for the simple model, the energy of a level increases rapidly as soon as any charge is added. At zero bias, the π^* state is pinned just above the gold E_F and is unoccupied, as shown in panels (a) and (b) of figure 5.10. As the voltage is increased so that the π^* state would move into the bias window, the leads will try to impose an occupation of one electron on it. However, as soon as any charge is inserted into this level, the discontinuous potential causes its energy to increase sharply. This keeps the level pinned above the higher chemical potential and outside of the bias window. The corresponding resonance in the transmission coefficients is also pinned outside the bias window, as shown in figures 5.11 and 5.12. This suppresses the current at low bias, opening up a conductance gap in the *I-V* curve. At 1V, the bias window is now large enough to contain both the π and π^* states. At this point, the leads will try to
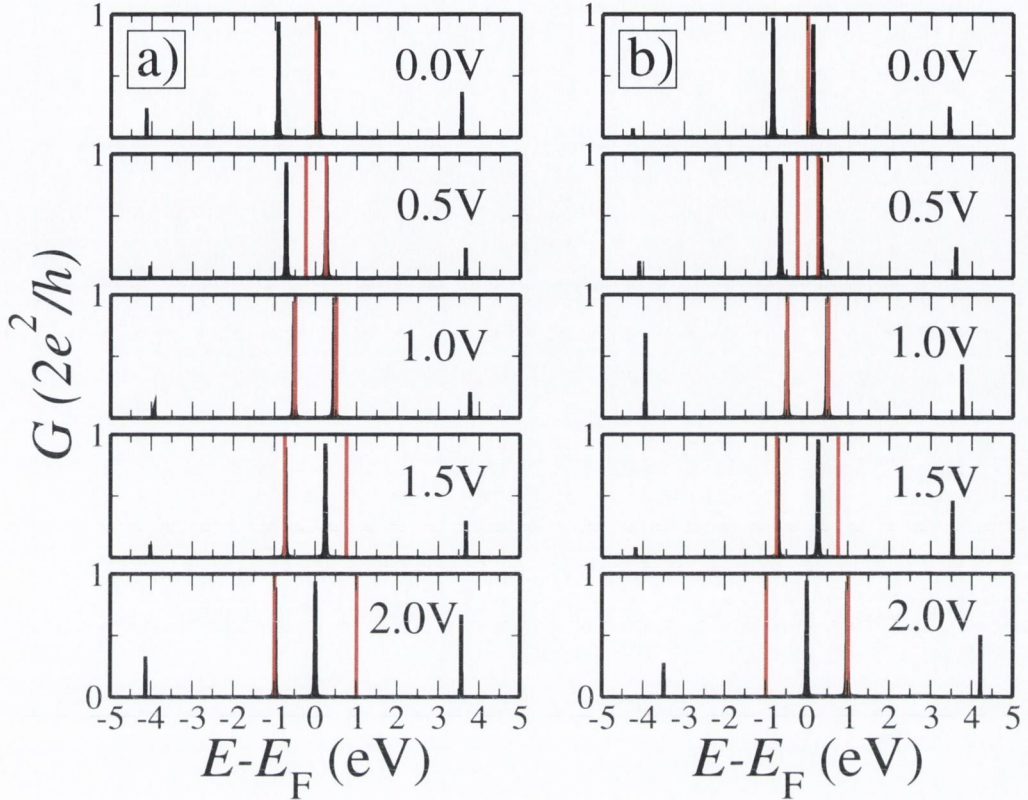
Figure 5.11: Transmission Coefficients calculated at 0.5V bias intervals for BDT on Gold
in the weak coupling limit (Au-S angle = 5°): (a) LDA-type potential and (b)
SIC-type potential.. The red vertical lines show the positions of the chemical
potentials of the leads, so that the region between them is the bias window.
The resonances in the transmission coefficients near the bias window corre-
spond to the π and π^* states in the DOS, and are narrow because of the weak
coupling between the leads and the molecule.

impose an occupation of one electron on each molecular level. This results in a re-
arrangement of the charge inside the molecule, with one electron moving from the π
state to the π^* state, as shown in figure 5.10(a). Since both states are mainly due to
the sulphur p orbitals, this does not actually involve any change in the occupation of
the atomic orbitals. Therefore, the values of the self-consistent potentials, and thus
the matrix elements of the Hamiltonian, are unaffected, and so the energies of the
molecular orbitals are unchanged. Both levels now start to conduct simultaneously
and the current increases rapidly, as shown in panels (c) and (d) of figure 5.10. Thus,
in the weak coupling limit, the derivative discontinuity has the effect of opening up
a conductance gap between -1V and 1V. Note that this gap is the same size as that
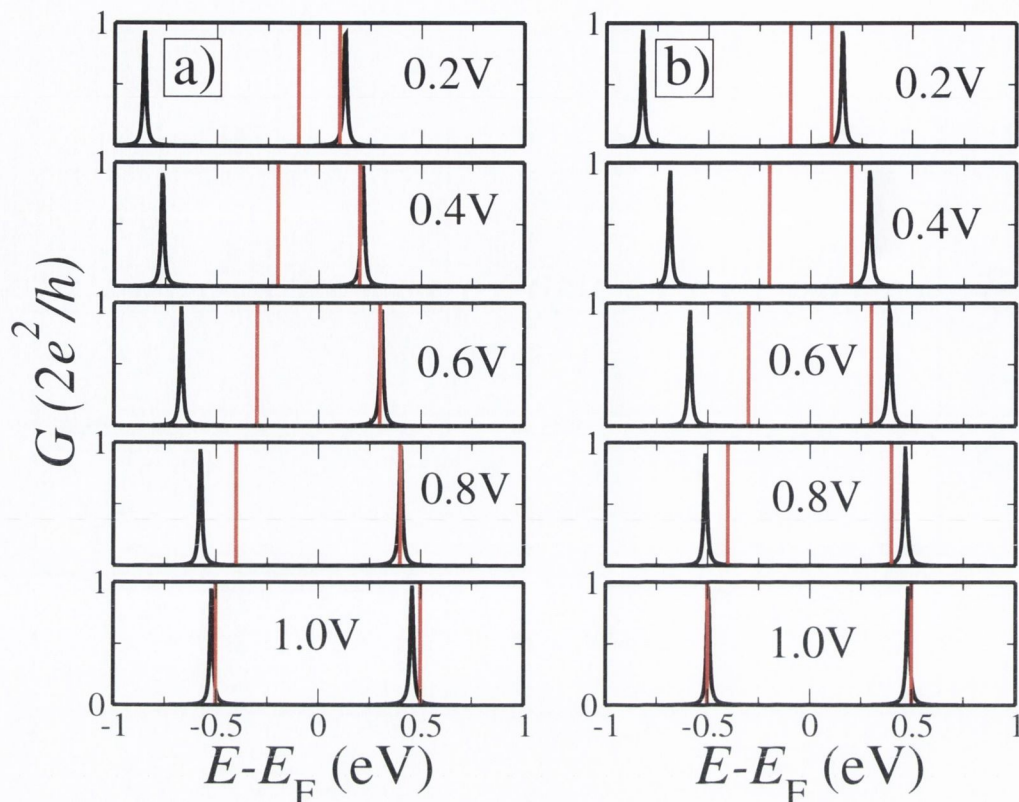observed in the experiments conducted by Reed et. al. [19].

Figure 5.12: Transmission Coefficients calculated at 0.2V bias intervals for BDT on Gold in the weak coupling limit (Au-S angle = 5°): (a) LDA-type potential and (b) SIC-type potential. The red vertical lines show the positions of the chemical potentials of the leads, so that the region between them is the bias window. The resonances in the transmission coefficients near the bias window correspond to the π and π^* states in the DOS, and are narrow because of the weak coupling between the leads and the molecule.

To explore the effect of increasing the strength of the metal-molecule coupling, the sulphur-gold angle was increased to 15°. As shown in the DOS in figure 5.13, increasing the coupling strength causes the molecular energy levels to broaden. As for the 5° angle, the SIC-type potential again causes the π^* state to be pinned above the gold E_F. For the LDA-type potential, the π^* state is also centred slightly above E_F, although a large proportion of its tail is below the Fermi level.

As shown in figure 5.14(a), this has the same result as for the 5° angle, with the π^* state having a much lower occupation at zero bias for the SIC-type potential than for the LDA-type potential. As the voltage is increased, the SIC-type potential again keeps the π^* state pinned somewhat above the bias window up to approximately 1V. The corresponding resonance in the transmission coefficients, shown in figure 5.15,
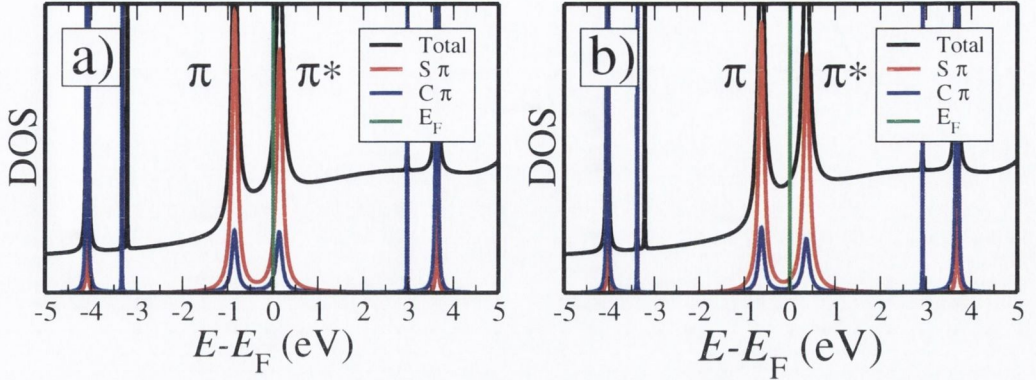
Figure 5.13: Density of states for tight-binding (a) LDA and (b) SIC for BDT on Gold where the Au-S angle is set to 15°. Note how the two states on either side of the gold E_F are mostly due to the sulphur π and π^* states. The gold E_F is pinned just below the π^* state for both types of charging potentials, although it is closer to the π^* state for the LDA-type potential. The molecular levels are broader than those shown in figure 5.9 due to the stronger coupling to the leads.

is also pinned outside the bias window. This again leads to the suppression of the low bias current as shown in figure 5.14(c).

However, the effect is not as strong as it was in the case when the Au-S angle was 5°. This is because the resonances in the transmission coefficients corresponding to the π and π^* states shown in figure 5.15 are broader, and they even overlap to some extent. Therefore, the transmission around E_F in the region between the two molecular levels is non-zero. This results in some conductance in the -1V to 1V bias window with the SIC-type potential, although the current in this region is still lower than that obtained for the linear potential.

Above 1V, the bias window is once again large enough to contain both the π and π^* states and the charges rearranges inside the molecule, as shown in figure 5.14(a). The current increases rapidly as conduction takes place through both of the levels.

In order to investigate the effect of the derivative discontinuity in the strong coupling limit, the Au-S angle was increased further to 30°. As can be seen from the DOS plotted in figure 5.16, the gold E_F is once more situated between the π and π^* molecular levels, which are greatly broadened by the strong coupling to the leads, so that they overlap to a large extent. Thus when the potential bias is applied the π state discharges while the π^* charges (figure 5.17(a)) in such a way that the total charge on the atoms in the molecule does not change very much. Therefore, as shown in figure 5.17(b), neither level moves much with bias, so that the exact nature of the
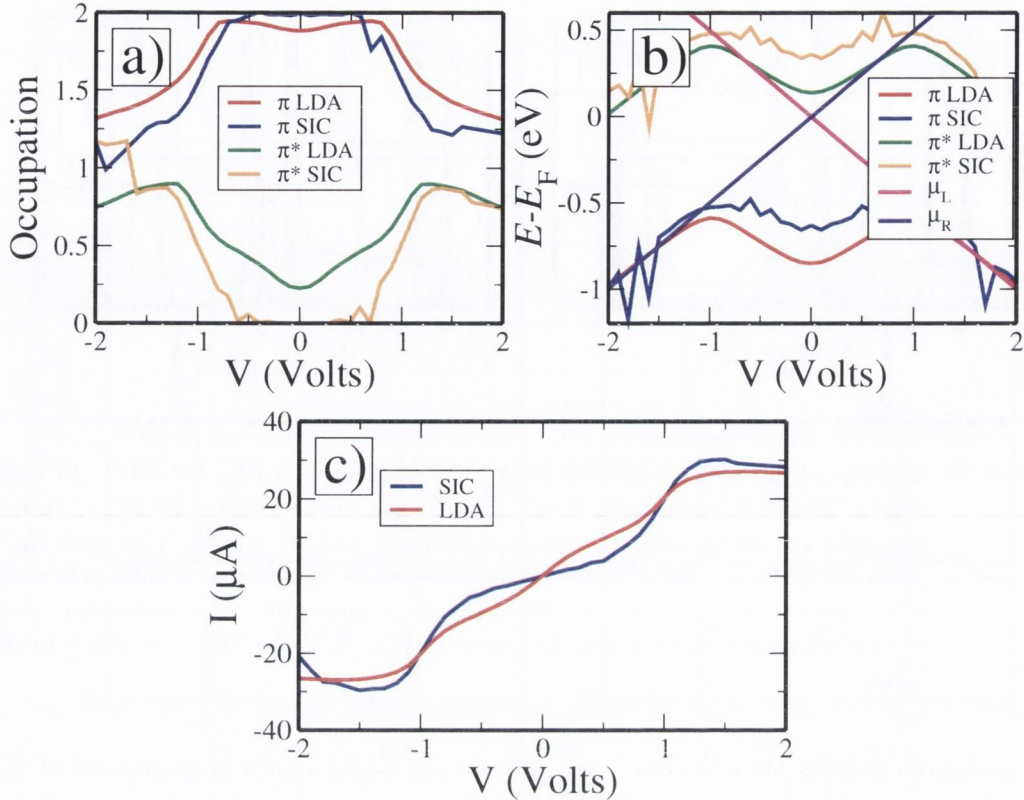
Figure 5.14: The (a) occupation and (b) position of the π and π^* states for both the LDA-type and SIC-type charging potentials for BDT on Gold, with the Au-S angle set to 15°. *I-V* curves (c) for bias range from -2V to +2V. The conductance gap between -1V and +1V for the SIC-type potential is now not as distinct as it was in the weak coupling limit.

charging potential is relatively unimportant. The resonances in the transmission coefficients shown in figure 5.18 are also very broad, and the transmission at the gold E_F is very high. Thus, although the π^* state is pinned at a slightly higher energy, its precise position is not as important as in the weak coupling limit. The zero-bias conductance for both types of potentials is high, and the *I-V* curves are very similar, as shown in figure 5.17(c).

5.5 Effect of derivative discontinuity for different level alignments

In the calculations described in the previous section, the alignment between the gold 6s band and the molecular orbitals was set artificially so as to give an *I-V* curve similar to that produced by SMEAGOL. An advantage of using the tight-binding
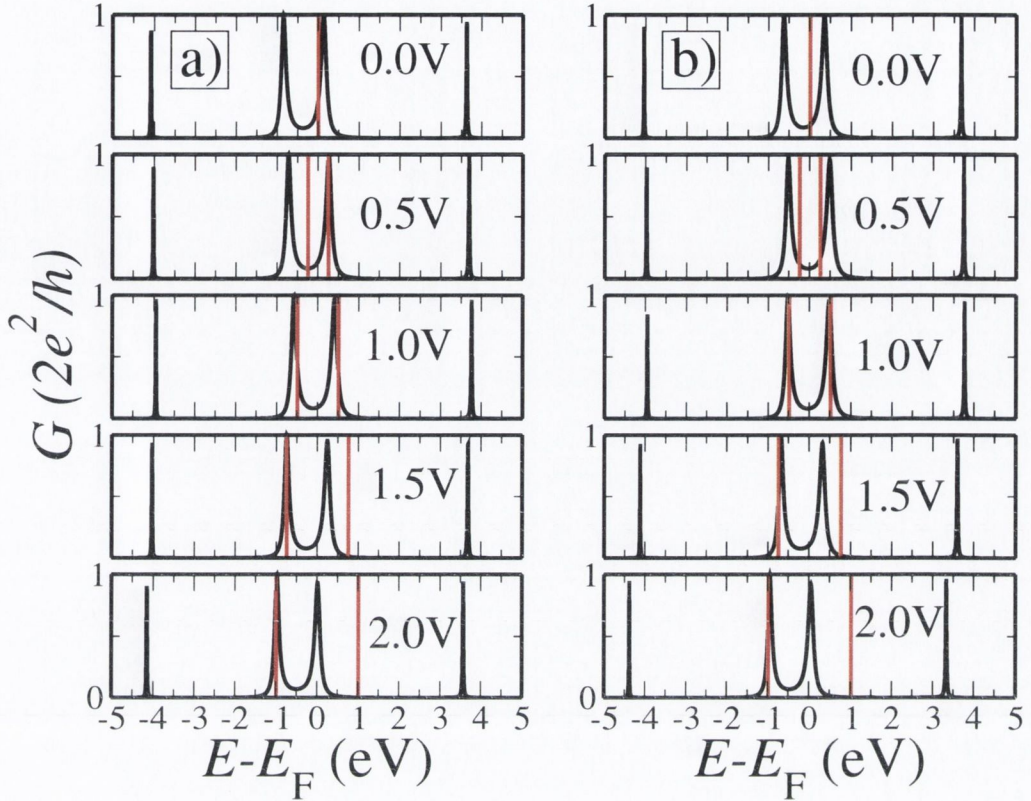
Figure 5.15: Transmission Coefficients at 0.5V bias intervals for BDT on Gold (Au-S angle
= 15°): (a) LDA-type potential and (b) SIC-type potential. The red vertical
lines show the positions of the chemical potentials of the leads, so that the
region between them is the bias window. The resonances in the transmission
coefficients near the bias window correspond to the π and π^* states in the
DOS. They are broader than the resonances shown in figure 5.11 because of
the stronger coupling between the leads and the molecule. Therefore, even
though the centre of the level is pinned outside the bias window with the
SIC-type potential, there is still some transmission at zero bias.

method is that parameters such as the position of band centres can be adjusted
easily to investigate the effect of altering the level alignment. The impact of the
level alignment on the effect of the derivative discontinuity on the conductance of
the device will now be described for the weak coupling limit (i.e. for the gold-sulphur
angle set to 5°).

The Au band centre was first shifted upwards by 2eV. The DOS for this system
is shown in figure 5.19. For the LDA-type potential, the gold E_F cuts across the
π^* state, while for the SIC-type potential it is pinned just below it. As shown in
figure 5.20(a), this state already contains one electron at zero bias for the LDA-type
potential, and so its occupation does not change much when the potential bias is
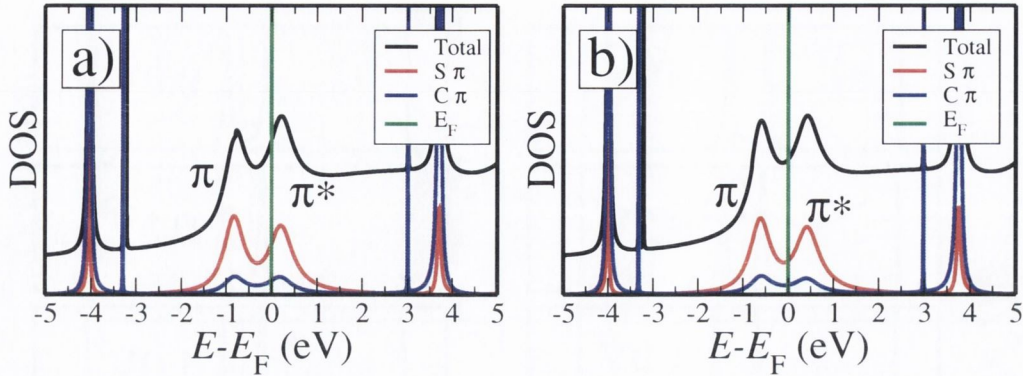
Figure 5.16: Density of states for tight-binding (a) LDA and (b) SIC for BDT on Gold
for the strong coupling limit where the Au-S angle is set to 30°. Note how
the two states on either side of the gold E_F are mostly due to the sulphur π
and π^* states. The molecular levels are very broad due to the strong coupling
between the molecule and the leads.

applied. Thus as the voltage is increased, the state remains at the centre of the
bias window, and it starts to conduct at zero bias. However, because the levels do
not move much, the π state remains outside the bias window at 1V and will not
conduct until a higher bias is applied. For the discontinuous potential, the π^* state
is still pinned above the gold E_F. However, the Fermi level is now closer to the top
of the charging potential of the atoms, so the dependence of the level position on its
occupation is no longer as steep as before. As shown in figure 5.20(b), the level is
now closer to the bias window, and while the low bias current is still suppressed, it
is larger than it was for the previous level alignment.

The gold band centre and Fermi level is then lowered by 2eV with respect to
the position used in section 5.4. The DOS for this configuration is shown in figure
5.21. For the SIC-type potential, the gold E_F is still pinned to the π^* state of the
molecule. However, for the LDA-type potential, E_F is just above the π state. Thus
for the the LDA-type potential the π^* state is unoccupied at low bias because of the
position of the Fermi level (figure 5.22(a)). The π state is not full, and it possesses
some amplitude in the bias window. Therefore, the conductance is initially through
the π state rather than the π^* state.

For the SIC-type potential, the π^* state is pinned just above the bias window.
As for the original case, the discontinuity prevents the level from charging, keeping
it out of the bias window, as shown in panels (a) and (b) of figure 5.22. Once again,
there is a conductance gap present in the I-V curve between -1V and 1V.

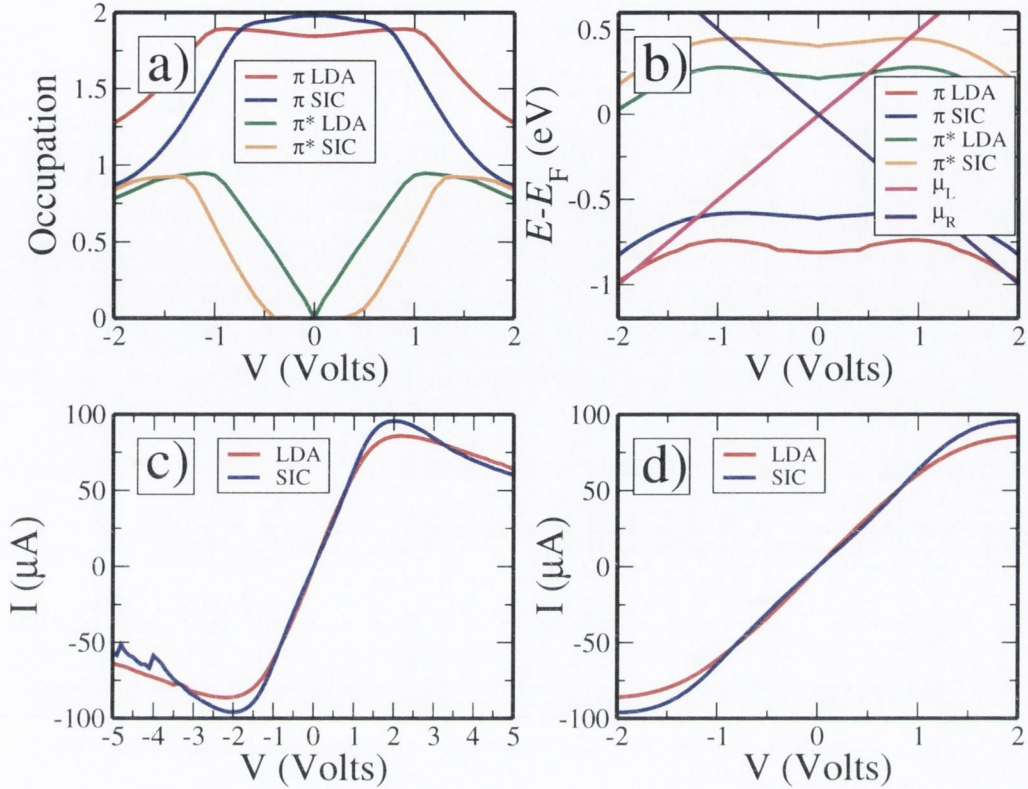The final band alignment configuration investigated is where the gold 6s band

Figure 5.17: The (a) occupation and (b) position of the π and π^* states for both the LDA-
type and SIC-type charging potentials for BDT on Gold. *I-V* curves for (c)
bias range from -5V to +5V, and (d)from -2V to +2V. The conductance gap
from -1V to +1V with the SIC-type potential has now disappeared, and the
I-V curves for both types of potentials are very similar. This is the for the
strong coupling limit, where the Au-S angle is set to 30°.

centre and Fermi level were raised by 4eV relative to the molecular orbitals. The
DOS for this configuration (again in the weak coupling limit) is shown in figure 5.23.
In this case, the gold E_F is just above the π^* state for both the LDA and SIC type
charging potentials.

As shown in panels (a) and (b) of figure 5.24, both the π and π^* states are
below the gold E_F at zero bias, and thus both are almost fully occupied. Therefore,
molecular levels will be in the flat part near the top of the SIC-type potentials as
shown in figure 5.4. Hence for this potential, the level can discharge to a large extent
without moving very much. As the voltage is increased, the level remains near the
centre of the bias window and will conduct strongly. The LDA-type potential, on
the other hand, behaves linearly. As the voltage is increased, it discharges more
gradually and remains pinned to the lower chemical potential. Therefore it does not
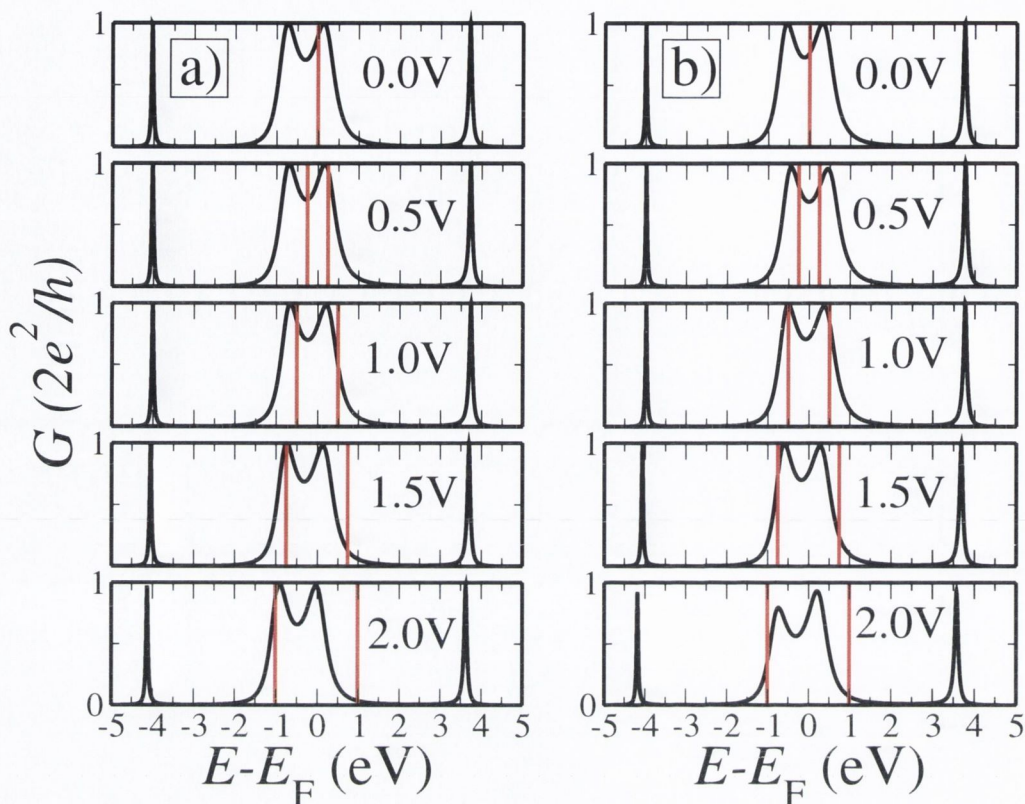
Figure 5.18: Transmission Coefficients at 0.5V bias intervals for BDT on Gold in the strong coupling limit (Au-S angle = 30°): (a) LDA-type potential and (b) SIC-type potential. The red vertical lines show the positions of the chemical potentials of the leads, so that the region between them is the bias window. The resonances in the transmission coefficients near the bias window correspond to the π and π^* states in the DOS, and are broad because of the strong coupling between the leads and the molecule, to the point where they overlap extensively at E_F, leading to a high zero bias conductance for both types of charging potential.

conduct as strongly as in the case of the SIC-type potential. This result is similar to the case described in chapter 3, when the Fermi level was placed near the top of the charging potential.

5.6   Conclusion

Under certain conditions, the derivative discontinuity can have a dramatic effect on the *I-V* characteristics of molecular devices. If the molecule is weakly coupled to the metallic leads, and the Fermi level of the metal is pinned just below a molecular state, the discontinuity will prevent the state from charging and will keep it out
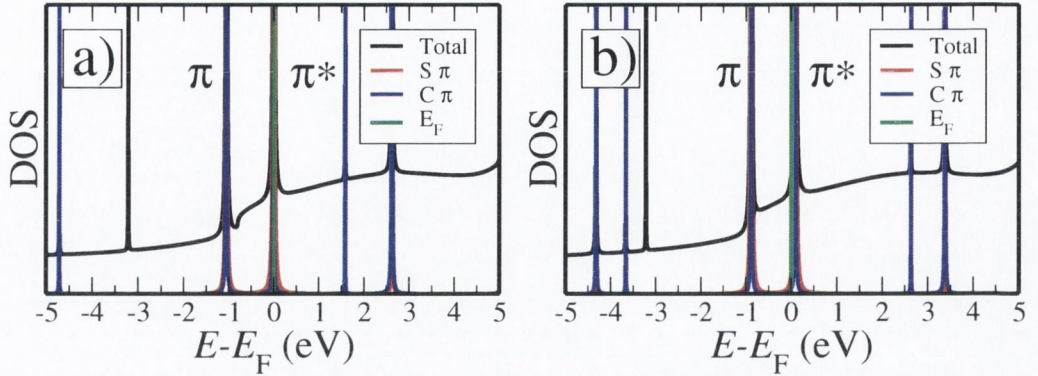
Figure 5.19: Density of states for tight-binding (a) LDA and (b) SIC for BDT on Gold for the weak coupling limit where the Au-S angle is set to 5°. The gold bands and Fermi level have been shifted upwards by 2eV relative to the molecule. The gold E_F is still pinned just below the π^* state for the SIC-type charging potential, and is at the π^* state for the LDA-type charging potential.

of the bias window. This will open up a conductance gap in the I-V curve which would not be present if a continuous exchange-correlation potential such as LDA is used. For BDT attached to gold, this conductance gap is from -1V to 1V, which is of the same size as the gap found in one of the experiments [19]. This might be a coincidence due to the choice of parameters in the approximate Hamiltonian used. The effect of the discontinuity also highlights the importance of calculating the I-V curve self-consistently at finite bias instead of simply integrating the zero-bias tranmission coefficients.

This conductance gap gradually disappears as the strength of the interaction between the molecule and the metal is increased. The molecular levels and the corresponding resonances in the transmission coefficients are broadened by stronger coupling, so that the transport properties are no longer as sensitive to the exact position of the level. Also, as the levels become broader, they charge more slowly as the bias window is opened, and hence do not respond as sharply to voltage changes.

The effect of the derivative discontinuity will also depend to some extent on the alignment of the molecular levels with the E_F of the leads. The discontinuity strongly suppresses the conductance when the Fermi level of the metal is pinned just below an unoccupied level in the molecule, as it will prevent this level from charging and keep it out of the bias window. Shifting the band alignment by 2eV in either direction did not have much effect on the I-V curve, with the conductance gap still being present for the SIC-type potential. However, if the band alignment is altered sufficiently so that E_F is just above an occupied level, then the SIC-type potential allows such a
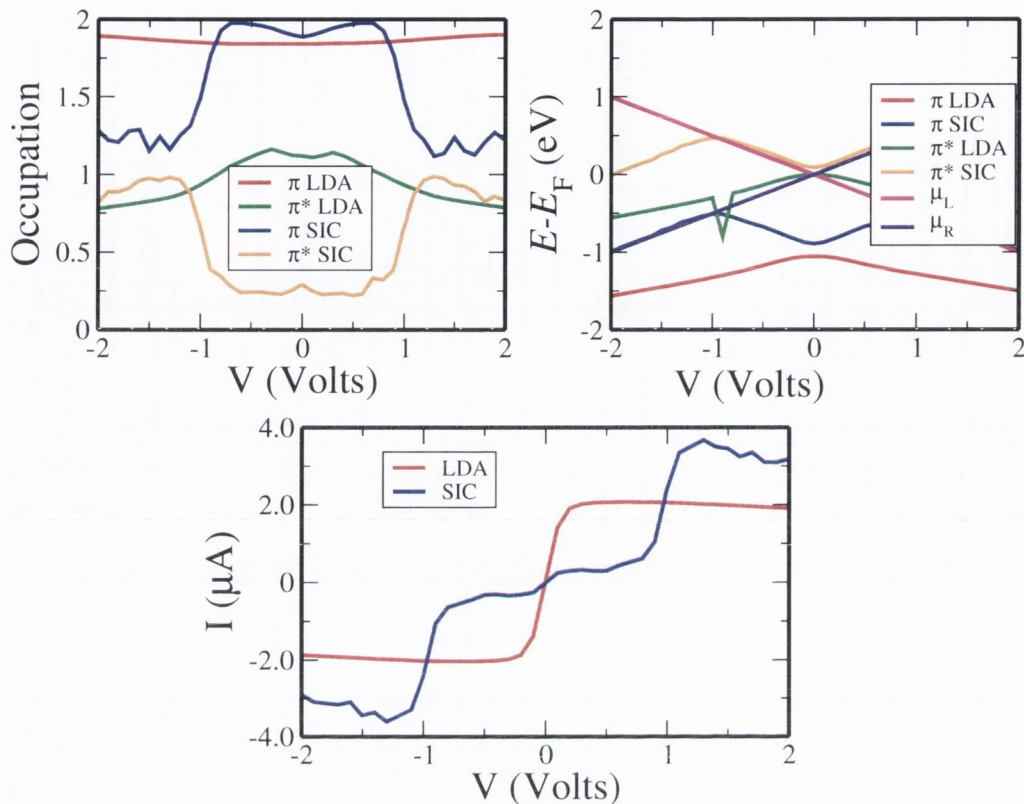
Figure 5.20: The (a) occupation and (b) position of the π and π^* states for both the LDA-type and SIC-type charging potentials for BDT on Gold. *I-V* (c) curves for a bias range from -2V to +2V. The gold bands and Fermi level have been shifted upwards by 2eV relative to the molecule. The conductance from -1V to +1V with the SIC-type potential is somewhat higher than for the original band alignment, although it is still much lower than for the LDA-type potential. This is the for the weak coupling limit, where the Au-S angle is set to 5°.

level to discharge easily and so the conductance can be large at low bias.

The electronic structure method used in this chapter is not an *ab initio* one. As such, certain features of the results may be artifacts of the approximations used. Therefore, it will still be necessary at some point to perform electron transport calculations for this system using an *ab initio* electronic structure method which naturally incorporates the derivative discontinuity. For DFT, methods which at least partially restore the derivative discontinuity include the full self-interaction correction to LDA [71] and exact-exchange [88, 114, 53]. Unfortunately, these methods are orbital dependent, and as yet there is no implementation of them for finite bias transport calculations.
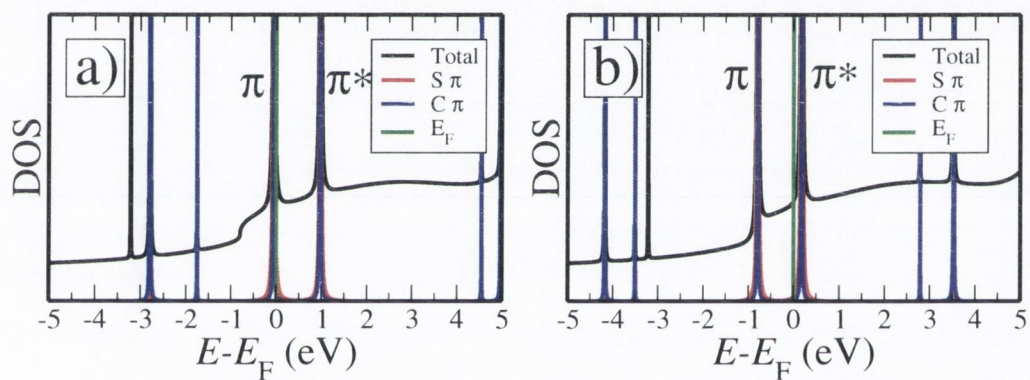
Figure 5.21: Density of states for tight-binding (a) LDA and (b) SIC for BDT on Gold for the weak coupling limit where the Au-S angle is set to $5°$. The gold bands and Fermi level have been shifted downwards by 2eV relative to the molecule. The gold E_F is still pinned just below the π^* state for the SIC-type charging potential, but is now at the π state for the LDA-type charging potential.
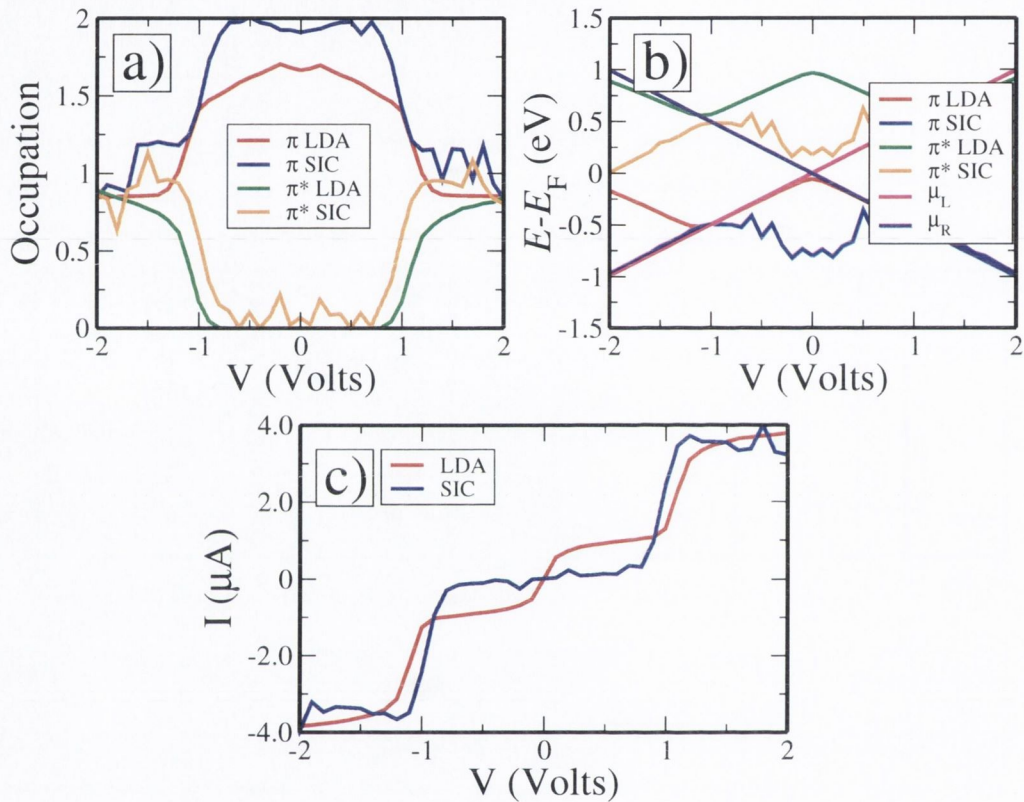
Figure 5.22: The (a) occupation and (b) position of the π and π^* states for both the LDA-type and SIC-type charging potentials for BDT on Gold. *I-V* (c) curves for a bias range from -2V to +2V. The gold bands and Fermi level have been shifted downwards by 2eV relative to the molecule. The conductance gap from -1V to +1V is still present for the SIC-type potential, and the low bias current for the LDA-type potential is lower than for the original band alignment. This is the for the weak coupling limit, where the Au-S angle is set to 5°.
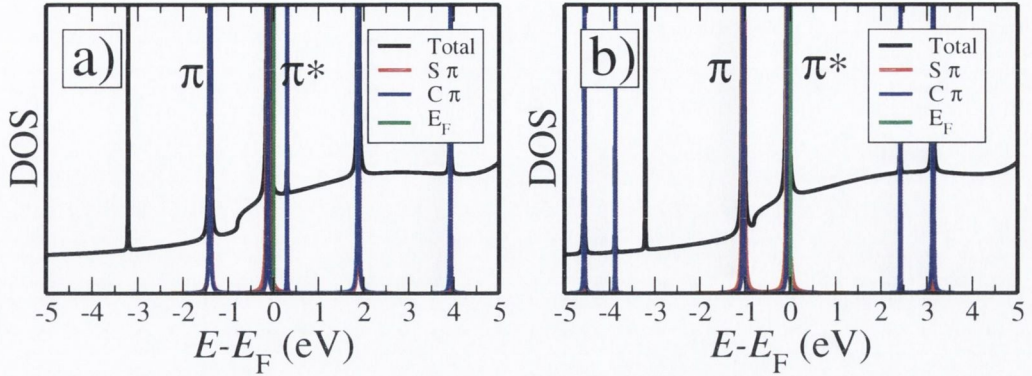
Figure 5.23: Density of states for tight-binding (a) LDA and (b) SIC for BDT on Gold for the weak coupling limit where the Au-S angle is set to 5°. The gold bands and Fermi level have been shifted upwards by 4eV relative to the molecule. The gold E_F is now just above the π^* state for both types of charging potential.
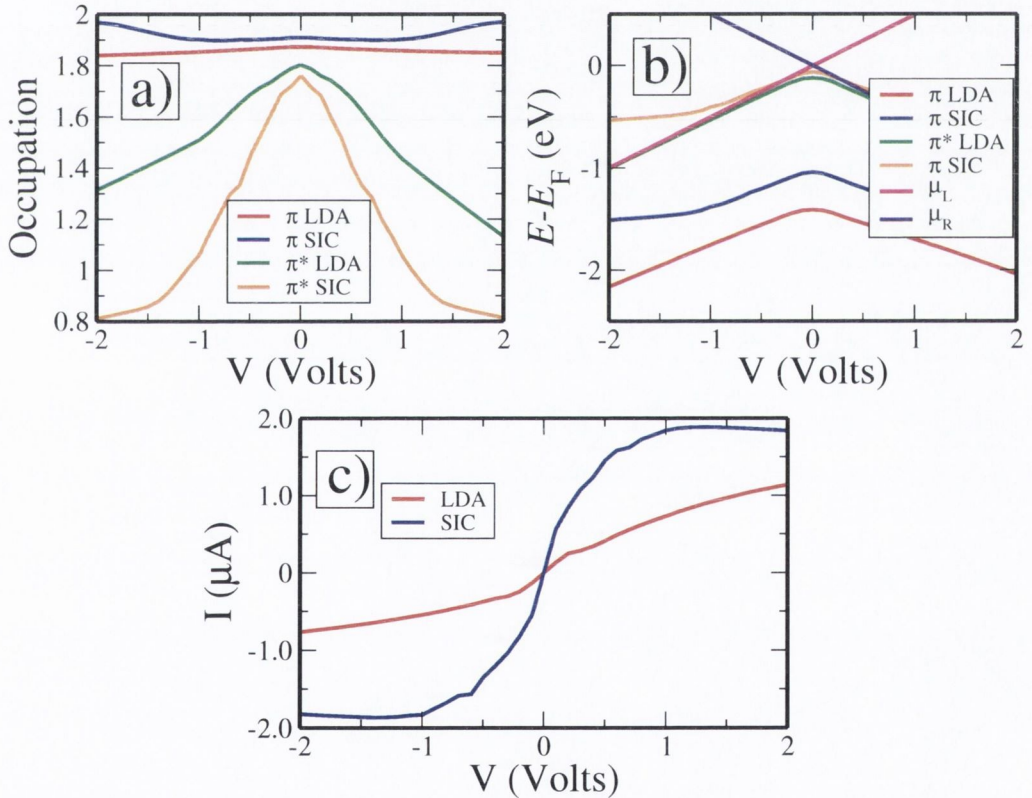

Figure 5.24: The (a) occupation and (b) position of the π and π^* states for both the LDA-type and SIC-type charging potentials for BDT on Gold. *I-V* (c) curves for a bias range from -2V to +2V. The gold bands and Fermi level have been shifted upwards by 4eV relative to the molecule. The low bias conductance is now higher for the SIC-type potential than the LDA-type potential. This is the for the weak coupling limit, where the Au-S angle is set to 5°.

Chapter 6

ASIC and Electron Transport in Organic Molecules

In the last decade, several examples of devices consisting of a single organic molecule sandwiched between two metallic electrodes have been constructed. Possible applications of molecular devices include high-performance computer components [2, 3, 4, 5, 12], which will be smaller, faster, consume less power and be cheaper to manufacture; highly sensitive chemical sensors [6, 7, 8], disposable electronics, as well as possible medical applications [9]. Another interesting application which has been suggested recently is to use electronic transport measurements to sequence strands of DNA, where individual base-pairs are distinguished by their conductance [10, 11].

Organic molecules for which transport measurements have been made include benzenedithiol (BDT), benzenedimethanethiol (BDMT) and biphenyldithiol (BPD). Such devices have been constructed using mechanically controllable break junctions [19, 24, 25], STM tips [25, 26], lithographically fabricated nanoelectrodes [29], and colloid solutions [30]. Unfortunately, there is much disagreement between the values obtained for the conductance using the different methods for these and other molecules. For BDT, values for the zero-bias conductance vary from as low as $10^{-5}G_0$ [19] up to $0.011G_0$ [26] or possibly even higher [24].

In order to explain the variations between the experiments, as well as to further understand the physics of electronic transport in such devices, several calculations have been performed using many different computational methods. These include NEGF [34, 35, 36] with empirical Hamiltonians such as tight-binding [46, 47, 48, 49], *ab initio* Hamiltonians such as DFT [43, 44, 37, 38, 39, 40, 41, 42], and many-body methods such as Hartree-Fock with configuration interaction [50, 51, 52, 53, 54, 55, 56]. However, the results obtained using different methods also vary, and tend not to reproduce the experiments well either [63, 64, 65, 66, 67, 68, 69, 70]. Calculations using NEGF and DFT with local XC functionals give results for the conductance

which are even higher than those obtained by any of the experiments. Altering the contact geometry to reduce the strength of the interaction between the molecule and the metal results in the HOMO of the molecule being pinned to the Fermi level of the metal, so that a high zero-bias conductance is still observed.

One explanation as to why the calculations fail to describe any of the experiments is that the local exchange-correlation (XC) functionals used in the calculations contain self-interaction errors [71], as described in chapter 2. The effect of the suppression of the derivative discontinuity [72, 73] on electronic transport in molecules [74] was explored in chapter 5. In this chapter, the results of calculations investigating another effect arising from the self-interaction correction, the correction of the band alignment between the molecule and the metal, will be presented. An atomic self-interaction correction (ASIC) [100, 75], as described in chapter 2, has been implemented in the localised atomic orbital code SIESTA [82, 83, 84] which is the DFT platform for our transport code SMEAGOL [37, 38, 39]. This ASIC gives good results for ionisation potentials for isolated molecules [75] compared to those obtained from uncorrected LDA.

The electronic transport properties for three different molecules have been calculated using LDA only and LDA with ASIC: 1,4-benzenedithiol (1,4-BDT), benzenedimethanethiol (BDMT), and biphenyldithiol (BPD). In all cases, the molecule is attached via the sulphur atom to fcc (111) gold electrodes on each side. Gold is the metal normally used for such experiments, due to its high conductivity and its resistance to corrosion. The sulphur atoms on the thiol molecules also form strong bonds with the gold surface. In the case of BDT, we investigate several different anchoring geometries, demonstrating how the transport properties vary with changes in the strength of the interaction between the molecule and the metal. In the case of BDMT, we investigate two different isomers of the molecule.

6.1 Calculation Details

The ASIC corrections are not applied to the gold atoms in the leads in the calculations presented here, as the self-interaction error for metals is small [75]. Unless otherwise specified, we use a double zeta polarised basis set [82, 83, 84] for carbon (C) and sulphur (S) s and p orbitals, double zeta for the $1s$ orbitals of hydrogen (H) and $6s$-only double zeta for gold (Au). The mesh cut-off is 200 Ry and we consider 500 real and 80 complex energy points for integrating the Green's function. Calculations were also performed using double zeta $6s$ and single zeta $5d$ and $6p$ orbitals for Au

in order to investigate the effect of these extra orbitals on the transport properties of the system. Results for calculations using both basis sets are presented in this chapter, with the 6s-only basis set used unless otherwise indicated in the legend of the relevant figure. For geometry optimisations and total energy calculations, the 5d6s6p basis set is used, as the 6s-only basis set gives incorrect lattice constants for gold. In calculating the I-V curves, the potential bias is always incremented in steps of 0.1V.

Five layers of gold atoms are included with the molecule to form the scattering region. This allows the potential and the charge density to converge to their bulk values. The shape of the unit cell and the ordering of the layers is chosen so that the end layers match up properly as SIESTA uses periodic boundary conditions in the transport direction to solve the Poisson equation. Each layer contains nine gold atoms. The size and shape of the unit cells of the lead in the directions perpendicular to the transport is chosen so that the gold atoms fill the unit cell. When the periodic boundary conditions are applied, this forms a surface in these directions. The advantage of this over forming a nanowire where there is a layer of vacuum in the unit cell is that it prevents the appearance of artificial band gaps due to quantum confinement effects.

6.2   Benzenedithiol

The first system which we applied this correction to was 1,4-benzenedithiol (1,4-BDT) on the gold fcc (111) surface. This is the same molecule that was investigated using the tight-binding method in chapter 5.

We consider a variety of anchoring geometries for the sulphur atoms, including the hollow site, the top site, the bridge site, (see figure 6.1), as well as asymmetric coupling where the sulphur atoms are attached to an adatom on one side and to the hollow site on the other. We also examine the effect of altering the angle which the molecule makes with the metal surface, and of varying the distance between the sulphur atom and the surface (i.e. varying the strength of the coupling between the molecule and the metal). Finally, we investigate the effect of leaving the hydrogen atoms attached to the sulphur atoms in the thiol group when the molecule is attached to the metal surface.

The actual contact geometry present in the experiments is unknown. Some electronic structure calculations indicate that the lowest energy configuration for the molecule attached to the surface occurs when the sulphur atom attaches to the hol-
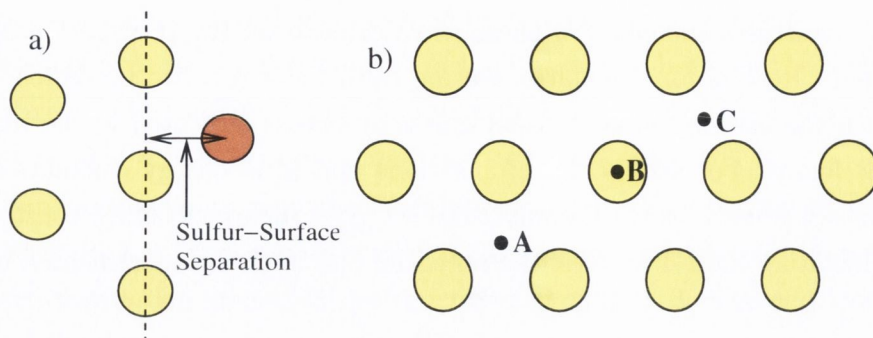
Figure 6.1: (a) The "sulphur-surface separation" is the separation between the sulphur atom and the plane of the gold surface. (b) Different possible anchoring sites of the sulphur atom (black dots) on the Au fcc (111) surface. **A** is the hollow site, **B** is the top site, and **C** is the bridge site. Colour code: Au atoms=yellow, S atoms=brown.

low site, whereas other calculations suggest that the bridge site configuration has a lower energy [115]. Recent X-ray standing wave measurements suggest that molecules in monolayers prefer to attach to adatoms on the metal surface [116]. Additionally, breaking junction experiments involve placing the molecule-metal interface under strain, and so the preferred anchoring geometry at equilibrium would not necessarily be the one present in the experiments. Hence, it is important to explore several different possible configurations in order to complete a thorough analysis of this system.

The orbital resolved density of states (DOS) for the isolated molecule is shown in figure 6.2, calculated with both regular LDA and with ASIC. Note how the ASIC lowers the energy of the occupied orbitals by about 4 eV, thus opening up the HOMO-LUMO gap. The highest occupied molecular orbital (HOMO, ϵ_{HOMO}^{KS}) is moved from -4.69 eV to -8.19 eV. Generally speaking, the ϵ_{HOMO}^{KS} obtained from ASIC tends to match the experimental values for the ionisation potentials very well for organic molecules such as BDT. For example, ASIC places ϵ_{HOMO}^{KS} for 1,2-BDT (a different isomer from the one used in these calculations) at 8.47 eV to compare with the LDA value of 4.89 eV and the experimental ionisation potential ~8.5 eV [117].

From figure 6.2, it can be seen that the π orbitals on the sulphur and carbon atoms are the ones which are closest to the Fermi level. From the local DOS plots shown in figure 6.3, it can be seen that these states are delocalised across the entire molecule, particularly the HOMO in panel (b), due to strong hybridisation between the carbon and sulphur orbitals. Therefore, these states would be expected to conduct strongly when bias is applied.
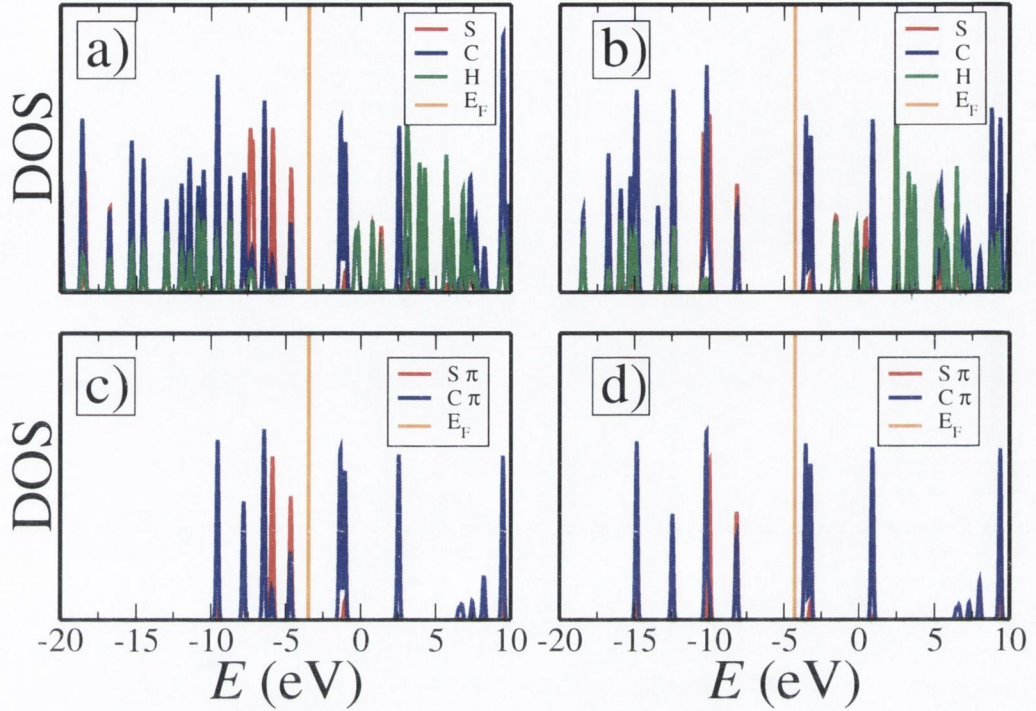
Figure 6.2: Orbital resolved DOS for the isolated BDT molecule. The left plots correspond
to LDA and the right ones to ASIC. The upper panels ((a) and (b)) are the
DOS of all of the orbitals on the molecule for each atomic species. The lower
panels are the DOS of the S and C π orbitals ((c) and (d)), which are the
orbitals closest to the Fermi level and thus are the orbitals involved in low bias
transport. The orange vertical lines labelled E_F separate the highest occupied
and lowest unoccupied orbitals of the molecule.

In order to calculate its transport properties, the molecule was first placed be-
tween two gold surfaces with the sulphur atom attached to the gold hollow site
between three surface atoms, as shown in figure 6.4. The distance of the sulphur
atom from the gold surface is optimised to a value of 1.9Å, which corresponds to
a distance of 2.53Å between the sulphur atoms and the nearest gold atoms on the
surface. This is in agreement with the results of previous calculations [65, 118].

The local DOS for the BDT molecule attached to the gold hollow site are shown
in figure 6.5. Panel (a) shows the HOMO, panel (b) shows the LUMO, and panel
(c) shows the level above the LUMO. Both states are derived from the molecular
π orbitals which are delocalised across the molecule, although the LUMO state is
somewhat more localised over the sulphur atoms. The peaks in the transmission
coefficients on each side of E_F in figure 6.6 correspond to the states shown in panels
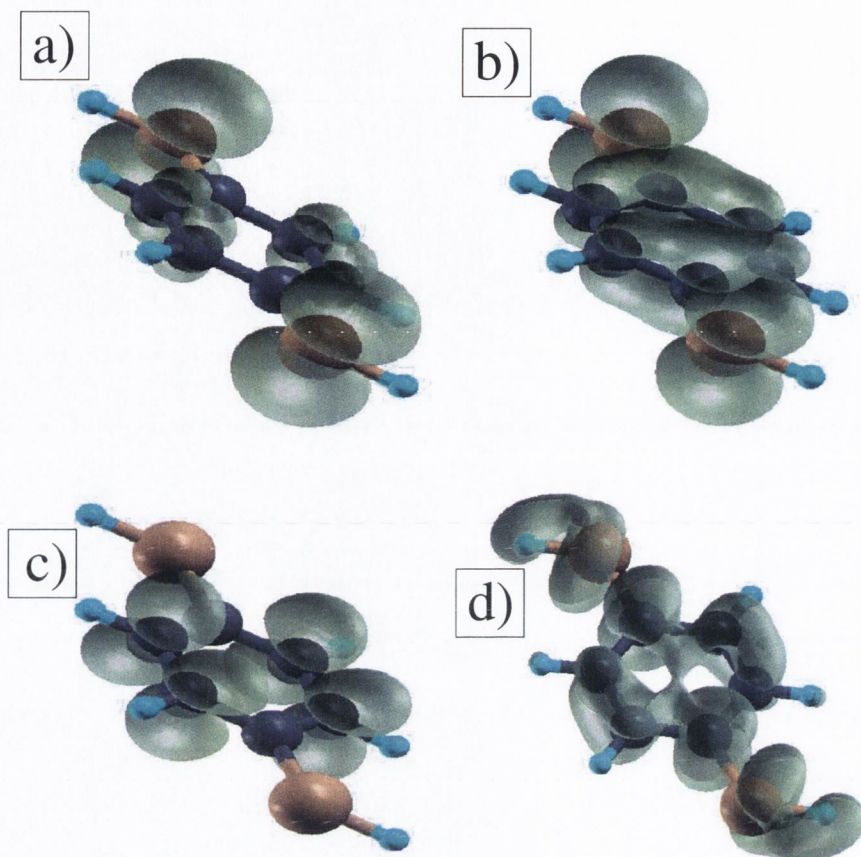(a) and (c).

Figure 6.3: Local density of states (molecular orbital isosurface) for the BDT molecule, calculated with LDA. The LDOS for the level below the HOMO and the HOMO are shown in panels (a) and (b), and the LDOS of the LUMO and the level above the LUMO are shown in panels (c) and (d). Note how the orbitals are delocalised across all of the sulphur and carbon atoms, except in the case of the LUMO, which is somewhat restricted to the carbon atoms.

The orbital resolved DOS, transmission coefficients and *I-V* curves for this configuration are presented in figure 6.6 for both LDA and ASIC. From the DOS (panels (a) and (b)) it is clear that the effect of ASIC is that of shifting the occupied orbitals downwards relative to E_F of the gold. The HOMO-LUMO gap is considerably larger than that of the LDA, and most importantly in the case of ASIC there is little DOS originating from the molecule at E_F. This has profound effects over the electron transmission. The LDA peaks of the transmission coefficients $T(E)$ arising from occupied orbitals are shifted downwards in energy and away from E_F. In contrast to LDA (figure 6.6(c)), where $T(E_F)$ is dominated by the resonance corresponding to ϵ_{HOMO}, the ASIC transmission (figure 6.6(d)) is through the BDT HOMO-LUMO
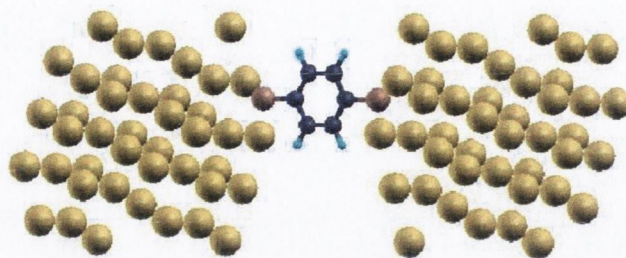
Figure 6.4: BDT molecule attached to the hollow site of the Au (111) surface. The sulphur-surface distance is 1.9Å. Colour code: Au=yellow, C=black, S=brown, H=blue.
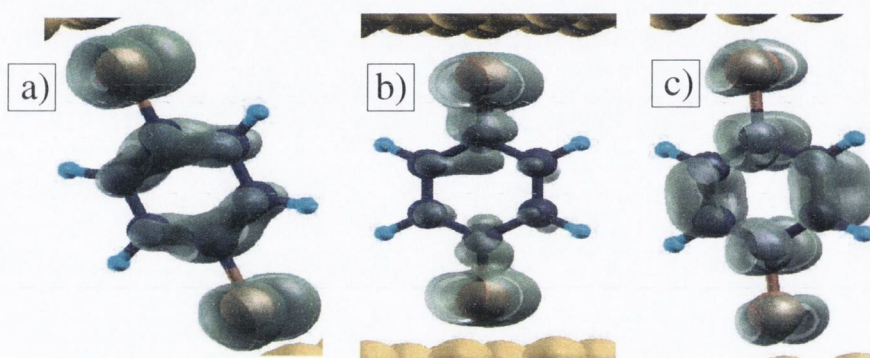

Figure 6.5: Local DOS (molecular orbital isosurface) for the BDT molecule attached to gold, calculated with LDA. The HOMO is in (a), the LUMO is in (b), and the LUMO+1 is in (c). Note how the orbitals are delocalised across all of the sulphur and carbon atoms. Colour code: Au=yellow, C=black, S=brown, H=blue.

gap. The current at this energy is thus due to tunnelling, which results in a drastic reduction of the low-bias current when going from LDA to ASIC (figure 6.6(e)). The ASIC-calculated conductance at zero bias is now about $0.06G_0$ ($G_0 = 2e^2/h$), compared to $0.23G_0$ of LDA. A conductance of $0.06G_0$ is much closer to the value of $0.011G_0$ obtained by Xiao et. al. [26] and is actually lower than values 0.09-$0.14G_0$ obtained by Tsutsui et. al. [24].

The basis set on the gold atoms was then changed to include $5d$ and $6p$ orbitals. The orbital resolved DOS, transmission coefficients and *I-V* curves are presented in figure 6.7 for both LDA and ASIC for this new basis set. As can be seen, the alteration of the basis set does not have a large effect on the electronic transport, particularly at low bias. As can be seen from figure 6.7e, the *I-V* curves calculated with the $6s$-only basis set on the gold are approximately the same as those calculated with the $5d6s6p$ basis up to about 1V for both LDA and ASIC cases. The zero-bias
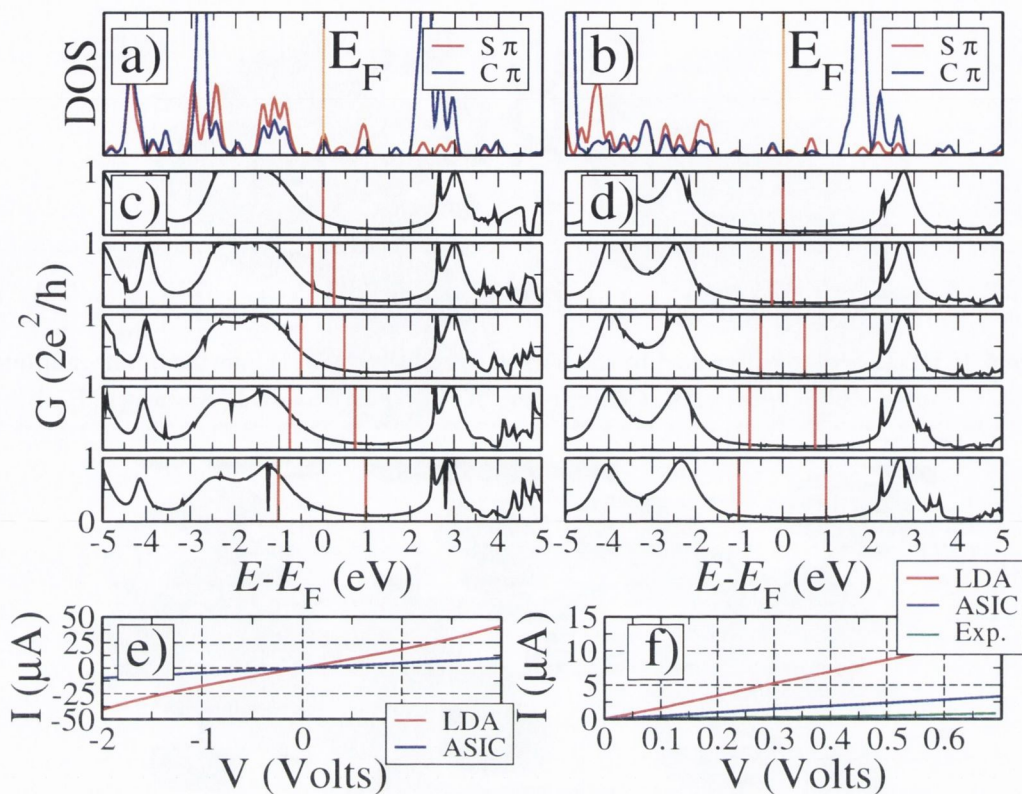
Figure 6.6: Transport properties of a BDT molecule attached to the gold (111) hollow
site. The left plots correspond to LDA and the right ones to ASIC. The upper
panels are the DOS of the S and C π orbitals ((a) and (b)), the middle are the
transmission coefficients as a function of energy for various bias ((c) and (d))
and the lower are the I-V curves. Figure (f) is a zoom of (e) and compares our
results with experiments from reference [26]. The vertical lines in (c) and (d)
mark the bias window.

conductances, from the transmission plots in panels (c) and (d) of figure 6.7, are very
similar to those for the 6s-only basis with values of $0.21G_0$ for LDA and $0.06G_0$ for
ASIC. This demonstrates that the 6s-only basis gives reliable results for electronic
transport properties at low bias.

Next, the transport properties of the system are calculated for different sulphur-
surface separations, as well as for different angles of the molecule with respect to the
direction of the transport. The S atoms remain attached to the hollow site on both
sides, while the sulphur-surface separation is increased. Calculations are performed
for distances of 1.8Å, 2.1Å and 2.5Å, and the resulting I-V curves are presented in
figure 6.9(a). The results for the molecule angled at 30° with respect to the direction
of transport (figure 6.8) but still connected to the gold hollow site on both sides are
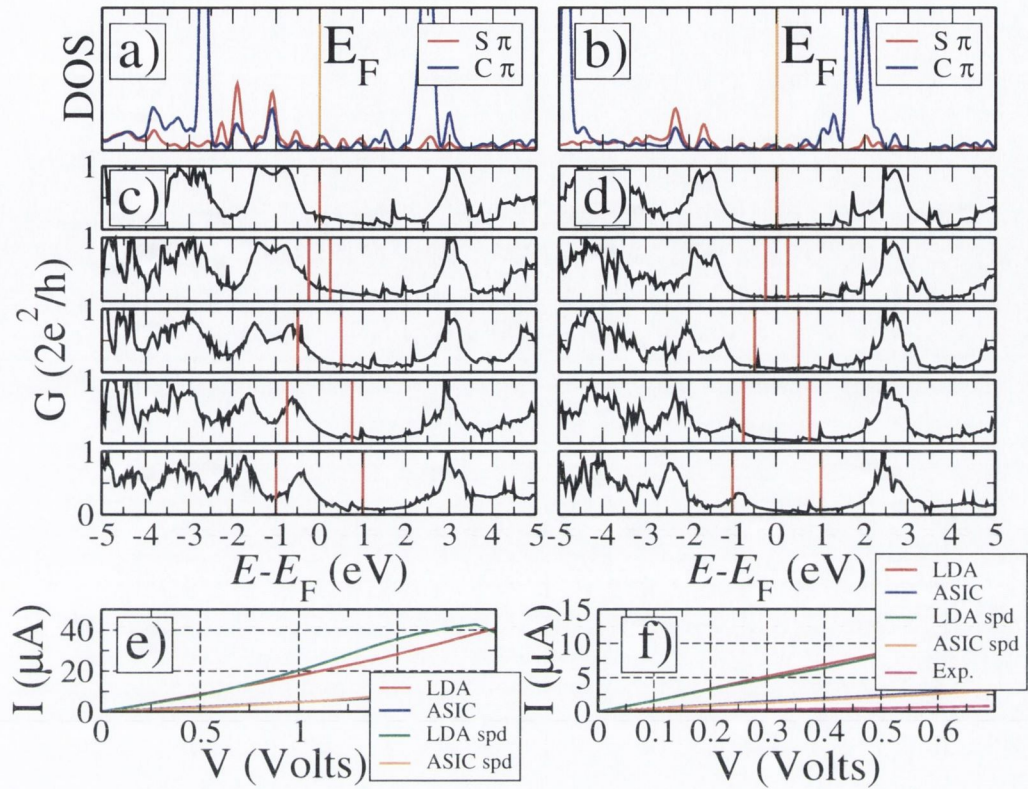
Figure 6.7: Transport properties of a BDT molecule attached to the gold (111) hollow site for the $5d6s6p$ Au basis. The left plots correspond to LDA and the right ones to ASIC. The upper panels are the DOS of the S and C π orbitals ((a) and (b)) and the middle are the transmission coefficients as a function of energy for various bias ((c) and (d)). The lower ((e) and (f)) are the I-V curves, including a comparison with the results shown in figure 6.6 for the $6s$-only basis set on the gold atoms. Figure (f) is a zoom of (e) and compares our results with experiments from reference [26]. The vertical lines in (c) and (d) mark the bias window.

presented in figure 6.9(b). The I-V curves for this system remain reasonably stable with these changes to the contact geometry. This is especially true in the case of the current calculated with ASIC in the bias range investigated here as shown in figure 6.9, where neither small changes to the sulphur-surface separation (panel (a)) nor changes in the contact angle (panel (b)) have a large effect on the current.

This stability of the current as a function of anchoring geometry calculated with ASIC is interesting since, experimentally, stable conductance histograms were observed when pulling on the molecule with an STM tip [26]. Also, note that the magnitude of the conductance may actually increase with sulphur-surface separation, especially at low bias. The zero bias conductance values calculated with LDA
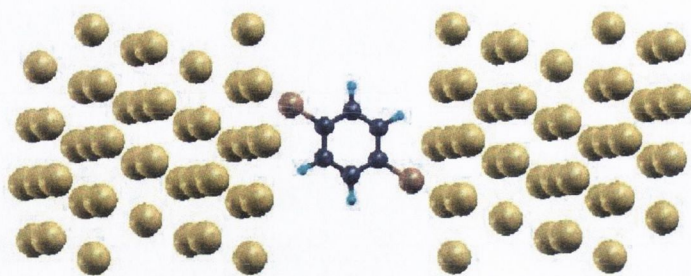
Figure 6.8: BDT molecule attached to the hollow site of the Au (111) surface at an angle of 30° to the direction of transport. The sulphur-surface distance is 1.9Å. Colour code: Au=yellow, C=black, S=brown, H=blue.
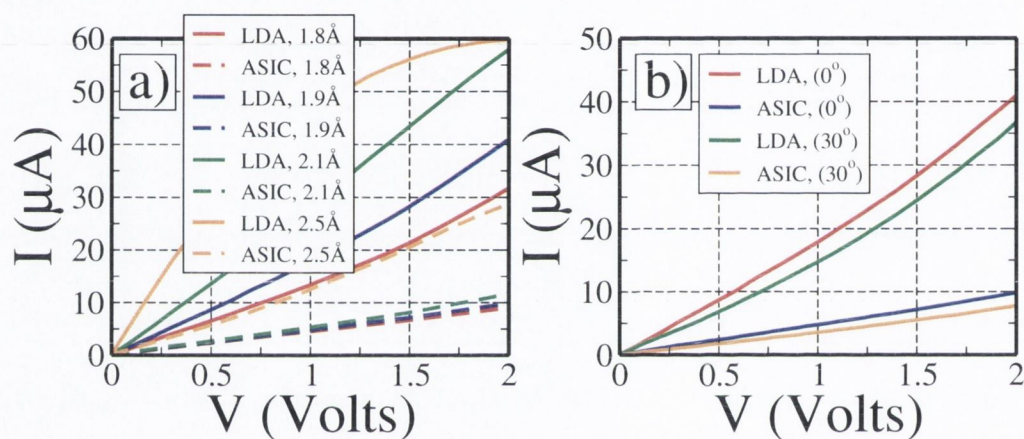

Figure 6.9: *I-V* curves for BDT attached to gold contacts at (a) different sulphur-surface separations and (b) different angles. Note how little the *I-V* for ASIC changes with small change in distance from the equilibrium value of 1.9Å.

are $0.16G_0$, $0.23G_0$, $0.32G_0$, and $0.77G_0$ for sulphur-surface separations of 1.8Å, 1.9Å, 2.1Å and 2.5Å respectively. The values for the same separations calculated with ASIC are $0.05G_0$, $0.06G_0$, $0.07G_0$, and $0.14G_0$. While counterintuitive, this is consistent with previous results [65, 67], and is due to the realignment of the HOMO of the molecule so that it gets closer to the gold E_F. This can be seen in the plot of the zero-bias transmission coefficients for different sulphur-surface separations in figure 6.10. As the distance between the molecule and the gold surface is increased, the transmission peaks (which correspond to molecular orbitals) become narrower as expected due to the weakening of the coupling. However, the charge transfer between the molecule and the metal is also affected, so that there are now more electrons on the actual molecule. This extra charge increases the energy of the molecular orbitals, so that the HOMO moves closer to E_F. This upward shift of the transmission peaks

closer to E_F compensates for the weaker coupling, increasing the low bias conductance. This effect can also be seen when the molecule is attached to adatoms on the metal surface, as shown below in figures 6.13, 6.15, 6.16 and 6.18. Because of this realignment of the HOMO, efforts made previously to explain the discrepancy between theory and experiment by adjusting the contact geometry to reduce the metal-molecule coupling may be misleading if the band alignment is not calculated self-consistently [63].
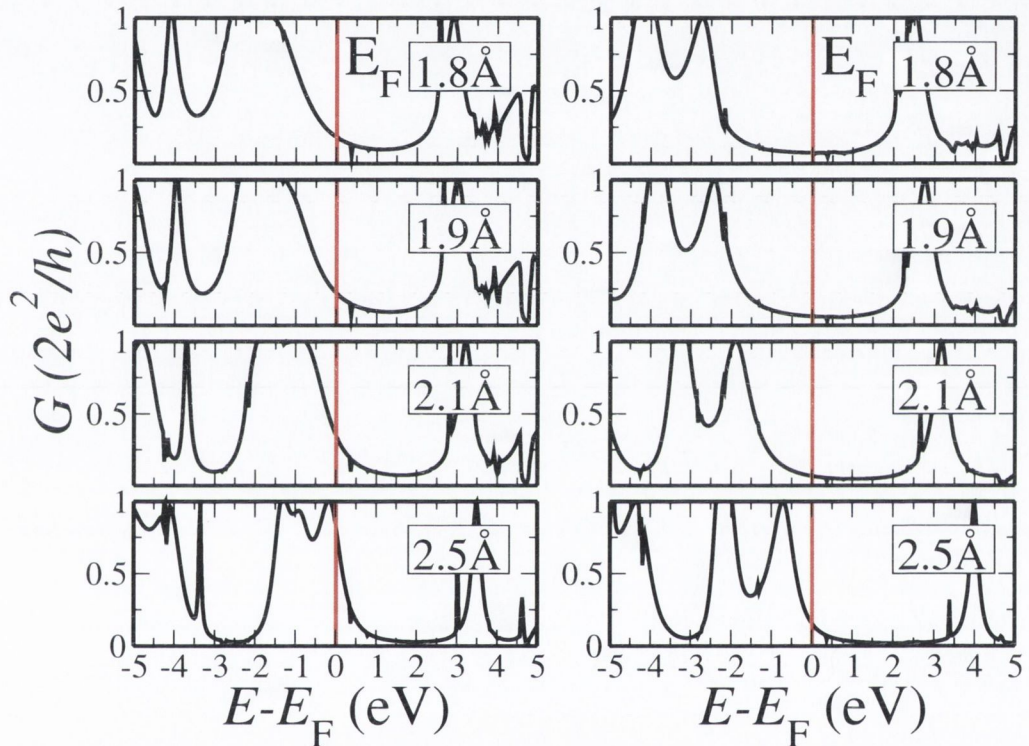

Figure 6.10: Transmission coefficients for BDT attached to gold contacts at different sulphur-surface separations. The left plots correspond to LDA and the right ones to ASIC. Note how the peaks narrow and how the HOMO peak moves closer to the gold E_F as the sulphur-surface separation is increased. This realignment of the HOMO of the molecule has the effect of compensating for the weakening of the coupling, even producing counterintuitive results such as an increase in the low bias conductance with increased sulphur-surface separation.

A second contact geometry investigated is that where the sulphur atom is connected to the bridge site of the gold fcc (111) surface, as shown in figure 6.11. The position of the bridge site on the fcc (111) surface is shown in figure 6.1(b). Some DFT total-energy calculations suggest that this configuration, with a sulphur-surface separation of 2.09Å, has a lower energy than that where the sulphur is joined to the
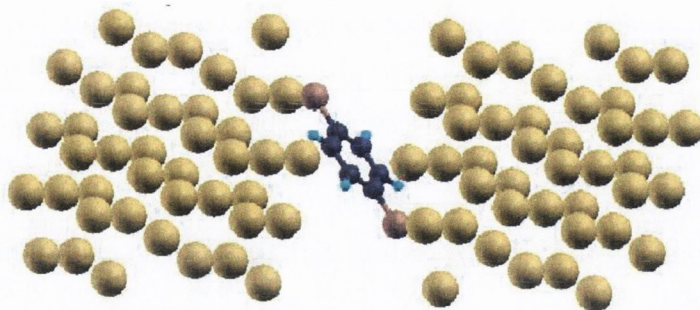
Figure 6.11: BDT molecule attached to the bridge site of the Au (111) surface. The sulphur-surface distance is 2.09Å. Colour code: Au=yellow, C=black, S=brown, H=blue.

hollow site [115]. Therefore, it is important to explore the effect of this configuration on the transport, although the anchoring geometry which would actually be present in a device under strain, such as would be the case in a breaking junction, is unknown. Figure 6.13(a) shows a comparison between I-V curves calculated for the molecule anchored to the bridge site and to the hollow site. The zero bias conductance for the bridge site is calculated to be $0.1G_0$ with LDA, which is lower than the value of $0.23G_0$ calculated for the hollow site. The low bias current for the bridge site is lower than that for the hollow site with LDA, as shown in the I-V curve in figure 6.13(a). For the bridge site, ASIC has the effect opening up the HOMO-LUMO gap, hence suppressing the current through the molecule in a manner similar to what happens in the case of the hollow site. The zero bias conductance for the bridge site is calculated to be $0.06G_0$ using ASIC, the same the hollow site. Hence, whether the molecule is anchored to the hollow site or the bridge site makes relatively little difference to the ASIC-calculated low-bias transport properties.

The transport properties of the molecule connected to the Au top site as shown in figure 6.12 are the next to be investigated. The position of the top site on the fcc (111) surface is shown in figure 6.1(b), and the sulphur-surface separation is set to 2.39Å. Figure 6.13(b) shows a comparison between the I-V curves calculated for when the molecule is connected to the top site on the gold surface and those calculated for the hollow site. The LDA zero-bias conductance is calculated to be $0.65G_0$, which is somewhat larger than the value of $0.23G_0$ calculated for the hollow site. In contrast, the ASIC conductance is calculated to be $0.12G_0$, showing a reduction of a factor of four compared to the LDA result. As in the situation where the sulphur-surface distance is increased when the bond was to the hollow site, the increase in the conductance for the top site anchoring geometry is due to a realignment of the
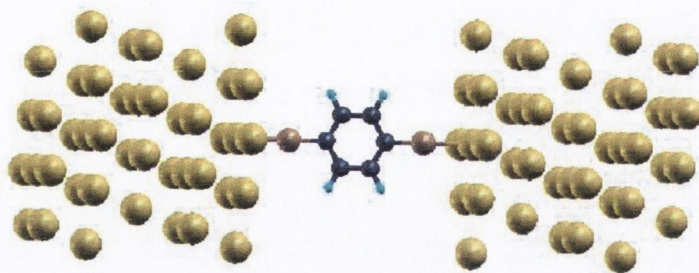
Figure 6.12: BDT molecule attached to the top site of the Au (111) surface. The sulphur-
surface distance is 2.39Å. Colour code: Au=yellow, C=black, S=brown,
H=blue.

HOMO of the molecule, which is now closer to the gold E_F. Hence, although the coupling between the molecule and the surface is weaker for the top than for the hollow or bridge sites, the current is larger, at least in the bias region investigated here.
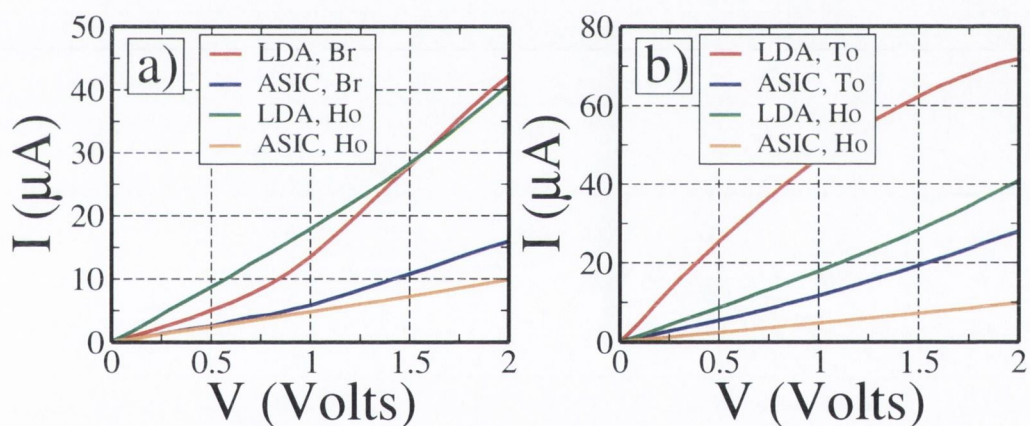

Figure 6.13: *I-V* curves for BDT attached to gold contacts with (a) the sulphur atoms attached to the gold bridge site and (b) the sulphur atoms attached to the gold top site.

The effect of an asymmetric contact geometry was investigated by attaching one of the S atoms to a gold adatom (figure 6.14) and the other to the hollow site. The usual sulphur-surface separations are the equilibrium values of 1.9Å and 2.39Å respectively for the hollow and top sites. Recent X-ray standing wave experiments [116] demonstrate that S atoms in thiol groups on gold may actually join more favourably to adatoms.

The orbital resolved DOS, transmission coefficients and *I-V* curves for this system are presented in figure 6.15 for both LDA and ASIC. This configuration shows the
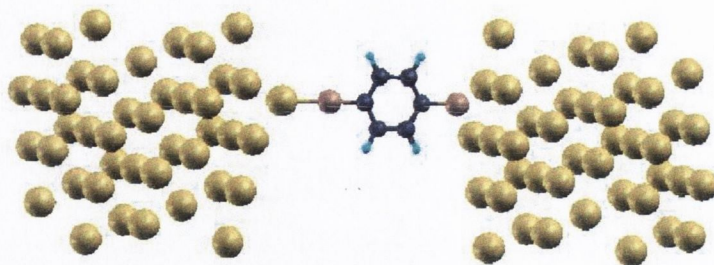
Figure 6.14: BDT molecule attached asymmetrically to the Au (111) surface. BDT is attached on one side to the hollow site with a sulphur-surface distance of 1.9Å as before, and on the other side to a single gold adatom. Colour code: Au=yellow, C=black, S=brown, H=blue.

largest difference between the conductance calculated with LDA with respect to that calculated with ASIC. The LDA-only conductance is $0.32G_0$, whereas when ASIC is applied the conductance drops by one order of magnitude to $0.03G_0$. Because of the weaker interaction between the π orbitals on the molecule and the gold in this configuration, the molecular orbitals in the DOS (figure 6.15a and figure 6.15b) and hence the peaks in the transmission coefficients (figure 6.15c and figure 6.15d) are narrower than those for the case where both of the sulphur atoms are attached to the hollow site. These narrower levels are closer to E_F, which results in the relatively high zero bias conductance. An effect similar to this is observed every time the strength of the coupling between the sulphur atoms and the metal is adjusted: strengthening the coupling causes the HOMO to broaden and shift downwards away from E_F; whereas weakening the coupling causes the HOMO to narrow and shift closer to E_F. This motion of the HOMO is usually large enough to compensate for the change in coupling strength at low bias. In some cases, it can produce the counterintuitive results seen in figure 6.9(a) and figure 6.10, where reducing the coupling strength actually causes an increase in the low bias conductance.

As in the case of the hollow site anchoring configuration, the basis set for the gold was changed to include the $5d$ and $6p$ orbitals. The orbital resolved DOS, transmission coefficients and I-V curves are presented in figure 6.16 for both LDA and ASIC for this new basis set. Similar to the case of the hollow site, the I-V curves for the two basis sets are very similar up to a bias of about 1V. The LDA-only conductance for this basis is $0.47G_0$, and when ASIC is applied the conductance drops to $0.05G_0$. This is a drop of about one order of magnitude, similar to that obtained with the 6s-only basis.

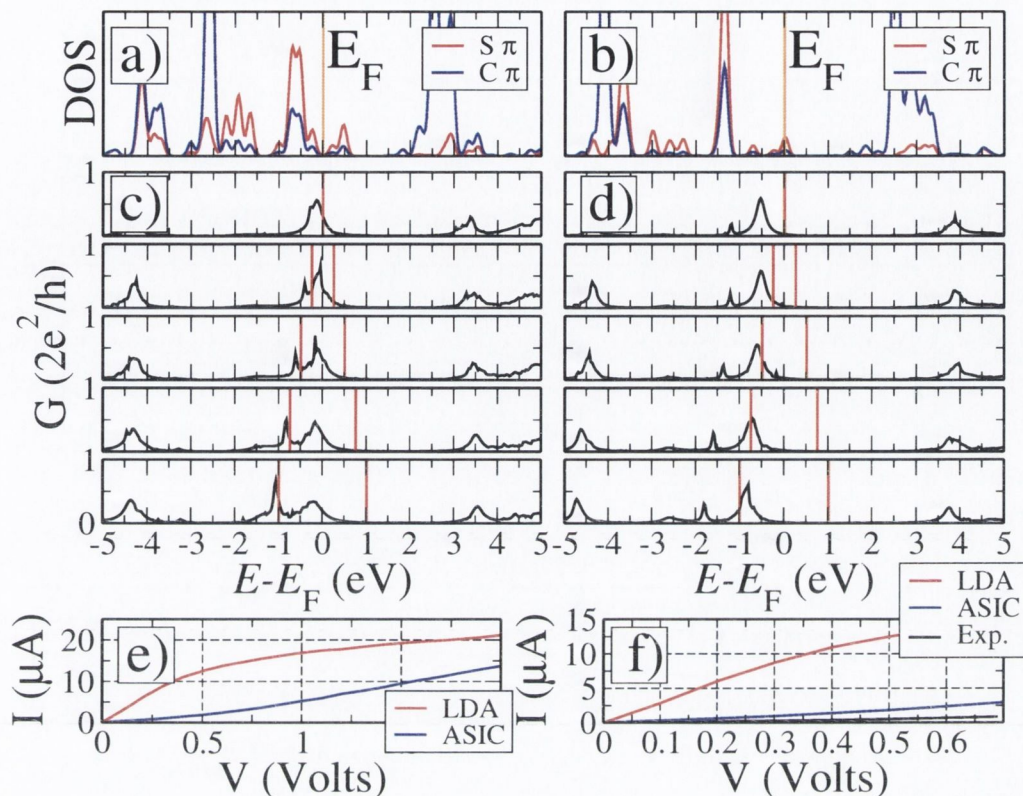Figure 6.17 shows the BDT molecule attached to an adatom at both surfaces.

Figure 6.15: Transport properties of a BDT molecule attached asymmetrically to the gold (111) surface. The left plots correspond to LDA and the right ones to ASIC. The upper panels are the DOS of the S and C π orbitals ((a) and (b)), the middle are the transmission coefficients as a function of energy for various bias ((c) and (d)) and the lower are the I-V curves. Figure (f) is a zoom of (e) and compares our results with experiments from reference [26]. The vertical lines in (c) and (d) mark the bias window.

In this case, the coupling is very weak, and the transmission coefficients have sharp peaks, as shown in figure 6.18. The LDA-only zero bias conductance calculated with the Au $5d6s6p$ basis is $0.43G_0$, and when ASIC is applied the conductance drops to $0.19G_0$. The HOMO transmission peak is pinned at the E_F of the system, similar to the weak coupling case discussed in chapter 5 using the tight-binding method [74]. In this situation, the derivative discontinuity, if present in the XC functional used, would be expected to have a significant effect on the transport properties of the molecule. Unfortunately, this discontinuity is not present in ASIC and so the conductance remains relatively large.

The final configuration to be studied is again for hollow site anchoring, but now the hydrogen atoms which are attached to the sulphur atoms in the thiol groups do
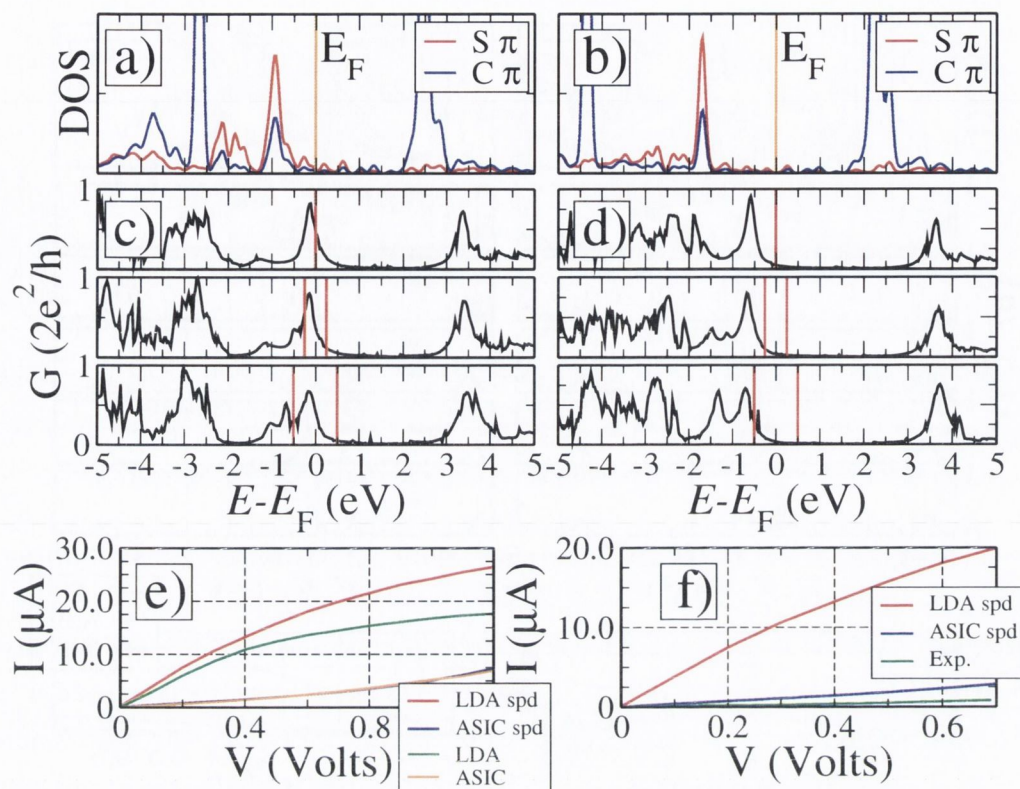
Figure 6.16: Transport properties of a BDT molecule attached asymmetrically to the gold (111) surface calculated with a $5d6s6p$ basis set for gold. The left plots correspond to LDA and the right ones to ASIC. The upper panels are the DOS of the S and C π orbitals ((a) and (b)), the middle are the transmission coefficients as a function of energy for various bias ((c) and (d)) and the lower are the I-V curves. Figure (f) is a zoom of (e) and compares our results with experiments from reference [26]. The vertical lines in (c) and (d) mark the bias window.
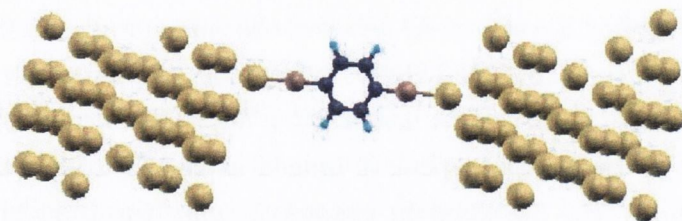

Figure 6.17: BDT molecule attached to adatoms on both of the Au (111) surfaces. Colour code: Au=yellow, C=black, S=brown, H=blue.

not dissociate. This set-up is shown in figure 6.19. The total energy for this system is calculated with DFT-LDA to be 1.465eV higher than for the case where the H
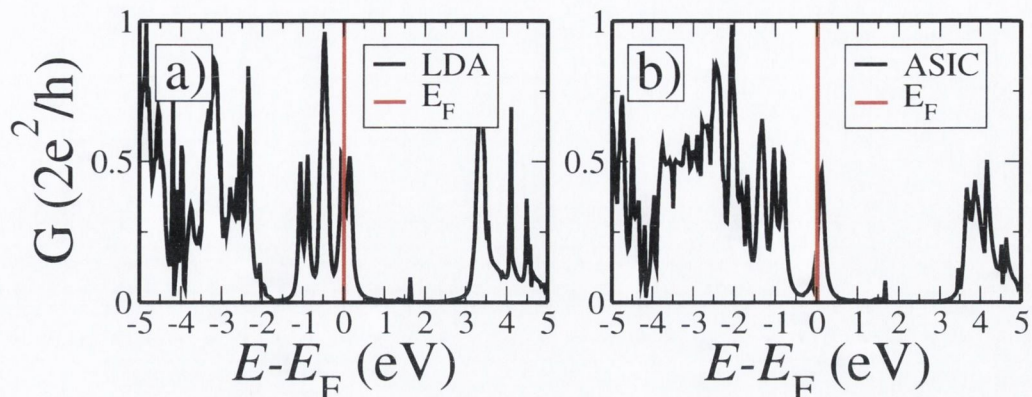
Figure 6.18: Transmission coefficients for a BDT molecule attached to adatoms on the gold
(111) surface with a $5d6s6p$ basis set for gold. Note how the HOMO is pinned
at the Fermi level.

atoms dissociate and form H_2. However, there may be an energy barrier to their
dissociation which may cause them to remain attached to the molecule, which makes
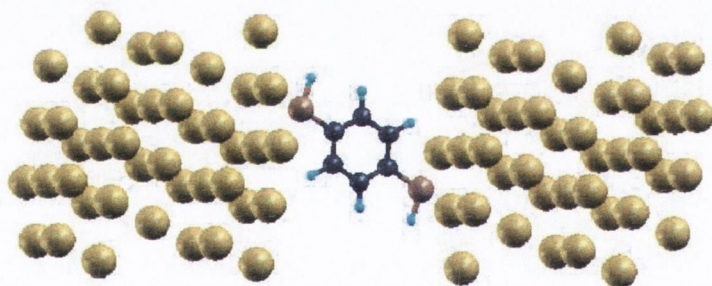investigating their effect important.

Figure 6.19: BDT molecule with hydrogen atoms still attached to the sulphur atoms and
anchored to the hollow site. The sulphur-surface distance is 1.9Å. Colour
code: Au=yellow, C=black, S=brown, H=blue.

The orbital resolved DOS, transmission coefficients and I-V curves for this system
are shown in figure 6.20. As can be seen from the DOS in panels (a) and (b) and
the transmission coefficients in panels (c) and (d) of figure 6.20, the transport is
now through the LUMO of the system, the energy of which is lowered slightly by
ASIC. Hence, the conductance of $0.09G_0$ calculated using ASIC is higher than that
of $0.06G_0$ calculated with LDA. However, this shift of the unoccupied orbitals is an
artifact of the atomic nature of ASIC, as unoccupied states have no self-interaction
error.

In conclusion, for the molecular device consisting of benzenedithiol attached to
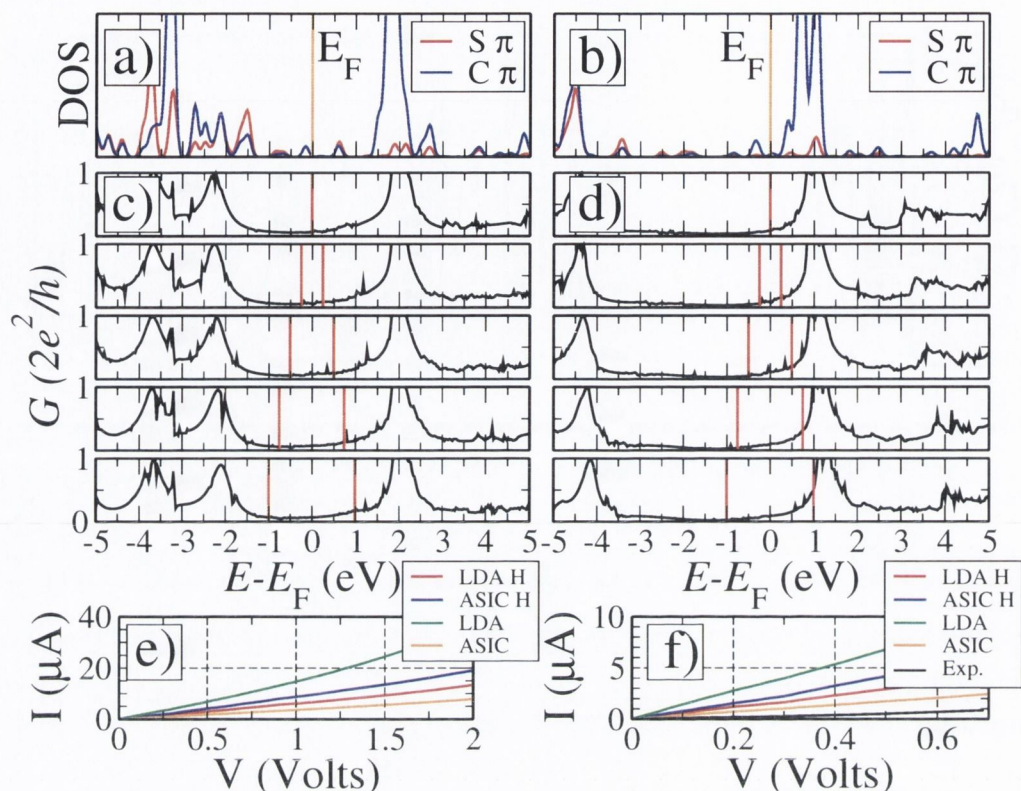
Figure 6.20: Transport properties of a BDT molecule for the configuration shown in figure 6.19. The left plots correspond to LDA and the right ones to ASIC. The upper panels are the DOS of the S and C π orbitals ((a) and (b)), the middle are the transmission coefficients as a function of energy for various bias ((c) and (d)) and the lower are the I-V curves for the system both with and without the hydrogen atoms attached to the sulphur. Figure (f) is a zoom of (e) and compares our results with experiments from reference [26]. The vertical lines in (c) and (d) mark the bias window.

gold, ASIC tends to reduce the low bias conductance by a factor of about four for the majority of the anchoring geometries investigated. The zero bias conductances for the different anchoring geometries calculated with both LDA only and with ASIC are summarised in table 6.1.

A comparison of the results calculated with SMEAGOL for both LDA and ASIC for BDT attached to the Au hollow site to various other theoretical and experimental results is shown in table 6.2. As shown, previous NEGF-DFT calculations in particular tend to give very high zero-bias conductances, whereas ASIC tends to lower the conductance, thus improving the agreement with experiment

Anchoring	d (Å)	G_{LDA} (G_0)	G_{ASIC} (G_0)
Ho	1.9	0.23	0.06
Ho	1.8	0.16	0.05
Ho	2.1	0.32	0.07
Ho	2.5	0.77	0.14
Ho (30°)	1.9	0.18	0.04
Br	2.09	0.11	0.06
Ad	2.39	0.11	0.10
Asy Ho	1.9/2.3	0.33	0.06
Ho/Ad	1.9/2.39	0.35	0.03

Table 6.1: Zero-bias conductance for different configurations of BDT on gold (111). The anchoring configurations investigated are: hollow site (Ho), bridge site (Br), Au adatom (Ad). Ho (30°) describes a hollow site with BDT at a 30° angle with respect to the transport direction, and the two last rows correspond to asymmetric anchoring to the two electrodes. d is the sulphur-surface distance.

Method	G (G_0)
Theory	
SMEAGOL LDA [76]	0.16, 0.23, 0.32, 0.77
SMEAGOL ASIC [76]	0.05, 0.06, 0.07, 0.14
TranSIESTA LDA [68]	0.36
TranSIESTA LDA [66]	0.47, 0.56, 0.79
CI [51]	10^{-3}
Experiment	
MCBJ [19]	10^{-5}
STM Break Junc. [26]	0.011
MCBJ [24]	0.004, 0.005, 0.011, 0.09, 0.14, 0.23
MCBJ [25]	0.011
Lith. Fab. Elec. [29]	0.1

Table 6.2: Zero-bias conductance for BDT attached to gold electrodes calculated or measured with a variety of different computational and experimental methods. Computational methods include NEGF combined with DFT (SMEAGOL [38, 76] and TranSIESTA [40, 66, 68]) and configuration interaction (CI) [51]. For the computational results listed, the molecule is connected to the hollow site, and a range of results for different sulphur-surface separations are shown where available. Experimental methods for manufacturing the molecular devices include mechanically controlled breaking junctions (MCBJ [19, 24, 25]), STM breaking junctions (STM break junc. [26]) and lithographic fabrication of the electrodes (Lith. Fab. Elec., [29]). In the MCBJ experiments performed by Tsutsui et. al. [24], a range of conductances were observed and are listed here.

6.3   Benzenedimethanethiol

The second system investigated is that of benzenedimethanethiol (BDMT) on the
fcc (111) gold surface. There are two different isomers for this molecule, as shown in
figure 6.21 and the electronic transport properties of both are investigated here. In
the first isomer, the sulphur atoms are in the plane of the benzene ring, and in the
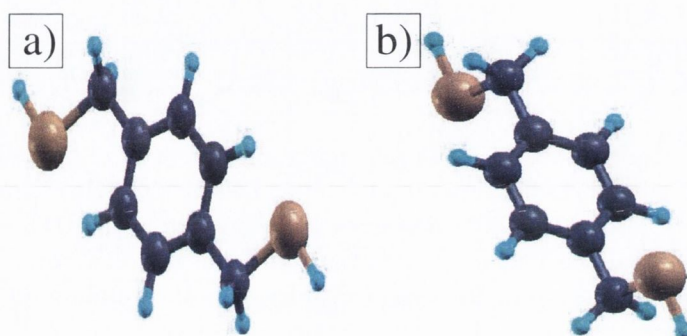second isomer they are out of the plane.

Figure 6.21: Two different isomers of the BDMT molecule.   Colour code: C=black,
S=brown, H=blue.

The DOS for first isomer of BDMT is shown in figure 6.22. The HOMO-LUMO
gap is somewhat larger than that of BDT. As for BDT, ASIC has the effect of lowering
the energy of the occupied orbitals, making this gap even larger. However, because of
the atomic nature of ASIC, it will also incorrectly affect unoccupied orbitals, reducing
their energy also. This can be seen in figure 6.22, where the LUMO calculated with
ASIC is noticeably closer to the Fermi level.

The local DOS for the first isomer of BDMT is shown in figure 6.23. The HOMO
(in panel (a)) is mainly localised on the sulphur atoms, whereas the LUMO (in panel
(b)) is mainly localised on the benzene ring. The π conjugation across the molecule
is broken by the extra methyl groups. Therefore, there are no states near the Fermi
level which are fully delocalised across the molecule in a way similar to that of BDT,
and so the conductance of this molecule at low bias is expected to be lower.

In order to calculate the electronic transport properties, the first BDMT isomer is
attached to the gold (111) hollow sites as shown in figure 6.24, with a sulphur-surface
separation of 1.9Å. The local DOS for the HOMO and the LUMO of this device are
shown in figure 6.25. As for the isolated molecule, the HOMO is mainly localised on
the sulphur atoms, whereas the LUMO is mainly localised on the benzene ring.

The orbital resolved DOS, transmission coefficients and I-V curves for this system
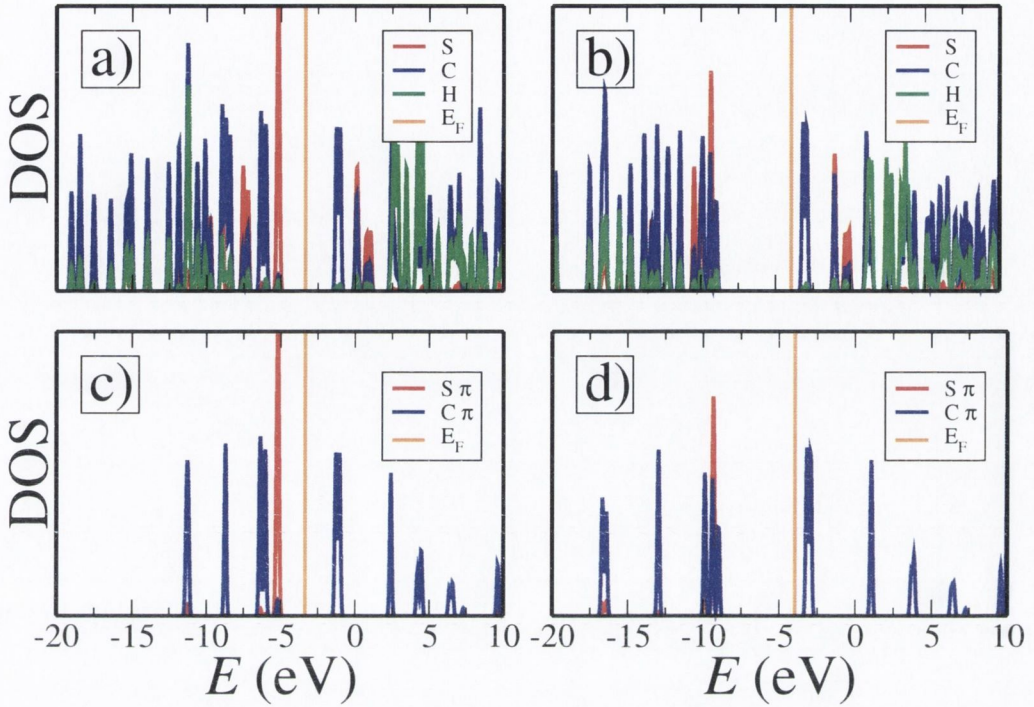
Figure 6.22: Orbital resolved DOS for the first isomer of the BDMT molecule. The left
plots correspond to LDA and the right ones to ASIC. The upper panels ((a)
and (b)) are the DOS of all of the orbitals on the molecule for each atomic
species. The lower panels are the DOS of the S and C π orbitals ((c) and
(d)), which are the orbitals closest to the Fermi level and thus are the orbitals
involved in low bias transport. The orange vertical lines labelled E_F separate
the highest occupied and lowest unoccupied orbitals of the molecule.

are presented in figure 6.26 for both LDA and ASIC. In this case however, as can
be seen from the DOS, the HOMO-LUMO gap is much larger than that for BDT.
Again, the ASIC has the effect of shifting the occupied orbitals downwards. The gap
between the resonances in the transmission due the HOMO and LUMO orbitals is
also much larger, with the resonances lying outside of the bias region investigated
in both cases. Therefore, although the size of the gap is increased with ASIC, the
actual transmission in the bias window does not change very much. The conductance
at zero bias is calculated to be $0.004G_0$ with ASIC, compared to $0.006G_0$ with LDA
only. Both of these values are an order of magnitude larger than the experimental
value of $0.0006G_0$ obtained by Xiao et. al. [26]. Hence, the I-V curves for LDA
with and without ASIC are quite similar, and are also an order of magnitude lower
than those for BDT. To see the difference in the I-V curves caused by ASIC, a much
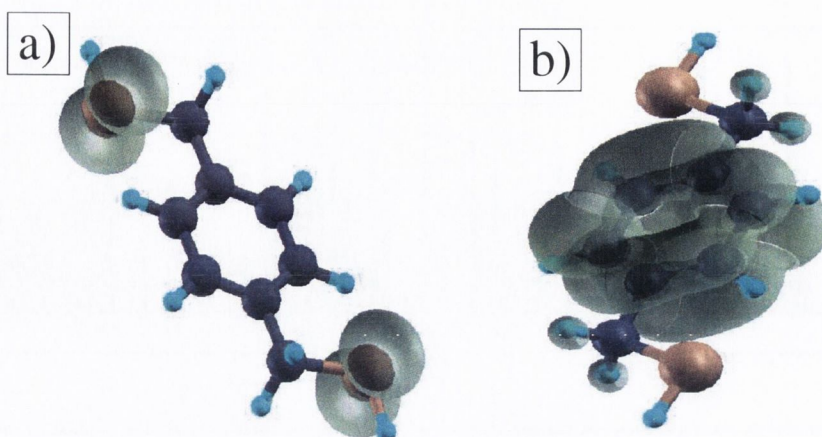higher bias needs to be applied.

Figure 6.23: Local DOS (molecular orbital isosurface) for first isomer of the BDMT
molecule, calculated with LDA. The LDOS for the HOMO and the LUMO
are shown in panels (a) and (b). Note how the HOMO is localised on the
sulphur atoms, whereas the LUMO is localised on the benzene ring. Colour
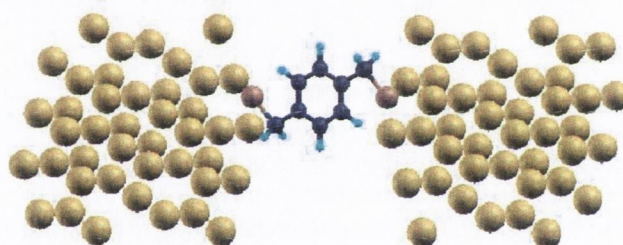code: C=black, S=brown, H=blue.

Figure 6.24: BDMT molecule attached to the hollow site of the Au (111) surface.
The sulphur-surface distance is 1.9Å. Colour code: Au=yellow, C=black,
S=brown, H=blue.

The properties of the second BDMT isomer (with the S atoms out of the benzene
plane) are also investigated. The DOS for second isomer of BDMT is shown in figure
6.27. The HOMO-LUMO gap in this case is similar to that of the first isomer, being
somewhat larger than that for BDT. Again, ASIC has the effect of lowering the
energy of the occupied orbitals, making this gap even larger.

The local DOS for the second isomer of BDMT is shown in figure 6.28. The
HOMO (panel (a)) is mainly distributed on the S atoms, whereas the LUMO (panel
(b)) is mainly distributed on the benzene ring. As for the first isomer, the π conjuga-
tion across the molecule is broken by the extra methyl groups, and so the conductance
of this molecule at low bias is expected to be low also.

In order to calculate the electronic transport properties of this second BDMT
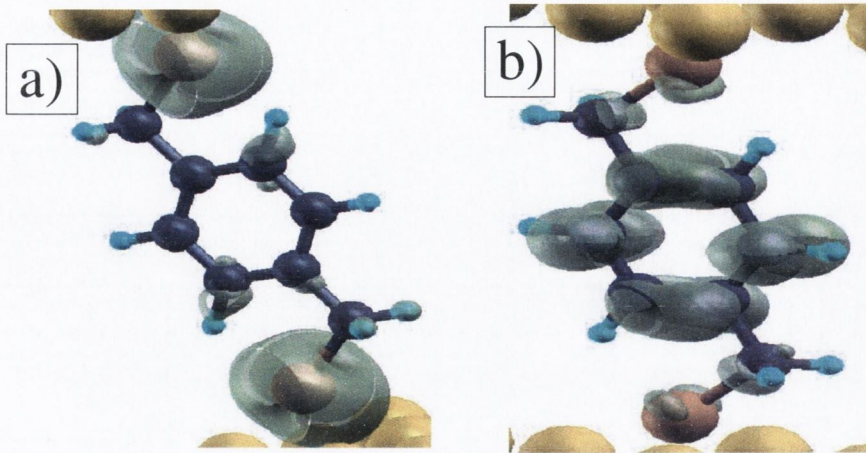
Figure 6.25: Local DOS (molecular orbital isosurface) for the Au/BDMT junction, calcu-
lated with LDA. The LDOS for the HOMO and the LUMO are shown in (a)
and (b) respectively. Note how the HOMO is localised on the suphur atoms,
whereas the LUMO is distributed over the benzene ring, similar to the case of
the isolated molecule. Colour code: Au=yellow, C=black, S=brown, H=blue.

isomer, the sulphur atoms are attached to the gold (111) hollow sites as shown in
figure 6.29 (sulphur-surface separation is 1.9Å). The local DOS for the HOMO and
the LUMO of this device are shown in figure 6.30. As for the isolated molecule, the
HOMO is mainly localised on the S atoms, whereas the LUMO is mainly distributed
over the benzene ring.

The orbital resolved DOS, transmission coefficients and I-V curves for this second
isomer are presented in figure 6.31 for both LDA and ASIC. The calculated current
for this isomer is larger by about a factor of three than that of the other isomer, as
shown in panel (e). The LDA conductance at zero bias is now $0.015G_0$, compared to
a value of $0.013G_0$ when ASIC is applied. As for the first isomer, the fact that ASIC
has little effect on the I-V curve is due to the large HOMO-LUMO gap.

A comparison of the results calculated with SMEAGOL for both LDA and ASIC
for BDMT attached to the Au hollow site to various other theoretical and experi-
mental results is shown in table 6.3. In contrast to the results for BDT, ASIC does
not appear to improve the agreement with experiment for either isomer of BDMT.
The large HOMO-LUMO gap means that adjusting the position of the resonances in
$T(E)$ does not have a large effect on the conductance around E_{F}. The most signifi-
cant source of error for this system probably lies in calculating the matrix elements
between the gold surface and the sulphur atom. This would not be improved by
ASIC, and more sophisticated approaches are required. In addition, here we have in-
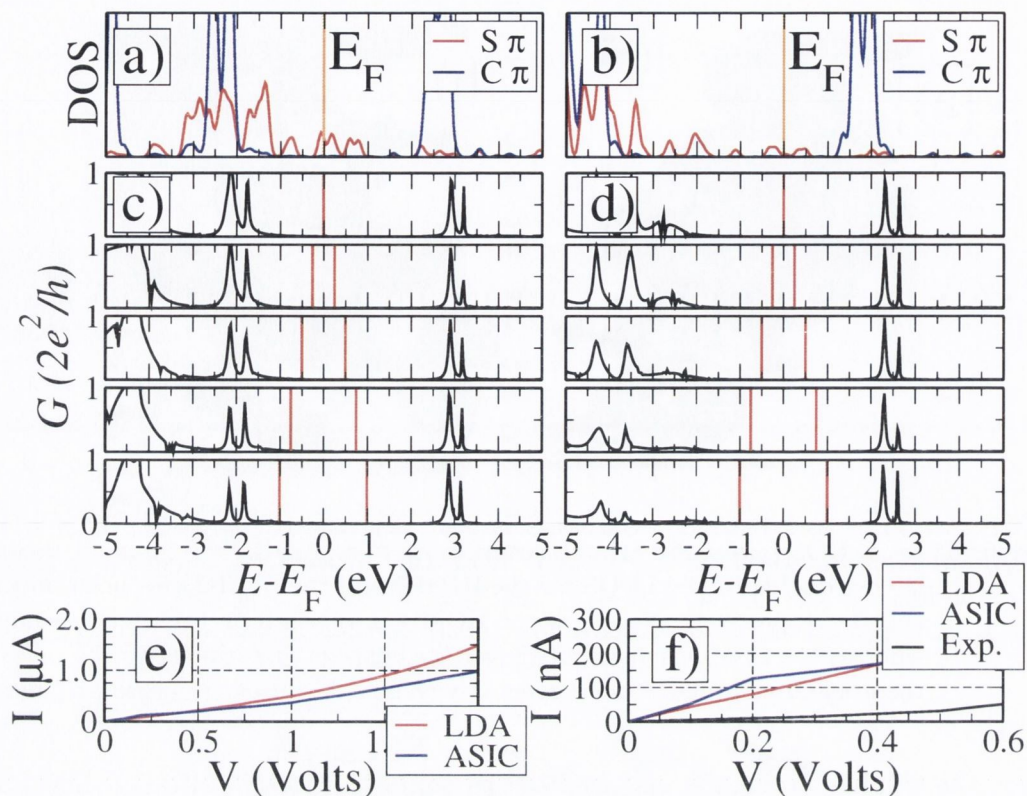
Figure 6.26: Transport properties of first BDMT isomer attached to the gold (111) hollow
site. The left plots correspond to LDA and the right ones to ASIC. The upper
panels are the DOS of the S and C π orbitals ((a) and (b)), the middle are the
transmission coefficients as a function of energy for various bias ((c) and (d))
and the lower are the *I-V* curves. Figure (f) is a zoom of (e) and compares
our results with experiments from reference [26]. The vertical lines in (c) and
(d) mark the bias window.

vestigated only one contact geometry, and a more extensive study is probably needed
in order to compare directly to experiments.

6.4 Biphenyldithiol

The third and final system investigated is that of biphenyldithiol (BPD) attached
to gold. This molecule consists of two benzene rings, which are rotated at an angle
known as the torsion angle relative to each other. The optimum value for this torsion
angle is 37° [119]. The orbital resolved DOS for the isolated molecule is shown in
figure 6.32, calculated with both regular LDA and with ASIC. Note how the ASIC
again lowers the energy of the occupied orbitals by about 4 eV, thus opening up the
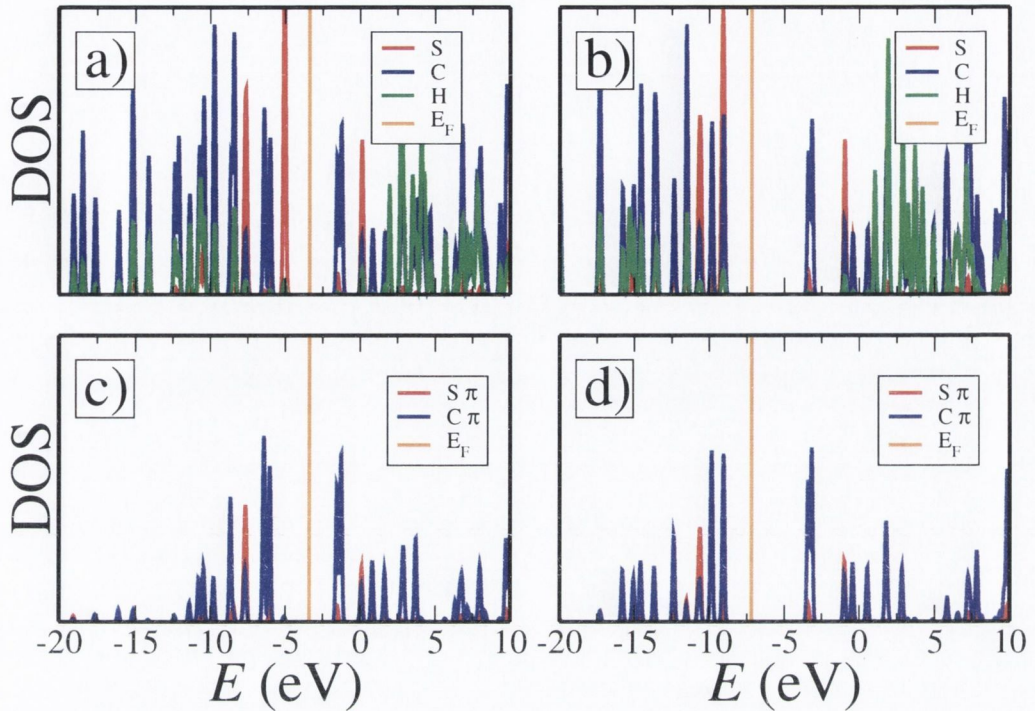
Figure 6.27: Orbital resolved DOS for the second isomer of the BDMT molecule. The left
plots correspond to LDA and the right ones to ASIC. The upper panels ((a)
and (b)) are the DOS of all of the orbitals on the molecule for each atomic
species. The lower panels are the DOS of the S and C π orbitals ((c) and
(d)), which are the orbitals closest to the Fermi level and thus are the orbitals
involved in low bias transport. The orange vertical lines labelled E_F separate
the highest occupied and lowest unoccupied orbitals of the molecule.

HOMO-LUMO gap.

From figure 6.32, it can be seen that the π orbitals on the sulphur and carbon
atoms are the ones which are closest to the Fermi level. From the local DOS plots
shown in figure 6.33, it can be seen that these states are delocalised across the
entire molecule, particularly for the case of the HOMO in panel (b), due to strong
hybridisation between the carbon and sulphur orbitals. Therefore, these states are
expected to conduct strongly when a bias is applied.

To calculate the electronic transport properties, the molecule is attached to the
gold (111) hollow sites as shown in figure 6.34, with a sulphur-surface separation
of 1.9Å. The local DOS for the HOMO and the LUMO of this device are shown in
figure 6.35. As for the isolated molecule, both of these states are delocalised across
the entire molecule, and so would be expected to conduct strongly when inside the
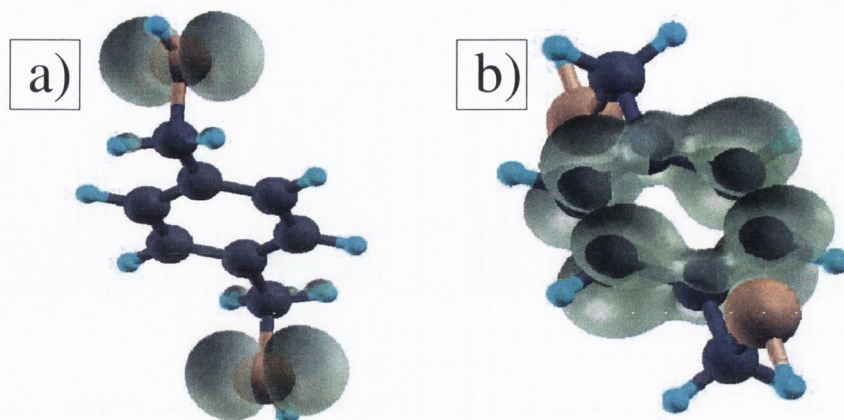bias window.

Figure 6.28: Local DOS (molecular orbital isosurface) for second isomer of the BDMT molecule, calculated with LDA. The LDOS for the HOMO and the LUMO are shown in panels (a) and (b). Note how the HOMO is localised on the suphur atoms, whereas the LUMO is distributed over the benzene ring. Colour code: C=black, S=brown, H=blue.
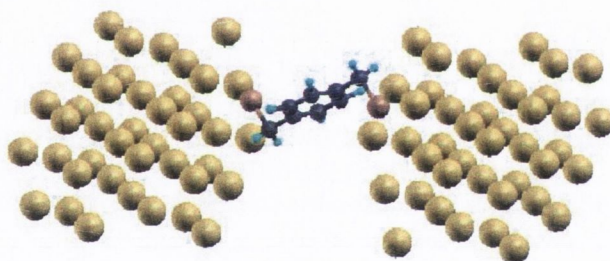

Figure 6.29: The second isomer of the BDMT molecule attached to the hollow site of the Au (111) surface. The sulphur atoms are now in the same plane as the benzene ring. The sulphur-surface distance is 1.9Å. Colour code: Au=yellow, C=black, S=brown, H=blue.

The orbital resolved DOS, transmission coefficients and I-V curves for this system are presented in figure 6.36 for both LDA and ASIC. Once again, ASIC has the effect of lowering the energy of the occupied molecular orbitals, as can be seen from the DOS (panels (a) and (b)). This has the effect of opening up the conductance gap in the transmission coefficients. For this molecule, the HOMO is near E_F as in BDT, giving a conductance of $0.07G_0$ at zero bias with LDA only. When ASIC is applied, the HOMO is shifted downwards out of the bias window and the conductance drops to $0.018G_0$ at E_F. This results in the low-bias I-V curve being suppressed, again similar to what happens for BDT.
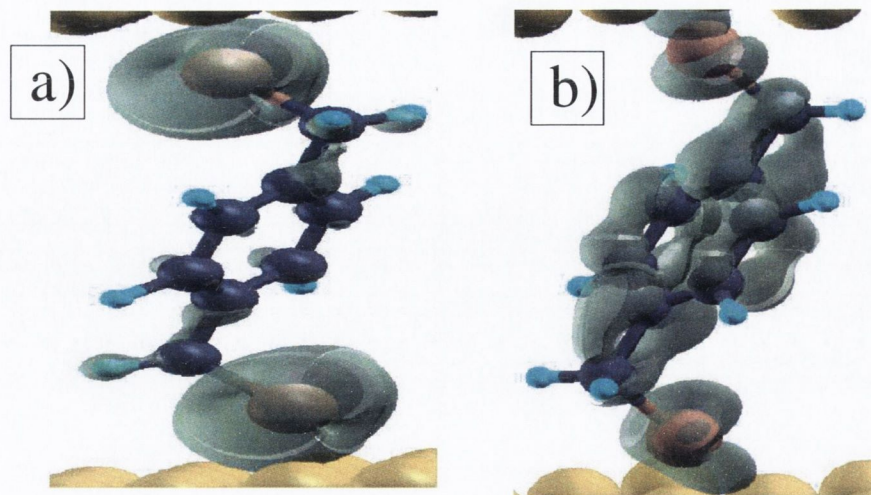
Figure 6.30: Local density of states (molecular orbital isosurface) for the Au/BDMT junction, calculated with LDA. The LDOS for the HOMO and the LUMO are shown in panels (a) and (b) respectively. Note how the HOMO is localised on the S atoms, whereas the LUMO is distributed over the benzene ring, similar to the case of the isolated molecule. Colour code: Au=yellow, C=black, S=brown, H=blue.

The optimum angle between the planes of the benzene rings (i.e. the torsion angle) is 37° [119]. However, this may fluctuate due to temperature or when the molecule is put under strain in a breaking junction. In fact, the total energy difference for the molecule with a 37° torsion angle and one where the torsion angle is 0° is only of the order of 150meV. Panel (e) of figure 6.36 shows the I-V curves calculated for the equilibrium torsion angle of 37°, whereas panel (f) shows the result for the case when the benzene rings are in the same plane (i.e. when the torsion angle is 0°). Reducing the torsion angle causes an increase in the transmission since the overlap between the π orbitals located on the two benzene rings is increased. The conductance at zero bias for a torsion angle of 0° is $0.09G_0$ with LDA only, and $0.024G_0$ when ASIC is applied.

These results show that ASIC has an effect on BPD similar to the one it has on BDT, shifting the HOMO downwards and reducing the zero-bias conductance. However, the results differ from those obtained experimentally by Dadosh et. al. [30] by several orders of magnitude. However, as in the case of BDMT, only one anchoring geometry has been investigated here, and a more comprehensive study would again be required in order to be able to compare directly to experiment.
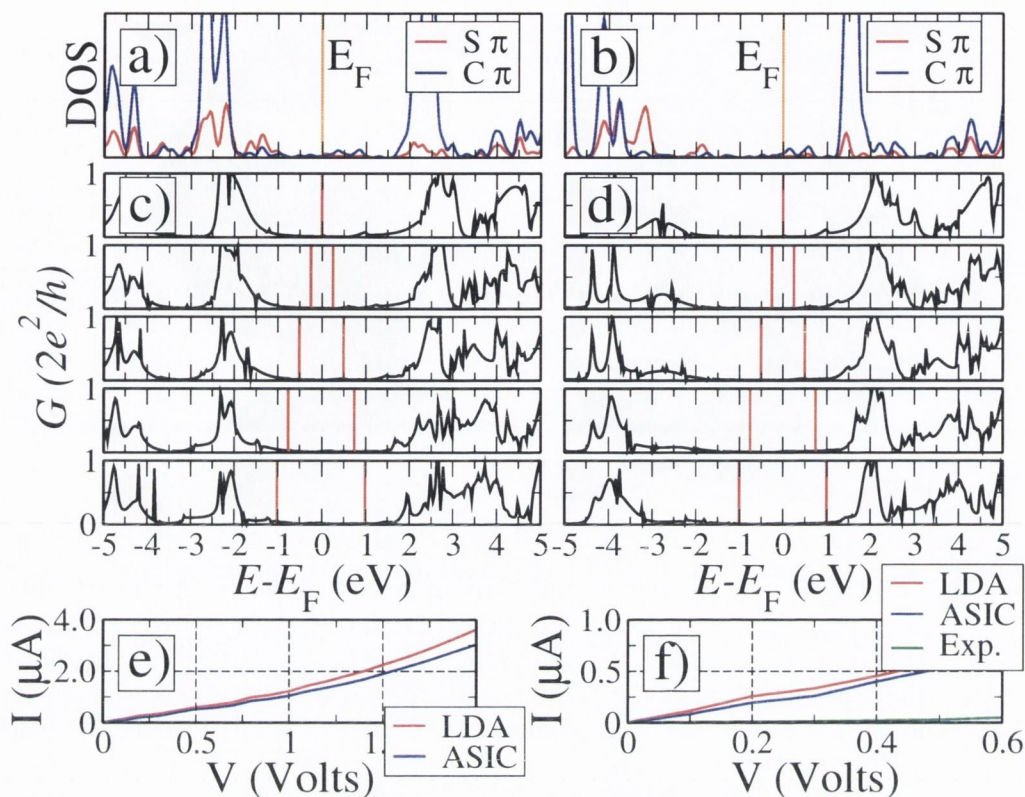
Figure 6.31: Transport properties of second BDMT isomer attached to the gold (111) hollow site. The left plots correspond to LDA and the right ones to ASIC. The upper panels are the DOS of the S and C π orbitals ((a) and (b)), the middle are the transmission coefficients as a function of energy for various bias ((c) and (d)) and the lower are the I-V curves. Figure (f) is a zoom of (e) and compares our results with experiments from reference [26]. The vertical lines in (c) and (d) mark the bias window.

6.5   Conclusion

ASIC is a simple, computationally efficient method for removing the self-interaction error present in local DFT exchange-correlation functionals. In particular, it corrects the ionisation potentials of organic molecules, giving remarkably good agreement with experimental values [75]. For electronic transport calculations, it corrects the metal-molecule band alignment, and opens up the HOMO-LUMO gap. This has the effect of reducing the low bias conductance for certain π conjugated molecules such as BDT and BPD, again improving the agreement with experimental results. It has less of an impact on molecules such as BDMT, in which the HOMO-LUMO gap is already quite large, and so whose low bias transport properties are not particularly

Method	G (G_0)
Theory	
SMEAGOL LDA	0.006, 0.015
SMEAGOL ASIC	0.004, 0.013
TranSIESTA LDA [66]	0.16, 0.017, 0.23
Experiment	
STM Break Junc. [26]	0.0006
MCBJ [25]	0.0002 to 0.004
Lith. Fab. Elec. [29]	0.0005
Col. Dimer [30]	10^{-7}

Table 6.3: Zero-bias conductance for BDMT attached to gold electrodes from a variety of different computational and experimental methods. Computational methods include NEGF combined with DFT (SMEAGOL [38, 76] and TranSIESTA [40, 66]). For both computational methods, the molecule is connected to the gold hollow site. Conductances from SMEAGOL calculations for both of the BDMT isomers investigated are listed. For the TranSIESTA, the range of results presented are for different sulphur-surface separations. Experimental methods for manufacturing the molecular devices include mechanical breaking junctions (MCBJ [19, 24, 25]), STM breaking junctions (STM break junc. [26]), lithographic fabrication of the electrodes (Lith. Fab. Elec., [29]), and formation of molecule-nanoparticle dimers by mixing gold colloid with solution (Col. Dimer, [30]).

sensitive to the exact position of the HOMO.

However, some disagreement between theory and experiment still remains. For the anchoring geometries investigated, the zero-bias conductance was still larger than the experimental value [26] by a factor of 3 to 5. Reducing the strength of the coupling between the metal and the molecule results in ϵ_{HOMO} moving closer to the gold E_F, which can actually cause the low bias conductance to increase. One possible explanation is that ASIC still overestimates the polarisability of molecules [89, 90], with a quantitatively incorrect prediction of the response exchange and correlation field. Secondly, we have applied the ASIC only to the molecular degrees of freedom, without correcting the Au atoms. It is thus likely that the Au 6s orbitals at the surface are too extended, leading to a larger current. It is possible that the use of XC potentials constructed from exact charge densities [120, 121] and correcting both the molecule and the metallic surfaces, may offer a solution to this problem.

Finally, ASIC does not contain the derivative discontinuity. As demonstrated in chapter 5, this discontinuity can have a profound effect on the I-V characteristics of molecular junctions. In particular, if the molecule is weakly coupled to the leads, a
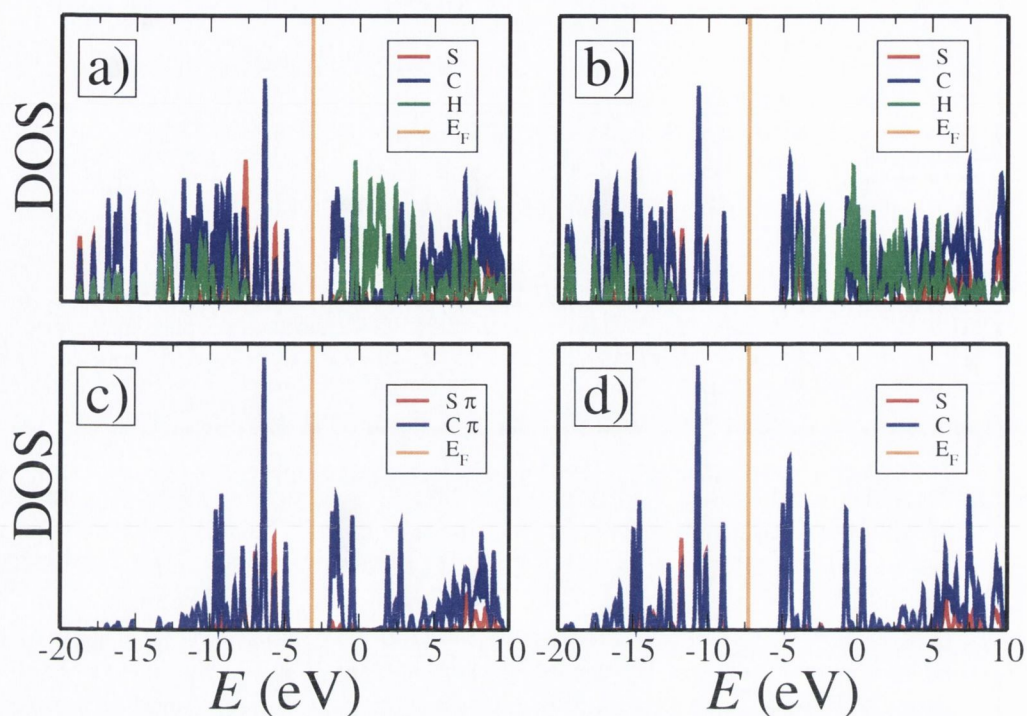
Figure 6.32: Orbital resolved DOS for the BPD molecule. The left plots correspond to LDA and the right ones to ASIC. The upper panels ((a) and (b)) are the DOS of all of the orbitals on the molecule for each atomic species. The lower panels are the DOS of the S and C π orbitals ((c) and (d)), which are the orbitals closest to the Fermi level and thus are the orbitals involved in low bias transport. The orange vertical lines labelled E_F separate the highest occupied and lowest unoccupied orbitals of the molecule.

state can become pinned just above E_F, as shown in figure 6.18. The derivative discontinuity would prevent this state from charging, keeping it out of the bias window and possibly opening up a conductance gap in the I-V curve.

Therefore, the ideal exchange-correlation potential for electronic transport calculations needs to be self-interaction free. It needs to give accurate results for the ionisation potentials of the molecules being investigated, and reproduce the correct derivative discontinuity for the molecular orbitals. It would also need to correctly describe the polarisability of the molecule and the long range behaviour of the orbitals. LDA with the full self-interaction correction [71], or exact-exchange methods [88, 70] have many of these properties, but both of these methods are orbital dependent. Although some calculations have been performed in the linear response limit [53], there are no implementations for finite bias. Finally, it would need to be combined with time-dependent DFT [57, 58], as when a finite bias is applied the system is no
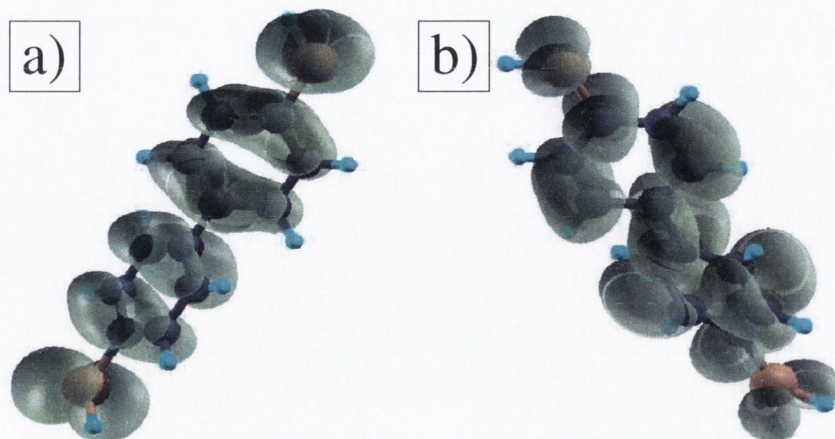
Figure 6.33: Local density of states (molecular orbital isosurface) for the BPD molecule, calculated with LDA. The LDOS for the HOMO and the LUMO are shown in panels (a) and (b). Note how the orbitals are delocalised across all of the sulphur and carbon atoms. Colour code: C=black, S=brown, H=blue.
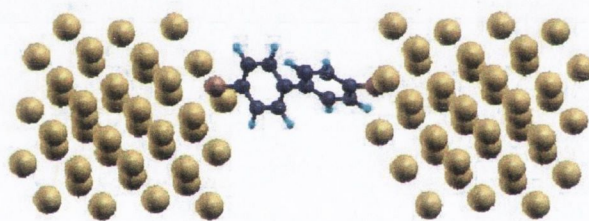

Figure 6.34: BPD molecule attached to the hollow site of the Au (111) surface. The sulphur-surface distance is 1.9Å. Colour code: Au=yellow, C=black, S=brown, H=blue.
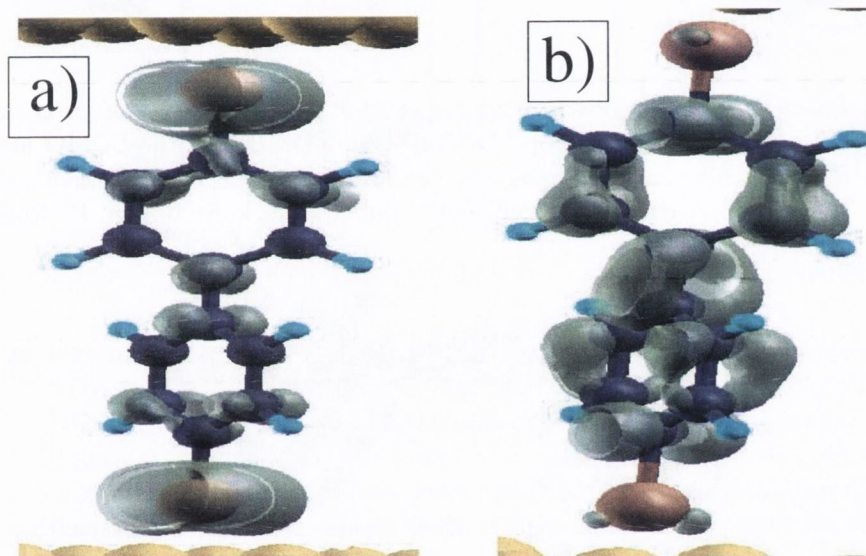
longer in a ground state.

Figure 6.35: Local density of states (molecular orbital isosurface) for the Au/BPD junction,
calculated with LDA. The LDOS for the HOMO and the LUMO are shown
in panels (a) and (b). Note how the orbitals are delocalised across all of the
sulphur and carbon atoms, similar to that of the isolated molecule. Colour
code: Au=yellow, C=black, S=brown, H=blue.
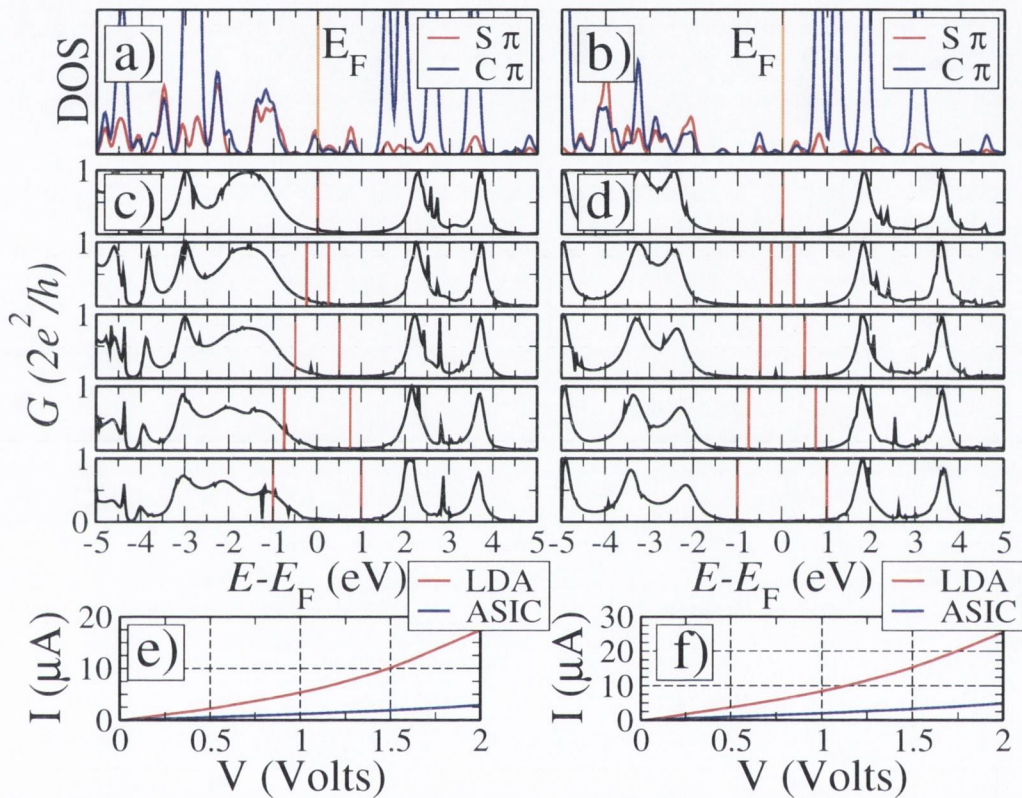
Figure 6.36: Transport properties of a BPD molecule attached to the gold (111) hollow site. The left plots correspond to LDA and the right ones to ASIC. The upper panels are the DOS of the S and C π orbitals ((a) and (b)), the middle are the transmission coefficients as a function of energy for various bias ((c) and (d)) and the lower are the *I-V* curves. Figure (e) is the *I-V* curve for a torsion angle of $37°$ and (f) is for a torsion angle of $0°$. The vertical lines in (c) and (d) mark the bias window.

Chapter 7

Simulating STM Transport in Alkanes

The Scanning Tunnelling Microscope (STM) [77, 78] is a tool with multiple applications in molecular electronics. It consists of an atomically sharp probe-tip constructed from a heavy metal such as platinum, tungsten or iridium. It can be used to map the positions of atoms and defects on surfaces, and to probe the local density of states of surfaces. It can also be used for depositing atoms and molecules on a surface to form nanoscale devices. A potential bias can be applied between the substrate and the STM tip, and thus the I-V characteristics of molecules and surface structures can be investigated.

In the past, calculations of STM currents were based on approximations such as that of Tersoff-Hamann [79, 80]. In this method, the tip is assumed to be sufficiently far from the molecule that it does not affect its electronic structure. However, such methods are not self-consistent with applied potential bias, i.e. they do not take into account the changes to the electronic structure caused by the interaction between the molecule and the probe. They are thus not reliable when the tip is relatively close to the molecule. Therefore, it is important to explore the use of self-consistent transport methods such SMEAGOL [37, 38, 39] to simulate STM experiments.

However, there are some specific problems with using SIESTA [82, 83, 84] or SMEAGOL to perform calculations for STM experiments. These occur when measuring tunnelling currents for probes far from the surface. Since SIESTA uses a localised basis set, the orbitals are artificially cut off beyond a certain radius, so there are no basis functions to describe the vacuum region. Hence, if the tip-surface separation is greater than a certain distance, the current will be artificially cut off. One solution to this problem is to insert ghost orbitals, which do not have an associated pseudopotential, into the vacuum region between the surface and the tip. However, this has to be done very carefully, as the spacing of the ghost orbitals can

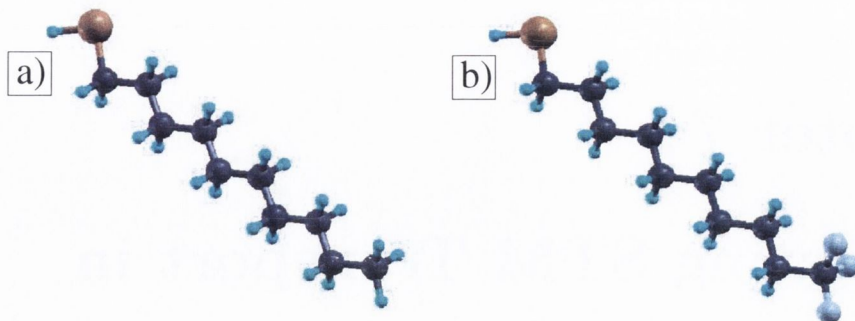create artificial oscillations in the conductance as a function of distance.

Figure 7.1: Decanethiol molecule (a) with CH_3-endgroup and (b) with CF_3-endgroup. Colour code: C=black, S=brown, H=blue, F=purple.

This problem will not occur if the STM tip-sample distance is sufficiently small. An example of an experiment where this is the case is that performed by Pflaum et. al. [81], in which a monolayer of alkanethiol molecules are deposited on a gold surface, and the transport properties are then probed using an STM tip. The resulting zero-bias conductance is low, being of the order of $10^{-7}G_0$ at zero bias. The *I-V* curves are asymmetric, and this asymmetry increases noticeably when the hydrogen atoms attached to the end carbon atom in the alkane chain (i.e. the one nearest to the STM tip) are replaced by fluorine atoms. The authors of the paper speculate that the extra asymmetry with the CF_3-endgroup is due to a rearrangement of the charge distribution near the end of the molecule caused by the high electronegativity of the fluorine atoms. This in turn causes an electrostatic forces between the STM tip and the molecule, the direction of which depends on the bias of the tip. This will cause the molecule to be repelled for one bias direction and attracted for the other, changing the tip-molecule distance and hence the current.

Calculations using the Tersoff-Hamann method have been performed for pentanethiol molecules on gold [122]. However, the nature of the Tersoff-Hamann method requires a large tip-molecule separation, and the current obtained in these calculations is an order of magnitude lower than that observed in the experiment. Also, tip-molecule interactions cannot be studied using this method.

In this chapter, some results of ongoing calculations for this system will be presented. The mechanism behind the asymmetry in the *I-V* curves will be discussed. However, the calculation of forces at finite bias has not yet been implemented in SMEAGOL, so the mechanism suggested by the experimentalists for the differences between the CH_3-endgroup and with CF_3-endgroup has not yet been investigated

quantitatively.

7.1   Electronic Structure of the Molecules

The molecules used in the experiment were methyl-terminated alkanethiols and fluorine-terminated alkanethiols. A range of different alkane chain lengths were studied, but the molecules predominantly used were decanethiol, as shown in figure 7.1(a), and decanethiol with the CF$_3$-endgroup, as shown in figure 7.1(b). Decanethiol consists of an alkane chain of ten carbon atoms, with a thiol (-SH) group at one end. The sulphur atom in the thiol group forms a strong bond with gold, and will anchor the molecule to the surface to form the monolayer. The CH$_3$-endgroup can be replaced by a CF$_3$-endgroup to form fluorine-terminated decanethiol, as shown in figure 7.1(b).

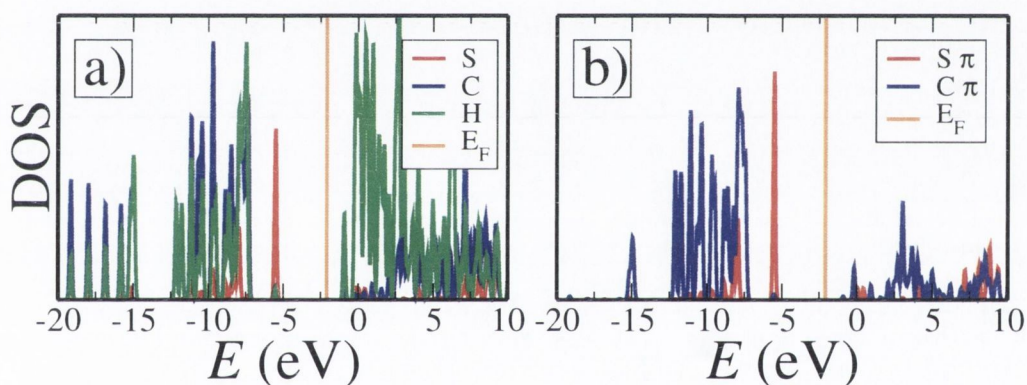

Figure 7.2: Orbital resolved DOS for the isolated decanethiol molecule with the CH$_3$-endgroup showing (a) the molecular valence states for the sulphur, carbon and hydrogen atoms and (b) the sulphur and carbon states due to the p orbitals perpendicular to the axis of the molecule. The orange vertical lines labelled E_F separate the highest occupied and lowest unoccupied orbitals of the molecule.

The orbital resolved density of states (DOS) for the isolated CH$_3$-terminated decanethiol molecule is shown in figure 7.2. The HOMO-LUMO gap is quite large, being of the order of 5eV. The HOMO state is about 2eV above the other occupied orbitals, and is mostly formed from the sulphur p states.

The local DOS for the isolated CH$_3$-terminated decanethiol molecule is shown in figure 7.3. The state below the HOMO is shown in (a), the HOMO is shown in (b) and the LUMO is shown in (c). The HOMO in particular is localised around the thiol group at one end of the molecule. Thus, it is unlikely to be able to transport charge across the molecule, and so would not be expected to contribute strongly to

the transmission. In contrast, the level below the HOMO is delocalised over most of the molecule, and so is more likely to conduct.
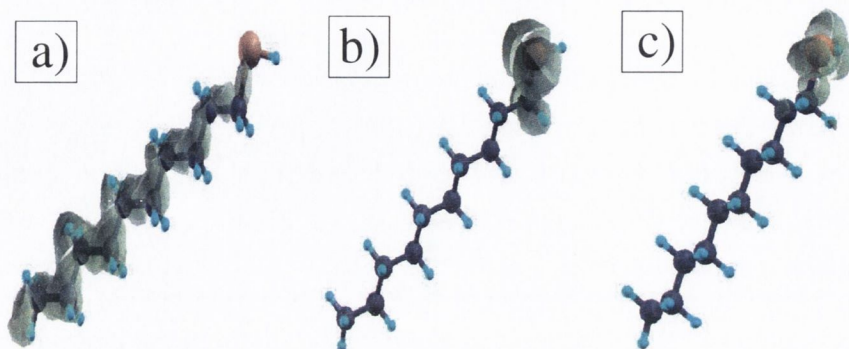

Figure 7.3: Local DOS (molecular orbital isosurface) for the isolated decanethiol molecule with the CH_3-endgroup showing (a) the HOMO-1 state (b) the HOMO and (c) the LUMO. Colour code: C=black, S=brown, H=blue, F=purple.

The orbital resolved DOS for the isolated decanethiol molecule with the CF_3-endgroup is shown in figure 7.4. The HOMO-LUMO gap is similar to that for CH_3-terminated decanethiol, being about 5eV. The HOMO state is again about 2eV above the other occupied orbitals, and is mostly formed from the sulphur p states. The fluorine p orbitals are situated about 3eV above the Fermi level and about 4eV below, mainly contributing to the LUMO and to the levels below the HOMO.
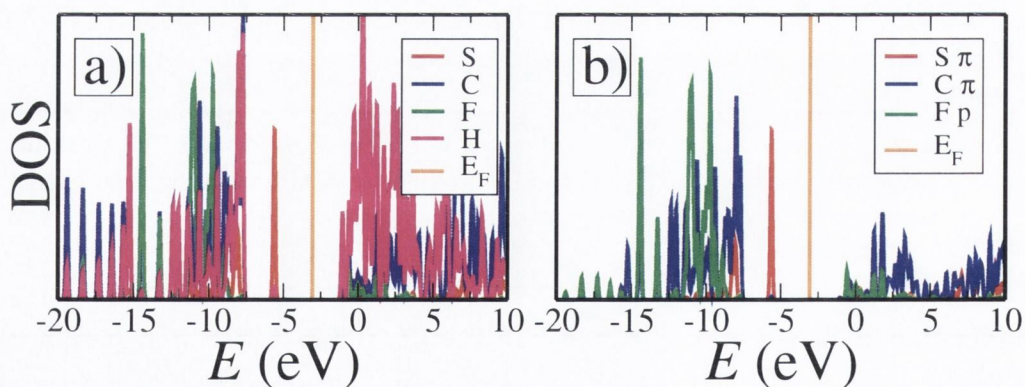
Figure 7.4: Orbital resolved DOS for the isolated decanethiol molecule with the CF_3-endgroup showing (a) the molecular valence states for the sulphur, carbon, fluorine and hydrogen atoms and (b) the sulphur and carbon states due to the p orbitals perpendicular to the axis of the molecule, and the fluorine p orbitals. The orange vertical lines labelled E_F separate the highest occupied and lowest unoccupied orbitals of the molecule.

The local DOS for the isolated CF_3-terminated decanethiol molecule is shown in figure 7.5. As for CH_3-terminated decanethiol, the HOMO in particular is localised around the thiol endgroup, and so probably will not contribute strongly to the current. In contrast, the level below the HOMO is delocalised over most of the molecule and so would be expected to conduct.

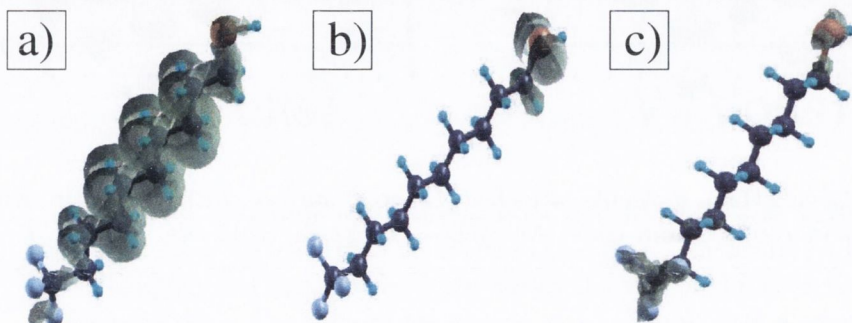Figure 7.5: Local DOS (molecular orbital isosurface) for the isolated decanethiol molecule with the CF_3-endgroup showing (a) the state below the HOMO, (b) the HOMO and (c) the LUMO. Colour code: C=black, S=brown, H=blue, F=purple.

7.2 Calculating the Transport Properties

To calculate the transport properties of these molecules, the sulphur atoms were attached to the gold fcc (111) hollow site with a sulphur-surface distance of 1.9Å. This is the equilibrium distance for this configuration [118], as discussed in chapter 6. The arrangement of the molecule on the surface and the tip is shown in figure 7.6 for the original CH_3-endgroup, and in figure 7.7 for the CF_3-endgroup. In the experiment, the molecules are tilted at an angle of $\sim 32°$. However, in order to simplify the calculations, the molecules are placed perpendicular to the surface. This allows the unit cell used to be smaller, which greatly reduces the computational requirements. A second simplification is the modelling of the STM tip by a gold electrode instead of using tungsten or platinum-iridium, as used in the experiments. As discussed in chapter 6, the gold leads can be represented by just the $6s$ basis set for transport calculations, which again dramatically reduces the computational requirements. Secondly, using two leads which are made of the same material also simplifies the calculations since they both have the same Fermi level. The STM tip itself is not modelled as atomically sharp, but it is slightly blunter. This improves the stability of the calculations.
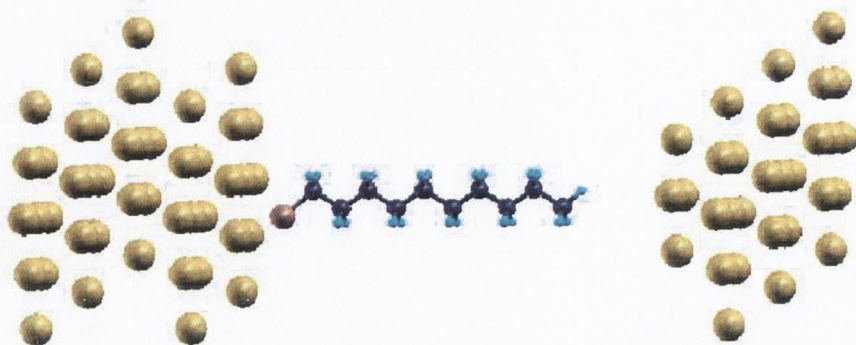
Figure 7.6: Decanethiol molecule attached to gold surface with STM tip with CH$_3$-endgroup. Colour code: Au=yellow, C=black, S=brown, H=blue, F=purple.

Figure 7.7: Decanethiol molecule attached to gold surface with STM tip with CF$_3$-endgroup. Colour code: Au=yellow, C=black, S=brown, H=blue, F=purple.

The size of the current is extremely sensitive to the distance between the tip and the molecule. By adjusting this distance, we can match the magnitude of the current obtained in experiments. Note that the direction of the I-V has been reversed in this graph, as in our calculations the convention for negative and positive bias is the opposite to that used in the experiment of reference [81]. As shown in the plot of the I-V curves for different distances shown in figure 7.8, the best match is for a distance between the last carbon atom in the molecule and the plane of the gold tip of 5.25Å. The results presented in the rest of this chapter will all be for this tip-molecule separation.

The orbital resolved DOS for CH$_3$-terminated decanethiol on gold is shown in figure 7.9. Note that the HOMO is relatively close to the gold E_{F}. However, as can be seen from the plot of the local DOS of the molecule in an energy window around
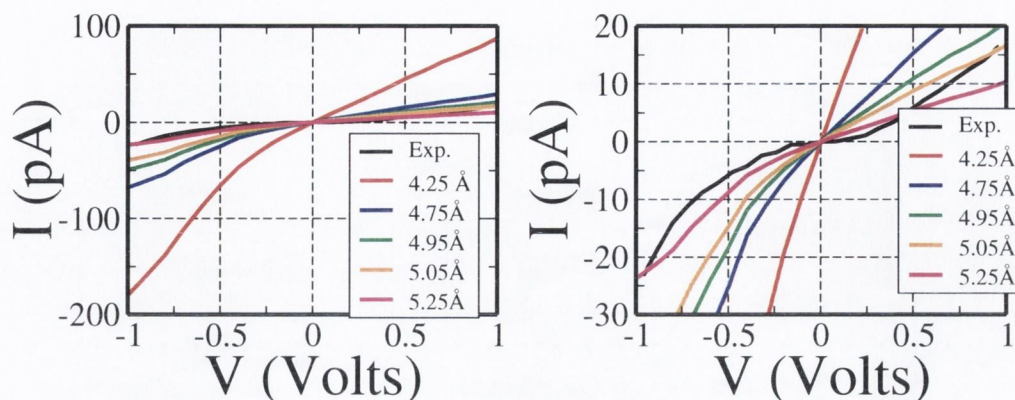
Figure 7.8: I-V curves for CH$_3$-terminated decanethiol attached to a gold surface for different distances between the end carbon atom on the molecule and the probe tip. Changing this distance by 0.1Å causes the size of the current to change by approximately one order of magnitude at 1V. Panel (b) is a zoom in (along the y-axis) of panel (a), showing the region between -30pA and 20pA.
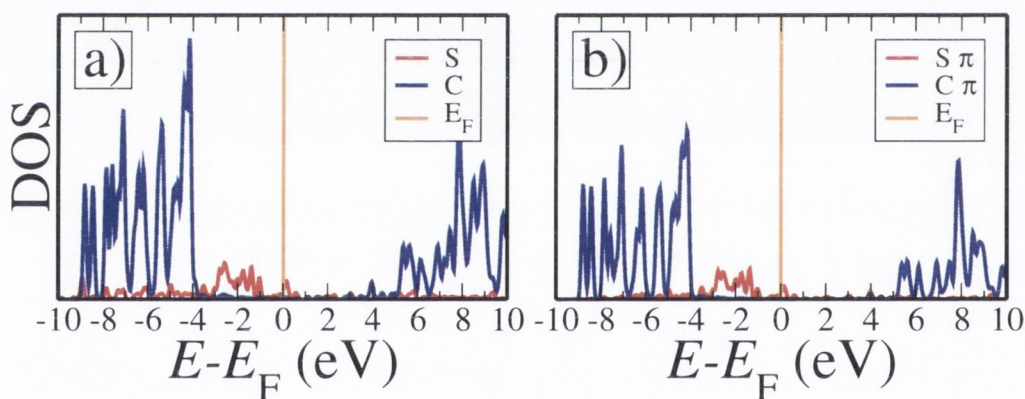
Figure 7.9: Orbital resolved DOS for the CH$_3$-terminated decanethiol molecule on the gold surface. All of the carbon and sulphur valence orbitals are shown in (a), and the p orbitals perpendicular to the axis of the molecule are shown in (b). The HOMO-LUMO gap is large, although the HOMO is about 1eV below E_F.

the HOMO (figure 7.10), this state is mainly localised around the single sulphur atom. The delocalised orbitals which are capable of transporting charge across the molecule are due to the carbon p orbitals, and are further away from the Fermi level. Thus a large conductance gap would be expected for this molecule, with just a tunnelling current present at low bias. This can be seen from both the transmission coefficients in figure 7.13 and the I-V curves in figure 7.14. There is a large gap in the resonances in the zero bias transmission coefficients of about 5eV on each side of the Fermi level, indicating that the HOMO does not contribute much to the electron

Figure 7.10: Local DOS (molecular orbital isosurface) for the CH$_3$-terminated decanethiol molecule on the gold surface, showing (a) the level below the HOMO, (b) the HOMO, and (c) the LUMO. Note how the HOMO is localised around the thiol endgroup. Colour code: Au=yellow, C=black, S=brown, H=blue.

transport. The current at 2V is of the order of 0.1nA, which is about five orders of magnitude less than that observed for the π-conjugated molecules discussed in chapter 6.

The orbital resolved DOS for decanethiol with the CF$_3$-endgroup on gold is shown in figure 7.11. As for the CH$_3$-terminated molecule, the HOMO is relatively close to the gold E_F. However, as can be seen from the plot of the local DOS of the molecule in
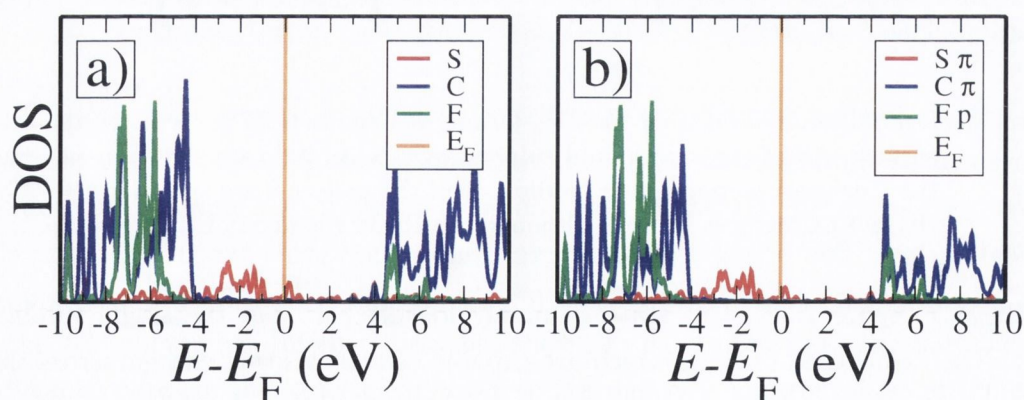
Figure 7.11: Orbital resolved DOS for the decanethiol molecule with the CF$_3$-endgroup on the gold surface. All of the carbon, sulphur and fluorine valence orbitals are shown in (a), and the p orbitals perpendicular to the axis of the molecule are shown in (b). The HOMO-LUMO gap is large, although the HOMO is about 1eV below E_F.

an energy window around the HOMO shown in figure 7.12, this state is again mainly localised in the single sulphur atom. The delocalised orbitals which are capable of transporting charge across the molecule are due to the carbon p orbitals, and are further from the Fermi level. Thus a large conductance gap would be expected for this molecule, with just a tunnelling current present at low bias. This can be seen
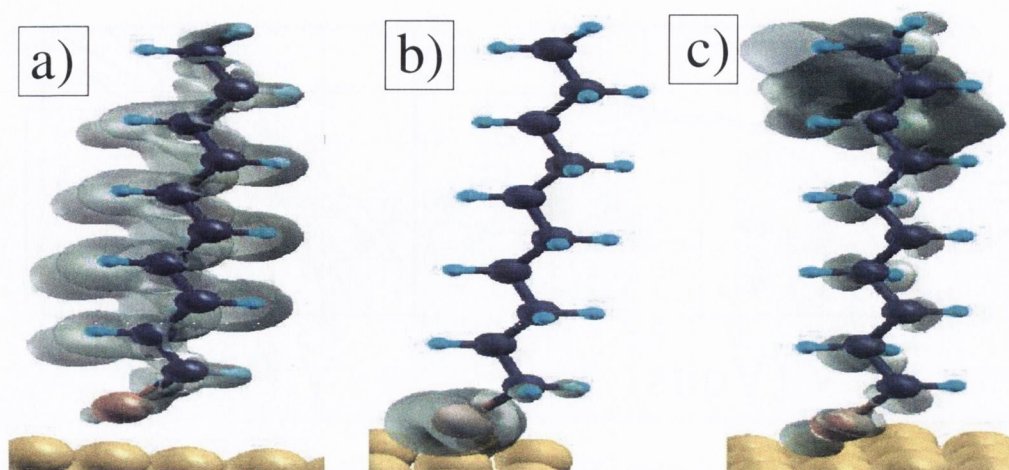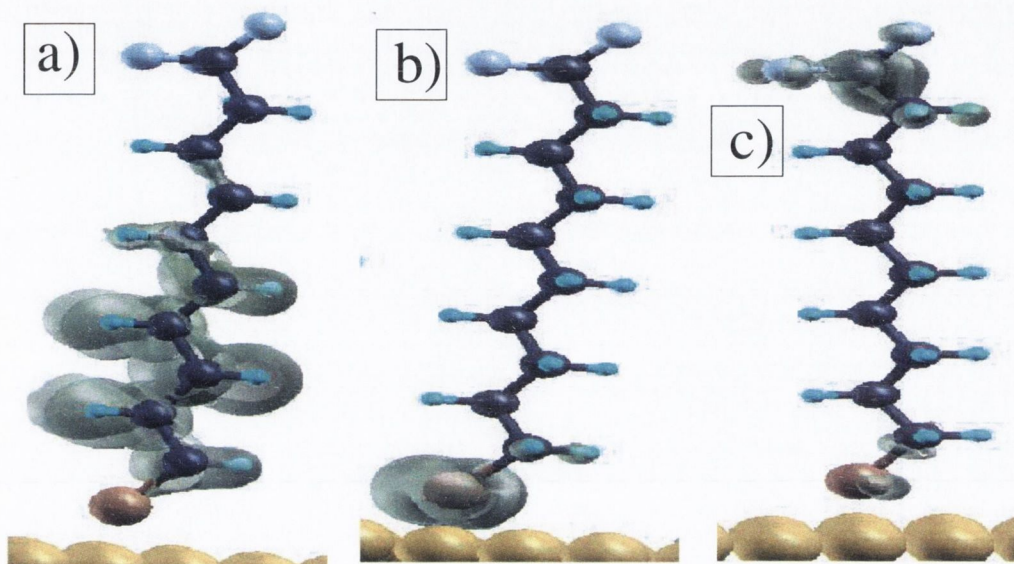

Figure 7.12: Local DOS (molecular orbital isosurface) for the CF_3-terminated decanethiol molecule on the gold surface, showing (a) the level below the HOMO, (b) the HOMO, and (c) the LUMO. Note how the HOMO is localised around the thiol endgroup. Colour code: Au=yellow, C=black, S=brown, H=blue.

from both the transmission coefficients in figure 7.13 and the I-V curves in figure 7.14. As for the CH_3-endgroup, there is a large gap in the resonances in the zero bias transmission coefficients of about 5eV on each side of the Fermi level. The current at 2V is of the order of 0.1nA, which is again similar to that obtained for CH_3-terminated decanethiol and is about five orders of magnitude less than that observed for the π-conjugated molecules discussed in chapter 6.

The most noticeable feature of the I-V curves and differential conductance shown in figure 7.14 is their asymmetry. The conductance at positive bias is about 2-3 times smaller than that for negative bias. The reason for this is the difference in the strength of the coupling between the molecule and the gold surface on one side, and the molecule and the STM tip on the other side. The sulphur atom in particular forms quite a strong bond with the gold surface, whereas as the tip is much further from the CH_3- and CF_3-endgroups. Therefore, as discussed in chapter 3 and as shown in the schematic illustration in figure 7.15(a), electrons can be transferred more easily
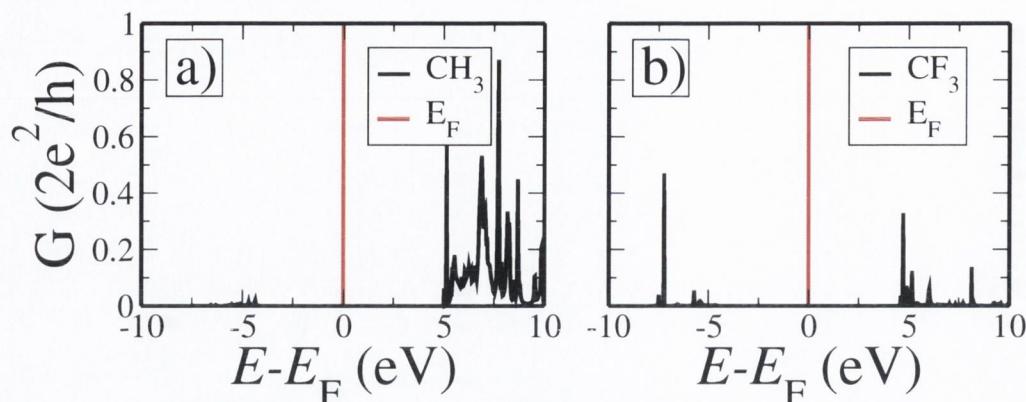
Figure 7.13: Transmission coefficients at zero bias for decanethiol attached to gold surface with (a) CH_3-endgroup and (b) CF_3-endgroup. Note the gap in the transmission of about 5eV on either side of the Fermi level.
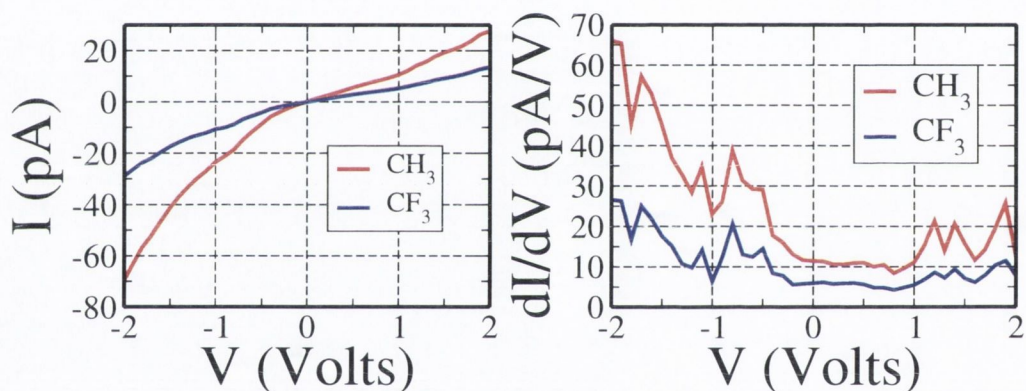
Figure 7.14: (a)I-V curves and (b) differential conductance for decanethiol with both CH_3 and CF_3-endgroups. Note the asymmetry with respect to bias direction, with the conductance at negative bias being 2-3 times larger than that for positive bias. The conductance is also lower for the CF_3-endgroup than the CH_3-endgroup.

between the molecule and the surface than the molecule and the tip. Thus, when the direction of bias is such that the chemical potential of the surface is higher than that of the tip, the molecule gains electrons. This extra charge increases the energy of the molecular orbitals, causing them to move closer to E_F. This can be seen in the plots of the transmission coefficients for different voltages shown in figures 7.16 and 7.17. At negative bias, the levels shift upwards so that the occupied levels are closer to the bias window. This increases the transmission in the bias window, which in turn increases the current. At positive bias, the electrons leave the molecule as the more strongly coupled lead has a lower chemical potential. Therefore, the occupied

Figure 7.15: (a) Schematic energy level diagram. The molecule is more strongly coupled
to the surface than to the tip, so when the chemical potential of the surface is
higher, charge is transferred into the molecule from the surface. When the bias
is reversed, the charge leaves into the surface faster than it can enter from the
tip. (b) Schematic showing electrostatic interaction between tip and molecule
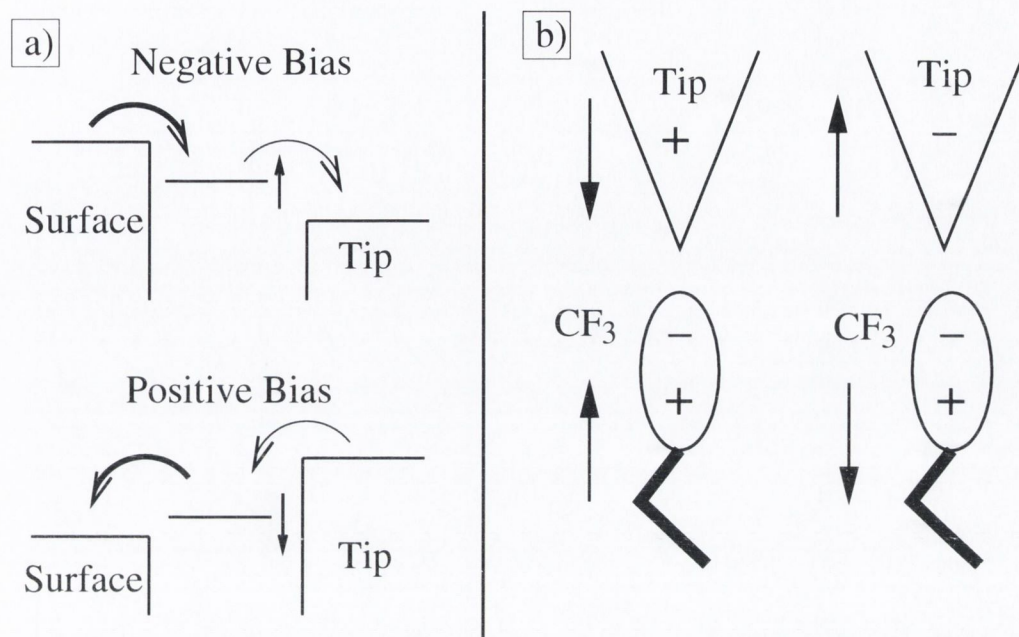endgroup. The CF_3-terminated decanethiol molecule forms an electric dipole,
and so will be attracted or repulsed by the STM tip, depending on the bias
direction.

levels shift downwards away from the bias window, and the current is lower. The
total shift in the transmission coefficients from -2V to 2V is approximately 1eV.

This change in the occupation of the molecules as a function of the applied bias
can be seen in the plots of their total Mulliken populations as a function of voltage
shown in figure 7.18. As the bias increases from negative to positive, the molecule
loses electric charge as the chemical potential of the substrate is lowered. This causes
the occupied levels to shift downwards away from E_F, opening up the HOMO-LUMO
gap and reducing the conductance.

The asymmetry in the conductance observed in these results is due to the asym-
metry in the coupling to the leads. Asymmetry was also observed in the experimental
conductance measurements for these molecules [81]. However, in the experimental
results, the CF_3-endgroup was found to produce a far more asymmetric I-V curve
than the CH_3-endgroup. This was not observed in our calculations described here,
where the asymmetry for both types of endgroup was similar. In the experimental

Figure 7.16: Transmission coefficients for positive and negative bias for decanethiol with the CH$_3$-endgroup. Note how the resonances in the tranmission coefficients due to the occupied states move up closer to the bias window at negative bias, and move downwards for positive bias.

work, it was argued that this asymmetry was due to a repositioning of the molecule due to electrostatic interactions between the endgroup and the STM tip, as indicated in the schematic illustration in figure 7.15(b). The high electronegativity of the fluorine atoms would be expected to attract a large net charge, which would then be strongly attracted or repelled by the STM tip, depending on its bias direction. Figure 7.19 shows a plot of the net charge on each group of atoms as a function of their distance along the axis of the molecule. Replacing the hydrogen atoms by fluorine atoms causes an increase in the occupation of the endmost carbon atom, although the endmost fluorine atom has a net positive charge. However, the total net charge on the CF$_3$-endgroup would be negative (as it has extra electrons), whereas the total net charge on the CH$_3$-endgroup is positive. Thus, the end of the molecule would be attracted towards the tip when it is at positive bias, reducing the separation and increasing the conductance, whereas it would be repelled when the tip is at a negative bias.
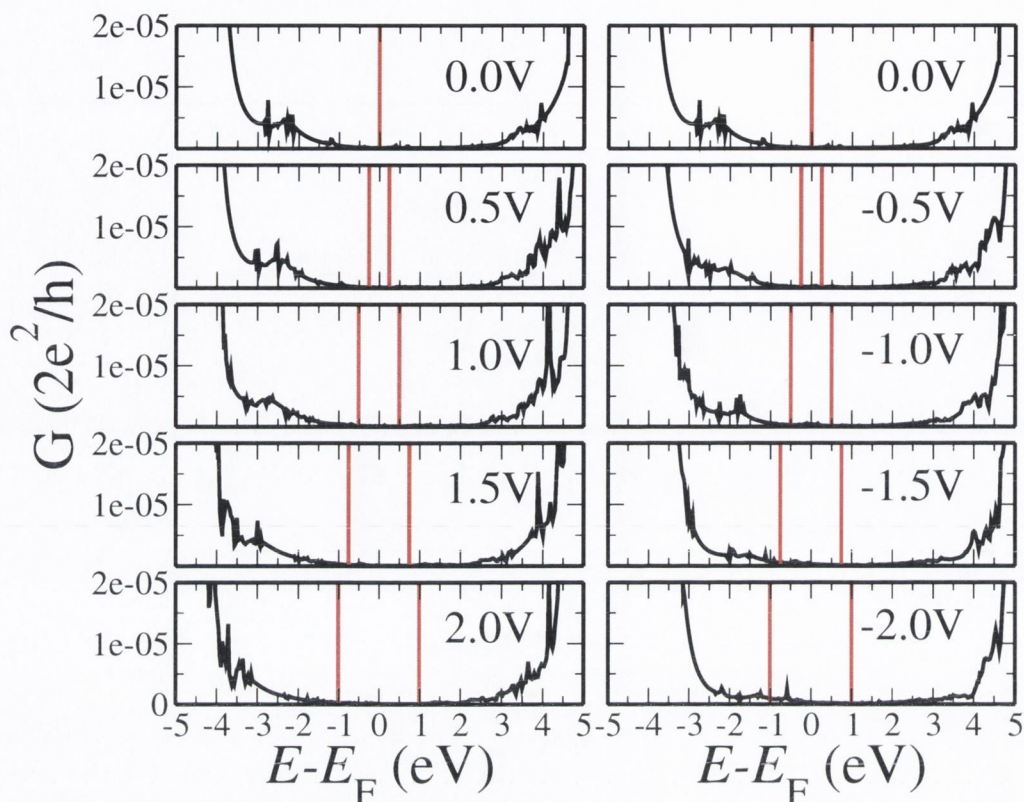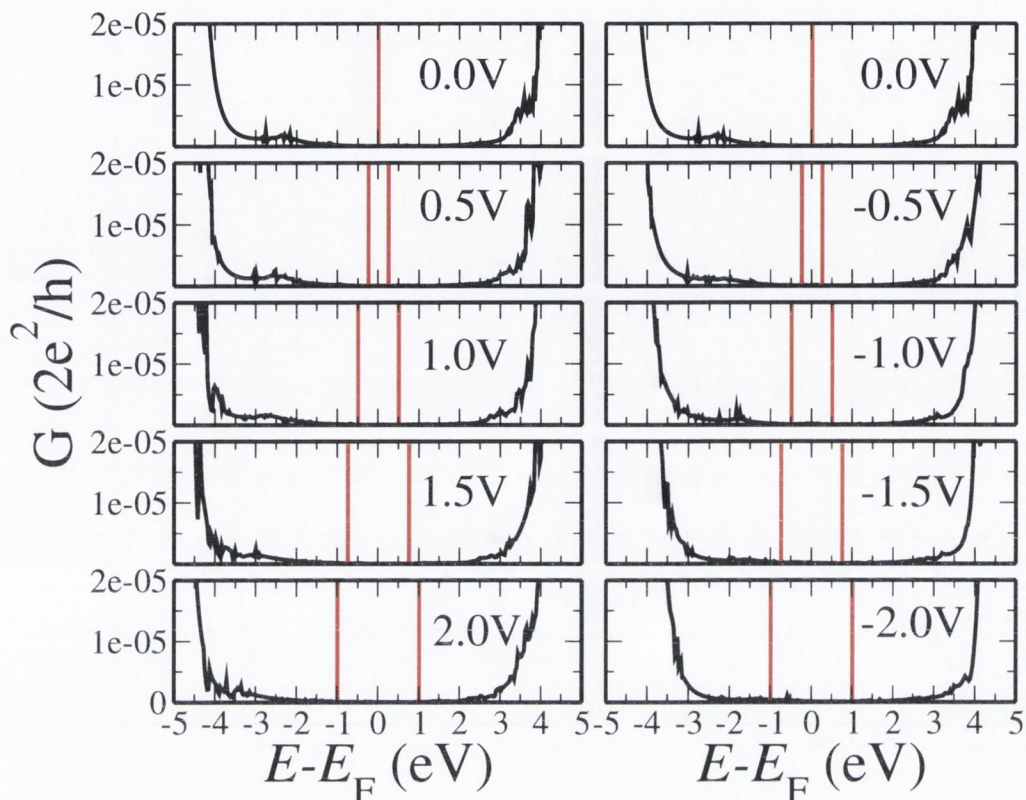
Figure 7.17: Transmission coefficients for positive and negative bias for decanethiol with the CF_3-endgroup. Note how the resonances in the tranmission coefficients due to the occupied states move up closer to the bias window at negative bias, and move downwards for positive bias.
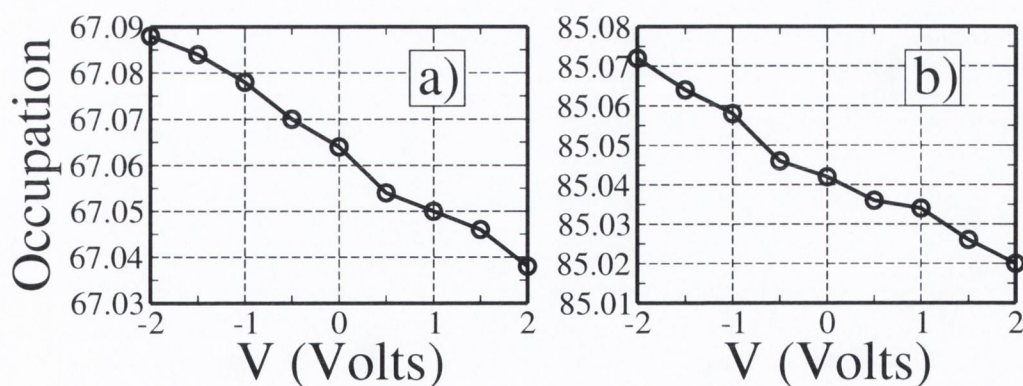
Figure 7.18: Mulliken populations for decanethiol molecule with (a) CH_3 and (b) CF_3-endgroups attached to gold surface. Note how the occupation of the molecule for both endgroups drops as the bias increases from negative to positive.
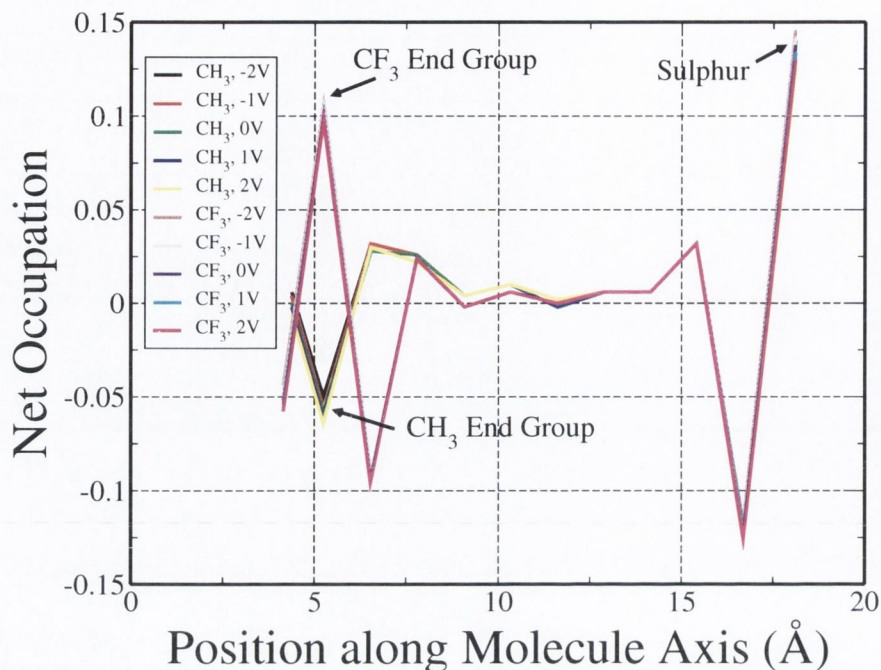
Figure 7.19: Net occupation of the atoms as the function of position along the axis of the molecule. The fluorine atoms in the CF_3-endgroup attract extra electrons onto the end carbon atom.

However, the calculation of forces at finite bias has not yet been implemented in SMEAGOL, so full self-consistent molecular dynamics simulations have not yet been performed. Hence, the strength of the interaction between the tip and the dipole in the endgroup cannot be calculated accurately. If this effect is not large, the asymmetry in the conductance due to the asymmetrical coupling between the molecule and the leads may swamp any effects due to the movement of the molecule.

The effect of ASIC [75] on this system was also investigated briefly. However, the HOMO-LUMO gaps in these molecules are relatively large, similar to the gap for the BDMT molecule discussed in chapter 6. Thus, although ASIC has the effect of lowering the occupied orbitals, it did not have much of an affect on the transport properties.

7.3   Conclusion

SMEAGOL can be used to simulate STM-type experiments, provided the tip-sample distance is sufficiently small that the basis orbitals have not been artificially cut off (i.e. where the vacuum region between the tip and the surface is still well described).

This allows the study of systems in which the tip is close to the molecule, and allows the effects of finite bias on the electronic structure of the molecule to be incorporated.

Calculations for alkanethiol molecules with in STM-type arrangements show strong asymmetry in the I-V curves, which can be explained by the asymmetry in the coupling to the two different leads. However, the asymmetry observed in these calculations is similar for both CH_3- and CF_3-terminated decanethiol, in contrast to the experimental measurements which showed a far stronger asymmetry for the CF_3-endgroup. The authors of the experimental work speculate that this asymmetry is due to electrostatic tip-endgroup interactions, which causes the distance of the molecule from the STM tip to change. However, this hypothesis cannot be tested as of yet, since calculations of the forces at finite bias have not yet been implemented in SMEAGOL.

The work described in this chapter is still in progress, and the effect of the tilt angle of the molecules on the transport properties is currently being tested using an enlarged unit cell. The effect of using tungsten or platinum-iridium tips instead of gold would also need to be investigated. Finally, the calculation of forces at finite bias is in the process of being implemented in SMEAGOL. This would allow molecular dynamics simulations to be performed for the molecule in the presence of an STM tip at finite bias. Hence, it should be possible to investigate the mechanism proposed to explain the difference between the conductance properties of CH_3- and CF_3-terminated decanethiol. However, such calculations would be very expensive computationally, as the basis set on the gold would have to be extended to at least include the $5d$ orbitals so as to give accurate values for the interatomic distances.

The results presented in this chapter were calculated using LDA. As discussed at length throughout this dissertation, LDA has several problems which can strongly affect electron transport calculations. However, approximate self-interaction corrections such as ASIC [75] are unlikely to offer much of an improvement, since the conductance is due to tunnelling, and would not be particularly sensitive to the exact position of the molecular orbitals. However, for these molecules, accurately calculating the electric polarisability would be important, and this is overestimated by LDA and only partially corrected by ASIC [89, 90].

Chapter 8

Conclusion

Molecular devices have a diverse range of potential applications. In the last few years, it has become possible to fabricate these devices, using a variety of different methods. Unfortunately, the values measured for the conductance of such devices, particularly those formed from π-conjugated molecules such as benzenedithiol, can vary by up to several orders of magnitude depending on which method is used to construct them [19, 26]. Researchers have thus turned to computational modeling to explain these discrepancies, as well as to help in understanding the transport mechanisms. However, electron transport calculations for these systems, particularly those using DFT-LDA, give higher conductances than those obtained from any of the experiments [63, 64, 65, 66, 67, 68, 70]. Explanations which have been suggested for these discrepancies include the fact that the exact geometry of the anchoring configuration between the molecule and the metal is unknown, as well as the errors inherent in the approximations used in the electronic structure methods.

The main focus of this dissertation has been on the effect of various aspects of the self-interaction error [71] contained in approximate exchange-correlation functionals used in DFT on electron transport calculations. In chapter two, I introduced DFT, including the problem of the self-interaction error, and showed how such an error could help in suppressing the derivative discontinuity which should occur in the energy at integer occupations [72, 73]. In chapter three, I used a simple model to show how a discontinuous charging potential, such as would be produced by the derivative discontinuity, can strongly affect the transport properties under certain circumstances, including opening up conductance gaps in the I-V curves [74]. This idea was taken further in chapter five, where a self-consistent tight-binding Hamiltonian which incorporated the derivative discontinuity was used to perform electron transport calculations for BDT attached to gold. Here, it was found that although the derivative discontinuity had little effect when the molecule was strongly coupled

153

to the leads, in the weak coupling limit it could open up a conductance gap. In this weak coupling limit, a molecular level is pinned at the Fermi level of the metal. With a continuous charging potential this level can be occupied as soon as a bias is applied and thus starts to conduct immediately. However, with a discontinuous potential, the level cannot charge and is pinned outside the bias window until its energy increases sufficiently for it to overcome the derivative discontinuity and accept one entire electron. This has the effect of opening up a conductance gap in the *I-V* curve. In fact, this conductance gap is the same size as that observed in one of the experiments [19], although this may have been an artifact of the model Hamiltonian used.

An approximate self-interaction correction in the form of ASIC [75] had been incorporated into SIESTA [82, 83, 84] and thus SMEAGOL [37, 38, 39], and this was used to investigate the self-interaction errors in *ab initio* transport calculations. Although ASIC does not contain the derivative discontinuity due to the atomic and linear scaling approximations, it does produce remarkably accurate values for the ionisation potentials of a variety of different molecules, which can be off by up to 4eV with standard LDA. This corrects the band alignment between the occupied states in the molecule and the Fermi level of the metal. In the case of BDT attached to gold leads, this results in a reduction of the low bias conductivity, improving agreement with experiments [76].

It now appears that the results of theory and experiment are starting to converge for these systems, although some discrepancy still remains. First of all, the exact form of the anchoring geometry between the metal and the molecule remains unknown. Another problem in LDA, which is only partially solved by ASIC, is the overestimation of the electric polarisability [89, 90]. Thirdly, while ASIC corrects the level alignment between the molecule and the metal, it does not reproduce the derivative discontinuity in the energy, which in chapter four was shown to have a strong effect on electron transport in the weak coupling limit. On the other hand, the calculations performed in chapter four using discontinuous potentials involved using a tight-binding Hamiltonian, and thus some of the results obtained may be artifacts of this model. Therefore, in order to understand the complete picture, calculations would have to be performed using an *ab initio* electronic structure theory which produced both the correct band alignment and the derivative discontinuity. These calculations would need to be performed for a variety of different metal-molecule configurations. The electronic structure would need to be recalculated at each bias step, as simply integrating over the zero bias transmission coefficients may not reproduce

some of the effects of the derivative discontinuity. Such work could potentially shed some light on the differences between some of the experimental results.

Potentials which both reproduce the derivative discontinuity and correct the band alignment include the full SIC [71], and exact exchange [88, 114, 53] with local correlation. These are currently in the process of being implemented in SMEAGOL, and it will be interesting to observe their effect on electronic structure calculations of molecular junctions. These methods should also help correct the electric polarisability of the molecules. Unfortunately, such methods are orbital dependent, and so are difficult to implement within NEGF at finite bias.

Finally, I presented the results of some ongoing calculations involving the simulation of STM transport measurements of CH_3- and CF_3-terminated alkanethiol monolayers on a gold surface [81]. The I-V curves were found to be strongly asymmetric due the molecules being coupled far more strongly to the substrate than to the probe tip. In the experimental measurements, the conductance for CF_3-terminated decanethiol was found to be far more strongly asymmetric than that for CH_3-terminated decanethiol, although this was not observed in our calculations. The authors of the experimental work speculate that this may be due to tip-molecule electrostatic interactions causing the molecule to move, but I have not yet investigated this using SMEAGOL.

These calculations are still in progress. The effect of a tilting angle on the transport properties is currently being investigated, and the effect of having the STM tip made of the same metal as that used in the experiments will need to be tested. The calculation of interatomic forces at finite bias is currently in the process of being implemented in SMEAGOL, which will allow the investigation of the effect of electrostatic interaction between the molecule and the tip on the molecule's position. It can then be tested whether or not this interaction is sufficient to explain the difference in the I-V curves for the CH_3- and CF_3-terminated decanethiol observed in the experiments [81].

In conclusion, I have demonstrated that accurate electron transport calculations of molecular devices require electronic structure theories which accurately reproduce both the derivative discontinuity and the correct band alignment between the metal and the molecule. These conditions require the method to be self-interaction free. Correcting these problems would dramatically increase the utility of computational methods in the design of molecular devices, which have the capacity to revolutionise a broad range of technological fields.

Bibliography

[1] A. Aviram and M. A. Ratner, Chem. Phys. Lett. **29**, 277 (1974).

[2] C. Collier, E. Wong, M. Belohradsky, F. Raymo, J. Stoddart, P. Kuekes, R. Williams, and J. Heath, Science **285**, 391 (1999).

[3] Y. Huang, X. Duan, Y. Cui, L. Lauhon, K. Kim, and C. Lieber, Science **294**, 1313 (2001).

[4] S. Tans, A. Verschueren, and C. Dekker, Nature **393**, 49 (1998).

[5] Z. Yao, H. Postma, L. Balents, and C. Dekker, Nature **402**, 273 (1999).

[6] P. Qi, O. Vermesh, M. Grecu, A. Javey, Q. Wang, H. Dai, S. Peng, and K. Cho, Nano Lett. **3**, 347 (2003).

[7] J. Novak, E. Snow, E. Houser, D. Park, J. Stepnowski, and R. McGill, Appl. Phys. Lett. **83**, 4026 (2003).

[8] Y. Cui, W. Qingqiao, H. Park, and C. Lieber, Science **293**, 1289 (2001a).

[9] F. Patolsky, G. Zheng, O. Hayden, M. Lakadamyali, X. Zhuang, and C. Lieber, Proc. Natl. Acad. Sci. USA **101**, 14017 (2004).

[10] M. Zwolak and M. Di Ventra, Nano Lett. **5**, 421 (2005).

[11] J. Lagerqvist, M. Zwolak, and M. Di Ventra, Nano Lett. **6**, 779 (2006).

[12] P. Kuekes, R. Williams, and J. Heath (2000).

[13] P. de Pablo, F. Moreno-Herrero, J. Colchero, J. Gomez Herrero, P. Herrero, A. Baro, P. Ordejon, J. Soler, and E. Artacho, Phys. Rev. Lett. **85**, 4992 (2000).

[14] A. Kasumov, M. Kociak, S. Gueron, B. Reulet, V. Volkov, D. Klinov, and H. Bouchiat, Science **291**, 280 (2001).

[15] B. Xu, P. Zhang, X. Li, and N. Tao, Nano Lett. **4**, 1105 (2004).

[16] E. Braun, Y. Eichen, U. Sivan, and G. Ben-Yoseph, Nature **391**, 775 (1998).

[17] K. Keren, R. Berman, E. Buchstab, U. Sivan, and E. Braun, Science **302**, 1380 (2003).

[18] J. Petta, S. Slater, and D. Ralph, Phys. Rev. Lett. **93**, 136601 (2004).

[19] M. Reed, C. Zhou, C. Muller, T. Burgin, and J. Tour, Science **278**, 252 (1997).

[20] C. Kergueris, J. Bourgoin, S. Palacin, D. Esteve, C. Urbina, M. Magoga, and C. Joachim, Phys. Rev. B **59**, 12505 (1999).

[21] J. Reichert, R. Ochs, D. Beckmann, H. Weber, M. Mayor, and H. v. Löhneysen, Phys. Rev. Lett. **88**, 176804 (2002).

[22] H. Weber, J. Reichert, F. Weigend, R. Ochs, D. Beckmann, M. Mayor, R. Ahlrichs, and H. v. Löhneysen, Chem. Phys. **281**, 113 (2002).

[23] H. Weber, J. Reichert, R. Ochs, D. Beckmann, M. Mayor, and H. v. Löhneysen, Physica E **18**, 231 (2003).

[24] M. Tsutsui, Y. Teramae, S. Kurokawa, and A. Sakai, Appl. Phys. Lett. **89**, 163111 (2006).

[25] J. Ulrich, D. Esrail, W. Pontius, L. Venkataraman, D. Millar, and L. Doerrer, J. Phys. Chem. B **110**, 2462 (2006).

[26] X. Xiao, B. Xu, and N. Tao, Nano Lett. **4**, 267 (2004).

[27] B. Xu and N. Tao, Science **301**, 1221 (2003).

[28] Z. Huang, F. Chen, P. Bennett, and N. Tao, J. Am. Chem. Soc. **129**, 13225 (2007).

[29] S. Ghosh, H. Halimun, A. Mahapatro, J. Choi, S. Lodha, and D. Janes, Appl. Phys. Lett. **87**, 233509 (2005).

[30] T. Dadosh, Y. Gordin, R. Krahne, I. Khivrich, D. Mahalu, V. Frydman, J. Sperling, A. Yacoby, and I. Bar-Joseph, Nature **436**, 677 (2005).

[31] M. Dorogi, J. Gomez, R. Osifchin, R. Andres, and R. Reifenberger, Phys. Rev. B **52**, 9071 (1995).

[32] D. Gittins, D. Bethell, D. Schiffrin, and R. Nichols, Nature **408**, 67 (2000).

[33] X. Cui, A. Primak, X. Zarate, J. Tomfohr, O. Sankey, A. Moore, T. Moore, D. Gust, G. Harris, and S. Lindsay, Science **294**, 571 (2001b).

[34] S. Datta, *Electronic Transport in Mesoscopic Systems* (Cambridge University Press, Cambridge, UK, 1995).

[35] C. Caroli, R. Combescot, P. Nozieres, and D. Saint-James, J. Phys. C **5**, 21 (1972).

[36] J. Ferrer, A. Martin-Rodero, and F. Flores, Phys. Rev. B (Rapid Comm.) **38**, 10113 (1988).

[37] A. Rocha, V. Garcia-Suarez, S. Bailey, C. Lambert, J. Ferrer, and S. Sanvito, Nature Materials **4**, 335 (2005).

[38] A. Rocha, V. Garcia-Suarez, S. Bailey, C. Lambert, J. Ferrer, and S. Sanvito, Phys. Rev. B **73**, 085414 (2006).

[39] A. Rocha, V. Garcia-Suarez, S. Bailey, C. Lambert, J. Ferrer, and S. Sanvito, *SMEAGOL: Spin and Molecular Electronics in Atomically Generated Orbital Landscapes (non-equilibrium electronic transport)*, URL www.smeagol.tcd.ie.

[40] M. Brandbyge, J. Mozos, P. Ordejón, J. Taylor, and K. Stokbro, Phys. Rev. B **65**, 165401 (2002).

[41] H. Taylor, J. Guo and J. Wang, Phys. Rev. B **63**, 245407 (2001).

[42] S. Ke, H. Baranger, and W. Yang, Phys. Rev. B **70**, 085410 (2004).

[43] H. Hohenberg and W. Kohn, Phys. Rev. **136**, B864 (1964).

[44] W. Kohn and L. Sham, Phys. Rev. **140**, A1133 (1965).

[45] R. Parr and W. Yang, *Density-Functional Theory of Atoms and Molecules* (vol. 16 of The International Series of Monographs on Chemistry, Oxford University Press, Oxford, UK, 1989).

[46] P. Kornilovitch and A. Bratkovsky, Phys. Rev. B **64**, 195413 (2001).

[47] A. Bratkovsky and P. Kornilovitch, Phys. Rev. B **67**, 115307 (2003).

[48] E. Emberly and G. Kirczenow, Phys. Rev. B **58**, 10911 (1998).

[49] P. Damle, A. Ghosh, and S. Datta, Phys. Rev. B (Rapid Comm.) **64**, 201403 (2001).

[50] M. Hettler, W. Wenzel, M. Wegewijs, and H. Schoeller, Phys. Rev. Lett. **90**, 076805 (2003).

[51] P. Delaney and J. Greer, Phys. Rev. Lett. **93**, 036805 (2004).

[52] B. Muralidharan, A. Ghosh, and S. Datta, Phys. Rev. B **73**, 155410 (2006).

[53] S. Ke, H. Baranger, and W. Yang, J. Chem. Phys. **126**, 201102 (2007).

[54] K. Thygesen and A. Rubio, J. Chem. Phys. **126**, 091101 (2007).

[55] G. Solomon, J. Reimers, and N. Hush, J. Chem. Phys. **121**, 6615 (2004).

[56] G. Solomon, J. Reimers, and N. Hush, J. Chem. Phys. **122**, 224502 (2005).

[57] E. Runge and E. Gross, Phys. Rev. Lett. **52**, 997 (1984).

[58] S. Kurth, G. Stefanucci, C. Almbladh, A. Rubio, and E. Gross, Phys. Rev. B **72**, 034308 (2005).

[59] D. Langreth and M. Mehl, Phys. Rev. B **28**, 1809 (1983).

[60] J. Perdew, Phys. Rev. Lett. **55**, 1665 (1985).

[61] J. Perdew, K. Burke, and M. Ernzerhof, Phys. Rev. Lett. **77**, 3865 (1996).

[62] P. Ordejón, E. Artacho, and J. Soler, Phys. Rev. B **53**, 10441 (1996).

[63] M. Di Ventra, S. Pantelides, and N. Lang, Phys. Rev. Lett. **84**, 979 (2000).

[64] Y. Xue and M. Ratner, Phys. Rev. B **68**, 115406 (2003a).

[65] Y. Xue and M. Ratner, Phys. Rev. B **68**, 115407 (2003b).

[66] H. Basch, R. Cohen, and M. Ratner, Nano Lett. **5**, 1668 (2005).

[67] D. Andrews, R. Cohen, R. Van Duyne, and M. Ratner, Jour. Chem. Phys. **125**, 174718 (2006).

[68] K. Stokbro, J. Taylor, M. Brandbyge, J. Mozos, and P. Ordejon, Comp. Mat. Sci. **27**, 151 (2003).

[69] F. Evers, F. Weigend, and M. Koentopp, Phys. Rev. B **69**, 235411 (2004).

[70] S. Ke, H. Baranger, and W. Yang, J. Chem. Phys. **122**, 074704 (2005).

[71] J. Perdew and A. Zunger, Phys. Rev. B **23**, 5048 (1981).

[72] J. Perdew, R. Parr, M. Levy, and J. Balduz Jr., Phys. Rev. Lett. **49**, 1691 (1982).

[73] J. Perdew and M. Levy, Phys. Rev. Lett. **51**, 1884 (1983).

[74] C. Toher, A. Filippetti, S. Sanvito, and K. Burke, Phys. Rev. Lett. **95**, 146402 (2005).

[75] C. Pemmaraju, T. Archer, D. Sanchez-Portal, and S. Sanvito, Phys. Rev. B **75**, 045101 (2007).

[76] C. Toher and S. Sanvito, Phys. Rev. Lett. **99**, 056801 (2007).

[77] G. Binnig, H. Rohrer, C. Gerber, and E. Weibel, Appl. Phys. Lett. **40**, 178 (1981).

[78] G. Binnig, H. Rohrer, C. Gerber, and E. Weibel, Phys. Rev. Lett. **49**, 57 (1982).

[79] J. Tersoff and D. Hamann, Phys. Rev. Lett. **50**, 1998 (1983).

[80] J. Tersoff and D. Hamann, Phys. Rev. B **31**, 805 (1985).

[81] J. Pflaum, G. Bracco, F. Schreiber, R. Colorado Jr., O. Shmakova, T. Lee, G. Scoles, and A. Kahn, Surface Science **89**, 498 (2002).

[82] J. Soler, E. Artacho, J. Gale, A. García, J. Junquera, P. Ordejón, and D. Sanchez-Portal, J. Phys. Cond. Matter **14**, 2745 (2002).

[83] E. Artacho, D. Sanchez-Portal, P. Ordejón, A. García, and J. Soler, Phys. Stat. Sol. **215**, 809 (1999).

[84] J. Soler, E. Artacho, J. Gale, A. García, J. Junquera, P. Ordejón, and D. Sanchez-Portal, *SIESTA: Spanish Initiative for Electronic Structure Calculations with Thousands of Atoms*, URL http://www.uam.es/departamentos/ciencias/fismateriac/siesta.

[85] M. Paulsson, F. Zahid, and S. Datta, Nanoscience, Engineering and Technology Handbook (2003), also on cond-mat/0208183.

[86] R. Martin, *Electronic Structure: Basic Theory and Practical Methods* (Cambridge University Press, Cambridge, UK, 1989).

[87] J. Janak, Phys. Rev. B **18**, 7165 (1978).

[88] A. Görling and M. Levy, Phys. Rev. A **50**, 196 (1994).

[89] C. Pemmaraju, S. Sanvito, and K. Burke, cond-mat/07082814.

[90] T. Körzdörfer, M. Mundt, and S. Kümmel, cond-mat/07082870.

[91] V. Anisimov, J. Zaanen, and O. Andersen, Phys. Rev. B **44**, 943 (1991).

[92] J. Hubbard, Proc. Roy. Soc., (London) **A276**, 238 (1963).

[93] A. Becke, J. Chem. Phys. **98**, 5648 (1993).

[94] C. Lee, W. Yang, and R. Parr, Phys. Rev. B **37**, 785 (1988).

[95] J. Tao, J. Perdew, V. Staroverov, and G. Scuseria, Phys. Rev. Lett. **91**, 146401 (2003).

[96] N. Troullier and J. Martins, Phys. Rev. B **43**, 1993 (1991).

[97] L. Kleinman and D. Bylander, Phys. Rev. Lett. **48**, 1425 (1982).

[98] O. Sankey and D. Niklewski, Phys. Rev. B **40**, 3979 (1989).

[99] D. Vogel, P. Krüger, and J. Pollmann, Phys. Rev. B **54**, 5495 (1996).

[100] A. Filippetti and N. Spaldin, Phys. Rev. B **67**, 125109 (2003).

[101] A. Filippetti, Phys. Rev. A **57**, 914 (1998).

[102] L. Keldysh, Sov. Phys. JETP **20**, 1018 (1965).

[103] E. Economou, *Green's Functions in Quantum Physics* (Spinger-Verlag, New York, 1983).

[104] W. Press, B. Flannery, S. Teukolsky, and W. Vetterling, *Numerical Recipes in Fortran* (Cambridge University Press, Cambridge, UK, 1992).

[105] M. Büttiker, Y. Imry, R. Landauer, and S. Pinhas, Phys. Rev. B **31**, 6207 (1985).

[106] D. Fisher and P. Lee, Phys. Rev. B **23**, 6851 (1981).

[107] Y. Meir and N. Wingreen, Phys. Rev. Lett. **68**, 2512 (1992).

[108] S. Sanvito, C. Lambert, J. Jefferson, and A. Bratkovsky, Phys. Rev. B **59**, 11936 (1999).

[109] E. Anderson, Z. Bai, C. Bischof, S. Blackford, J. Demmel, J. Dongarra, J. Du Croz, A. Greenbaum, S. Hammarling, A. McKenney, et al., *LAPACK Users' Guide* (Society for Industrial and Applied Mathematics, Philadelphia, PA, 1999).

[110] A. Sutton, *Electronic Structure of Materials* (Oxford University Press, Oxford, UK, 1993).

[111] W. Harrison, *Electronic Structure and the Properties of Solids: the physics of the chemical bond* (Dover Publications, New York, 1989).

[112] D. Porezag, T. Frauenheim, T. Köhler, G. Seifert, and R. Kaschner, Phys. Rev. B **51**, 12947 (1995).

[113] A. Rocha, Ph.D. thesis, Trinity College Dublin (2006).

[114] W. Yang and Q. Wu, Phys. Rev. Lett. **89**, 143002 (2002).

[115] R. Pontes, F. Novaes, A. Fazzio, and A. da Silva, J. Am. Chem. Soc. **128**, 8996 (2006).

[116] M. Yu, N. Bovet, C. Satterley, S. Bengio, K. Lovelock, P. Milligan, R. Jones, D. Woodruff, and V. Dhanak, Phys. Rev. Lett. **97**, 166102 (2006).

[117] W. Shen and G. Nyberg, J. Electron Spectrosc. Relat. Phenom. **60**, 225 (1992).

[118] H. Sellers, A. Ullman, Y. Shnidman, and J. Eilers, J. Am. Chem. Soc. **115**, 9389 (1993).

[119] Y. Kim, S. Jang, and W. Goddard III, J. Chem. Phys. **122**, 244703 (2005).

[120] R. van Leeuwen and E. Baerends, Phys. Rev. A **49**, 2421 (1994).

[121] O. Gritsenko, P. Schipper, and E. Baerends, Chem. Phys. Lett. **302**, 199 (1999).

[122] Q. Sun and A. Selloni, Jour. Phys. Chem. A **110**, 11396 (2006).

Appendix A

Publications stemming from this work

- Efficient Atomic Self-Interaction Correction Scheme for Nonequilibrium Quantum Transport, C. Toher and S. Sanvito, Phys. Rev. Lett., **99**, 056801 (2007). Also, cond-mat/0611617.

- Self-Interaction Errors in Density-Functional Calculations of Electronic Transport, C. Toher, A. Filippetti, S. Sanvito, and Kieron Burke, Phys. Rev. Lett., **95**, 146402 (2005). Also, cond-mat/0506244.

- Effects of self-interaction corrections on the transport properties of phenyl-based molecular junctions, C. Toher and S. Sanvito, accepted by Phys. Rev. **B**. Also, cond-mat/07121747.

- Simulation of STM Quantum Transport Measurements in Alkanes, in preparation, C. Toher and S. Sanvito, in preparation.

- Use of Embedding Method for Non-equilibrium Transport Calculations, C. Toher, M. Khadilkar, I. Rungger, and S. Sanvito, in preparation.